Marjut Hukkanen

Penning-Trap Mass Spectrometry: Commissioning of PIPERADE and Measurements of Neutron-Rich A = 100 – 120 Nuclei at JYFLTRAP

université
de BORDEAUX

UNIVERSITY OF JYVÄSKYLÄ
FACULTY OF MATHEMATICS
AND SCIENCE

Marjut Hukkanen

Penning-Trap Mass Spectrometry: Commissioning of PIPERADE and Measurements of Neutron-Rich $A = 100 - 120$ Nuclei at JYFLTRAP

Esitetään Jyväskylän yliopiston matemaattis-luonnontieteellisen tiedekunnan suostumuksella
julkisesti tarkastettavaksi yliopiston Ylistönrinteen salissa FYS1
heinäkuun 21. päivänä 2023 kello 12.

Academic dissertation to be publicly discussed, by permission of
the Faculty of Mathematics and Science of the University of Jyväskylä,
in Ylistönrinne, auditorium FYS1, on July 21, 2023 at 12 o'clock noon.

Cotutelle dissertation between
Department of Material and Light Sciences University of Bordeaux
and Department of Physics University of Jyväskylä

université
de **BORDEAUX**

JYVÄSKYLÄN YLIOPISTO
UNIVERSITY OF JYVÄSKYLÄ

JYVÄSKYLÄ 2023

Editors
Ilari Maasilta
Department of Physics, University of Jyväskylä
Ville Korkiakangas
Open Science Centre, University of Jyväskylä

ABSTRACT

Hukkanen, Marjut
Penning-trap mass spectrometry: commissioning of PIPERADE and measurements of neutron-rich $A = 100 - 120$ nuclei at JYFLTRAP

Penning-trap mass spectrometry allows to measure masses of atomic nuclei with a very high precision. Nuclear binding energies, determined from the atomic masses, are used to study the structure of exotic nuclei, and are also key inputs for nucleosynthesis models. In this thesis, two Penning traps have been utilized. The PIPERADE (PIèges de PEnning pour les RAdionucléides à DESIR) double Penning trap was commissioned at the LP2i Bordeaux. The results from the first trapping of ions, the implementation of the buffer gas cooling technique, a method to select the ions of interest, all the way to the results of the first time-of-flight ion-cyclotron-resonance (TOF-ICR) mass measurement, are reported. PIPERADE will be dedicated to precision mass measurements and ion of interest selection in the new research facility DESIR (Désintégration, Excitation et Stockage d'Ions Radioactifs) at the GANIL (Grand Accélérateur National d'Ions Lourds) Accelerator laboratory.

The JYFLTRAP double Penning trap was utilized at the Ion Guide Isotope Separator On-Line (IGISOL) facility of the Accelerator Laboratory of University of Jyväskylä to perform precision mass measurements of neutron-rich rhodium, ruthenium, molybdenum, niobium, zirconium and yttrium isotopes in the mass region $A \approx 100 - 120$. In total 15 ground- and eight isomeric-state masses were measured. Altogether eight masses were determined for the first time, while for the rest the precision of the atomic mass was improved significantly. The phase-imaging ion-cyclotron-resonance technique (PI-ICR) allowed for the first time the separation of the isomeric states from the ground states, and precision mass measurement of each state independently. The most exotic rhodium, ruthenium, molybdenum and niobium isotopes were measured using the TOF-ICR technique. In addition, the half-lives of the ground and isomeric states of ^{112}Rh were measured. From the measured masses, several observables, such as the two-neutron separation energies, were extracted and compared to the values predicted by the Hartree-Fock-Bogoliubov based global mass models BSkG1 and BSkG2. The impact of the new mass values on the neutron-capture rates needed for the astrophysical rapid neutron capture process was also studied.

Keywords: Penning trap, PIPERADE, JYFLTRAP, isomers, nuclear structure.

TIIVISTELMÄ (ABSTRACT IN FINNISH)

Hukkanen, Marjut
Massaspektrometriaa Penningin loukulla: PIPERADE-loukun käyttöönotto ja massa-alueen $A = 100 − 120$ neutronirikkaiden ydinten massamittaukset JYFLTRAP-loukulla

Penningin loukku on massaspektrometri, jolla voidaan mitata atomimassoja erittäin tarkasti. Atomimassoista laskettuna ydinten sidosenergiaa käytetään eksoottisten ydinten ydinrakenteen tutkimiseen, ja se on yksi merkittävimmistä parametreista alkuainesynteesin mallintamisessa. Tässä väitöskirjassa tehtiin tutkimusta kahta eri Penningin loukkua hyödyntäen. PIPEDADE (PIèges de PEnning pour les RAdionucléides à DESIR) koostuu kahdesta Penningin loukusta, ja se otettiin käyttöön LP2i-laboratoriossa Bordeaux'ssa. Tutkimuksessa ionit vangittiin PIPERADE-loukkuun ensimmäistä kertaa. Tutkittavat ionit valittiin jäädyttämällä puskurikaasun avulla ensimmäisessä loukussa ja niiden massat mitattiin lentoaikasyklotroniresonanssitekniikalla (TOF-ICR) jälkimmäisessä loukussa. PIPERADE-loukkua tullaan käyttämään korkean tarkkuuden massamittauksiin, sekä kohdeionien valintaan uudessa DESIR (Désintégration, Excitation et Stockage d'Ions Radioactifs) tutkimuslaitoksessa GANIL (Grand Accélérateur National d'Ions Lourds)-kiihdytinlaboratoriossa.

JYFLTRAP on kahdesta Penningin loukusta koostuva massaspektrometri Jyväskylän yliopiston kiihdytinlaboratorion IGISOL (Ion Guide Isotope Separator On-Line)-laitteistolla. Sen avulla mitattiin tarkasti neutronirikkaiden rodium-, rutenium-, molybdeeni-, niobium-, zirkonium- ja yttriumisotooppien atomimassoja massa-alueella $A = 100 − 120$. Kaikkiaan mitattiin 15 perustilan ja kahdeksan isomeerisen tilan atomimassaa. Yhteensä kahdeksan atomimassaa määritettiin ensimmäistä kertaa, muissa tapauksissa tarkkuutta parannettiin huomattavasti kirjallisuusarvoihin verrattuna. Ionien vaihekulman määrittämiseen perustuvalla syklotroniresonanssitekniikalla (PI-ICR) saatiin ensimmäistä kertaa erotettua isomeeriset tilat perustiloista, ja mitattua tilojen massat erikseen. Eksoottisimpien rodium-, rutenium-, molybdeeni- ja niobiumisotooppien atomimassat mitattiin lentoaikasyklotroniresonanssitekniikkaa (TOF-ICR) käyttäen. Lisäksi ^{112}Rh-isotoopin perustilan ja isomeerisen tilan puoliintumisajat mitattiin. Mitattujen massojen avulla määritettiin useita ytimen sidosenergiaan liittyviä arvoja, kuten kahden neutronin separaatioenergiat. Näitä määritettyjä arvoja verrattiin globaaleihin Hartree-Fock-Bogoliubov-massamalleihin BSkG1 ja BSkG2. Uusien massojen vaikutus neutronisieppausreaktioihin selvitettiin. Näitä tarvitaan astrofysikaalisen nopean neutronisieppausprosessin tutkimuksessa.

Avainsanat: Penningin loukku, PIPERADE, JYFLTRAP, PI-ICR, isomeerit, ydinrakenne.

RÉSUMÉ (ABSTRACT IN FRENCH)

Hukkanen, Marjut
Spectrométrie de masse avec des pièges de Penning : mise en service du dispositif PIPERADE et mesures de masses des noyaux riches en neutrons dans la région de masse A=100-120 avec le dispositif JYFLTRAP

La spectrométrie de masse avec des pièges de Penning permet de mesurer les masses des noyaux atomiques avec une très grande précision. Les énergies de liaison nucléaire, déterminées à partir des masses atomiques, sont utilisées pour étudier la structure des noyaux exotiques et sont également des données essentielles pour les modèles de nucléosynthèse. Dans cette thèse, deux pièges de Penning ont été utilisés. Le double piège de Penning PIPERADE (PIèges de PEnning pour les RAdionucléides à DESIR) a été mis en service au LP2i Bordeaux. Les résultats du premier piégeage d'ions, de la mise en œuvre de la technique de refroidissement par gaz tampon, d'une méthode de sélection des ions d'intérêt et les résultats de la première mesure de masse par résonance en temps de vol (TOF-ICR) sont présentés. A l'avenir, PIPERADE sera dédié aux mesures de masse de précision et à la sélection des ions exotiques d'intérêt dans la nouvelle installation de recherche DESIR (Désintégration, Excitation et Stockage d'Ions Radioactifs) du laboratoire GANIL (Grand Accélérateur National d'Ions Lourds). Le double piège de Penning JYFLTRAP a été utilisé auprès de l'installation IGISOL (Ion Guide Isotope Separator On-Line) du laboratoire de l'accélérateur de l'Université de Jyväskylä pour effectuer des mesures de masse de précision des isotopes riches en neutrons de rhodium, ruthénium, molybdène, niobium, zirconium et yttrium dans la région de masse A 100 - 120. Au total, 15 masses d'états fondamentaux et 8 masses d'états isomériques ont été mesurées. Huit masses ont été déterminées pour la première fois, tandis que pour les autres, la précision a été considérablement améliorée. La technique d'imagerie (PI-ICR) a permis pour la première fois de séparer les états isomères des états fondamentaux et de mesurer avec précision la masse de chaque état indépendamment. Les isotopes les plus exotiques du rhodium, du ruthénium, du molybdène et du niobium ont été mesurés à l'aide de la technique TOF-ICR. Enfin, les demi-vies de l'état fondamental et l'état isomérique du ^{112}Rh ont été mesurées. À partir des masses mesurées, plusieurs observables, telles que les énergies de séparation de deux neutrons, ont été extraites et comparées aux valeurs prédites par les modèles de masse de type Hartree-Fock-Bogoliubov BSkG1 et BSkG2. L'impact des nouvelles valeurs de masse sur les taux de capture de neutrons importants pour décrire le processus astrophysique de capture rapide de neutrons a également été étudié.

Piège de Penning, PIPERADE, JYFLTRAP.

Author   Marjut Hukkanen
                      Department of Physics
                      University of Jyväskylä
                      Finland

                      Université de Bordeaux, LP2i Bordeaux
                      France

Supervisors   Professor Anu Kankainen
                      Department of Physics
                      University of Jyväskylä
                      Finland

                      Dr. Tommi Eronen
                      Department of Physics
                      University of Jyväskylä
                      Finland

                      Dr. Pauline Ascher
                      Université de Bordeaux, LP2i Bordeaux
                      France

                      Dr. Stéphane Grévy
                      Université de Bordeaux, LP2i Bordeaux
                      France

Reviewers   Associate professor Julia Even
                      University of Groningen
                      Netherlands

                      Associate professor Maxime Brodeur
                      University of Notre Dame
                      USA

Opponent   Professor Michael Block
                      Johannes Gutenberg University of Mainz
                      Germany

PREFACE

The work presented in this thesis has been carried out in the IGISOL group of University of Jyväskylä, Finland, and in the NEX group of LP2i Bordeaux, France.

I would like to start by thanking my opponent Prof. Michael Block for taking your time to review my thesis, I am sure we had a fruitful discussion at the defense. I would like to express my gratitude to the reviewers of my thesis Assoc. Prof. Julia Even and Assoc. Prof. Maxime Brodeur for your careful work reviewing my thesis and I am truly grateful for all the kind feedback you gave me. I thank the rest of my jury members, Assoc. Prof. Tuomas Grahn, Dr. Beatriz Jurado and Dr. Christine Marquet, for accepting the jury duty.

My deepest gratitude and biggest thank you's go to my supervisors Prof. Anu Kankainen, Dr. Pauline Ascher, Dr. Tommi Eronen and Dr. Stéphane Grévy. Thank you Anu for your guidance over all these years and for always looking out for my best. Thank you Pauline for your support and mentoring during the PhD and sharing your expertise. Thank you to Tommi for sharing your expertise with the Penning traps, and to Stéphane for the insightful thoughts on various physics topics. I would like to thank the administrative and practical help both from JYU and UB/LP2iB especially from Minttu Haapaniemi, Marjut Hilska, Isabelle Moreau and Nadine Carmona. I also acknowledge the help received from the mechanical and electrical workshops.

I want to thank the past and present people of the IGISOL group. I am especially grateful to Dr. Dmitriy "trap-master" Nesterenko for your endless wisdom on Penning traps and always answering my questions. Thank you to Dr. Marek Stryjczyk for all the help, invaluable advice and endless knowledge on references. I would also like to acknowledge the present and past JYFLTRAP/mass measurement team members, and to the next mass-PhD students Ville, Arthur and Jouni, you are doing great and good luck!

To the NEX group at the LP2I Bordeaux I owe you all a heartfelt thank you. I arrived in Bordeaux in March 2020, while the world was in chaos due to the painful COVID19 pandemic. You took me in and supported me through the difficult time as best as possible. A special thank you to the PIPERADE team: Pauline, Mathias, Stéphane, Audric, Antoine, Mathieu, Dinko, Laurent, Philippe. Thank you to Dr. Antoine de Roubin for your always positive attitude and encouraging words over the years. I am grateful to Dr. Audric Husson and Mathieu Flayol for all the company during long lab hours. To Victoria and Veronika thank you for your friendship starting from our time in Bordeaux. Merci beaucoup!

I would like to express my gratitude to Dr. Wouter Ryssens and Dr. Michael Bender, without you this work would have truly been lacking an important part. Your expertise on the realm of nuclear theory and patience in explaining is truly appreciated. Thank you Dr. Stylianos Nikas for your contributions on the r-process studies.

To the newly appointed Doctors Lama, George and Daniel: thank you for your friendship and all the memories we made. Hussam, Wouter, Sarina and

Minna, thank you as well. I am grateful to all the people I have met during this journey, your friendship and advice is greatly acknowledged. Thank you to the Naisfyysi(k)ot for being there from the beginning to the end and beyond. Thank you Anna, my dearest bestest friend, for your support and always telling me that I am the smartest person you know. Thank you to Daniel for the years of shared everyday and your support. Thank you to my family for the support. Kiitos!

In Jyväskylä, June 2023

Marjut Hukkanen

ACKNOWLEDGEMENTS

LIST OF INCLUDED ARTICLES

PI   M. Hukkanen, W. Ryssens, P. Ascher, M. Bender, T. Eronen, S. Grévy, A. Kankainen, M. Stryjczyk, L. Al Ayoubi, S. Ayet, O. Beliuskina, C. Delafosse, W. Gins, M. Gerbaux, A. Husson, A. Jokinen, D. A. Nesterenko, I. Pohjalainen, M. Reponen, S. Rinta-Antila, A. de Roubin and A. P. Weaver. Odd-odd neutron-rich rhodium isotopes studied with the double Penning trap JYFLTRAP. *Physical Review C, 107:014306*, 2023.

PII   M. Hukkanen, W. Ryssens, P. Ascher, M. Bender, T. Eronen, S. Grévy, A. Kankainen, M. Stryjczyk, L. Al Ayoubi, S. Ayet, O. Beliuskina, C. Delafosse, Z. Ge, M. Gerbaux, W. Gins, A. Husson, A. Jaries, S. Kujanpää, M. Mougeot, D. A. Nesterenko, S.Nikas, H. Penttilä, I. Pohjalainen, A. Raggio, M. Reponen, S. Rinta-Antila, A. de Roubin, J. Ruotsalainen, V. Virtanen and A. P. Weaver. Binding energies of ground and isomeric states in neutron-rich Ru isotopes: measurements at JYFLTRAP and comparison to theory. *Submitted to Physical Review C.*

PIII P. Ascher, L. Daudin, M. Flayol, M. Gerbaux, S. Grévy, M. Hukkanen, A. Husson, A. de Roubin, P. Alfaurt, B. Blank, K. Blaum, B. Lachacinski, D. Lunney, E. Minaya Ramirez, S. Naimi, S. Perard and B. Thomas. PIPERADE: A double Penning trap for mass separation and mass spectrometry at DESIR/SPIRAL2. *Nuclear Instruments and Methods in Physics Research Section A: Accelerators, Spectrometers, Detectors and Associated Equipment*, 2021.

The author of this thesis has contributed to the attached articles PI and PII by being a part of writing the proposal and proposing the experiment, participated in the two(/three) experiments conducted and was the spokesperson of these two experiments. The author did the analysis of the measured data, contributed to the writing of the manuscripts and was part of interpreting the data. Contribution of the author on the article PIII was the commissioning part, from the first ion trapping to the successful tests of the buffer-gas cooling technique.

CONTENTS

1 INTRODUCTION

An atom consists of protons and neutrons forming a nucleus, and of electrons orbiting the nucleus. Almost all of the mass of an atom is in the nucleus, while electrons contribute only a little to the total mass of the atom. One of the most fundamental properties of the nucleus is its mass, reflecting its binding energy i.e. the interactions between its constituents. In Fig. 1 the nuclear chart is presented where experimentally known nuclei are shown as a function of their neutron (N) and proton (Z) number. Nuclei which have the same proton number but a different amount of neutrons in the nucleus are called isotopes. Thus when one moves horizontally on the nuclear chart, one moves along an isotopic chain. If the nuclei have the same mass number $A = Z + N$, but different proton and neutron numbers, they are called isobars. An isomer is a long-living excited state of the nucleus. The experimental data used to plot the nuclear chart of Fig. 1 is from the Atomic Mass Evaluation 2020 (AME20) [1]. The AME collects experimental data and compiles it into atomic mass data tables. The latest evaluation was published in 2020, listing 2550 experimentally measured ground-state masses and 406 isomeric-state masses, which are listed in NUBASE20 published at the same time [1, 2].

Nuclear binding energies can be derived from the atomic masses and used to study the nuclear structure properties of the said nuclei. The structure of a nucleus can be explained via nucleons occupying discrete energy single-particle levels, which form shells. When the shells are separated by a large energy gap, the corresponding number of nucleons is called a "magic number". For example, the magic numbers of protons or neutrons, for which the nucleus is much more bound, have been evidenced thanks to mass spectrometry. Moving away from these magic numbers, the shape of the nucleus is no longer spherical but the nucleus exhibits deformation. Nuclear mass does not give a direct indication of the size of the deformation, but it can be used to probe the shape transitions and other structural effects via studying trends of mass differences, the so-called mass filters. This thesis studies neutron-rich refractory nuclides with $Z = 39 - 45$, which are known for having vastly changing shapes [3]. If one looks at the nuclear chart in Fig. 1, these nuclei are located in the midshell region between the
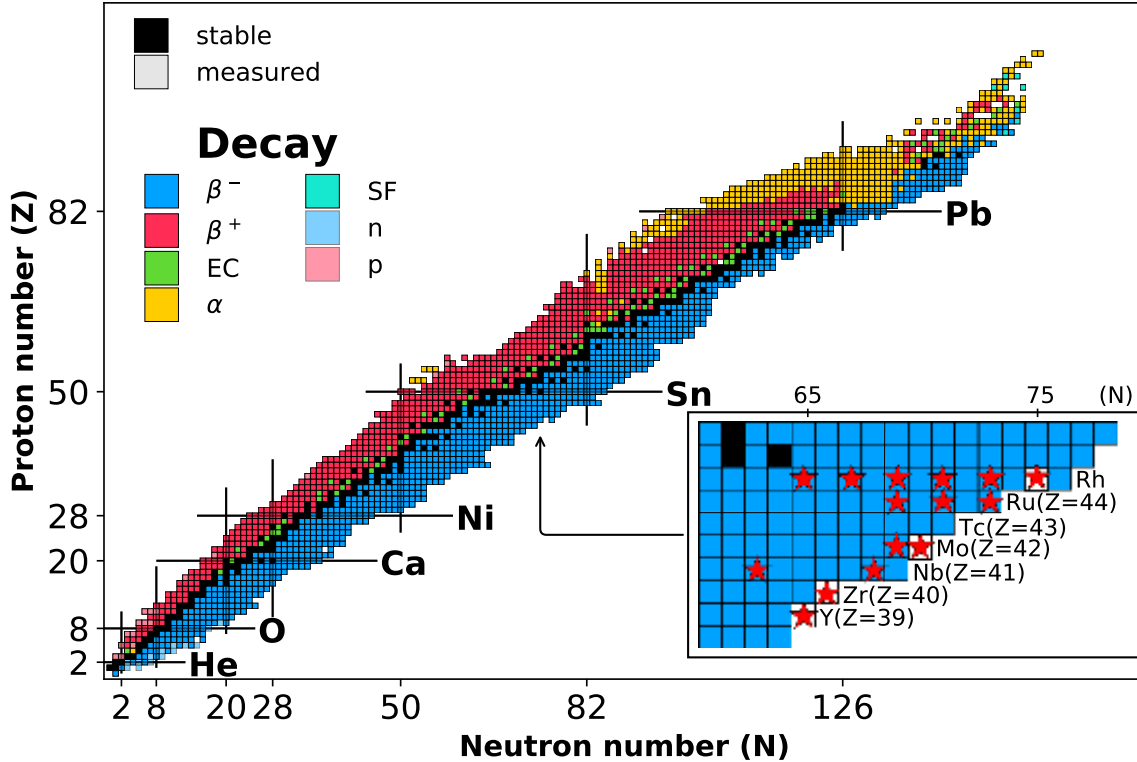
FIGURE 1   The nuclear chart with the region of interest in these measurements high-lighted. Magic proton and neutron numbers are indicated with black lines. Adapted from J. Karthein 2019 [5].

magic neutron numbers $N = 50$ and 82, and magic proton numbers $Z = 28$ and 50.

The masses of neutron-rich nuclei far from stability are also of importance for the astrophysical nucleosynthesis calculations, especially for the rapid neutron-capture process [4], the r-process, which is responsible for around half of the heavy elements produced in our universe. The process develops close to the neutron dripline, where experimental properties of the nuclei are mostly out of reach of the experimental facilities of today. The properties of exotic nuclei reachable with experimental techniques help to develop models that can further predict the properties of the nuclei needed for simulating the r-process, for which nuclear masses/nuclear binding energies are one of the key inputs.

The most precise way of measuring the mass of an atom is to use a device called Penning trap, developed by F.M. Penning and H. Dehmelt [6, 7]. It utilizes a strong magnetic field and a quadrupolar electric field to confine charged particles in radial and axial directions. In a Penning trap the eigenmotions of a charged particle can be manipulated using radio frequency electric fields and utilizing buffer gas, most importantly even mass-selectively. These manipulations allow to perform high-precision mass measurements, but also to select the ions of interest from a contaminated beam. Penning traps are found in many modern radioactive ion beam (RIB) facilities: JYFLTRAP- JYFL-ACCLAB [8], ISOLTRAP-CERN, CPT-Argonne just to name a few. The JYFLTRAP double Penning trap, utilized in this thesis, is found at The Ion Guide Isotope Separator On-Line (IGISOL) facility of

the Accelerator Laboratory of University of Jyväskylä (JYFL-ACCLAB), Finland. The JYFLTRAP double Penning trap has been in use for the past two decades successfully performing mass measurements and ion beam purification/selection. Penning traps keep being a vital tool in RIB facilities and are a sought after device for the new upcoming radioactive ion beam facilities. In the context of a new upcoming facility called DESIR, a double Penning trap device called PIPERADE is being commissioned at the LP2i Bordeaux laboratory. This thesis reports on its first commissioning in 2020-2021.

The IGISOL facility has a long history of studying the refractory region elements. Due the chemical nature of these nuclei they are difficult to produce in other facilities, but the ion-guide technique, developed in Jyväskylä in 1980s [9], is chemically insensitive and has thus given a good opportunity to study these elements. Their nuclear properties have been investigated for example via laser spectroscopy in Ref. [10] (charge-radii), via decay studies [11, 12, 13, 14, 15, 16, 17] (half-lives, spin/parities) and mass measurements [18, 19, 20, 21]. This thesis expands the mass measurements of the neutron-rich refractory nuclides in the region $A = 100 - 120$, highlighted in Fig. 1. The newer high-resolution phase-imaging ion-cyclotron-resonance (PI-ICR) technique [22] was used to separate and measure masses of ground states and low-lying isomers. Many of these isomer excitation energies were measured directly for the first time, since the previous mass measurement technique utilized at JYFLTRAP, time-of-flight ion-cyclotron-resonance (TOF-ICR) [23], did not have high enough resolving power.

This thesis is organized as follows: Chapter 2 describes the scientific motivations for the precision mass measurements conducted in this work in the neutron-rich refractory nuclei region $A = 100 - 120$. Chapter 3 introduces the theoretical background of Penning-trap mass spectrometers and the mass measurement techniques relevant for this work. Chapters 4 and 5 portray one future and two existing facilities, DESIR, LP2iB and IGISOL, and the two Penning traps used in this work namely PIPERADE and JYFLTRAP. Chapter 4 also includes the results obtained for the commissioning of the PIPERADE double Penning trap during this work. Chapter 6 describes the methods used for the analysis of the JYFLTRAP mass measurement data, while Chapter 7 shows the results and discussions related to the mass measurements performed at the JYFLTRAP in the neutron-rich refractory region of mass $A = 100 - 120$ during this work. Finally the thesis is closed with a Summary and Outlook in Chapter 8.

2 SCIENTIFIC MOTIVATIONS

2.1 Mass and binding energy

The atomic nucleus, where most of the mass of the atom is located, consists of bound nucleons: N neutral neutrons and Z positively-charged protons. The nucleons are held together by an interaction called the nuclear strong force [24], whereas the electrons orbiting the nucleus are bound by the Coulomb force. If the mass of Z protons and the mass of N neutrons are added together, the obtained value is larger than the mass of the corresponding nucleus. The difference comes from the binding energy, which reflects the sum of all the interactions between the nucleons. The binding energy $BE(Z, N)$ of an atom can be expressed as follows

$$BE(Z, N) = \{Zm_p + Nm_n - [m(Z, N) - Zm_e]\}c^2 \tag{1}$$

where m_p and m_n are the mass of the proton and the neutron, $m(Z, N)$ is the atomic mass of an element with Z protons and N neutrons, m_e is the electron mass and c is the speed of light in vacuum. The electron binding energy has been neglected since it is much smaller compared to the total nuclear binding energy and the precision reached in this work. To discuss the masses in terms of atomic mass units, the constant c^2 can be used as a unit conversion factor $c^2 = 931.49432 \, \text{MeV/u}$.

The binding energy per nucleon as a function of the mass number A is shown in Fig. 2. Only the most bound isotope for each mass number is shown. Isotopes with the highest binding energy per nucleon are found at around $BE/A \approx 8.8$ MeV and are ^{62}Ni and ^{56,58}Fe. This curve shows that when lighter nuclei are fused together, or heavier nuclei are broken apart (fission), energy is released because of the binding energy difference. This is the reason why fusion reactions in stars can only reach iron, but not further. Other processes are needed to produce elements beyond iron (see Chapter 2.4). To further understand this binding energy curve, and the nuclear structure physics behind it, the semi-empirical mass formula is discussed in the next Section 2.2.1.
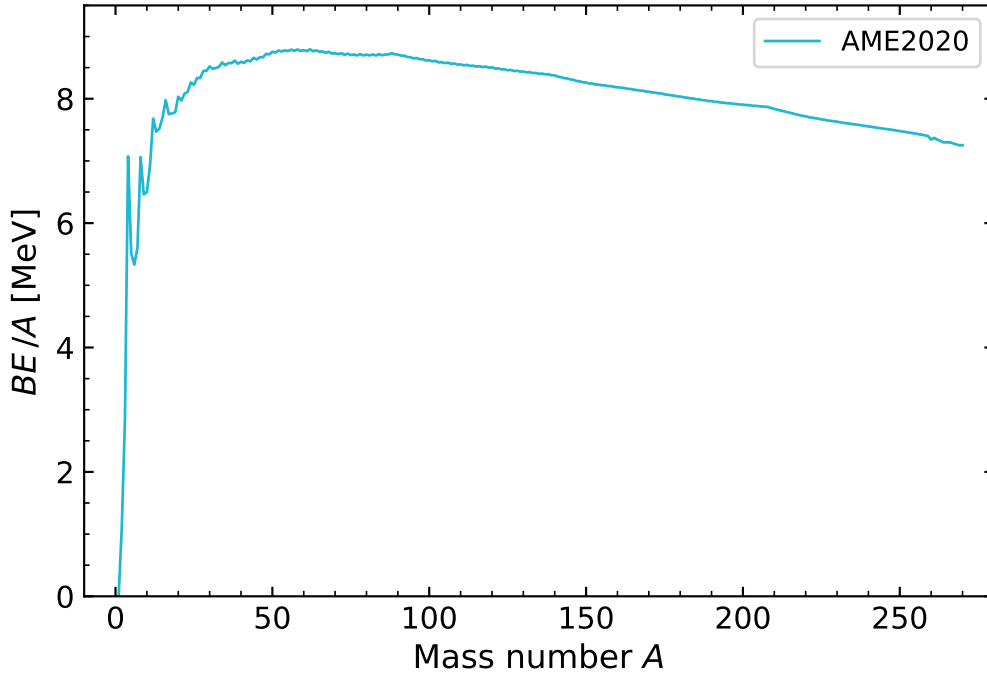
FIGURE 2   Binding energy $BE(Z, N)$ per nucleon as a function of the mass number A for the most bound isotope for a given A. Based on the experimental masses reported in the Atomic Mass Evaluation 2020 [1].

The mass excess is defined as:

$$ME(Z, N) = [m(Z, N) - Am_u]c^2, \tag{2}$$

where $m(Z, N)$ is the atomic mass, A is the mass number and m_u is the atomic mass unit, which is equal to $1/12$ of ^{12}C mass. The mass excess is often used instead of mass values, and is listed for example in the Atomic Mass Evaluation [1]. Many observables, such as reaction- or decay-Q values or binding energies, become more straightforward, when mass-excess values are used instead of atomic masses.

2.2   Theoretical models

No theory has yet perfectly described all of the nuclei simultaneously, due to the complexity of the nucleon-nucleon interaction and the many-body problem [24]. Over the years macroscopic, macroscopic-microscopic and finally microscopic models have been developed to describe and predict the properties of nuclei. They depend of several parameters and experimental masses are often used as an input for the mass models and are also invaluable in testing the theoretical mass models. In the following only models of close relevance to this work are described, though a wide variety of models exist [25]. The general approach discusses the liquid drop model, the Finite-Range Droplet Model [26, 27], the shell

model [28] and the Hartree-Fock [28] approach, while the deformation, Nilsson model [29, 30] and BSkG-models [31, 32] are described in the second part.

2.2.1 General approach

Macroscopic models aim at describing collective properties of the nuclei, such as their masses, shapes and dynamical behaviour, such as the fission process. In one of the earliest global macroscopic models, the liquid drop model [33, 34] the nucleons behave like molecules in a drop of liquid. The nucleus is therefore described as made of incompressible charged fluid droplet, where the mass density inside is constant. In such an approach the binding energy of the nucleus is given by the semi-empirical mass formula, or the so-called semi-empirical Weizsäcker formula

$$BE(Z, N) = a_{vol} \times A - a_{sur} \times A^{2/3} - a_{Coul} \times \frac{Z^2}{A^{1/3}} - a_{asymm} \times \frac{(N-Z)^2}{A} + \delta(A).$$
(3)

The terms a_X are contributions obtained by fitting to experimental data and are introduced next. The term $a_{vol} \times A$ describes the volume term of the binding energy which accounts for the nucleons interacting with their neighbouring nucleons. The $a_{sur} \times A^{2/3}$ is related to the surface of the nucleus, where the nucleons are not surrounded by other nucleons from all sides, reducing the binding energy. The repulsive Coulomb force of the protons, reducing the binding energy, is described by $a_{Coul} \times Z^2/A^{1/3}$. The asymmetry term $a_{asymm} \times (N-Z)^2/A$ describes the effect of Pauli principle [35], which would lead to higher energy levels (i.e. less bound) if the nucleus was made just from one type of nucleon, and lastly the pairing of nucleons to spin-zero pairs increasing the binding energy is taken into account by the pairing term δ [36]. The liquid drop model is a macroscopic description of a nucleus, ignoring some microscopic effects of the nuclear structure, thus lacking in the description of certain nuclei. For example this model does not reproduce the binding energies of the nuclei at the experimentally observed magic numbers.

The liquid drop model has been further used in the development of the macroscopic part of the macroscopic-microscopic finite-range droplet model (FRDM) [26, 37]. On top of the liquid drop model description microscopic corrections are added: for example to take into account the finite thickness of nuclear surface, finite compressibility of nuclear matter and the finite range of the nuclear force. The FRDM accounts for deformation, and the latest model includes also triaxial deformation [27], which is introduced in the next Section. In this work the FRDM model was used in relation to the nuclear astrophysics calculations in Chapter 7.7.

In a microscopic model the nuclear interaction is considered from the point of view of individual nucleons: the nucleus is described as a quantum mechanical object. To calculate the energy levels in the nucleus, it is needed to solve the

Schrödinger equation, where the nucleons are described by their wavefunctions ψ:

$$\hat{H}|\psi\rangle = E|\psi\rangle, \tag{4}$$

where $\hat{H}$ is the Hamiltonian describing the interaction between the nucleons, having a kinetic energy term T and the nucleon-nucleon interaction potential term V. The Hamiltonian is written thus as follows:

$$\hat{H} = T + V = \sum_{i=1}^{A} -\frac{\hbar^2}{2m}\Delta_i + \sum_{i<j}^{A} V_{ij}, \tag{5}$$

where m is the mass of the nucleon and V_{ij} the interaction potential between nucleons i and j [28, 38, 39, 40]. In reality, it is impossible to solve exactly such a N-body problem: first the bare nucleon-nucleon interaction is unknown, and secondly, the computational resources needed to perform such calculations are out of reach.

To overcome these limitations, the basic idea is to assume that the result of the complicated two-body interactions among nucleons is an average self-binding potential. This approach is referred to as the independent particle model. The aim is to find a one-body potential that represents as good as possible, or at best the real nuclear potential, i.e. a potential that reproduces the experimentally measured observables. Moreover, when the nucleons are confined inside a potential, it naturally emerges that their energies are discretized, forming what is
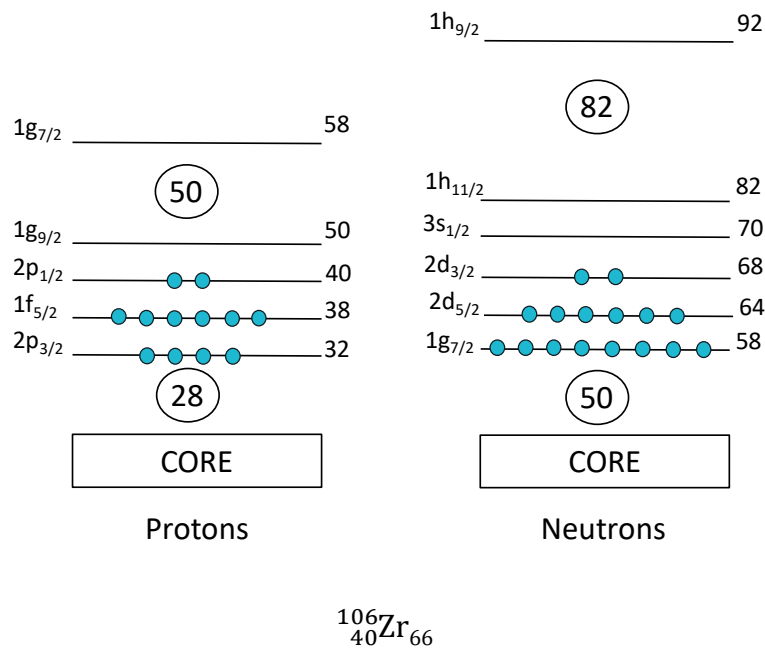

FIGURE 3 A schematic of the single particle energy levels in a shell-model picture for ^{106}Zr. Note: the ground-state of ^{106}Zr is not spherical, and is used here just to illustrate shell model energy levels.

referred as shell structure [28, 40, 41]. To describe this potential an infinite square well and a spherical harmonic oscillator potential were originally used, but a more accurate description was reached when the Woods-Saxon potential [42] was applied. But this did still not fully produce the experimentally observed magic numbers, in particular above 20. To produce the higher magic numbers as well, a nuclear spin-orbit interaction needed to be added, originally introduced by Mayer [43], Haxel, Suess and Jensen [44]. This causes a splitting of the orbitals and gives a rise of the correct energy gaps i.e. magic numbers. Since the nucleus is formed by neutrons and charged protons, a Coulomb term is added to the potential concerning protons. The potential finally assumed for the shell model, the Woods-Saxon potential, spin-orbit interaction and Coulomb interaction term for the protons, was assumed to be spherical. Nucleons are fermions, thus they are placed on these orbitals obeying the Pauli exclusion principle [35].

In modern shell model calculations, the residual interaction between nucleons not accounted for in the mean field potential, has to be considered. This can be established by considering an inert core, to which a valence space of multiple interacting valence nucleons is built on top [45, 46]. Also a no-core shell model exists [47]. Considering the residual interaction leads to the Hamiltonian of Eq. (5) becoming as follows:

$$\hat{H} = H_0 + H_{res}, \tag{6}$$

where

$$H_0 = \sum_{i=1}^{A}(T_i + U_i), \tag{7}$$

$$H_{res} = \sum_{i,j=1}^{A} V_{i,j} - \sum_{i=1}^{A} U_i. \tag{8}$$

The U_i is the one-body mean field potential. In Fig. 3 a schematic of the single particle structure according to the shell model is shown, where on top of the core the valence space nucleons have been built. The shell model is often used for calculations in the vicinity of magic numbers, due to the complexity of the valence space calculations. Among other nuclear properties, the nuclear shell model can be used to calculate nuclear binding energy differences, such as the two neutron separation energy S_{2n} (see Section 2.3).

Since in the shell model the assumption is that the potential is spherical, the deformed nuclei have to be handled differently. In the next section nuclear deformation and the so-called deformed potential shell model namely Nilsson model are described.

Another microscopic method to solve the Schrödinger equation is the Hartree-Fock-Bogoliubov approach [28, 39, 48]. The Hamiltonian in Eq. (5) needs simplifications, since it is too difficult to solve for heavier nuclei ($A > 10$ [39]). The Hartree-Fock method is used to extract a single particle potential from the sum of two-body interactions using trial wavefunctions [28]. An iteration process is performed to produce a single-particle potential, which minizes the energy expectation value ($E_{HF} =< \psi|H|\psi >$) of the system. The Bogoliubov extension to

the Hartree-Fock describes pairing correlations between the nucleons. The reader is referred to Refs. [28, 39] for a more complete description of the methods described above. In this work, the Hartree-Fock-Bogoliubov approach is a building block of the BSkG1 and BSkG2 models, used to interpret the nuclear structure behind the measured masses.

2.2.2 Nuclear deformation and theoretical approaches for deformed nuclei

Nuclear deformation is spoken of when the nucleus takes a non-spherical shape. Deformed nuclei are typically found in regions between the magic nuclei, where there are orbitals that are not fully filled (mid-shell region) [24, 38]. The nucleus is deformed when the projection of the angular momentum, thus the magnetic substate distribution, is not divided equally to all directions i.e. the nucleons are divided anisotropically on the orbits.

The deformed nucleus can acquire different shapes named as follows: the elongated shape is called prolate (Fig. 4: $y > x = z$), the flattened shape is called oblate (Fig. 4: $z < x = y$) and when all the axes differ in size, the nucleus is called to have a triaxial shape (Fig. 4: $x \neq y \neq z$). The deformation can happen for the ground states as well as for the excited states. Deformation can be described via the dimensionless deformation parameter β_2 and triaxiality angle γ defined as follows:

$$\beta_2 = \frac{4\pi}{3R^2A}\sqrt{Q_{20}^2 + 2Q_{22}^2}, \tag{9}$$

$$\gamma = \mathrm{atan}(\sqrt{2}Q_{22}/Q_{20}), \tag{10}$$

where $R = 1.2A^{1/3}$ fm. The quadrupole moments Q_{20} and Q_{22} have been defined using integral of the nuclear density distribution ($\rho(\mathbf{r})$) and spherical harmonics as $Q_{2m} = \int d^3r r^2 \rho(\mathbf{r})\mathrm{Re}\{Y_{2m}(\mathbf{r})\}$, where $m = 0, 2$ [49]. The β_2 gives the size of the quadrupole deformation, but does not implicate if the deformation is axially symmetric (prolate, oblate) or not (triaxial). In triaxial deformation the nuclear deformation has no symmetry axis. A potential energy surface (PES) of a nucleus can be calculated to describe triaxial deformation of nucleus, where the calculated
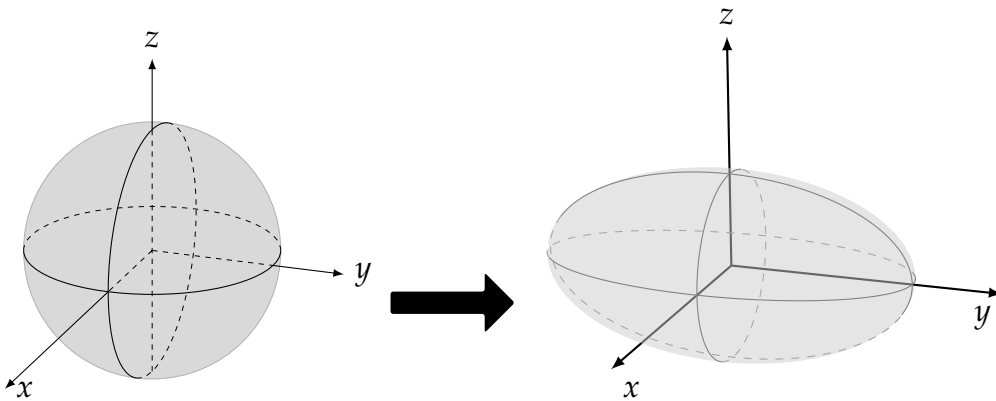

FIGURE 4   A spherical shape and an elongated ellipsoid shape with its axes to describe nuclear deformation.
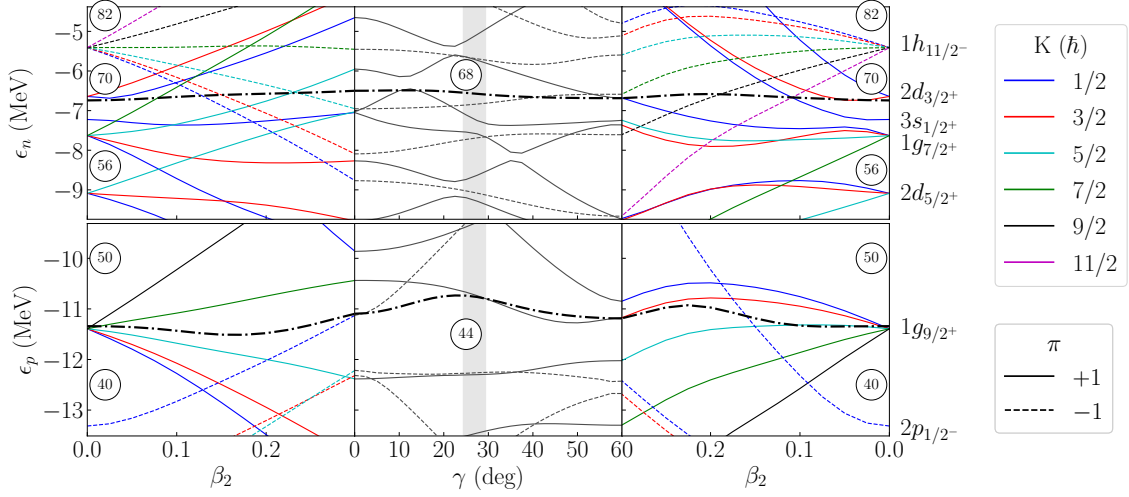
FIGURE 5 A Nilsson diagram of the single-particle states for ^{112}Rh for neutrons (top panel) and protons (bottom panel). The left panel describes the orbitals as a function of prolate deformation, middle panel as a function of triaxiality angle γ and the right panel as a function of oblate deformation. Reprinted with permission from Ref. [49] (attached article PI) 2023, American Physical Society.

potential energy is shown as a function of the deformation parameter β_2 and the triaxiality angle γ. In a potential energy surface (PES) if the energy minimum is not a well-localized deep minimum, but spreads out over the potential energy surface, the nucleus is called exhibiting γ-softness.

Possibly the most successful model describing nuclear structure of deformed nuclei is the Nilsson model [29, 30] where the single-particle motion of nucleons is defined in a deformed potential field. Thus the Nilsson model gives the single-particle orbital energies as a function of deformation. Due to the broken symmetry, the quantum numbers used in the spherical shell model are not anymore good quantum numbers. The $(2j + 1)$ degeneracy of the spherical shell model states is also not valid and only two nucleons can be placed on each deformed orbital. If the deformation is axially symmetric, the quantum number K of the z-component of angular momentum $\mathbf{J}_z$ is preserved since the symmetry axis of the nucleus can be aligned with the z-axis. In Fig. 5 a Nilsson diagram of the single particle states for ^{112}Rh calculated using the BSkG1 model (described below) is shown. The left side of the three panels shows the prolate deformation shape (the lowest K orbits interact more closely with the core) and the right side shows single-particle orbitals for the oblate deformation side (the highest K orbit interacts more closely with the core). In the middle panel, the single-particle levels for different triaxial deformation is shown, but due to the axial symmetry breaking the K quantum number can not be regarded as a good quantum number. The Nilsson diagram can give insight to the single particle level structure of the deformed nucleus.

The two advanced global mass models supporting this work were the BSkG1 [31] and BSkG2 [50] models. Both of the models are based on self-consistent Hartree-Fock-Bogoliubov (HFB) calculations utilizing empirical Skyrme energy density functional (EDF). The aim of these models is a microscopic description

of the nuclear structure over the whole nuclear chart, i.e. to be a global model. The models allow for symmetry broken Bogoliubov states, thus both triaxial and axially symmetric deformation can be accounted for. In the BSkG1 and BSkG2 models the binding energy is formed by the self-consistent mean-field HFB energy and of a collection of perturbative corrections. The mean-field HFB energy further consists of contributions from kinetic energy, Skyrme interaction, pairing interaction, Coulomb force and center-of-mass correction, see the detailed equations in Refs. [31, 50].

The BSkG1 and BSkG2 models have been adjusted using all experimentally known masses, as well as other experimentally measured parameters (for example charge radii). In addition, the BSkG2 model takes into account the so-called "time-odd" terms of the energy density functional and has incorporated information on fission barriers of actinides in the parameter adjustment of the fit [50]. But both of the models are expected to perform similarly regarding the binding energies (see attached article PII).

The biggest impact of triaxial deformation predicted by the BSkG1 model, i.e. the biggest gain in binding energy compared to axially symmetric deformation, is exactly at the region of interest in this thesis: the neutron-rich refractory nuclei around $Z \approx 40, N \approx 60$ (shown in Ref. [31] Fig. 5 top right panel). The deformation predicted by the BSkG1 model for the ions of interest in this work is further given in the Chapter 2.5.

Some well-known regions of deformed nuclei are in the $A \approx 110$ region [18, 20, 21], also rare-earth region $A \approx 165$ [51] and actinide and superheavy region $A > 220$ [52]. The nuclear deformation can be studied experimentally in many ways: via γ-ray spectroscopy, laser spectroscopy or mass measurements just to name a few. As an example of deformation in the region of neutron-rich refractory elements ($A \approx 110$) in the isotopic chain of zirconium ($Z = 40$), the change of the nuclear shape when crossing the $N = 60$ has been seen via a big change in the charge-radii in laser spectroscopic measurements [10] and in rotational-band structures via γ-ray spectroscopy [53].

The mass of the nucleus in itself does not give direct information about deformation. The mass measurements can though provide interesting observables, often called mass-filters, where the biggest shape changes can be seen as a deviation from the expected trend. The $N = 60$ shape change in zirconium is also observed from mass measurements as a change of the calculated two-neutron separation energy S_{2n} observable trend [20, 21] (see Fig. 6). The next Section discusses the two-neutron separation energy and other relevant mass filters in more detail.

2.3 Mass filters

Systematic studies of nuclear binding energies and their derivatives along isotopic or isotonic chains can provide essential information on the evolution of nu-

clear structure. In Fig. 6 a) the binding energy of zirconium isotopes is shown as a function of neutron number N. It can be observed that the trend of binding energies shows only a smooth decreasing trend, even if we know that at $N = 60$ the nuclear ground-state experiences a big change in shape. Other observables, which are more sensitive are needed.

The binding energy difference between neighbouring isotopes is known as the neutron separation energy S_n:

$$S_n(Z, N) = BE(Z, N) - BE(Z, N - 1) = ME(Z, N - 1) - ME(Z, N) + ME_n. \tag{11}$$

It tells how much energy is needed to separate one neutron from the nucleus. A phenomenon called the odd-even staggering (OES) is seen in the one neutron separation energy S_n when plotted as a function of neutron number N, see Fig. 6 b). This is related to the pairing of the neutrons, which translates as a higher binding of the isotopes with paired neutrons. In the liquid drop model, discussed previously, a pairing term is added to account for like-nucleon pairing. The same effect can be seen in the trend of one proton separation energies S_p. The one neutron separation energy S_n is also crucial for simulating the neutron-capture reaction rates for the r-process path simulations (see Chapters 2.4 and 7.7).

To eliminate the odd-even staggering effect, the two-neutron separation energy

$$S_{2n}(Z, N) = BE(Z, N) - BE(Z, N - 2) = ME(Z, N - 2) + 2ME_n - ME(Z, N), \tag{12}$$

as a function of neutron number N or proton number Z is used. Generally within an isotopic chain the two-neutron separation energy S_{2n} exhibits a smooth decreasing trend. Discrepancies to this trend can be seen for example at magic numbers: a deep decrease of the two-neutron separation energy is seen when a neutron is placed on a orbital after the magic neutron number shell has been filled. Also discrepancies can be observed when a shape change occurs, like seen in zirconium crossing the $N = 60$, see Fig. 6 c).

The binding energies can also be used to determine the empirical two-neutron shell-gap energies

$$\delta_{2n}(Z, N) = S_{2n}(Z, N) - S_{2n}(Z, N + 2), \tag{13}$$

which can be further compared to theoretical predictions. This observable can help to quantify the changes seen in the two-neutron separation energy S_{2n}. When crossing a shell closure the two-neutron separation energy experiences a steep decrease, which is seen as an increase of the two-neutron shell-gap energy. This has been used extensively to study the changes in S_{2n} trend in the articles included to this work, see PI and PII. In Fig. 6 d) the empirical two-neutron shell-gap of zirconium isotopes is shown.

Another mass filter which can be used to study the pairing of neutrons, is the so-called odd-even staggering parameter/three-point formula $\Delta_n^{(3)}$ (see Fig. 6 e)):

$$\Delta_n^{(3)}(Z,N) = \frac{(-1)^N}{2}\left[ME(Z,N+1) + ME(Z,N-1) - 2ME(Z,N)\right]. \quad (14)$$

This quantity is affected by the mass of the isotope N and its neighbours $N+1$ and $N-1$. Discontinuities in the trend of this observable can also reveal a change of the shape of the nucleus. All these mass filters have been shown in Fig. 6 and have been extensively used to study the nuclei of interest in attached articles PI and PII. Chapter 7.4 gives a summary of the findings discussed in the included articles.
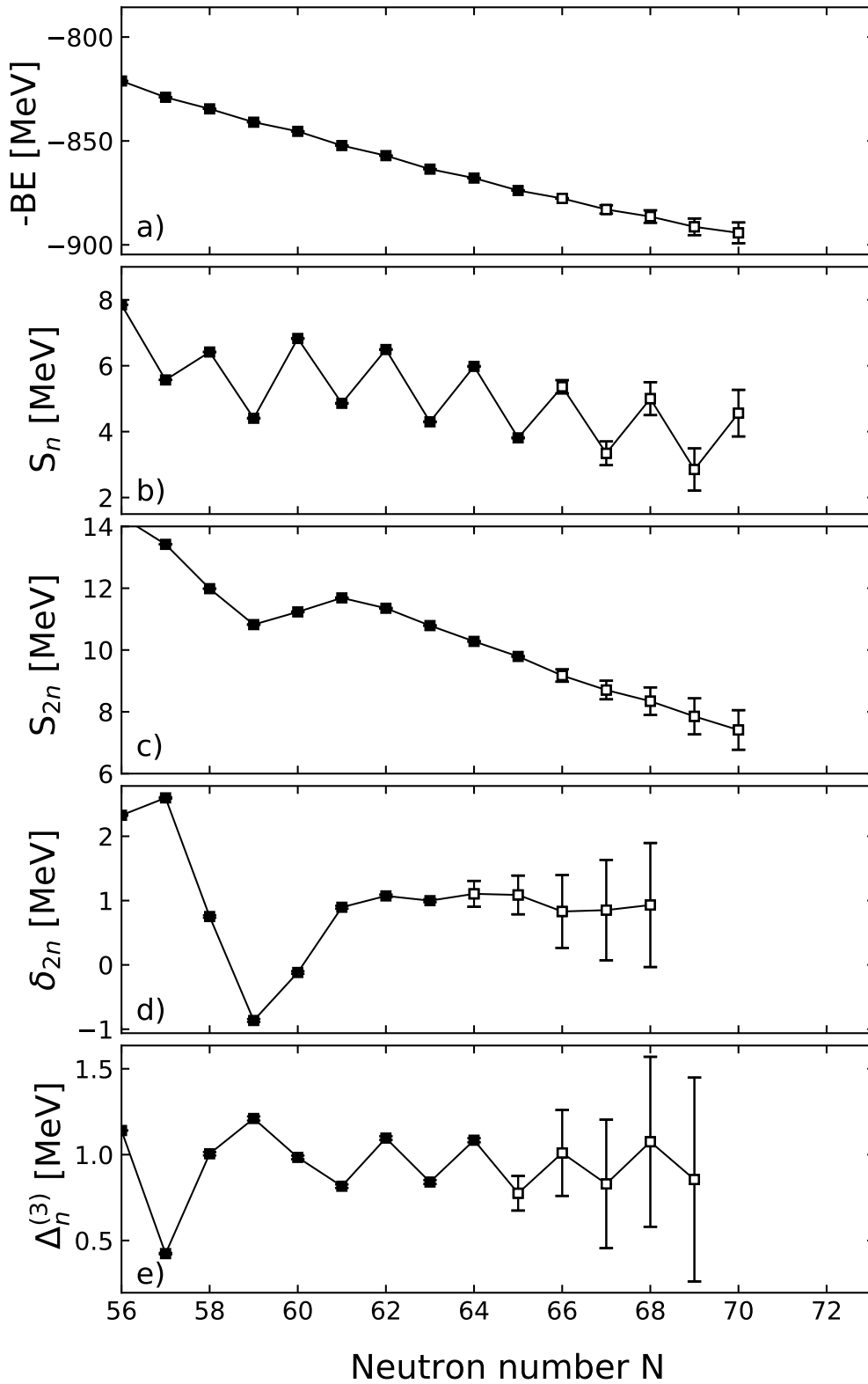
FIGURE 6   The binding energy (BE) (a), one neutron separation energy S_n (b), two-neutron separation energy S_{2n} (c), empirical two-neutron shell gap δ_{2n} (d) and the three-point formula $\Delta_n^{(3)}$ (e) as a function of the neutron number N for neutron-rich zirconium $(Z = 40)$ isotopes. The data have been collected from AME20 [1], where the solid symbols represent the experimentally measured values and the open symbols show the extrapolated values.

2.4 Nuclear astrophysics and the r-process

One of the biggest questions in physics is how the heavier elements than iron are produced in our Universe. Most of the lighter nuclei are produced in stars via different processes, mainly through fusion (see e.g. Ref. [54] for details). Energy can be produced via fusion reactions only up to around iron ($Z = 26$), see Fig. 2. The two main processes responsible for the production of heavier elements than iron are the slow neutron-capture process (s process) and the rapid neutron-capture process (r process) [4, 55]. It is also discussed if intermediate neutron-capture process (i-process) [56, 57] exists and contributes to the observed abundance patterns. These processes are highly dependent on the environment, such as temperature and neutron flux, but also on the underlying nuclear structure properties.

The r-process utilizes a neutron-rich environment for rapid captures of neutrons via (n, γ) reactions on seed nuclei. The environment suitable for the main r-process has to have a high neutron density ($n_n \approx 10^{24}/\text{cm}^3$) and temperatures of around $T \approx 1 - 2$ GK. Previously the astrophysical site of r-process was under debate, but the experimentally observed binary neutron-star merger event at LIGO/Virgo gravitational wave detectors [58, 59] in 2017 solidified the neutron-star merger as a production site of heavy elements. A kilonova was observed following the neutron-star merger, being powered by the radioactive decay of neutron-rich elements, providing evidence of nucleosynthesis via r-process [60].

The r-process path evolves close to the neutron dripline. The environment has to be highly neutron-rich for the neutron captures to be fast enough to compete with the β^--decays of the very exotic i.e. short-living nuclei. When the β^- decay over competes the neutron capture, the nucleus decays to the daughter nucleus, from which the neutron-capture reactions will continue further. This leads the r-process to climb higher in the proton number, producing heavier elements.

At the magic neutron numbers, the r-process experiences a phenomenon called the waiting point. A big change in the neutron-capture Q-value is expected at these magic numbers, leaving more room for the β^- decay, moving the process higher up in the proton number Z. At the waiting points material usually accumulates, thus when the r-process stops, due to environmental reasons for example the neutron flux running out, thus higher peaks in the produced abundance pattern are seen when following the β^- decay chain to stability.

One of the fundamental nuclear physics parameters needed for simulating the r-process are the (n, γ) reaction Q-values, which are further calculated from the masses of nuclei. Thus the masses of nuclei close to the path of the r-process represent a fundamental building block of simulating the r-process [61, 62]. The r-process travels far in the neutron-rich side of the nuclear chart, close to the neutron drip-line, thus masses are needed to be extracted from theoretical mass models. But many mass models still do not describe exotic neutron-rich nuclei perfectly, resulting to large variations with different models. To constrain the models better, masses of neutron-rich elements have to be measured.

2.5 Motivation for mass measurements at A $\approx 100 - 120$

2.5.1 Isomers of rhodium and ruthenium

In the neutron-rich odd-odd rhodium ($Z = 45$) isotopes, isomers are known to exist based on decay-spectroscopy measurements [2], but the masses of the isomers, thus the excitation energy E_x, in ^{110,114,116,118}Rh were not known before this work (see Chapter 7 and included article PI). The masses of neutron-rich rhodium isotopes had been measured before by utilizing JYFLTRAP double Penning trap [18], but the measurement technique used at the time did not have sufficient resolving power to separate the isomers from the ground states. This led to the mass being measured to be a mixture of both the ground and isomeric states. It is important that the ground and isomeric states are separated, so that the correct mass can be assigned to each state.

The ^{113}Ru and ^{115}Ru also have isomeric states with unknown energies. Experimental indications of the existence of these states had been made (Refs. [63, 15] for ^{113}Ru, Ref. [16] for ^{115}Ru), but the energies of the isomeric states had not yet been directly measured. The attached article PII discusses the mass measurements of these isomeric states, performed in this work.

The isomers studied in this work decay dominantly via β decay, making it challenging (or impossible) to determine their excitation energies directly via internal transition. The only way is to directly measure their binding energy via mass spectrometry. The studied isomeric states had to be sufficiently long lived ($T_{1/2} > 50$ ms), to be suitable to be measured using a Penning trap.

2.5.2 Shape changes and masses

Neutron-rich $A \approx 100 - 120$ nuclei are known for complex nuclear structure and deformation. In neutron-rich rhodium ($Z = 45$) isotopes triaxial deformation was studied for example in Ref. [64] via γ-ray spectroscopy of the rotational bands, compared to the predictions of the triaxial projected shell model (TPSM) [65]. These calculations showed that to reproduce the experimentally observed rotational band structure, a substantial and nearly constant triaxial deformation was needed. As mentioned before, in the BSkG1 model the biggest impact of triaxial deformation is in that region.

In the context of this thesis, the deformation calculated by the BSkG1 and BSkG2 models was studied via comparing mass measurements of neutron-rich rhodium and ruthenium isotopes to the mass-surface trends produced by the model (see Chapter 7 and included articles PI and PII). In Fig. 7 the deformation parameter β_2 and the triaxiality angle γ produced by the BSkG1 model is given for the isotopic chains of rhodium and ruthenium. For the neutron-rich rhodium and ruthenium nuclei the BSkG1 model predicts for the triaxial deformation to stay rather constant until neutron number $N \approx 74$ and $N \approx 75$, respectively, after which the triaxial deformation will vanish nearly completely. The predicted
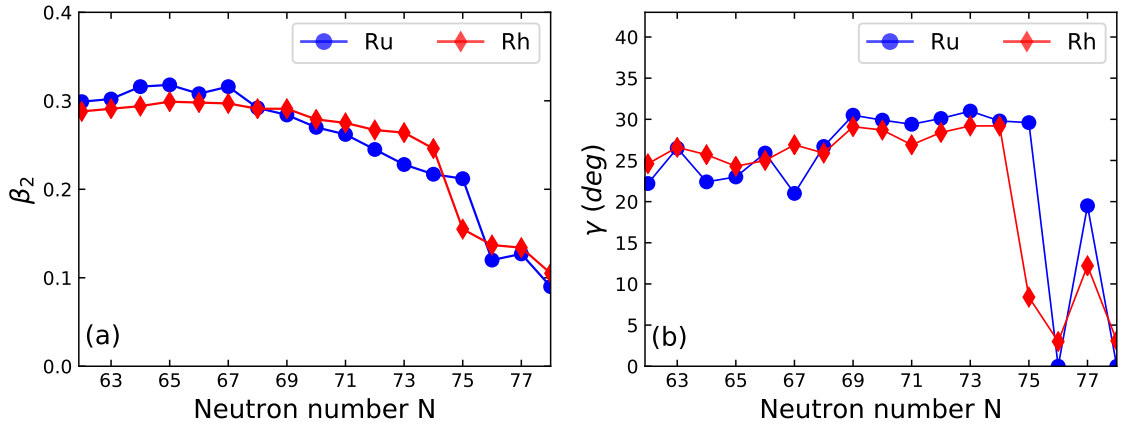
FIGURE 7 The deformation parameter β_2 and triaxiality angle γ calculated using the BSkG1 global mass model [31] for neutron-rich ruthenium ($Z = 44$) and rhodium ($Z = 45$) isotopes. Adapted with permission from Ref. [49] (attached article PI) 2023, American Physical Society.

quadrupole deformation β_2 also decreases at these neutron numbers. This could mean that when moving towards the $N = 82$ shell closure the ground-state nuclei become less and less deformed to finally reach sphericity at $N = 82$.

Deformation in the more neutron-rich zirconium ($Z = 40$) isotopes has been studied for example in Refs. [66, 67, 68]. In the γ-ray spectroscopic studies of Ref. [66] the energy of the $E(2_1^+)$ state in ^{106}Zr was found to be similar with isotopes of $A = 100, 102$ and 104, leading to the assumption that the size of the deformation would be similar. In Ref. [67] half-life measurements of the 2_1^+ in ^{106}Zr were compared to model calculations, indicating prolate deformation. The mass of ^{106}Zr was measured in this work, and the discussion related to it can be found in Chapter 7 and in a future publication.

2.5.3 r-process

The region of neutron-rich refractory nuclei, is located between the first ($A \approx 80$) and the second ($A \approx 130$) abundance peaks of the r process. This region is very difficult to model, since the abundance of these nuclei is likely to come from many different processes [69] (such as the weak r-process, the main r-process, perhaps the i-process). The weak r-process differs from the main r-process in the production environment: expected to happen in environments where the neutron flux is not high enough to produce the heaviest r-process elements such as neutrino winds of core-collapse supernovae [70]. The region is also known for isomers and the importance of isomeric states is not yet much explored in r-process path simulations, but the process flows through these nuclei when the produced nuclei are decaying toward stability. The masses measured in this work help advance the mass models predicting the properties of extremely neutron-rich nuclei located at the main r-process path in this region. The effects of the measured masses on the r-process path are presented in Chapter 7.7.

3 PENNING TRAP MASS SPECTROMETRY

The following chapter gives a description of Penning traps and the behaviour of a charged particle in a Penning trap. The ideal and real Penning traps are briefly explained. The mass separation and measurement techniques used in the context of this work are also described.

3.1 Ideal Penning trap

An ideal Penning trap combines a uniform strong magnetic field ($\mathbf{B} = B_0 \mathbf{e_z}$) and an electrostatic quadrupole field ($\mathbf{E} = -\nabla\Phi$, for Φ see Eq. 16) to trap a charged particle. The z-axis is assigned to be the magnetic field axis, thus denoted as the axial direction. Generally, two different geometries are used to achieve the electric potential: hyperbolic and cylindrical. Both Penning traps used in this work, PIPERADE and JYFLTRAP, have a cylindrical geometry (see Chapters 4.2 and 5.2).

The following describes the magnetic and electric fields and the equations of motion of a charged particle in a Penning trap. A more thorough description can be found in Refs. [6, 71, 72, 73]. In a homogeneous magnetic field B_0, without any electric fields, a charged particle with a charge q and a mass m exhibits a circular motion with an angular frequency

$$\omega_c = \frac{q}{m} B_0 = 2\pi \nu_c, \tag{15}$$

where ν_c is the charged particle's cyclotron frequency. This motion is perpendicular to the axis of the magnetic field. Homogeneous magnetic field does not confine the particle's axial motion. For this, an electrostatic quadrupole potential of the form

$$\Phi(z, \rho) = \frac{U_0}{2d^2} \left(z^2 - \frac{\rho^2}{2} \right), \tag{16}$$

is superimposed with the magnetic field. The potential $\Phi(z, \rho)$ is given in cylindrical coordinates. The term U_0 is the trapping potential determined as the volt-

age applied between the central ring electrode and two so-called endcap electrodes (see Fig. 16 for ring and endcap electrodes). The trap geometrical factor d^2 is defined as follows:

$$d^2 = \frac{1}{2}\left(z_0^2 - \frac{\rho_0^2}{2}\right),$$

(17)

where z_0 is the axial distance between the ring and endcap electrodes and ρ_0 is the distance from the middle of the ring electrode to the inner edge of the ring electrode (inner trap radius).

An ion with a charge q travelling with a velocity $\mathbf{v}$ in a magnetic field $\mathbf{B}$ and in an electric field $\mathbf{E}$ feels the Lorenz force:

$$\mathbf{F} = q(\mathbf{v} \times \mathbf{B} + \mathbf{E}).$$

(18)

First, the Newton's equation of motion in the axial direction is solved, and since the movement is parallel to the magnetic field axis, it is unaffected by the magnetic field ($\mathbf{v} \times \mathbf{B} = 0$). Thus the motion is described as follows from Eq. (18):

$$F = m\ddot{z} = qE_z,$$

(19)

resulting in the following when the z-component of $\mathbf{E} = -\nabla\Phi$ and Eq. (16) are considered:

$$\ddot{z} + \frac{qU_0}{md^2}z = 0.$$

(20)

This is the equation of motion for a one-dimensional harmonic oscillator with the angular frequency of

$$\omega_z = \sqrt{\frac{qU_0}{md^2}}.$$

(21)

From Eq. (21) it is seen that the axial motion is dependent on the trapping potential applied (U_0) and the geometry parameter (d^2).

Next, the equation of motions in the radial direction (ρ) is considered. The force experienced by the charged particle q in the radial direction based on Eq. (18) and Newton's second law is

$$\mathbf{F} = m\ddot{\boldsymbol{\rho}} = q(E_{\rho} + \dot{\boldsymbol{\rho}} \times \mathbf{B}).$$

(22)

When utilizing Eqs. (15), (16), (21) and the relation for the magnetic field $\mathbf{B} = B_0\mathbf{e_z}$, Eq. (22) can be written as

$$\ddot{\boldsymbol{\rho}} - \dot{\boldsymbol{\rho}} \times \omega_c\mathbf{e_z} - \frac{1}{2}\omega_z^2\boldsymbol{\rho} = 0.$$

(23)

The differential equation of Eq. (23) can be expressed in Cartesian coordinates, written in vector form for simplicity, as follows:

$$\begin{bmatrix} \ddot{x} \\ \ddot{y} \end{bmatrix} - \omega_c\begin{bmatrix} \dot{y} \\ -\dot{x} \end{bmatrix} - \frac{\omega_z^2}{2}\begin{bmatrix} x \\ y \end{bmatrix} = 0.$$
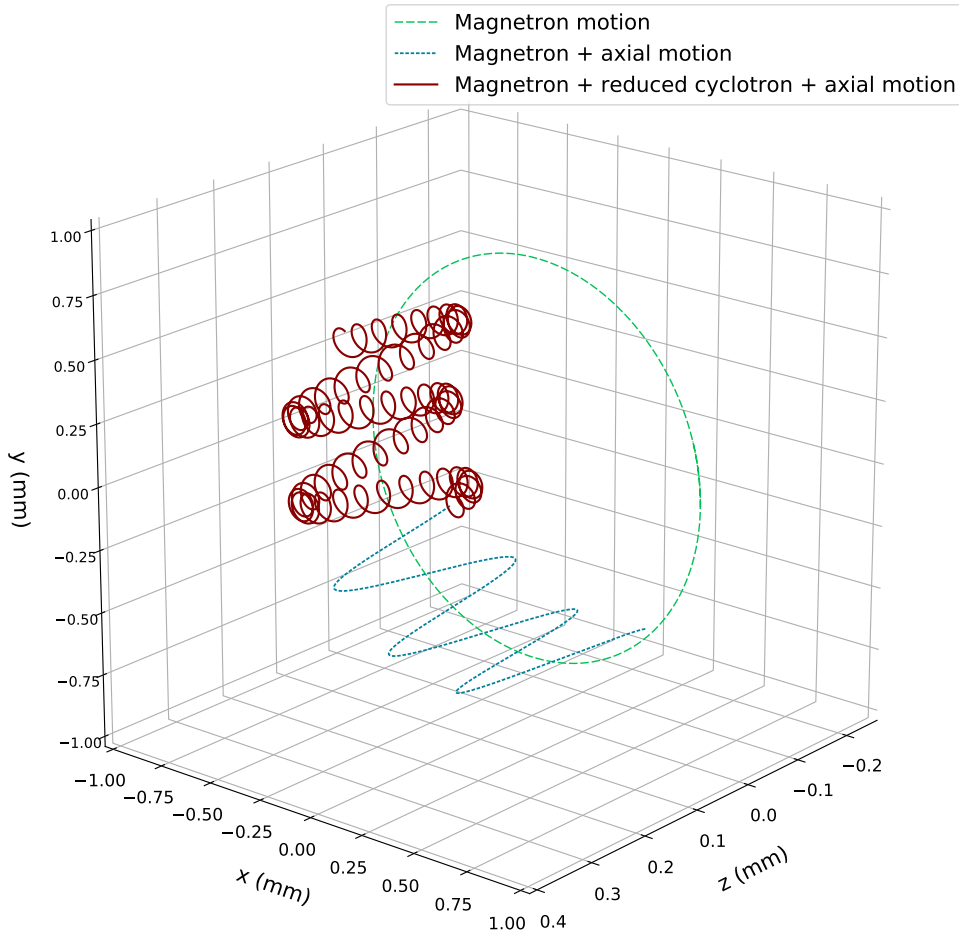
(24)

FIGURE 8   A schematic of the three eigenmotions of a charged particle in a Penning trap. The pure magnetron motion is shown in green, the magnetron motion combined with the axial motion in blue and all the three motions combined in dark red. The z-axis is along the magnetic field axis.

To solve the Eq. (24) a complex variable is defined as $u = x + iy$. Applying this to Eq. (24) leads to the relation:

$$\ddot{u} + i\omega_c \dot{u} - \frac{\omega_z^2}{2} u = 0. \tag{25}$$

If an ansatz of $u = e^{-i\omega t}$ is applied to Eq. (25) a quadratic expression for the frequency is reached:

$$\omega^2 - \omega_c \omega + \frac{\omega_z^2}{2} = 0. \tag{26}$$

This has the two following angular eigenfrequency solutions:

$$\omega_\pm = \frac{\omega_c}{2} \pm \sqrt{\frac{\omega_c^2}{4} - \frac{\omega_z^2}{2}}, \tag{27}$$

which are known as the reduced or modified cyclotron motion frequency ω_+ and the magnetron motion frequency ω_-. Thus, the motion of a charged particle in

a Penning trap consists of a combination of two radial motions and one axial motion. These are illustrated in Fig. 8. The magnitude of these frequencies is $\omega_c > \omega_+ \gg \omega_z \gg \omega_-$. These motions can be manipulated using for example multipolar time-varying electric fields, described in Section 3.3.

These equations of motions for a charged particle in a Penning trap also raise conditions that need to be fulfilled for the movement to be bound. Eq. (21) requires $qU_0 > 0$ for the charged particle, otherwise it escapes within the axial direction. From the radial motion Eq. (27) a condition of $\omega_c^2 - 2\omega_z^2 > 0$ arises for the root to be real. When ω_c from Eq. (15) and ω_z from Eq. (21) are applied to this condition, it becomes as follows

$$\frac{|q|}{m}B_0^2 > \frac{4|U_0|}{d^2},\qquad(28)$$

for the motion to be bound.

The invariance theorem [6] connects the eigenmotions to the cyclotron frequency of the charged particle in a Penning trap as follows:

$$\omega_c^2 = \omega_+^2 + \omega_-^2 + \omega_z^2,\qquad(29)$$

which applies with high precision and is highly unaffected by misalignments of the fields (B and E). These effects are more discussed in relation to the real Penning trap in Section 3.2. The following relations also apply for the eigenmotions:

$$2\omega_+\omega_- = \omega_z^2\qquad(30)$$

$$\omega_c = \omega_+ + \omega_-.\qquad(31)$$

If a series expansion is applied for the radial motions described by Eq. (27), it follows that the magnetron motion is of the form:

$$\omega_- \approx \frac{U_0}{2d^2B}.\qquad(32)$$

This shows that the magnetron motion is mass-independent (to the first order). The reduced cyclotron motion frequency after the series expansion becomes

$$\omega_+ \approx \omega_c - \frac{U_0}{2d^2B},\qquad(33)$$

which is clearly dependent on the mass of the charged particle via ω_c.

The energy of a charged particle in a Penning trap can be described in a quantum mechanical way by the following relation:

$$E = \hbar\omega_+(n_+ + 1/2) + \hbar\omega_z(n_z + 1/2) - \hbar\omega_-(n_- + 1/2),\qquad(34)$$

where $\hbar$ is the reduced Planck constant and n is the quantum number of the eigenmotion. Each eigenmotion has a contribution to the total energy, and as the Eq. (34) shows, the reduced cyclotron motion has a positive contribution while

the magnetron motion has a negative one. This means that if a charged particle experiences a loss of energy, the magnetron motion quantum number n_- increases. This quantum number is tied to the amplitude of the motion, thus the amplitude will increase. For the reduced cyclotron and axial motions the quantum number n will decrease, thus the amplitudes will decrease. These features are utilized for example in the buffer gas cooling technique described in Section 3.4.

As an example, the eigenmotion frequencies at JYFLTRAP Penning trap for a mass $m = 100$ u, a charge q of the ion of $+e$ and a magnetic field strength of $B = 7$ T are as follows: $\nu_+ \approx 1$ MHz, $\nu_z \approx 50$ kHz and $\nu_- = 1.7$ kHz. The trapping potential and geometry of JYLFTRAP are described in Chapter 5.2.

3.2 Real Penning trap

In the previous section, an ideal Penning trap was described. In reality, some considerations need to be made, since no trap is ideal. Any departure from purely homogenous magnetic field and harmonic electrostatic potential can cause amplitude-dependent frequency shifts, reducing the precision of the frequency measurement. Below, the main considerations are briefly discussed.

The electric field of a Penning trap, both for the hyperbolic and cylindrical geometries, experiences disruptions in the harmonicity. In the hyperbolic geometry, the electric field is in principle closer to a pure quadrupole distribution than in a cylindrical Penning trap, but, for example, holes are needed in the endcap electrodes to accommodate the injection and extraction of ions. In both geometries, the electric quadrupolar potential is also affected by the segmentation of the ring electrode (for RF application) and there are certain limits in precision of machining the electrodes. Correction electrodes are needed to compensate for these imperfections of the electric potential. Both Penning traps utilized in this work, PIPERADE and JYFLTRAP, have a cylindrical geometry with correction electrodes (see Chapters 4.2 and 5.2).

The magnetic field can drift, have inhomogeneties and fluctuations, and the field axis can be misaligned with respect to the electric field. The drift of the magnetic field over time, caused by the so-called flux creep phenomenon [74], can be corrected to a certain degree with compensation coils. To take into account the field drift in mass measurements, two reference measurements are performed before and after the mass measurement of the ion of interest, and the B-field used for the mass determination is a linear interpolation between the reference measurements. In addition, a systematic uncertainty related to magnetic field fluctuations is added (see Chapter 6). The inhomogeneities of the magnetic field and the misalignement cause shift on the measured cyclotron frequency ν_c and the eigenfrequencies. To limit as much as possible the impact of the imperfections of the magnetic field, the ion motion amplitudes should be kept small.

The measured cyclotron frequency ν_c can also be affected if multiple ions are stored in the trap during the measurement. The Coulomb interaction can

modify the ion motions in the Penning trap, causing a frequency shift. The ion-ion interaction needs to be considered when setting up the measurement and analysing the data (see countrate class analysis in Chapter 6.4.1).

For the JYFLTRAP and PIPERADE Penning traps, more detailed explanations on how the imperfections described above have been considered can be found in Refs. [8, 75, 76].

3.3   Manipulating ion motion in the trap

To manipulate the ion motions in a Penning trap, time-varying radio-frequency electric potentials (RF) applied to the split ring or endcap electrode are used. These can be applied in various multipolar configurations. A dipole excitation is used to manipulate a single eigenmotion. If there is no initial motion amplitude and the excitation frequency is set in resonance with the eigenfrequency, then the corresponding motion amplitude increases linearly. Figure 9 shows a segmented ring electrode, for which the dipole excitation is applied to two opposite segments with opposite phases (0 and π) to manipulate radial motions (marked as $\nu_{\mp}$). For the axial motion the dipolar field is applied between the endcap electrodes.

In the first trap of JYFLTRAP and PIPERADE the dipolar excitation at the magnetron frequency ν_- is used in the buffer gas cooling technique, described in detail in Chapter 3.4, to increase the radius of the magnetron motion. The Phase-Imaging Ion-Cyclotron-Resonance technique (PI-ICR), described in Chapter 3.5.2, uses dipolar ν_+ excitation.

In case the ions are not perfectly injected into the trap, some initial motion, either or both in the radial or axial direction, can be present. Usually this initial motion is unwanted and needs to be decreased. An important parameter for the RF-excitation is the phase of the RF-signal. If the RF-field is in phase with the ion motion, the amplitude of the motion will increase. If the RF-field is in opposite phase, it results in a reduction of the ion motion amplitude (until the center is crossed). Thus the dipolar excitation can be used to damp this unwanted motion, when applied at the eigenfrequency of the motion, correct phase and amplitude for the decrease of the motion amplitude. This is often used in preparation for the PI-ICR technique at JYFLTRAP (see Chapter 3.5.2).

The quadrupolar excitation is used to couple and convert one eigenmotion to another at the sum or difference of the eigenfrequencies. Figure 9 shows how the quadrupolar field is achieved with the same (phase) RF-signals applied to two opposite segments, marked as ν_c. Most commonly at JYFLTRAP and PIPERADE the quadrupolar excitation is used to couple the reduced cyclotron motion ν_+ and the magnetron motion ν_-, as stated in Eq. (31). The quadrupolar field drives a periodic conversion, so called beating conversion, between the two motions. An example of the periodic conversion between these two motions is shown in Chapter 4.2.1 (Fig. 24). The relation between the amplitude of the exciting RF-
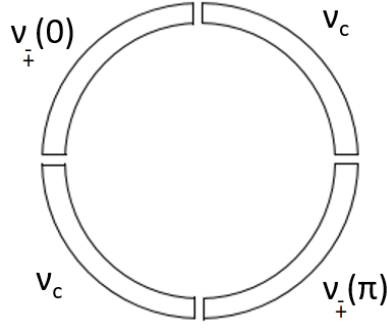
FIGURE 9   A four-fold segmented ring electrode where the segments used for the dipolar RF-field are marked as $\nu_\mp$ and quadrupolar RF-field as ν_c.

field V_{RF} and the excitation time T_{RF} is the following:

$$V_{RF} = 4\rho_0^2 B \frac{\pi}{T_{RF}}, \tag{35}$$

where ρ_0 is the inner radius of the ring electrode [23].

The PIPERADE Penning trap has an eight-fold segmented ring electrode, thus an octupolar excitation can be applied. The octupolar excitation was not implemented yet at PIPERADE, and will thus not be discussed in more detail. The reader is referred to the following publications by S. Eliseev *et al.* [77] and M.Rosenbush *et al.* [78] for more information on octupolar excitation.

3.4   Sideband buffer gas cooling technique

Measuring the properties of exotic nuclei are important for the studies of nuclear structure and astrophysical processes, as highlighted in Chapter 2. In a radioactive ion beam facility, producing an exotic nucleus is very challenging: usually exotic nuclei have low yields, while other less exotic nuclei are produced in high amounts. One of the most important tasks of a Penning trap is its ability to select the low-produced ions of interest from the highly-produced unwanted ions and deliver it for experimental studies. Below one of such selection/purification techniques, called the sideband buffer gas cooling method [79], is described.

The buffer gas cooling method is the main purification method utilized both at the JYLFTRAP and PIPERADE. It utilizes a Penning trap filled with buffer gas. After an ion bunch has been injected to the buffer-gas filled Penning trap, a time is allocated first for cooling the reduced cyclotron and axial motion amplitudes, by dissipating energy thanks to interactions with the buffer gas. Reducing the reduced cyclotron and axial motions amplitude leads to the ions occupying smaller space, but at the same time the magnetron motion amplitude slowly increases. The ions will be axially better centered at the ring electrode position, which is used to perform excitations by applying dipolar or quadrupolar RF-fields. An example of a scan on the cooling time needed, for the trapped ion bunch to be ready for excitations, at the PIPERADE double Penning trap can be found in the
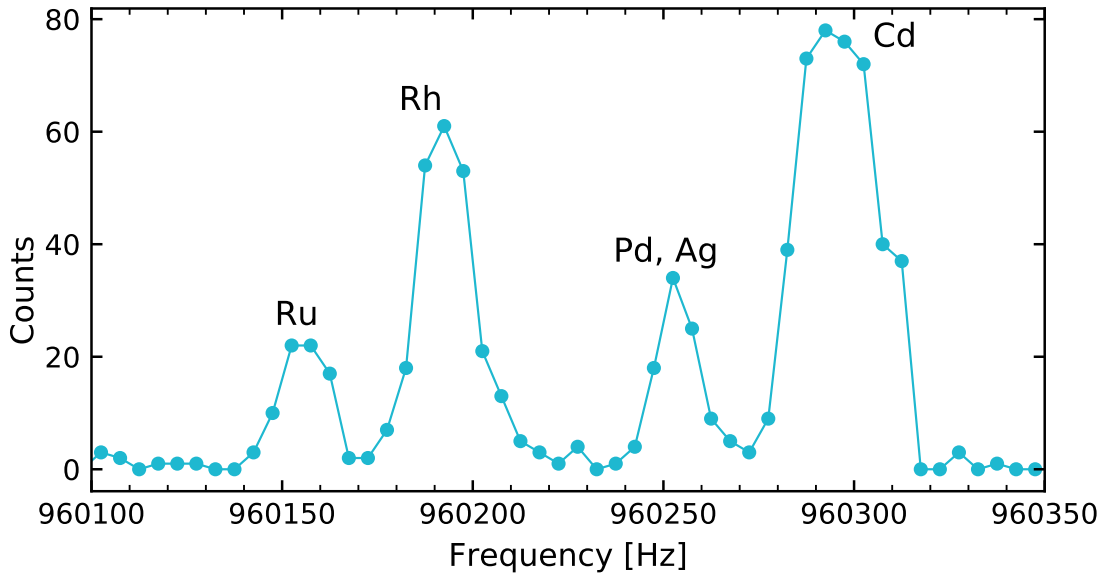
FIGURE 10   An example of a 150 ms quadrupolar excitation frequency scan using buffer gas cooling technique for A= 112 isobars in the purification trap of JYFLTRAP Penning trap.

Chapter 4.2.1. The cooling time depends on the initial energy of the ions and the pressure of the buffer gas. Usually noble gases are used as a buffer gas, because the high ionisation energy of the gas atoms will better conserve the charge state of the ions. At JYFLTRAP and PIPERADE helium is used as a buffer gas.

After the initial cooling, the ions of interest (IOI) will be selected from the ion bunch, discarding the other so-called contaminant ion species (this selection is later referred as purification of the ion sample). First, a dipolar excitation at the magnetron frequency ν_- is applied. This increases the magnetron motion radius of all the ions in the trap, since the magnetron frequency is in the first order mass-independent (see Eq. (32) in Section 3.1). The excitation amplitude and duration is chosen such that after the excitation the radius of the motion is more than the radius of the diaphragm between the first and second traps (JYFLTRAP diameter $d = 1.5$ mm, PIPERADE $d = 4$ mm). For example at JYFLTRAP the dipolar excitation is generally applied for 10 ms at the frequency of $\nu_- = 1.7$ kHz. After the magnetron motion radius ρ_- has been increased satisfactorily, a quadrupolar excitation is applied to the ring electrode at ν_c frequency of the desired species with the purpose of converting the magnetron motion to the reduced cyclotron motion, via the relation in Eq. (31). Since this conversion frequency is mass-dependent (see Eq. (31)), only ions within a narrow frequency band are affected by this conversion. The reduced cyclotron motion is a fast motion, thus the ions interact more frequently with the buffer gas atoms, losing energy in the interaction. This way the movement amplitude diminishes and the ions fall into the center of the trap.

The final selection is performed utilizing the diaphragm electrode, when the ions are ejected from the trap. Ions with bigger motion amplitude than the open aperture of the diaphragm will not survive the ejection, while the ions that

were selected in the quadrupolar excitation and had the time to loose energy and be centered, survive. The purified ion sample can then be captured in the second trap or be directed to post-trap experiments. This purification method [79] generally reaches a mass resolving power of $R = m/\Delta m \approx 10^5$ (for ions with $A/q = 100$ [80]).

In Fig. 10 a scan of the quadrupolar frequency in the purification trap of JYFLTRAP Penning trap (see Chapter 5.2) is shown for mass $A = 112$. The quadrupolar excitation was done with 150 ms excitation time with an amplitude of 450 mV. The first implementation and results of the buffer gas cooling technique at the PIPERADE Penning trap are described in Chapter 4.2.1.

In some cases the buffer gas cooling method is not enough to resolve and select the ions of interest from the close isobaric or isomer contaminants. For this a method called the Ramsey cleaning method [80] can be applied. At JYFLTRAP this method is performed in the precision trap under high-vacuum. The purification is performed with a dipolar excitation at the modified cyclotron frequency ν_+, which excites the contaminant ions, mass-selectively to a large radius. A good knowledge of the contamination and its ν_+ frequency is thus required so that the contaminant can be driven to a large orbit, while the ion of interest gets minimal radius increase. The excited ion sample is sent back to the first trap, and as in the buffer gas cooling method, any ion that has larger motional amplitude than the opening of the diaphragm electrode, is lost. For the dipolar excitation, a specific Ramsey-type time-separated field is commonly used, where the exciting RF signal is temporally divided into two pulses, with a waiting time in between, as explained for the Ramsey's method of time-separated oscillatory fields in Section 3.5.1. In Ref. [81] a mass resolving power of $R = 1 \times 10^6$ was reached.

3.5 Mass measurement with a Penning trap

The mass of an ion in Penning-trap measurements is determined using the relation between its mass and its measured cyclotron frequency ν_c (see Eq. 15). To know the magnetic field with a high precision, reference measurements of ions with a well-known mass are performed. In articles PI and PII, ^{133}Cs$^+$ and ^{85}Rb$^+$ were used as reference ions. The frequency ratio $r = \nu_{c,ref}/\nu_{c,ioi}$ between the reference and the ion of interest gives the mass m of a singly-charged atom as follows:

$$m = r \times (m_{\text{ref}} - m_e) + m_e, \tag{36}$$

where m_{ref} is the atomic mass of the reference and m_e is the mass of the electron. A more detailed explanation of the mass determination is given in Chapter 6.6, where the analysis of the experimental data is described. The following two sections describe the techniques used at JYFLTRAP to measure the cyclotron frequencies. The same techniques will be utilized at the PIPERADE Penning trap, from which the first implementation of the TOF-ICR technique is described in

Chapter 4.2.1.

3.5.1 Time-of-Flight Ion-Cyclotron-Resonance technique

The Time-Of-Flight Ion-Cyclotron-Resonance technique [23] (TOF-ICR) is used to determine the cyclotron frequency ν_c from the measured time-of-flight resonance. This is one of the two primary mass measurement techniques used at JYFLTRAP and has been implemented for the first time for the PIPERADE Penning trap in the framework of this thesis (see Chapter 4.2.1). TOF-ICR is performed in a Penning trap operated under high-vacuum, since interactions with gas atoms can cause shifts in the ion motion or some damping of the resonance effect. For JYFLTRAP and PIPERADE the technique is performed in the second trap (precision trap and measurement trap, respectively), see Chapters 5.2 and 4.2.

Assuming the ion sample has been purified first and captured in the second trap, the first step of the TOF-ICR technique can be applied: some magnetron motion is excited with a dipolar excitation at the ν_- frequency. The second step is to convert the magnetron motion to a reduced cyclotron motion by applying a quadrupolar excitation. Coupling of the motions is the strongest at the conversion frequency $\nu_c = \nu_+ + \nu_-$ (Eq. 31). The quadrupolar RF frequency is scanned over a certain frequency range covering the ν_c frequency. The duration of this excitation determines the width of the resonance: the longer the excitation, the narrower the resonance.

After the excitations, the ions are extracted from the Penning trap to a time-of-flight detector downstream. When exiting the trap region, the magnetic field strength starts to decrease, creating a magnetic field gradient. During the ion's travel through the magnetic field gradient, an interaction of the orbital magnetic moment $\mu(\omega_{RF})$ of the ions with the magnetic field gradient leads to the ions to experience an axial force:

$$F(\omega_{RF}, z) = -\mu(\omega_{RF}) \cdot \nabla \mathbf{B}(\mathbf{z}) \tag{37}$$

turning the radial kinetic energy acquired in the quadrupolar excitation into axial kinetic energy. The orbital magnetic moment is defined as:

$$\mu(\omega_{RF}) = \frac{E_r(\omega_{RF})}{B}, \tag{38}$$

where the radial kinetic energy can be expressed as

$$E_r(\omega_{RF}) = E_-(\omega_{RF}) + E_+(\omega_{RF}) \approx E_+(\omega_{RF}) = \frac{1}{2} m (\rho_+(\omega_{RF}))^2 \omega_+^2, \tag{39}$$

since the angular eigenfrequencies follow the relation $\omega_+ \gg \omega_-$.

When the magnetron motion is fully converted to reduced cyclotron motion, i.e. $\omega_{RF} = \omega_c$ the ions will be most accelerated in the magnetic field gradient, which will be observed as a shorter time-of-flight on the recorded resonance. Thus in the TOF-ICR method, the quadrupolar frequency is scanned over a certain frequency range while the time of flight is recorded.
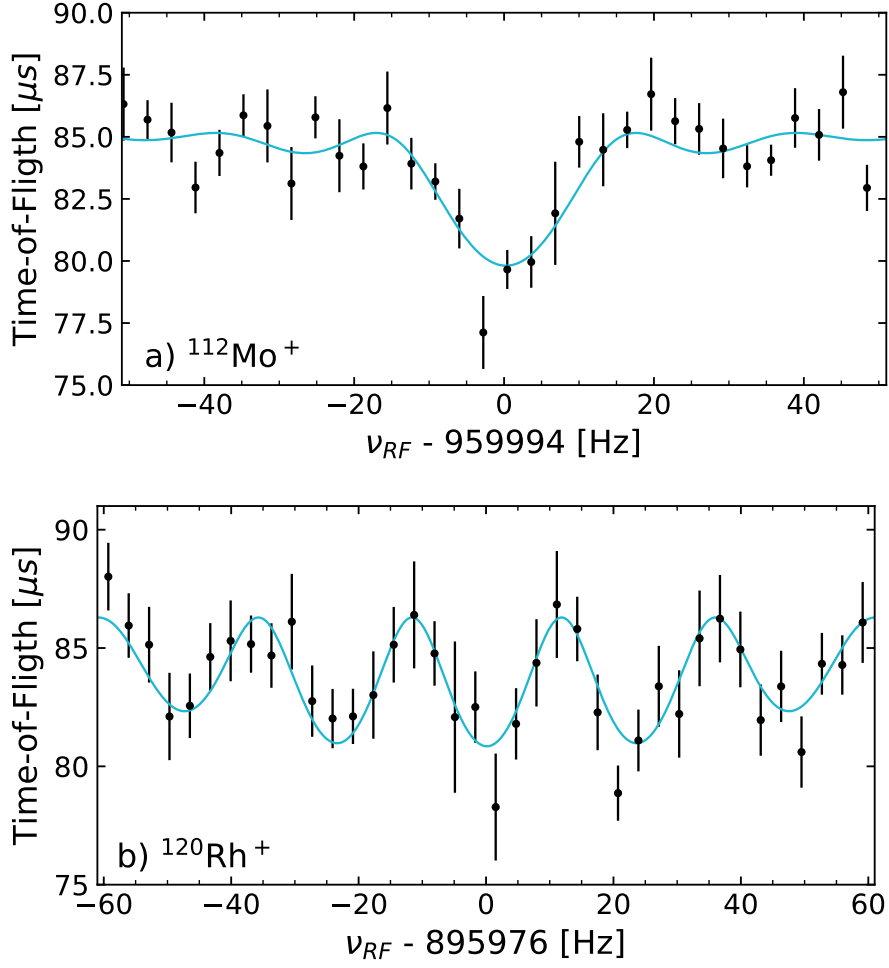
FIGURE 11 a) 50 ms TOF-ICR resonance of ^{112}Mo$^+$ and b) a 10-30-10 ms (off-on-off) Ramsey type TOF-ICR resonance of ^{120}Rh$^+$ performed at JYFLTRAP Penning trap. The blue curve represents the fit of the theoretical curve to the measured data.

The time of flight is calculated as follows:

$$T(\omega_{RF}) = \sqrt{\frac{m}{2}} \int_{z_0}^{z_1} \sqrt{\frac{1}{E_0 - q \times V(z) - \mu(\omega_{RF}) \times B(z)}} \, dz, \qquad (40)$$

where the limits of the integral are from the trap center z_0 to the position of the detector z_1. E_0 is total energy of the ion and μ is the orbital magnetic moment of the charged particle. The electric field and magnetic field are described by $V(z)$ and $B(z)$, respectively. In Fig. 11 a TOF-ICR resonance for ^{112}Mo$^+$, measured in the context of this thesis, is shown. The magnetron excitation was applied for 1 ms while the quadrupole excitation was applied for 50 ms at 224 mV amplitude.

Precision of the conventional TOF-ICR can be increased using the Ramsey's method of time-separated oscillatory fields [80, 82, 83, 84, 85]. The preparation of the ion sample is the same as for the conventional TOF-ICR, but the quadrupolar excitation pulse in the second trap is divided into two pulses and separated by a

waiting time where no exciting RF-field is applied. The excitation RF-field is set up in a way that the phase coherence is preserved over the waiting time. In the recorded TOF-resonance the sideband structure is enhanced and the precision is improved due to the narrower full-width at half-maximum (FWHM) of the resonance peak. Due to the enhanced sideband structure, a single-pulse TOF-ICR is performed to determine the central TOF-minimum before the Ramsey's method is used. S. George et al. [85] found two to three time increase in the precision and a 40% reduction of the central peak width compared to the conventional, single quadrupolar pulse, TOF-ICR. The Ramsey's method of time-separated oscillatory fields requires a clean ion sample: background ions can make the lineshape fitting difficult and another ion species (for example isomeric state) cannot necessarily be separated and recognized from the enhanced sideband structure.

This method has been utilized in articles PI and PII for the mass measurements of the exotic nulcei ^{120}Rh$^+$ and ^{117}Ru$^+$. Figure 11 b) shows a Ramsey type TOF-resonance for ^{120}Rh$^+$ measured with the timing pattern of 10-30-10 ms (On-Off-On) at JYFLTRAP Penning trap. For the PIPERADE Penning trap the Ramsey method has not yet been applied at the time of this work. The Ramsey method utilized for purifying an ion sample was described briefly in Chapter 3.4.

3.5.2 Phase-Imaging Ion-Cyclotron-Resonance technique

The Phase-Imaging Ion-Cyclotron-Resonance (PI-ICR) technique [22, 86] is a mass measurement technique where ion's cyclotron frequency ν_c is determined based on projecting the ions positions in the trap onto a position-sensitive ion detector. This allows the determination of the final phase of the ions at the moment of extraction. Details about the detectors used at JYFLTRAP and at PIPERADE can be found in Chapters 5.2 and 4.2, respectively. PI-ICR can also be used for phase-dependent purification [86], but this technique is not further discussed in this work.

A PI-ICR measurement begins with injecting the ion sample to the trap. Misalignment of the magnetic and electric fields of the Penning trap induces initial magnetron motion in the second trap and non-ideal transfer of the ions to the second trap leads to initial axial motion. For high-precision mass measurements, these initial motions need to be carefully minimized before the RF excitation for the PI-ICR can commence. In Fig. 12 the excitation pattern schemes for PI-ICR and its preparation steps used at JYFLTRAP are shown. The magnetron motion is damped with a dipolar RF-pulse at the ν_- frequency with carefully adjusting the amplitude, duration and the phase of the excitation pulse to minimize the amplitude of the ion's magnetron motion (see Fig. 12, step 2a). The same is done to the initial axial motion ν_z frequency (see Fig. 12, step 2b).

After the ion motions have been damped, a measurement of the two radial motion phases, magnetron motion phase ϕ_- and the reduced cyclotron motion phase ϕ_+, accumulated during a time T_{acc} is performed. Based on the phase accumulated during T_{acc} the total phase difference is calculated as $\phi = \phi_+ - \phi_-$, which relates to the charged particle's cyclotron frequency ν_c as follows:
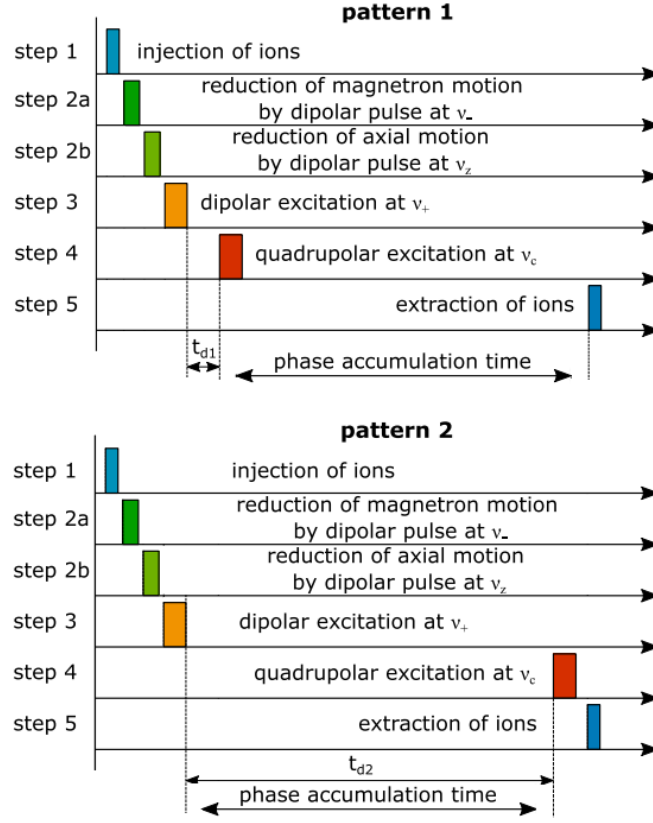
FIGURE 12   The PI-ICR measurement patterns used at JYFLTRAP Penning trap. Pattern 1 and Pattern 2. Figure adapted from D.A. Nesterenko et al. [75] under the CC BY 4.0 licence http://creativecomm ons.org/licenses/by/4.0/.

$$\nu_c = \frac{\phi + 2\pi(n_+ + n_-)}{2\pi T_{\mathrm{acc}}}, \qquad (41)$$

where n_+ is the number of full turns the charged particle performs in modified cyclotron motion and n_- in magnetron motion. In Fig. 12 the phase accumulation time is given $T_{acc} = t_{d2} - t_{d1}$.

To measure the accumulated magnetron ϕ_- and reduced cyclotron ϕ_+ motion phases the patterns 1 and 2 in Fig. 12 are used, respectively. First a dipolar excitation at the ν_+ frequency is applied to increase the reduced cyclotron motion to a controlled radius (see Fig. 12, step 3). This motion is fast and if the ions are extracted right after the ν_+ excitation, it would lead to a deformed phase spot, due to the time-of-flight dispersion of the ion bunch being comparable to the period of the cyclotron motion. To avoid the deformed phase spot, a quadrupolar excitation is used to convert the reduced cyclotron motion into a slow magnetron motion. In the case of the magnetron phase ϕ_- measurement, the conversion is performed right after the ν_+ excitation, to let the ions evolving at ν_- motion during the accumulation time T_{acc}, before extraction (step 4, pattern 1 in Fig. 13). When the reduced cyclotron motion phase ϕ_+ is measured, the ions accumulate phase for T_{acc} before the quadrupolar conversion at ν_c is applied (step 4, pattern 2 in Fig. 13). To calculate the difference between ϕ_- and ϕ_+ the trap center "phase"
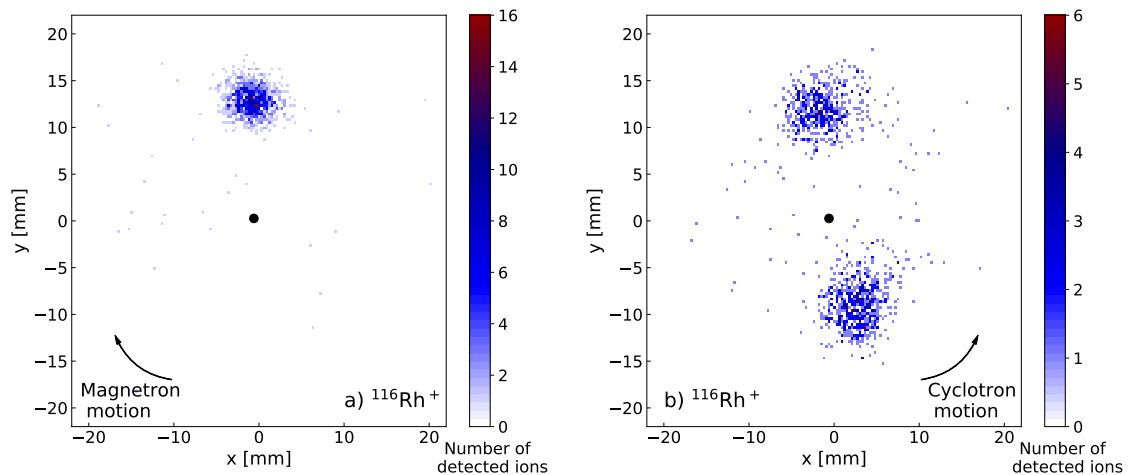
FIGURE 13   The accumulated a) magnetron phase ϕ_- and b) cyclotron phase ϕ_+ for ^{116}Rh$^+$ PI-ICR measurement. Both phase spots were measured with an accumulation time of 450 ms. The black point represents the trap center.

spot is also measured, by applying no excitation in the trap.

In Fig. 13 a phase accumulation time T_{acc} of 450 ms was applied for ^{116}Rh$^+$ and the resulting a) magnetron phase ϕ_- and b) cyclotron phase ϕ_+ are shown. In Fig. 13 b) the ground and isomeric states of ^{116}Rh have been separated in the 450 ms accumulation time. The PI-ICR technique provides a 40-fold increase in resolving power and five times increase in precision compared to the Ramsey type TOF-ICR [22]. The PI-ICR technique was used to separate the isomeric states from the ground states and to measure the masses of both states in article PI and PII.

4   PIPERADE DOUBLE PENNING TRAP

This chapter describes the offline commissioning of the PIPERADE (PIèges de PEnning pour les RAdionucléides à DESIR) double Penning trap for the upcoming DESIR/SPIRAL2 facility (Decay, Excitation and Storage of Radioactive Ions) [87]. This work has been conducted at the Laboratoire de Physique des 2 Infinis Bordeaux, France (LP2I Bordeaux). In the following chapter, the DESIR/SPIRAL2 facility is first introduced, followed by a section describing the PIPERADE double Penning trap. The last part of the chapter presents the commissioning results obtained in this work, from which the first results of buffer gas cooling technique have been reported in attached article PIII.

4.1   DESIR/SPIRAL2 facility

The GANIL (Grand Accélérateur National d'Ions Lourds) Accelerator Laboratory, located in Caen, France, has a new generation radioactive ion beam (RIB) facility extension underway named SPIRAL2, which will provide access to exotic nuclei far from stability. This new facility will consist of three experimental halls: NFS (Neutrons for Science), S3 (Super Separator Spectrometer) and DESIR (Decay, Excitation and Storage of Radioactive Ions, see Fig. 14), from which NFS and S3 have already been built. The DESIR hall will be dedicated to low-energy high-precision nuclear physics experiments and it will receive the first experimental setups in 2025.

The experimental setups at DESIR will receive 10-60 keV RIBs provided by the S3 facility [88] and the upgraded SPIRAL1 facility [89]. S3 will produce neutron-deficient and super-heavy nuclei with unprecedented intensities via fusion-evaporation reactions, in which a high-intensity stable ion beam from the SPIRAL2 accelerator will hit a carefully selected target producing a highly-excited compound nucleus. The formed nucleus will get rid of this excitation energy by evaporating particles (for example protons, neutrons etc.) and γ radiation, forming the isotope of interest. These reactions give access to neutron-deficient
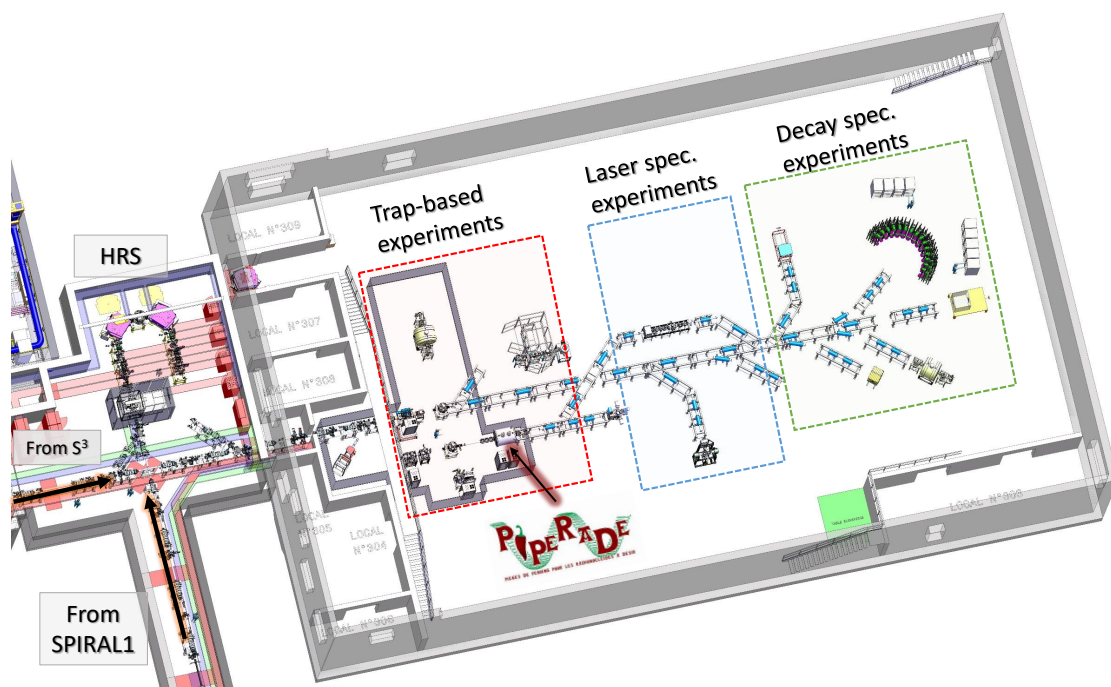
FIGURE 14   A layout of the DESIR facility and the arrival of the S3 and SPIRAL1 beams is shown.

nuclei (from N = Z up to super-heavy nuclei). SPIRAL1 produces light exotic nuclei via fragmentation reactions. The experimental setups in the DESIR hall (see Fig. 14) will be used to study nuclear structure of exotic nuclei (deformation, shell effects etc.), nuclear astrophysics and weak interaction via decay spectroscopy, laser spectroscopy and ion trap based techniques.

When exotic nuclei are produced, usually it is accompanied with a high amount of unwanted isobaric or molecular contamination, due to the non-selective production and ionization methods. In order to perform high-precision measurements on these exotic nuclei, they need to be isolated from the isobaric and molecular contamination. In this context multiple devices are being built and commissioned at LP2I Bordeaux, namely a double Penning trap PIPERADE [76] and a magnetic dipole High Resolution Separator (HRS) [90]. The HRS will be placed before the entrance of the DESIR hall (see Fig. 14) and is expected to reach a mass resolving power of $2x10^4$.

For the beam quality a General Purpose Ion Buncher (GPIB) [91] will be placed at the entrance of the DESIR hall and is being also commissioned at LP2I Bordeaux. The GPIB will provide continuous or bunched ion beams for the experimental setups in DESIR, with low transverse emittance and controlled energy and time dispersions. Finally, PIPERADE will be able to further purify, isobarically or even isomerically, the ion bunches received from the GPIB. After the purification performed with PIPERADE the selected ion sample can be directed back to main DESIR beamline to post-trap spectroscopy setups or high-precision mass measurements can be performed with the second trap of PIPERADE. In the following a few example regions for mass measurements at DESIR utilizing the

PIPERADE double Penning trap are discussed. First, masses of nuclei in the region around ^{80}Zr and ^{100}Sn are aimed to be measured to improve knowledge of the rapid proton capture process and of nuclear structure. Second, masses of nuclei along the $N = Z$ can be measured to study for example the Wigner effect. Nuclei at $T_z = -1, -3/2, -2$ lines will be measured to study the Isobaric Multiplet Mass Equation (IMME), while the Q-values of $0^+ \rightarrow 0^+$ transition nuclei are measured to study the weak interaction. In the region of superheavy nuclei recent mass measurements have already probed ^{257}Rf [92] and ^{252}Db [93], but the aim at DESIR is to push to even heavier nuclei, starting from the Rf and Db elements. A more detailed description of the PIPERADE double Penning trap and its commissioning at LP2I Bordeaux is given below (Section 4.2).

4.2 PIPERADE Penning trap at LP2I Bordeaux facility

The PIPERADE (PIèges de PEnning pour les RAdionucléides à DESIR) double Penning trap [76] consists of a 7 T superconducting magnet, from the company CRYOGENIC, and two cylindrical Penning traps housed in a warm bore. The magnetic field has two homogeneous regions 20 cm apart, where the centers of the two cylindrical traps are placed, see Ref. [76] for a more detailed description. The main aims of PIPERADE are to deliver isobarically or isomerically selected samples of ions for the DESIR facility described above and to perform high-accuracy mass measurements.

The PIPERADE Penning traps, together with the GPIB, are being commissioned at LP2I Bordeaux. The commissioning beamline assembly is shown in Fig. 15. The stable ion beam is provided by a Forced Electron Beam Induced Arch Discharge (FEBIAD) type ion source on a 30 kV high-voltage platform. The source can produce either alkali elements (surface ionization) or ionized gas elements (FEBIAD mode). During the commissioning discussed in this thesis the source was used only in surface ionization mode. The beamline is equipped with
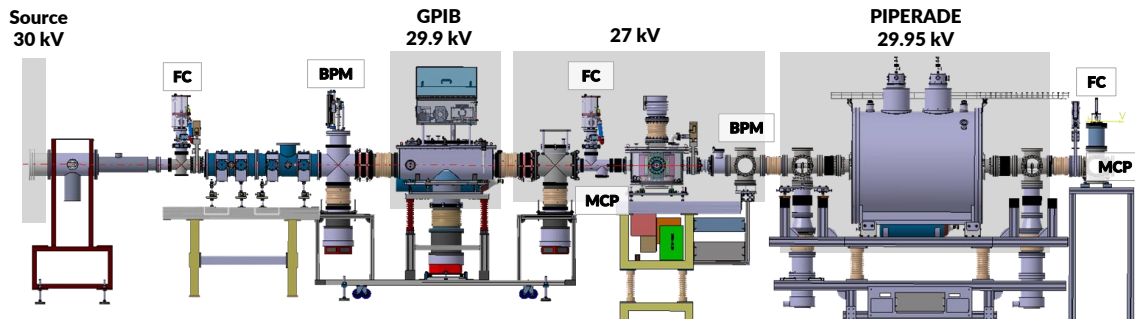

FIGURE 15   Layout of the LP2I Bordeaux PIPERADE commissioning beamline assembly with the high-voltage platform areas marked. The beamline starts with a FEBIAD ion source, from which downstream are the GPIB and the PIPERADE Penning traps. The detectors are shown: Faraday Cups FC, beam profile monitors BPM and microchannel plate detectors MCP.

ion beam optics elements (steerers, einzel lenses, quadrupole triplets) to control the ion beam and with different detectors for ion counting/beam monitoring: faraday cups, MCP detectors (Topag MCP-MA33/2) and beam profiler monitors (see Fig 15). The ions are injected into the gas-filled GPIB, which is floated to 29.9 kV voltage for an optimal injection of the ions. The GPIB provides 1 μs ion bunches, at the time of this work, for the PIPERADE Penning trap downstream. The transfer region between the GPIB and PIPERADE is at a 27 kV high-voltage potential while the PIPERADE Penning trap is at 29.95 kV. Behind PIPERADE, on the ground potential side, is the ion detection which at the time of this work was done using an MCP detector and a Faraday cup. More detailed information about the detection setup can be found in Refs. [76, 94].

As stated before, PIPERADE has two cylindrical Penning traps: the first one called the Purification Trap and the second one known as the Measurement Trap. The purification trap, which is used for ion of interest selection (i.e. purification), has a eight-fold segmented ring electrode, neighboured by a set of correction electrodes and eight endcap electrodes (four on each side, see Fig. 16). The first trap has a larger diameter (d = 64 mm) than the measurement trap (d = 20 mm), to offer a possibility for higher-capacity purification of ions. For example at JYFLTRAP, described in Chapter 5.2, both traps have the same diameter (d = 32 mm). The aim with the bigger first trap at PIPERADE is to separate up to $10^4 - 10^5$ ions per bunch. The first trap of PIPERADE utilizes the buffer gas cooling technique [79] as the main purification technique, which can reach a mass resolving power of $m/\Delta m = 10^5$. This technique utilizes helium buffer gas and is described in more detail in Chapter 3.4. In the Section 4.2.1 below the commissioning of the buffer gas cooling technique is explained and results obtained are shown.
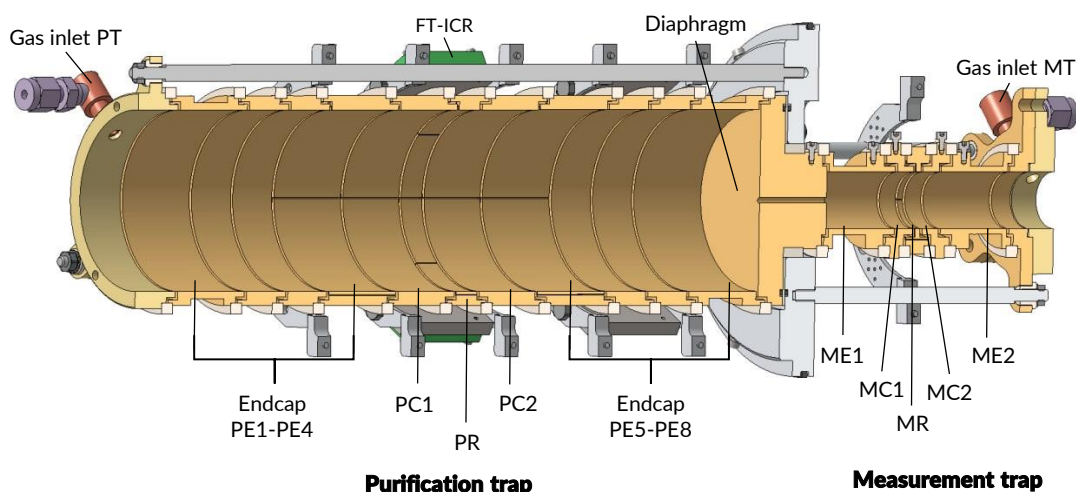

FIGURE 16   A schematic of the PIPERADE double Penning trap tower assembly. The purification trap has eight endcap electrodes (PE1-PE4 and PE5-PE8), two correction electrodes (PC1 and PC2) and a ring electrode (PR). Also the gas inlet and FT-ICR electronics are shown. The measurement trap consists of two endcap electrodes (ME1 and ME2), two correction electrodes (MC1 and MC2) and ring electrode (MR).

The measurement trap is designed to be used for precision mass measurements, accumulation of the purified ions or high-resolution purification. It has a four-fold segmented ring electrode, neighboured by a set of correction electrodes and a set of endcap electrodes (see Fig. 16). The preparation and measurement traps are separated with a diaphragm which at the time of this work had a diameter of 4 mm. This acts as a barrier between the two traps to reduce the amount of helium gas in the measurement trap, since it is ideally operated under high vacuum ($< 1 \times 10^{-8}$ mbar). The diaphragm also plays an important role in the selection of the purified ions in the buffer gas cooling method, see Chapter 3.4. More details about the geometrical design of the PIPERADE trap tower assembly can be found in Ref. [76]. The mass measurement techniques planned for PIPERADE are the TOF-ICR method (see Chapter 3.5.1) and the PI-ICR method (see Chapter 3.5.2). The first commissioning of the TOF-ICR technique at PIPERADE is described in more detail below (see Section 4.2.1). For studies of the PI-ICR technique at PIPERADE a new delay line detector (RoentDek HEX75bL with DLD80) has been installed in October 2022. Studies of the new delay line MCP detector, and thus PI-ICR technique, were outside of the timeframe of this thesis.

The move of the PIPERADE Penning trap from LP2I Bordeaux to DESIR is planned for the year 2025 and first radioactive ion beam tests are planned to begin in 2027.

4.2.1 Results of the first commissioning

In the context of this work the commissioning of the PIPERADE double Penning trap was done in 2020-2021. These tests included the very first trapping of ions with PIPERADE, the implementation of the buffer gas cooling technique (see Chapter 3.4) for isobar separation in the purification trap and all the way to the very first TOF-ICR resonance in the measurement trap. The first results on the buffer gas cooling technique at PIPERADE have been published in the attached article PIII ([76]). Only the highlights of the tests performed during the time frame of this work are presented below. Future tests needed to complete the offline commissioning are briefly discussed at the end of the chapter. All of the tests have been performed with a 4 mm diameter diaphragm, which is the largest diaphragm machined for the PIPERADE double Penning trap.

To trap ions in a Penning trap the ions need to be injected into a strong magnetic field, decelerated and captured without inducing energy dispersion. At PIPERADE the deceleration of the ion bunch is achieved with the different platform voltages (see Fig. 15) and the injection optics. The 3-keV ion bunch is slowed down by the potential difference between the transfer platform (27 kV) and the trapping platform (29.95 kV). To avoid the sudden decrease of energy due to the platform difference the first injection electrodes are set to about -3 kV (compared to the trap platform) and then a gradient is applied up to the trap.

The voltages applied on the trap electrodes, used for the tests described below, are tabulated in Table 1 and a schematic of the trapping principle is shown in Fig. 17. At the beginning of the trapping cycle all of the trapping potentials are in the closed state (see Fig. 17 scheme 1). When an ion bunch is released from the cooler-buncher (GPIB, see Fig. 15) the injection side potential wall is lowered to the open state (see Fig. 17 schemes 2 and 3) allowing for the ion bunch to be injected into the Penning trap. At PIPERADE the injection potential wall is formed by the voltages applied to the PE1 to PE4 endcap electrodes and the PC1 correction electrode (see Fig. 16 and Table 1). After the ion bunch passes the

TABLE 1 Voltages applied on the different electrodes (see Fig. 16) of the purification and measurement trap in "open" and "closed mode, most commonly used in the commissioning stage of the PIPERADE Penning trap. Note that the purification trap has a diameter of $d = 64$ mm and the measurement trap $d = 20$ mm.

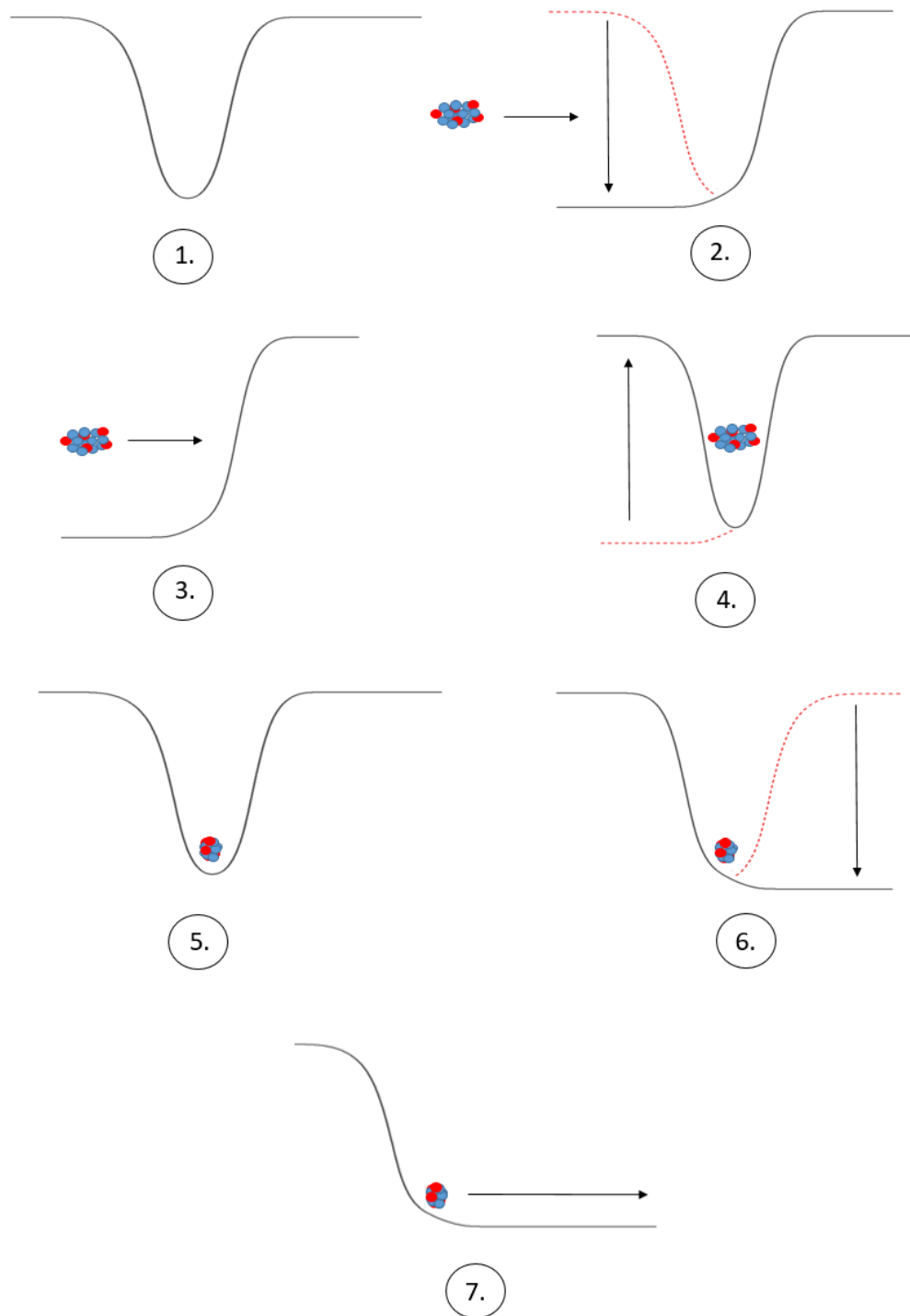|	Purification trap		Measurement trap		
Electrode	Open [V]	Closed [V]	Electrode	Open [V]	Closed [V]
PE1-4	-85	0	ME1	-85	0
PC1	-85	-70	MC1	-85	-70
PR	-80	-80	MR	-80	-80
PC2	-85	-70	MC2	-85	-70
PE5-8	-85	0	ME2	-85	0
Diaphragm	-85	0			

FIGURE 17 The trapping principle: 1. The trap voltages are in the closed state, 2. the ion bunch is released from the GPIB and the injection side potential wall is lowered, 3. the ion bunch travels over the open state injection potential wall, 4. the ion bunch has passed the injection side potential wall which is switched to closed state, 5. the ions are trapped and RF excitation can be applied, 6. the ion bunch is released from the trap by lowering the extraction side potential wall to the open voltage state, 7. the ion bunch is extracted.

injection side potential wall, thus entering the trap, the injection side potential wall voltages are switched back to the closed state (see Fig. 17 scheme 4). The time when these electrode voltages are switched to the closed state has to be well optimized, to ensure maximum capture efficiency. While the ions are trapped (Fig. 17 scheme 5) their eigenmotions (Fig. 8) can be manipulated through different RF-excitations or even with buffer gas (see Chapter 3.4). The closed state trapping voltages (Table 1) are set in such a way that the electrical field anharmonicities are reduced. The extraction potential for the purification trap is created with the PC2 correction electrode and the PE5 to PE8 endcap electrodes. The ion bunch is extracted from the trap by switching these extraction electrodes to the open voltage position (Fig. 17 schemes 6 and 7). When the ion bunch is extracted from the purification trap of PIPERADE, it travels through a diaphragm electrode, utilized in the buffer gas cooling method (see Chapter 3.4). The ions are extracted either to the MCP detector or to be trapped in the second trap.

In Fig. 18 a schematic TOF-ICR measurement sequence for $^{39}K^+$ is shown. The duration of each timing step is carefully determined by performing different timing scans. In the following studies and optimization of each step will be described. The last step (8.) represents both the extraction step and the length of the timing gate, 160 μs, given for the MCP detector in which the signal detected is recorded.

The first step in the timing pattern of Fig. 18 is the injection of the ion bunch into the purification trap of PIPERADE. The first tests on injecting ions to the magnetic field of PIPERADE and trapping these ions started in 2020. For choosing the correct injection time, i.e. how long the potential wall voltages need to be in the open state for the ion bunch to be captured (see Fig. 17 scheme 4), an injec-
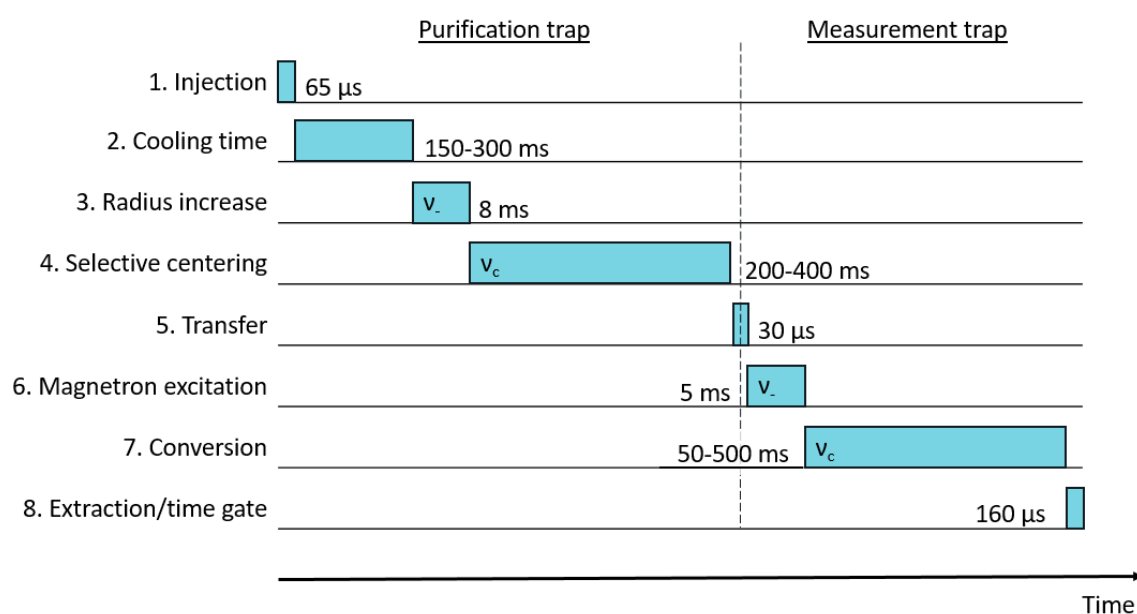

FIGURE 18   A schematic of the timing pattern used for a TOF-ICR measurement at the PIPERADE Penning trap. Examples of most commonly used durations for each step when $^{39}K^+$ ions were used are shown.

tion time scan was conducted, where the amount of ions in a bunch was plotted against the time for closing the potential wall. For the following tests the optimum injection time of 65 μs, for which a maximum number of ions was detected, was used.

After the ions are trapped in the purification trap (schema 5 in Fig. 17), a cooling time for the ion sample needs to be allocated before the excitations are performed, shown as the timing step 2 in Fig. 18. This ensures that the axial and cyclotron motions gained during the injection of the ion sample are damped by the interaction with the helium buffer gas. The helium gas pressure is controlled with a flowmeter and during the following measurements the gas flow was set to 1.0 % unless stated otherwise, leading to a reading of 1.4×10^{-7} mbar on the Penning type gauge located at the cross before the injection (see Fig. 15). At 0 % gas flow the pressure reading was 2.3×10^{-8} mbar.

Figure 19 shows a scan of the cooling time: the time of flight between the trap and the MCP detector is shown as a function of the time the ion bunch spends in the purification trap. No excitations are applied in the first trap, and the ion bunch is not captured in the second trap (only steps 1,2,8 of Fig. 17). The cooling time is selected based on how a significant reduction of the TOF-spread can be achieved in a reasonable time. For example from 110 ms to 250 ms the reduction in the TOF-spread is around 73 %, while no significant gain is attained going from 250 ms to 330 ms (around 19 % reduction). Thus based on the Fig. 19 a cooling time of 240 ms at 1.0 % gas flow was selected for the timing step 2 in Fig. 18.
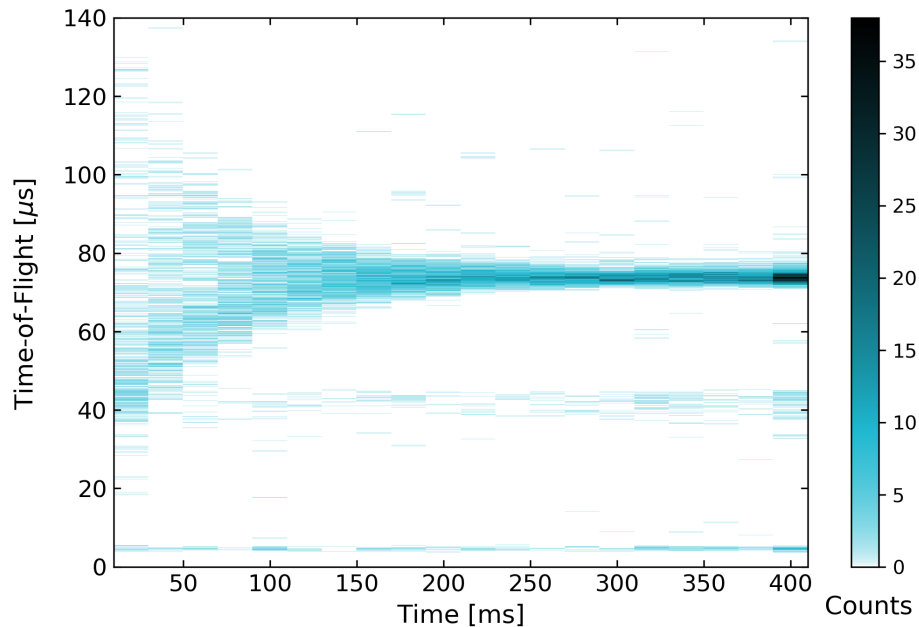

FIGURE 19   Time of flight of ions from the fist trap to the MCP detector as a function of the trapping time before any excitations are applied. The helium buffer gas flow is set to 1 %. At TOF of around 5 μs a signal created by the ionized helium gas escaping the purification trap is seen. The signal at 40 μs corresponds to the TOF of water molecules, which are most likely formed due to the rest gas in the beamline or the impurities in the helium buffer gas.
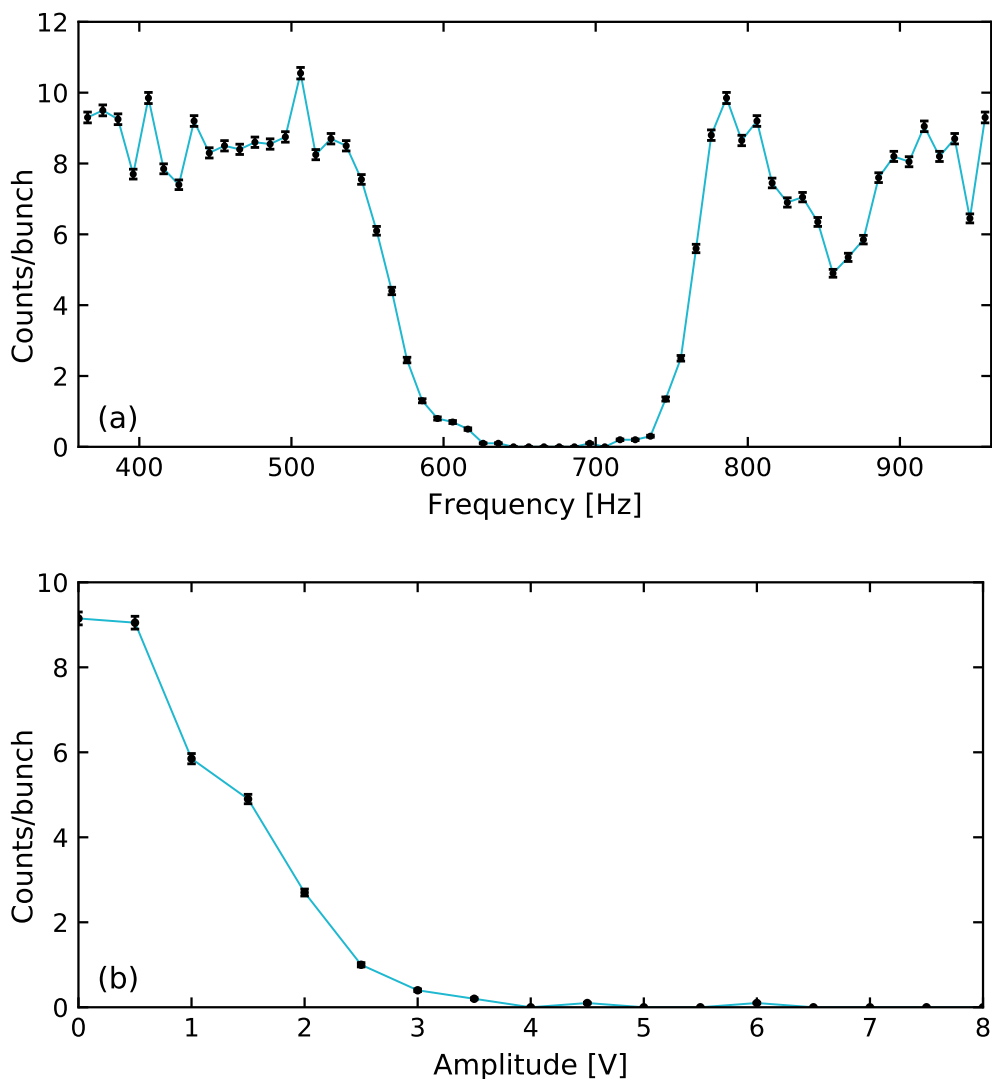
FIGURE 20   Dipolar magnetron excitation: number of counts per bunch detected on the MCP detector as a function of a) the excitation frequency ν_- (Hz) and b) the excitation amplitude (V).

Once the ion bunch is captured and a sufficient cooling has been performed the manipulation of the ion motions is performed using the RF-fields applied to the ring electrode (PR). At PIPERADE, the buffer gas cooling technique will be the main technique to select the isobar of interest, or even a highly-excited isomer, and to discard the unwanted ion species (referred as purification, see Chapter 3.4) in the purification trap. In the following paragraphs the implementation of this technique, steps 3 and 4 in Fig. 18, is discussed.

The first step is to increase the magnetron motion radius of the ions to a bigger orbit than the diaphragm electrode radius ($r = 2$ mm). This is performed by applying a dipolar RF-field at ν_- to the ring electrode: at PIPERADE two generator channels are connected to two opposite ring electrode segments, and a 180° RF-phase difference is applied. The RF-generator is set to an N-cycle mode, thus a certain amount of periods at the selected frequency is performed, determining

the length of the applied excitation.

With the dimensions and properties of the Penning trap, the magnetron frequency can be calculated (see Eq. 32 in Chapter 3.1). In the case of PIPERADE the factor U_0/d^2 was taken from SIMION simulations of the electric field potential, leading to a calculated magnetron frequency of 660 Hz for the purification trap. The first successful magnetron excitation in the first trap was performed in March 2021. The dipolar excitation was applied for 8 ms in the timing pattern, but the number of N-cycles was fixed to five. At 660 Hz this amount of N-cycles leads to an excitation time of 7.5 ms (Fig. 18 step 3).

In Fig. 20 a) the dipolar excitation frequency is scanned in the vicinity of the calculated magnetron frequency, while the amplitude is set to a high value (10 V). The number of ions per bunch detected on the MCP detector is recorded. At the correct frequency, and a high enough amplitude, all the ions are moved to a radius bigger than the diaphragm between the first and the second trap. When extracted after this excitation, all ions hit the diaphragm, and do not reach the MCP detector. As expected based on the calculated magnetron frequency, the measured ν_- is about 660 Hz.

In Fig. 20 b) the dipolar excitation amplitude, with the excitation frequency set to 660 Hz, is scanned while the number of ions detected in each bunch is recorded. The magnetron motion radius is expected to evolve linearly with the applied excitation amplitude. The amplitude where the number of ions per bunch goes to zero (i.e. the ions are on a larger orbit than the diaphragm size) is selected. For the tests to follow the magnetron excitation amplitude has been set to 5 V.

The next step of the buffer gas cooling technique is to mass-selectively center the ions of interest (Fig. 18 step 4). This is achieved with a quadrupolar RF-field applied at the conversion frequency $\nu_c = \nu_+ + \nu_-$ (see Eq. 31 in Chapter 3.1). In the purification trap of PIPERADE the quadrupolar field is formed with two RF-generator channels connected to four segments of the ring electrode (PR, see Ref. [76] for a more detailed connection diagram). The RF-generators are used in the gated burst mode, thus the applied excitation will end when the timing gate given by the user ends. The quadrupolar excitation at $\nu_c = \nu_+ + \nu_-$ converts the magnetron motion into a modified cyclotron motion for the specific mass ions, and the modified cyclotron motion will then be damped due to interaction with the helium buffer gas. Since the conversion is highly mass dependent, the frequency needs to be carefully selected. The excitation time and amplitude are chosen to reach the desired resolving power.

The first successful mass centering utilizing the quadrupolar excitation in the first trap of PIPERADE was performed in May 2021. The number of ions per bunch was recorded as a function of the quadrupolar excitation frequency, close to ν_c of $^{39}K^+$, shown in Fig. 21 a). The quadrupolar excitation was performed with a 400 ms excitation time and a 2.0 V amplitude (Fig. 18 step 4). A radial cooling of 1 ms in the first trap was added to the timing pattern before the extraction to the MCP detector. A Gaussian fit to the frequency scan shown in Fig 21 a) gives a FWHM of 19.4 Hz leading to a mass-resolving power of around 140000.
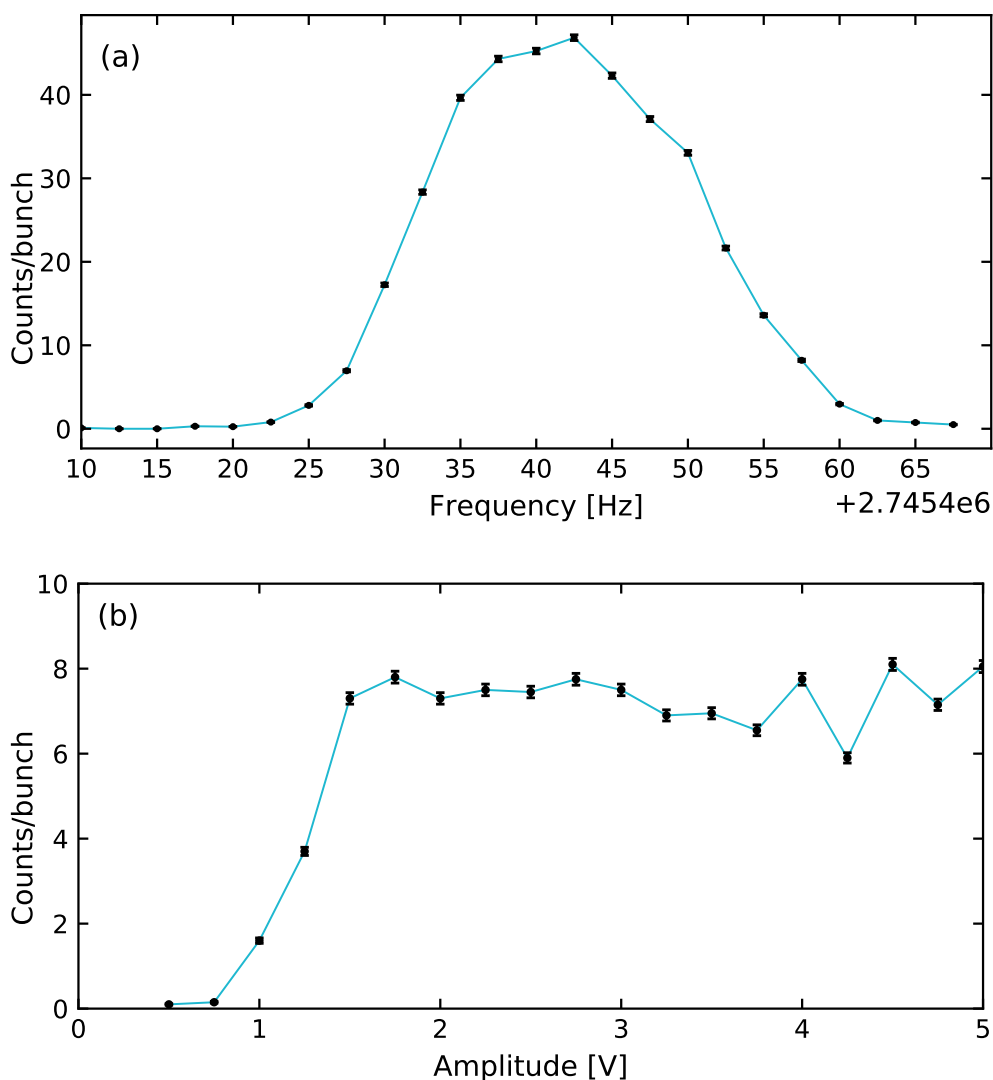
FIGURE 21   Number of ions in a bunch recorded on the MCP as a function of the quadrupolar excitation (a) frequency and (b) amplitude performed in the purification trap. The amplitude measurement was done with a lower intensity ion beam.

Many tests on the buffer gas cooling technique were performed and the targeted mass-resolving power of $m/\Delta m \approx 10^5$ was reached [76].

Figure 21 b) shows the number of ions per bunch detected on the MCP detector as a function of the quadrupolar excitation amplitude. The quadrupolar excitation amplitude is selected where the maximum amount of ions in each bunch is reached i.e. the ions have been centered and they can pass the aperture on the diaphragm electrode. In Fig. 21 b) the ions are centered when around 1 V amplitude is applied.

The ions selected using the buffer-gas cooling method, as described above, are transferred to the second trap by switching the transfer voltage potential to the open state (see Fig.17 schema 6). At PIPERADE the transfer potential wall

is formed by the voltages applied to PC2, PE5-PE8, diaphragm, ME1 and MC1 electrodes. When the ion sample has passed through, the same transfer potential wall is switched to closed voltage state (similarly to Fig.17 schema 4). If the ion bunch is captured in the second trap, the closing time of the transfer potential has to be carefully selected to not induce axial motion to the ion sample. Capturing the ion bunch in the second trap has the same principle as in the first trap, shown in Fig. 17.

In Fig. 22 the time of flight of the ion bunch has been recorded on the MCP detector as a function of the transfer time, i.e. the time that the electrodes between the two traps are in the open state voltage position (Fig. 18 step 5). The time when the TOF-spread is the smallest is selected as the optimal transfer-time, which is around 30.2 μs (see Fig. 22)

In the second trap (measurement trap), the ion bunch is captured and further purification and/or mass measurements can be performed. At PIPERADE no more purification techniques (for example Ramsey cleaning) were yet explored but the TOF-ICR mass measurement technique (see Chapter 3.5.1) was implemented in late 2021. The ring electrode (MR) of the measurement trap is four-fold segmented (see connection diagram in Ref. [76]), and the dipolar excitation at ν_- or ν_+ can be applied using one or two opposite segments. If two segments are used, opposite phase for the RF-field needs to be applied to form a dipolar
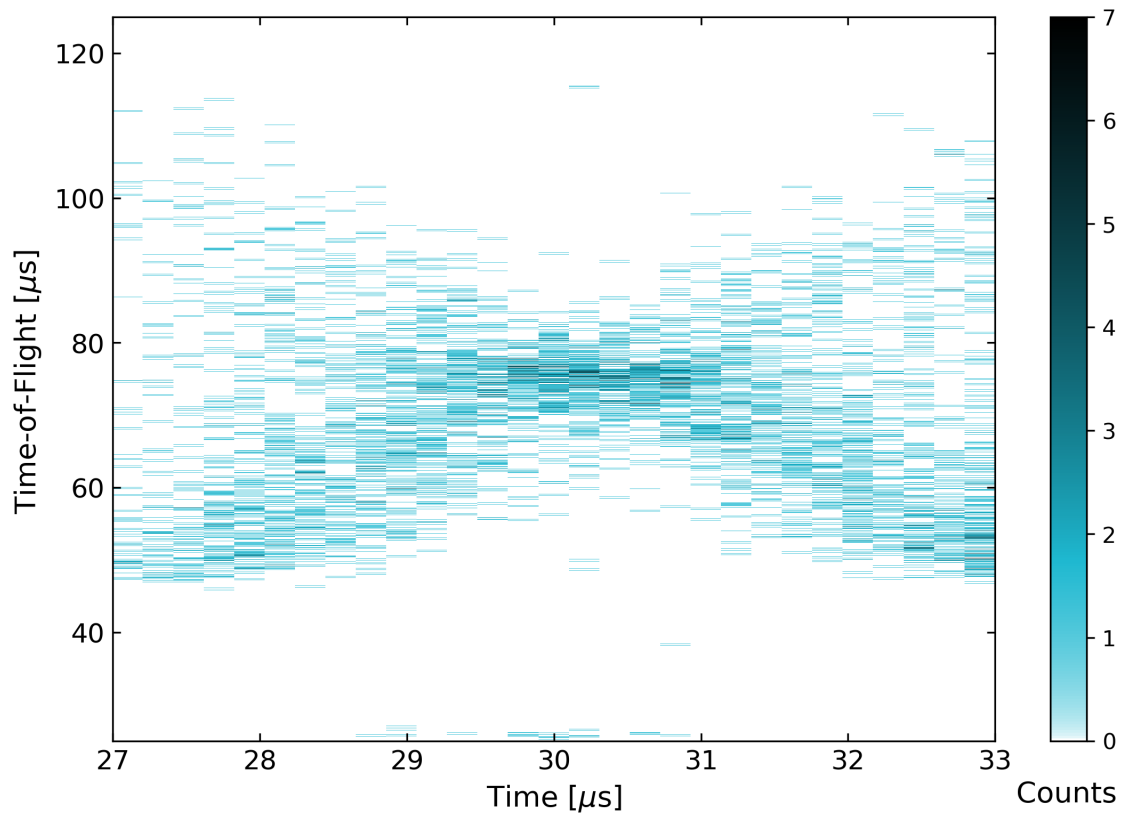

FIGURE 22 Time-of-flight of the ions from the second trap to the MCP detector as a function of the transfer time for the ^{39}K$^+$ ion bunch between the PT and MT.

field. The quadrupolar excitation is applied using the two other segments with the same RF-phase. The measurements described below were done using ^{39}K$^+$ ions, which have a precisely known mass.

In TOF-ICR, as described in Chapter 3.5.1, the magnetron motion radius is first enlarged with a dipolar excitation. After a quadrupolar excitation is then scanned close to the $\nu_c = \nu_+ + \nu_-$ frequency to convert the magnetron motion to a reduced cyclotron motion. The measurement trap is operated in high vacuum conditions, thus no damping of the motion is expected. When the excitation frequency is equal to ν_c, the energy gained by the ions is maximum, thus the time of flight measured with the MCP detector is the shortest (see Chapter 3.5.1 for more detailed explanation).

The first step of the tests in the measurement trap was to determine the magnetron frequency. For that, a long magnetron excitation was applied, with a frequency close to the calculated ν_- frequency (MT calculated ν_- is 6.76 kHz), see Fig. 18 step 6. Since the width of the resonance depends on the excitation time as follows $\Delta\nu_{FWHM} \approx 1/T_{RF}$, a broadband quadrupolar excitation at the expected $\nu_c(^{39}K^+)$ was then applied by using a short pulse for the RF excitation. By doing such a broadband excitation, even if the ν_c was not precisely known (due to the not well-known magnetic field), the conversion could be performed. The frequency of the first magnetron exitation was scanned and if the frequency is correct (i.e. the ν_- frequency), the ions gain magnetron motion, which is then converted into cyclotron motion and seen as a shorter TOF. If the dipolar frequency is not correct, a time-of-flight reduction would not be observed. Another way to determine the magnetron frequency is to use the first step of the buffer gas cooling technique, as it was performed in the first trap. A dipolar excitation at a certain frequency was applied and the ion sample was sent back to the first trap. If the dipolar excitation frequency was at the magnetron frequency ν_-, the ion sample would hit the diaphragm electrode. Next the ion sample was extracted from the first trap, directly to the MCP detector. A similar scan of the dipolar excitation frequency was performed as in 20 a). In both ways the magnetron frequency in the measurement trap was measured to be around 6.52 kHz. The difference in magnetron frequency in the measurement trap (d = 20 mm) compared to the purification trap (d = 64 mm) is due to the size difference of the traps.

After the magnetron frequency was determined, the magnetron excitation time was reduced to a shorter time (for example 5 ms, 25 N-cycles, Fig. 18 step 6) and the scans of the quadrupolar excitation were performed. The quadrupolar excitation frequency was scanned while the TOF was measured with the MCP detector. This way a TOF-ICR resonance is recorded, where the correct ν_c frequency of the ion can be seen as a shorter TOF. The quadrupolar excitation time is chosen based on the aimed level of precision on ν_c, taking in consideration other constraints like for example the half-life of the ion of interest ($\Delta\nu_c = 1/T_{RF}$). Thus for exotic radioactive ion species a compromise between the precision of the measurement and decay losses has to be found. In Fig. 23 a) a 100 ms quadrupolar excitation TOF-ICR of ^{39}K$^+$ is shown. The resonance has been fitted with the lineshape (see Eq. 40) resulting in the cyclotron frequency of 2745652.7(0.4) Hz.

In Fig. 23 b) a TOF-ICR resonance with a 500 ms quadrupolar excitation is shown. Compared to the 100 ms excitation time resonance it can be seen that the resonance with 500 ms quadrupolar excitation is much damped and unclear. This is due to the collisions with the residual gas which has leaked from the first trap into the second trap. A change of the diaphragm size is foreseen, to reach resonances with better resolution using longer excitation times. Though it is noteworthy, that with the longer excitation time higher resolution is reached (see the differing x-scales in Fig. 23).
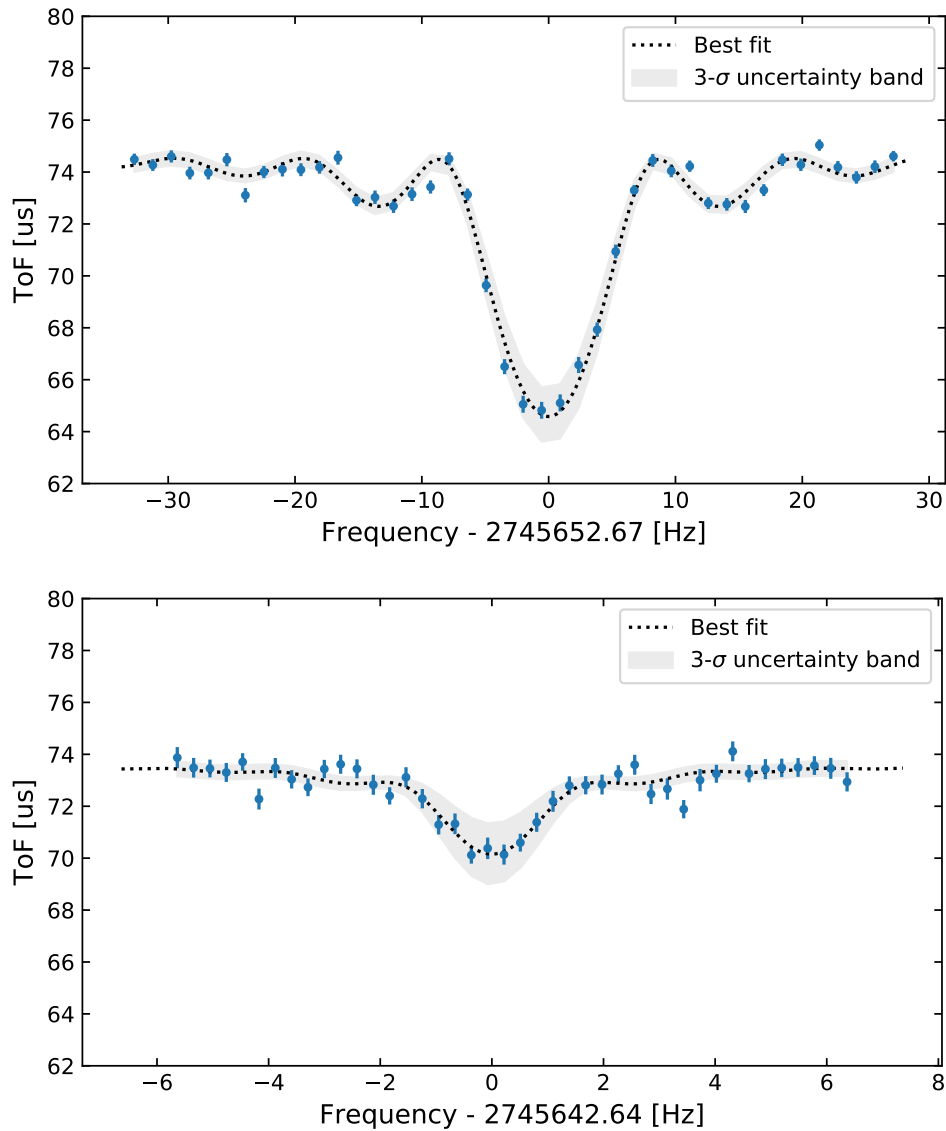

FIGURE 23 The time-of-flight recorded at the MCP detector as a function of the quadrupolar excitation frequency for two different excitation times: a) 100 ms TOF-ICR resonance of $^{39}K^+$ and b) 500 ms TOF-ICR resonance of $^{39}K^+$.

When the quadrupolar frequency is set at ν_c frequency of the ions of interest, the specific ion's magnetron motion is changed into the cyclotron motion (notation Eq. 31). To have a well defined TOF-resonance the quadrupolar excitation amplitude needs to be set so that a full conversion from magnetron motion to full cyclotron motion is observed. A scan of the amplitude of the quadrupolar excitation (excitation time 100 ms) at the cyclotron frequency ν_c of $^{39}K^+$ is shown in Fig. 24. This scan shows multiple conversions from magnetron motion to reduced cyclotron motion, the so-called conversion beating curve. It is desired that one full conversion is performed, leading to maximum resolution. Thus the amplitude is selected accordingly. Based on the scan in Fig. 24 the selected quadrupolar excitation amplitude is 0.2 V.
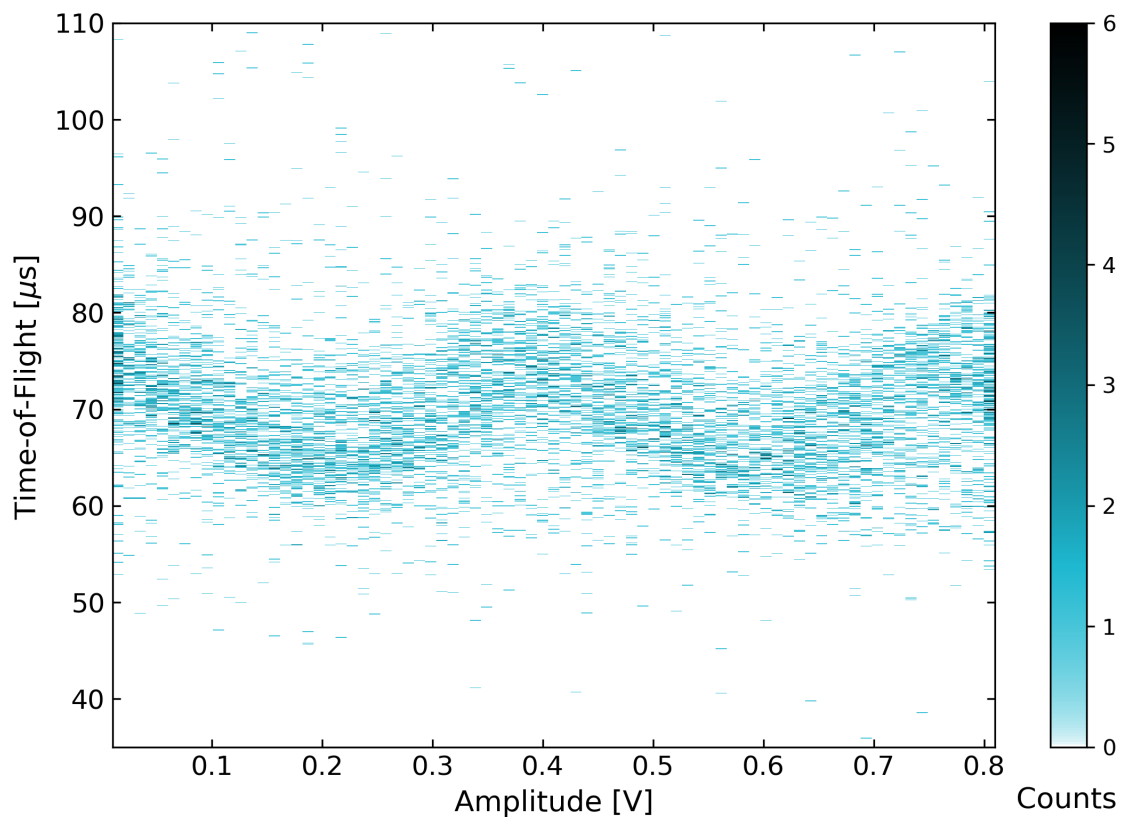

FIGURE 24   The time-of-flight recorded at the MCP detector as a function of the quadrupolar excitation amplitude when a 100 ms excitation has been selected at the ν_c frequency of $^{39}K^+$.

To conclude, this chapter discussed the results of the first commissioning of the PIPERADE double Penning trap. Results were shown, starting from the first injection of ions into the first trap, to the implementation of the buffer gas cooling technique and the first excitations in the second trap. The buffer gas cooling technique in the purification trap reached the desired resolving power of $\approx 10^5$. The very first TOF-ICR resonances, performed in the second trap are shown. But clear implications of the helium buffer gas leaking from the first trap to the second trap can be noticed. This limits the precision of the TOF-ICR measurements to $\approx 10^{-7} - 10^{-8}$ (≈ 100 ms excitation times).

To improve the TOF-ICR resonance, the diaphragm between the traps is planned to be changed to a smaller aperture (from 4 mm to 2 mm diameter) in the future. This will allow to perform longer excitation times of the quadrupole excitation. In the measurement trap the correction ring potentials, which affect the harmonicity of the trapping potential, also need to be optimized. If the harmonicity of the trapping potential is not well optimised the ion motion is affected, causing shift to the frequencies (see Chapter 3.2). The first TOF-ICR mass measurements of $^{39}K^+$ against $^{41}K^+$ have recently been performed at PIPERADE. The systematic studies of the TOF-ICR technique (B-field fluctuations, mass-dependent errors and residual systematic uncertainties) still need to be explored. The 2D MCP detector has been installed at PIPERADE in late 2022, which will open the commissioning for the PI-ICR technique.

5 IGISOL IV FACILITY AND JYFLTRAP

This chapter describes the Ion Guide Isotope Separator On-Line (IGISOL) facility [95], where the experiments of articles PI and PII were conducted. The JYFLTRAP Penning trap [8], the main device used in this work, is also introduced.

5.1 IGISOL IV facility and radioactive ion beam production

The Ion Guide Isotope Separator On-Line (IGISOL) facility [95, 96], for which the layout is shown in Fig. 25, is located at the Accelerator Laboratory of the University of Jyväskylä, Finland. A detailed description of the facility can be found in Ref. [96]. The IGISOL technique [9] is an ISOL-type (Isotope Separation On-Line) radioactive ion beam (RIB) production method, but the IGISOL utilizes thin targets and a gas volume (usually helium) to stop the reaction products. This provides access to certain chemically sensitive elements, for example the refractory nuclei studied in this work, that would otherwise be unattainable. At IGISOL, RIBs are produced via fission, fusion evaporation and multi-nucleon transfer reactions.

The ions of interest (IOI) in this work were produced via nuclear fission utilizing the fission ion guide (see Ref. [97]) with a thin natural uranium target (15 g/mm^2) mounted inside (for ^{113}Ru a ^{232}Th target was used). From the K130 cyclotron (see Fig. 25) a 25 MeV proton beam was impinging on the thin ^{nat}U target producing neutron-rich fission products. The target is tilted to maximize the surface area hit by the proton beam and the target has been separated from the helium gas volume with a thin foil in order to avoid ionization of the helium buffer gas. The fission reaction products are highly charged when released from the target. Travelling through the helium-filled gas cell, the charge of the fission fragments reduces to $+2e$ due to charge-exchange reactions with the helium atoms. The first ionization potential of a helium atom is higher than the second ionization potential for most of the produced elements. This leads to the charge-exchange process with helium atoms to not proceed further. However,
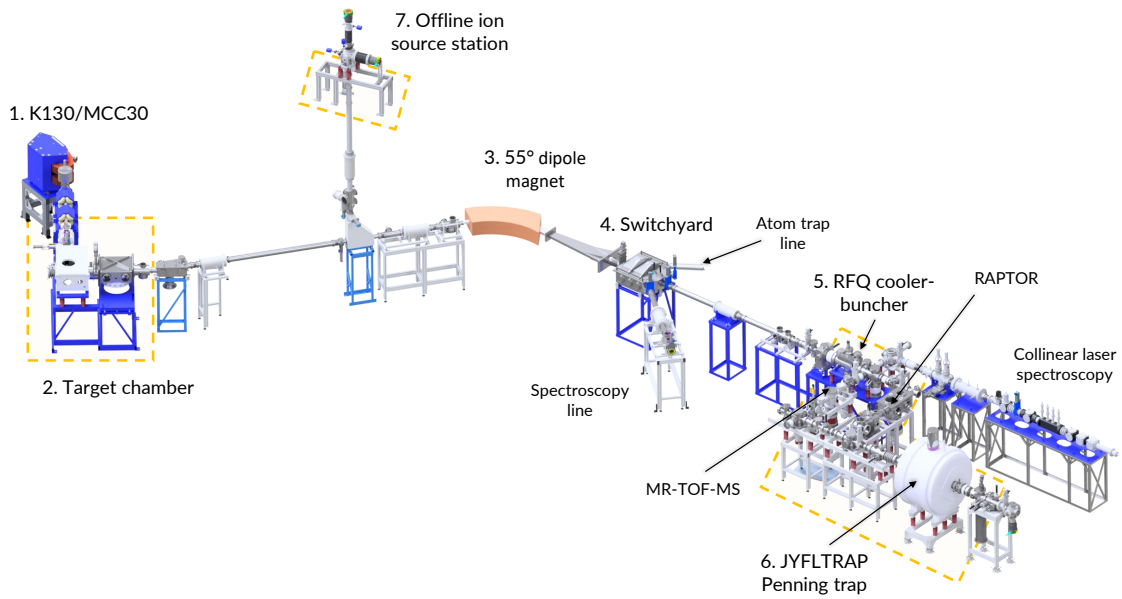
FIGURE 25   The IGISOL facility layout where the primary beam is delivered by the K130 cyclotron (1) to the target chamber (2). The secondary beam is accelerated to 30 kV and mass separated with the $55°$ dipole magnet (3). The electrostatic switchyard (4) directs the ion beam to the RFQ cooler-buncher (5) and JYLFTRAP double Penning trap (6). Offline ion source station (7) was also used in this work. The 30 kV high-voltage platforms are shown in yellow.

the impurities in the gas (O_2, N_2, Ne and H_2O) continue the charge-exchange process and the fission fragments reach $+e$ charge state [98], and the helium gas can also be ionized by the fission fragments, providing more electrons. A high amount of impurities can cause molecular formation, thus to ensure the purity of the helium gas it is brought to the target chamber via a cold trap purification system [99]. In this work the fission products were stopped in helium at pressure of around 300 mbar. The helium pressure was optimised based on the yield of the radioactive isobars at mass number A= 112 measured on a silicon detector at the switchyard (see Fig. 25).

The fission reaction products are extracted out of the helium gas cell using a sextupole ion guide (SPIG) [100] and accelerated to 30q kV, where q is the charge of the ions, for further transport. The separation of an isobaric chain is done using the $55°$ dipole magnet, reaching a mass resolving power of $m/\Delta m \approx 500$. The electrostatic switchyard (see Fig. 25) provides the isobaric ion beam to three different directions: to the spectroscopy beamline (used for example in [101]), to the radio frequency quadrupole cooler-buncher (RFQ) [102] or to the atom trap line [103]. At the switchyard a fast switch is connected to a kicker electrode, to control the amount of ions injected to the RFQ cooler-buncher (beamgate).

The RFQ cooler-buncher is a linear Paul trap filled with buffer gas (He) to cool the ion sample injected into it. In the RFQ cooler-buncher the ion confinement is achieved in radial direction utilizing radio frequency (RF)-fields and in the axial direction using a DC voltage potential. This linear Paul trap provides

ion bunches with widths of $5 - 15$ μs to both the collinear-laser spectroscopy beamline and to measurements at JYFLTRAP. During 2022 upgrades to the RFQ cooler-buncher have been made to reach bunch widths of 40 ns, suitable for the Multi-Reflection Time-Of-Flight mass spectrometer (MR-TOF-MS). In this work the MR-TOF-MS was not yet utilized for ion sample purification, but in the future it can be used for a faster purification of the ion sample before precision mass measurement performed with the Penning trap JYFLTRAP [8].

After the preparation in the RFQ cooler-buncher, the cooled ion bunch is injected to the JYFLTRAP double Penning trap (described in detail below, see Section 5.2) for further ion manipulation and high-precision mass determination. The JYFLTRAP double Penning trap can also be used for isobaric or even isomeric beam purification for post-trap decay spectroscopy measurements.

For Penning trap mass measurements, the magnetic field strength of the Penning trap has to be known with high precision. This is done utilizing reference measurements of an ion species with a well-known mass value (see Chapter 3). The IGISOL offline ion station [51] provides stable reference ions from either a surface ionisation source or a glow discharge ion source. The ^{85}Rb and ^{133}Cs reference ions used in this work were produced using the surface ionization ion source.

5.2 JYFLTRAP double Penning trap

Main results of this work were carried out utilizing the JYFLTRAP Penning trap [8], which is a double cylindrical Penning trap housed inside a 7 T superconducting magnet. The JYFLTRAP tower assembly consists of cylindrical gold-plated copper electrodes that have an inner diameter of 32 mm, excluding the injection diaphragm ($d = 4$ mm), diaphragm between the traps ($d = 1.5$ mm, $l = 50$ mm) and the last two extraction electrodes ($d = 52$ mm). The two trap centers are 20 cm apart and are separated by a diaphragm. The trap tower dimensions have been described in detail in Ref. [8], except for the modifications made to the extraction electrodes to accommodate for the PI-ICR technique (see Ref. [86]). Both traps have a eight fold segmented ring electrode, which is used to manipulate the ion motions in each trap utilizing RF-fields. The ring electrode is neighboured by a set of two correction electrodes and endcap electrodes, which provide the rest of the electric potential and correct for its anharmonicities (see Fig. 26). The JYFLTRAP Penning trap is located on a 30 kV high-voltage platform.

The first trap, called the purification trap, is filled with helium buffer gas ($10^{-4} - 10^{-5}$ mbar) and is utilized for ion sample purification with the buffer gas cooling technique [79]. This technique is described in more detail in Chapter 3.4. An example of this technique at JYFLTRAP is shown in Fig.10 in Chapter 3.4 where the quadrupolar excitation (RF2) frequency in the purification trap has been scanned for an ion sample consisting of fission products at mass A = 112. After purification the ion sample is transferred and caught in the second trap for
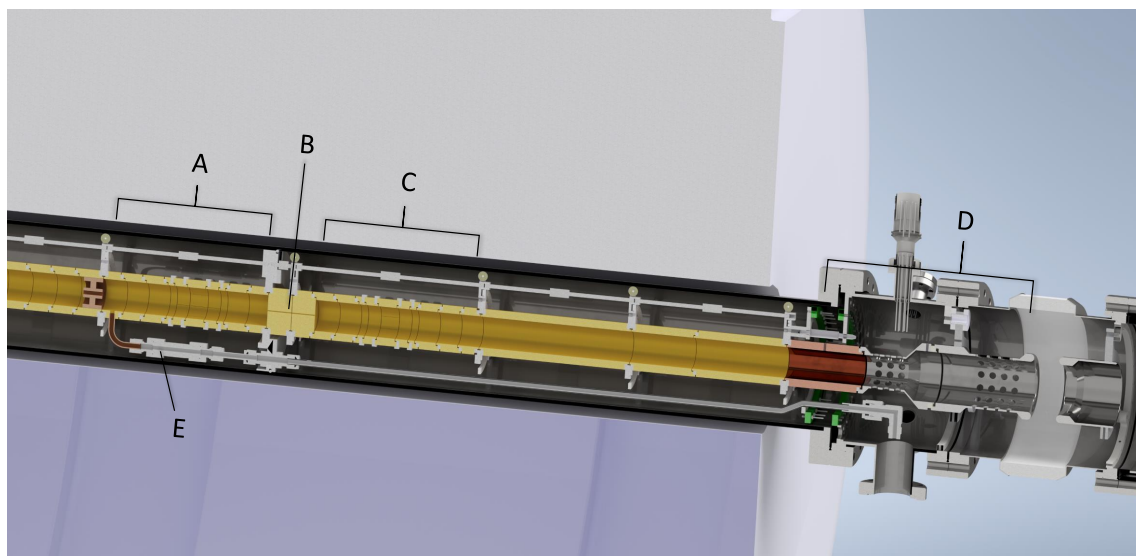
FIGURE 26   Schematic figure of the JYFLTRAP double Penning trap assembly. The purification trap has been marked with A, diaphragm with B, the precision trap with C and the buffer gas line with E.

further studies, or transferred to the post-trap experimental setup.

The second trap, called the precision trap, is used for the precision mass measurements utilizing the TOF-ICR and PI-ICR techniques described in Chapters 3.5.1 and 3.5.2, respectively. The precision trap is operated in high vacuum, 10^{-7} mbar or lower depending on the He-gas pressure of the purification trap, to avoid any frequency shifts due to interactions with residual gas. If additional purification of the ion sample is needed, for example due to molecular contamination (see attached article PI), an additional purification technique called Ramsey cleaning method [80], can be applied in the precision trap (see Chapter 3.4). For PI-ICR technique an additional cooling step can be used: the ion sample is returned back to the first trap for a short cooling, before it is sent to the precision trap for the phase accumulation. The advantage is that the size of the phase spots becomes smaller - which reduces the uncertainty of the position of the phase spots (see Chapter 3.5.2).

After applying the TOF-ICR or PI-ICR technique the ions are extracted from the 30 kV platform to a position-sensitive delay-line microchannel plate detector (MCP, RoentDek GmbH and DLD40 delay-line anode) on the ground potential. A Si-detector is also located behind the JYFLTRAP Penning trap and can be utilized for example for half-life measurements of the Penning trap purified ions (see attached article PI).

The analysis of the PI-ICR data has been performed utilizing both the Py-MassScanner and Cloudberry programs while the TOF-ICR collected data has been analysed using the Lakritsi and COMA programs [104, 105]. The analysis procedure utilized at JYFLTRAP is explained in the following Chapter 6. Systematic uncertainties related to the temporal fluctuations of the magnetic field, mass-dependent frequency ratio shifts and a residual systematic uncertainty are taken into account during the analysis and are explained in Chapter 6.5 as well

as in Ref. [75].

6 ANALYSIS OF JYFLTRAP MASS MEASUREMENT DATA

This chapter will give a brief overview of the data-analysis principles concerning the PI-ICR and TOF-ICR mass measurement data collected at JYFLTRAP. This chapter will discuss the gating of the measurement data and the ν_c frequency ratio determination. The countrate class analysis to account for the ion-ion interaction due to multiple ions stored in the trap simultaneously during the measurement is introduced. The systematic uncertainties added to the statistical uncertainty of the cyclotron frequency ratio are briefly explained. Finally, how to obtain the mass of the ion of interest and the excitation energy of the isomer from the measured cyclotron frequency ratio is described.

6.1 Data selection

Once the mass measurement has been performed with the JYLFRTAP double Penning trap, either utilizing the PI-ICR (see Chapter 3.5.2) or the TOF-ICR (see Chapter 3.5.1) technique, the cyclotron frequencies of the reference ion and the ion of interest needs to be extracted from the collected data. In PI-ICR it is calculated from the $x - y$ positions of the ions (see Chapter 3.5.2) and for TOF-ICR the theoretical lineshape needs to be fitted. The following section will describe the gating applied to the data, to pinpoint the correct ions to be used for the fitting procedures of PI-ICR and TOF-ICR data.

The JYFLTRAP Penning trap is controlled (timings, RF-excitations etc.) and the data is collected with a Python based program called PyMassScanner, developed by Dr. T. Eronen and the JYFLTRAP team. In PyMassScanner the data are first gated based on the ion time-of-flight (TOF-gate) from the trap to the detector and/or by the detected ion's position on the position sensitive 2D MCP detector (position-gate). Using these two gates, the true events around a given TOF and position on the detector can be selected for further analysis, and the unwanted noise counts can be discarded. The measured data can also be gated by the num-
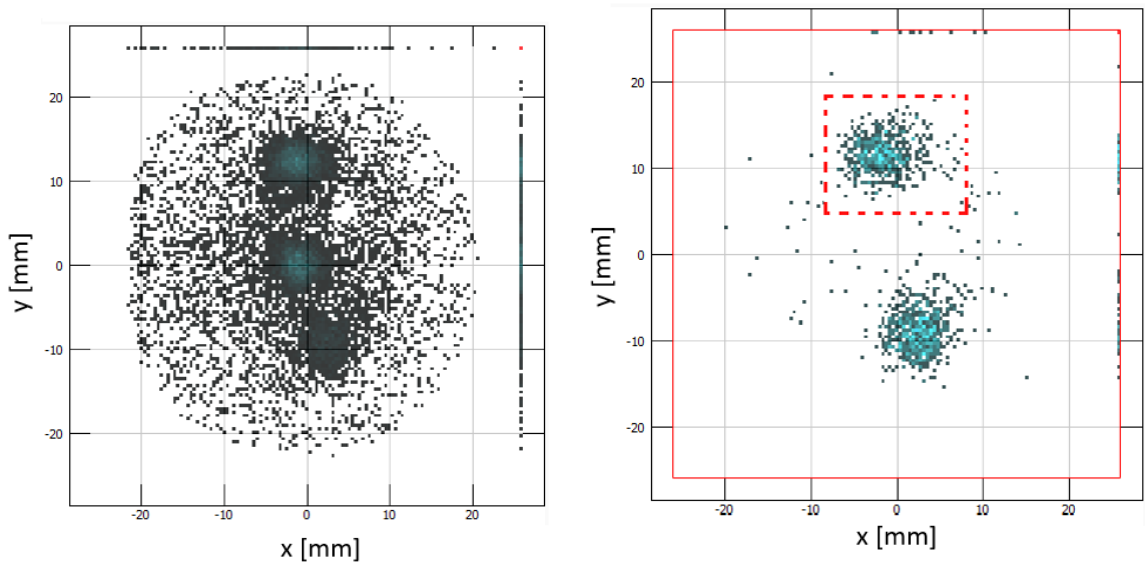
FIGURE 27   The reduced cyclotron phase spot ϕ_+ for the ground state and isomer of ^{116}Rh$^+$ where a) no gating has been performed and b) the TOF-gate and number of ions/bunch gate has been applied, and the position gate to be applied is shown in red dashed line. The line of detected ions in both a) and b) at $x = 25$ mm and $y = 25$ mm are ions with at least one missed position information signal.

ber of counts detected in a bunch (counts/bunch-gate). This allows to study the ion-ion interaction in the trap. In Fig. 27 a reduced cyclotron motion phase ϕ_+ measured for ^{116}Rh$^+$ is shown (ions that arrive during 200 μs after trigger), where in a) no gates have been applied and in b) the TOF-gate of $40 - 44$ μs, accompanied with a gate of one to five counts detected in a bunch, have been applied. The position-gate to be applied for the fitting of the ground state reduced cyclotron motion phase spot ϕ_+ is shown in red dashed line. In Fig. 27 a) the counts outside of the phase spots are mainly decay products of ^{116}Rh$^+$ and ionised helium coming from the traps. The biggest impact between Fig. 27 a) and b) is due to the TOF-gating. In TOF-ICR measurements the TOF-gate is carefully selected to include both resonant and non-resonant ions of the ion species of interest.

In mass measurements performed with the PI-ICR technique (see Chapter 3.5.2), the gates are applied for each recorded phase (magnetron, cyclotron or center) separately. The gated PI-ICR data is fitted directly in the PyMassScanner program, while the gated TOF-ICR data is sent to the Lakritsi-program for fitting and extraction of the cyclotron frequency.

6.2   Fitting and analysis of PI-ICR data

After application of the gates described above, the maximum likelihood method is used to obtain the x- and y-positions of the phase spots. For this, a position gate, either circular or rectangular, is set and peak position is obtained. Next, the

gate is moved so that the obtained position center is also the gate center and the fit is redone. This iteration is repeated at least three times. Once the position has been fitted for each phase (magnetron ϕ_-, reduced cyclotron ϕ_+ and center) of each ion species (IOI and reference), the results are transferred to the Cloudberry analysis program for the calculation of the cyclotron frequencies of the reference ions and the ions of interest.

The cyclotron frequency ν_c is calculated as given in Eq. (41). It requires the angle difference ϕ, the number of full rounds the ions performed in the trap n and the precise accumulation time T_{acc}. The x- and y-positions are used to calculate the angle difference between the measured accumulated magnetron and reduced cyclotron phase spots. The settings made during the measurement, the ν_c frequency used for the conversion and the delay times applied to the RF-generator to start the quadrupolar conversion, are needed for the determination of the full rounds n and the precise accumulation time T_{acc}. After the cyclotron frequencies of the reference ion and ion of interest have been determined, the cyclotron frequency ratio is calculated. This is explained in the Section 6.4 below.

6.3 Fitting and analysis of TOF-ICR data

During this work, the TOF-ICR technique was used for the mass measurement of the most exotic nuclei in the isotopic chains, see Chapter 7 and attached articles PI and PII. In these measurements the number of ions produced was very low, thus no gate on the number of counts recorded in a bunch was needed, since most of the bunches were either empty or had just one detected ion.

The Lakritsi program [80, 105] is a TOF-ICR data analysis program for fitting and additional gating or division of the data recorded at JYFLTRAP. The time-of-flight for a single peak TOF-ICR measurement is given by Eq. (40) in Chapter 3.5.1, and can be referred as the single peak König fit. A more complete description of the fit parameters has been recently given in the PhD thesis of L. Canete [105]. The Ramsey TOF-ICR is fitted with an ideal Ramsey lineshape fitting function [80, 85]. The fitting gives, most importantly, the ν_c frequency of the fitted resonance.

The fitting results are then imported to the "Complicated Offline Mass Analyser" (COMA) program, which calculates the frequency ratios $\bar{r}$ from the fit results. The following section will discuss the frequency ratio determination applicable for both TOF-ICR and PI-ICR cyclotron frequencies.

6.4 Calculation of the cyclotron frequency ratio

The frequency ratio r is determined for the PI-ICR measurements in the Cloudberry program, while for TOF-ICR measurements it is determined in the COMA

program. The following procedure is valid for both programs, unless otherwise stated.

The cyclotron frequency ν_c for both the reference ion and the ion of interest is used to calculate the cyclotron frequency ratio $r = \nu_{c,ref}/\nu_{c,ioi}$. There are different ways of defining the ν_c frequency of the reference ion for the frequency ratio calculation. Most commonly the ν_c frequency of the reference ion is interpolated linearly to the time of the measurement of the ion of interest frequency (linear interpolation method). For this, a reference measurement is done before and after the ion of interest measurement. This gives one individual frequency ratio r. Interpolating the reference frequency helps to account for the linear drift of the magnetic field and for other changes in the conditions during the measurement. The frequency ratio can also be calculated without interpolating the reference frequency. This can be done when the reference ion cyclotron frequency and the ion of interest frequency are measured alternately in a rapid succession, thus assuming that the reference and IOI are measured almost simultaneously. These two methods were utilized in this work. A more detailed mechanism of the interpolation methods has been explained in Refs. [75, 80].

Once the suitable interpolation method is used, the cyclotron frequency ratio is calculated $r = \nu_{c,ref}/\nu_{c,ioi}$. The uncertainty of an individual cyclotron frequency ratio r is calculated as follows:

$$dr = \sqrt{\left(\frac{d\nu_{c,ref}}{\nu_{c,ref}}\right)^2 + \left(\frac{d\nu_{c,ioi}}{\nu_{c,ioi}}\right)^2} \times r, \qquad (42)$$

where $d\nu_{c,ref}$ and $d\nu_{c,ioi}$ is the cyclotron frequency uncertainty of the reference ion and ion of interest, respectively. Usually multiple Ref.-IOI-Ref. measurements are done, and the final cyclotron frequency ratio is calculated as a weighted mean of the individual ratios, denoted as $\bar{r}$. An inner and outer statistical uncertainty of the final cyclotron frequency ratio is determined, obtaining the Birge ratio [106], from which the higher value is selected as the final statistical uncertainty. The inner and outer errors are calculated as follows, respectively,

$$dr_{inn}^2 = \frac{1}{\sum_i \frac{1}{dr_i^2}} \qquad (43)$$

and

$$dr_{out}^2 = \frac{\sum_i \frac{1}{dr_i^2}(r_i - \bar{r})^2}{(N-1)\sum_i \frac{1}{dr_i^2}} \qquad (44)$$

where dr_i is the individual cyclotron frequency ratio uncertainties, r_i is the individual cyclotron frequency ratio, $\bar{r}$ is the weighted mean cyclotron frequency ratio and N is the number of measurements. Fig. 28 shows individual cyclotron frequency ratios determined in mass measurement of $^{114}Rh^+$ ground state performed in this work.

The next section describes the countrate class analysis performed to study the ion-ion interaction, and to obtain the cyclotron frequency ratio, when multiple
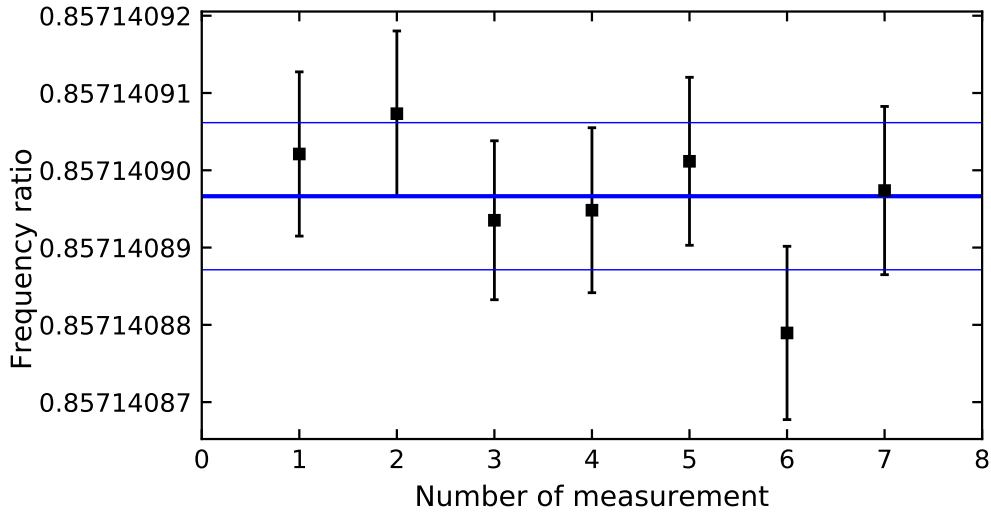
FIGURE 28   The frequency ratios $r = v_{c,ref}/v_c$ for PI-ICR measurement of the ground state of $^{114}Rh^+$. In black are the individual frequency ratios while in blue is the weighted mean frequency ratio, and its error.

ion species are in the trap simultaneously. The systematic uncertainties added to the uncertainty of the frequency ratio are described in Section 6.5.

6.4.1 Countrate class analysis

When multiple ions are stored in a Penning trap, the Coulomb interaction between the ions needs to be considered. In Refs. [107] and [75] studies of the ion-ion interaction utilizing the TOF-ICR and PI-ICR techniques, respectively, were reported. It was found that when only one ion species is stored in the trap (at least up to 5 detected counts/bunch of such species), the space charge does not affect the mass center of such ion cloud and no shift in the cyclotron frequency was observed. When two or more ion species, with different masses, are stored in the trap, the recorded cyclotron frequencies shifted closer to each other. The shift of the cyclotron frequency was found to be proportional to the amount of ions in each ion species (and their ratio) and to the magnitude of the difference in the cyclotron frequencies of the ion species.

In this work, the cyclotron frequencies of multiple ground- and isomeric-states were measured. In these measurements the cyclotron frequency shift due to the ion-ion interaction between the two states needed to be considered. This was studied via the so-called countrate class analysis [75], whenever it was statistically feasible.

In the countrate class analysis at JYFLTRAP the measured data is divided into sections based on the number of counts detected in a bunch (called classes). For each class the cyclotron frequency ratio was calculated, see Fig. 29. The classes were corrected with the efficiency of the MCP detector: one detected count based on the measured detector efficiency curve corresponds to 3.4 ions on average. This detector efficiency was valid for the period of 02/2019-03/2020. The
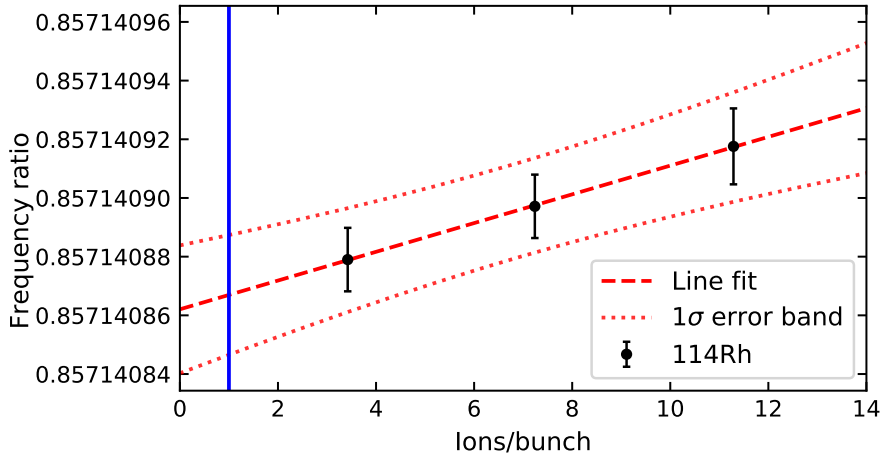
FIGURE 29   The measured frequency ratios for ^{114}Rh$^+$ for three different classes used in the analysis and the extrapolated value at one ion/bunch.

detector was later moved to a smaller residual magnetic field region and a new efficiency curve was measured. The determined cyclotron frequency ratios are plotted as a function of the corrected ion class in Fig. 29, where this is shown for a measurement of the ground state of ^{114}Rh$^+$. Then a linear fit is performed and an extrapolation to one ion per bunch is done to determine the correct cyclotron frequency ratio, as if only one ion would have been stored in the JYFLTRAP Penning trap during the measurement. This cyclotron frequency ratio, and its uncertainty, is then used for the calculation of the mass, described in more detail in section 6.6.

In this work the countrate class analysis was performed only for the data measured using the PI-ICR technique since it was not statistically feasible for the data measured with the TOF-ICR technique. The TOF-ICR technique was used only for the most exotic nuclei in this work, for which mostly one count/bunch was detected, thus the ion-ion interaction . In the next Section the systematic uncertainties affecting the cyclotron frequency ratio $\bar{r}$ and its uncertainty at JYFLTRAP are discussed.

6.5   Systematic uncertainties

When a high-precision mass measurement is performed, certain systematic effect need to be accounted for. In the previous sections obtaining the cyclotron frequency ratio $\bar{r}$ and its statistical uncertainty $d\bar{r}$ from the measured data were described. Below a brief description of the systematic uncertainties at JYFLTRAP are discussed. The most recent study of the systematic uncertainties considered at JYFLTRAP can be found in Ref. [75].

For data measured with either TOF-ICR or PI-ICR techniques, the higher-order temporal magnetic field fluctuations, mass-dependent uncertainty and residual systematic uncertainty are added to the statistical uncertainty of the cyclotron frequency ratio dr.

As mentioned before, reference measurements to determine the magnetic field strength are performed. Due to the flux creep phenomena, the magnetic field strength B drifts over time (described in Chapter 3.2). Also changes in the environment (temperature, pressure etc.) affect the magnetic field strength of the Penning trap. In Ref. [75] a study of the temporal magnetic field fluctuations was performed and a systematic uncertainty of $\delta B/B\delta t = 2.01(25) \times 10^{-12}$ min^{-1} was determined. This is quadratically added to the individual frequency ratios depending on the time interval δt between the two references. This uncertainty accounts for any drifts that can appear beyond the linear interpolation.

The second systematic effect added to the uncertainty of the cyclotron frequency ratio uncertainty is dependent on the mass difference between the reference ion and the ion of interest. The mass of the reference should be selected as close to the mass of the ion of interest as possible. Mass-dependent shifts in the cyclotron frequency can be due to for example imperfections of the quadrupolar electric field or misalignements of the magnetic and electric fields (discussed in Chapter 3.2), since different mass ions may have different motional amplitudes and thus probe different regions of these imperfections causing motion-amplitude dependent frequency shifts. When the reference mass has a different mass than the IOI, a mass-dependent uncertainty of $\delta_m r/r = -2.35(81) \times 10^{-10}$/u $\times (m_{ref} - m_{ioi})$ is added in quadrature to the final cyclotron frequency ratio uncertainty. If a reference of same mass number was used, for example ground state versus isomer, the mass-dependent uncertainty cancels out.

Finally, in Ref. [75] an additional residual systematic uncertainty was determined. This uncertainty of $\delta_{res} r/r = 9 \times 10^{-9}$ is quadratically added to the final cyclotron frequency ratio uncertainty. For mass doublets the residual systematic uncertainty cancels out in the same way as for the mass dependent uncertainty.

For data collected with the PI-ICR technique certain additional systematic uncertainties and corrections can be taken into account during the analysis. First, when two or more ion species are simultaneously trapped, a correction is performed due to different phase advancement of each ion species before the phase accumulation in the magnetron phase ϕ_- measurement. As described in Chapter 3.5.2, the magnetron phase ϕ_- is measured by first performing a ν_+ dipolar excitation promptly followed by the quadrupolar excitation to convert the reduced cyclotron motion to magnetron motion, which is further followed by the phase accumulation. During the ν_+ dipolar excitation, during the time delay between the dipolar and quadrupolar excitations (marked as t_{d1} in Fig. 12) and during the quadrupolar excitation, different ion species will have time to accumulate different phases (since the ions start with the fast ν_+ motion). A correction is applied depending on the cyclotron frequencies of each ion species, on the amount of ions detected for each ion species and on the time used in each forementioned excitation step. Thus the recorded magnetron spot is actually a weighted average of the magnetron spots of each ion species in the trap. A more detailed explanation with the relevant equations has been given in Ref. [75].

Second, a systematic uncertainty and a correction to the calculation of the phase angles can be added due to the distortion of the ions flight path, see Ref. [75].

This distortion can result from for example misalignements of the electric and magnetic fields (see Chapter 3.2) or the plane of the MCP detector being tilted with respect to the trap electrodes.

After considering the systematic effects, the final cyclotron frequency ratio with its uncertainty, containing both statistical and systematic considerations, is achieved. In the following Section the use of the final cyclotron frequency ratio $\bar{r}$ and its uncertainty $d\bar{r}$ in determining the mass of the ion of interest is explained.

6.6 Mass from the cyclotron frequency ratio

The analysis of the measured data, as described above, provides the final weighted mean of the cyclotron frequency ratio $\bar{r}$ and its uncertainty $d\bar{r}$, see Section 6.2. In Chapter 3.5 it was briefly described how the atomic mass m_{ioi} is determined from the measured weighted mean of the cyclotron frequency ratio and is described below with more detail. The atomic mass m_{ioi} of the ion of interest with a charge q_{ioi} is determined as follows:

$$m_{ioi} = \bar{r}\frac{q_{ioi}}{q_{ref}} \times (m_{ref} - q_{ref}m_e + B_{ref}) + q_{ioi}m_e - B_{ioi}, \tag{45}$$

where m_{ref} is the atomic mass and q_{ref} the charge of the well-known reference ion and m_e the mass of an electron. The total binding energy of all missing electrons B_{ref} and B_{ioi} is neglected for the singly and doubly charged ions used in this work due to it being smaller than the precision reached. It is noteworthy to mention that when the mass of the ion of interest is determined from Eq. (45), the uncertainty of the atomic mass of the reference will affect the final uncertainty of the ion of interest. Thus the reference needs to be selected carefully. The uncertainty of the measured mass is calculated as follows:

$$dm_{ioi} = \frac{q_{ioi}}{q_{ref}}\sqrt{((m_{ref} - q_{ref}m_e)\overline{dr})^2 + (\bar{r}dm_{ref})^2}. \tag{46}$$

In Table 3 of Chapter 7.1 the cyclotron frequency ratios determined in this work with the used references are tabulated, and if the reference mass is measured with higher precision in the future, the resulting masses of the ions of interest can be recalculated.

The measured cyclotron frequency ratio in the case of a ground state against the isomeric state can be used to determine the excitation energy of the isomer. From the measured weighted mean cyclotron frequency ratio, when the ground state was measured against the isomeric state, the excitation energy is determined as follows:

$$E_x = (\bar{r} - 1)[m_{ref} - m_e]c^2, \tag{47}$$

for singly charged ions.

7 RESULTS AND DISCUSSION

This Chapter summarizes the results obtained utilizing the JYFLTRAP Penning trap in this work. The main results are the mass measurements performed for neutron-rich isotopes around the refractory region (A $\approx 100 - 120$), from which results related to rhodium ($Z = 45$) and ruthenium ($Z = 44$) isotopes have been reported in the attached articles PI and PII.

In total 23 masses were measured in three experiments conducted at the JYFLTRAP Penning trap of the IGISOL facility. These experiments utilized proton-induced fission on a $^{nat.}$U target, except for the mass measurement of ^{113}Ru where a ^{232}Th target was used. The proton beam had an energy of around 25 MeV and the intensity was varied between $1 - 10$ μA. The IGISOL facility and the radioactive ion beam production method have been described in more detail in Chapter 5.2.

In the following chapter the mass excesses determined in this work are first reported, followed by a discussion related to the so-called mass filters, derived from the mass values (S_{2n}, S_n and $\Delta_n^{(3)}$, see Chapter 2.3) which are compared to the BSkG1 [31] and BSkG2 models [50]. In this work, not only ground-state masses were measured but also isomer binding energies. These results related to isomers are then described. A section about a specific case, ^{112}Rh, reports the measurements of both the masses and the half-lives of the two states of this isotope, which were produced in different ways. Finally, the last part of this chapter presents the neutron-capture reaction rates calculated utilizing the masses determined in this thesis.

7.1 Mass-excess values

In this work precision mass measurements were performed for the following nuclei: ^{110,110m}Rh, ^{112,112m}Rh, ^{114,114m}Rh, ^{116,116m}Rh, ^{118,118m}Rh and ^{120}Rh (article PI), ^{113,113m}Ru, ^{115,115m}Ru and ^{117}Ru (article PII), ^{104}Y, ^{106}Zr, ^{104,104m}Nb, ^{109}Nb, ^{111}Mo and ^{112}Mo (forthcoming publication). Altogether 15 ground-state masses and

eight isomeric-state masses were measured. Of these, 19 were measured using the PI-ICR technique while four were measured using the TOF-ICR technique. These techniques have been described in Chapters 3.5.2 and 3.5.1. Table 2 specifies the accumulation/excitation times, as well as the technique used for each measurement. The recorded frequency ratios $\bar{r}$ and the mass-excess values are tabulated in Table 3, including the literature values taken from AME20 [1].

From the masses measured in this work eight were newly measured, having only an extrapolated value in the AME20. Measurements conducted in this work improve the precision of multiple mass values and resolve the ground- and isomeric states for the first time in many cases. In Fig. 30 a comparison of the measured mass-excesses against the AME20 values is shown. One of the largest absolute deviation in ground-state mass to the literature value was found for ^{106}Zr with the difference of 166(200) keV. In AME20 the ground-state mass of ^{106}Zr has an extrapolated value, $-58749(200)\#$ keV, the value of this work, $-58582.7(43)$ keV, being then in agreement. The mass of ^{106}Zr has also been measured using the storage ring at GSI [108], reporting a mass-excess of $-58550(173)$ keV, however, the value was excluded from AME20 due to a large difference to the mass surface trend. The value measured in this work agrees with the storage-ring result, confirming that there is a shift (see Fig. 31) on the mass surface at the neutron midshell $N = 66$.

One of the most significant differences in mass can be found in the mea-

TABLE 2   The accumulation/excitation times ($T_{acc./ exc.}$) used for each measured isotope of interest. The reference nuclide used is given (Ref.) while the measurements with the accumulation/excitation times marked with a superscript a were done using the TOF-ICR technique.

Nuclide	Ref.	$T_{acc./ exc.}$ [ms]	Nuclide	Ref.	$T_{acc./ exc.}$ [ms]
^{110}Rh	^{110}Rh^{m}	700	^{113}Ru	^{133}Cs	557
^{110}Rh^{m}	^{133}Cs	700	^{113}Ru^{m}	^{113}Ru$^{g.s.}$	557
^{112}Rh	^{85}Rb	300	^{113}Ru^{m}	^{113}Ru$^{g.s.}$	220
^{112}Rh^{m}	^{133}Cs	1000	^{115}Ru	^{133}Cs	200
	^{112}Rh	1000	^{115}Ru^{m}	^{115}Ru	100
^{114}Rh	^{133}Cs	450	^{117}Ru	^{133}Cs	10-30-10^{a}
^{114}Rh^{m}	^{114}Rh	450	^{104}Y	^{133}Cs	30
^{116}Rh	^{133}Cs	450	^{106}Zr	^{133}Cs	54
^{116}Rh^{m}	^{116}Rh	450	^{104}Nb^{gs}	^{133}Cs	311
^{118}Rh	^{133}Cs	170	^{104}Nb^{gs+m}	^{133}Cs	200
^{118}Rh^{m}	^{118}Rh	170	^{109}Nb	^{133}Cs	50^{a}
^{120}Rh	^{133}Cs	10-30-10 ^{a}	^{111}Mo	^{133}Cs	100
			^{112}Mo	^{133}Cs	50^{a}

^{a} Measured using TOF-ICR technique.

sured neutron-rich rhodium ($Z = 45$) isotopes (article PI). Due to the high resolving power of the PI-ICR technique the low-lying isomeric states could be separated from the ground-states. Previous measurements had typically measured mixtures of the ground and isomeric states [18]. For example the ground-state masses of ^{110,112,118}Rh measured in this work are not in agreement with the literature values. They deviate from the literature value by over 6σ for ^{110}Rh, over 3σ for ^{112}Rh and over 4σ for ^{118}Rh. For the neutron-rich rhodium isotopes the more detailed discussion of the origin of the literature values can be found in the attached article PI. In Fig. 30 the previously measured masses using the JYFLTRAP Penning trap by Hager *et al.* [18] are also given (in blue). It can be seen that those masses, measured with the TOF-ICR technique, have been mostly a combination of both states, depending on their production ratio.

Another large difference in the rhodium masses is related to the isomeric-state excitation energy in ^{112}Rh. In literature the isomeric-state excitation energy is $E_x = 370(40)$ keV, which was based on β-decay endpoint energy measurements, privately communicated to the AME [109] (already found in AME03 [110]). The excitation energy measured in this work is only $E_x = 38.4(19)$ keV (see Table 4). In Section 7.6 the mass measurement of ^{112}Rh (g.s. and isomer) and half-life measurements to confirm the assignments of the observed states, are discussed in more detail.

The masses determined in this work have been compared to the predictions of the BSkG1 [31], see attached article PI Section IV.B, and/or BSkG2 [50] models. The comparison to these models and what is predicted for the ground-state shape is discussed in the next sections.

TABLE 3   Frequency ratios ($\bar{r}$) and mass excess (*ME*) values measured in this work and
the literature mass-excess values (*ME$_{lit.}$*) from the AME20 are given. *N* de-
notes the neutron number of the measured nuclide. The reference masses
were taken from AME20 [1] for ^{133}Cs and ^{85}Rb, and from this work for the
other cases (Ref.). For the AME20 values # marks an extrapolated value.

Nuclide	N	Ref.	$\bar{r} = \nu_{c,ref}/\nu_c$	ME [keV]	ME$_{lit.}$ [keV]
^{110}Rh	65	^{110}Rh^m	0.999999629(15)	-82702.4(23)	-82829(18)
^{110}Rh^m	65	^{133}Cs	0.826987604(15)	-82664.3(18)	-82610(150)#
^{112}Rh	67	^{85}Rb	0.659002526(11)^a	-79603.7(17)	-79730(40)
^{112}Rh^m	67	^{133}Cs	0.842060991(16)	-79565.2(19)	
		^{112}Rh	1.000000368(27)	-79565.4(33)	
	Weighted mean:			-79565.2(17)	-79390(60)
^{114}Rh	69	^{133}Cs	0.857140868(21)	-75662.7(26)	-75710(70)
^{114}Rh^m	69	^{114}Rh	1.000001045(30)	-75551.8(41)	-75510(170)#
^{116}Rh	71	^{133}Cs	0.872229073(17)	-70729(2)	-70740(70)
^{116}Rh^m	71	^{116}Rh	1.000001119(18)	-70608.3(28)	-70540(170)#
^{118}Rh	73	^{133}Cs	0.887323752(40)	-64994(5)	-64887(24)
^{118}Rh^m	73	^{118}Rh	1.000001720(55)	-64804.9(78)	-64690(150)#
^{120}Rh	75	^{133}Cs	0.902423642(470)^c	-58614(58)	-58620(200)#
^{113}Ru	69	^{133}Cs	0.849647289(12)	-71874.7(15)	-71870(40)
^{113}Ru^m	69	^{113}Ru$^{g.s.}$	1.000000951(10)	-71774.6(1.8)	
^{113}Ru^m	69	^{113}Ru$^{g.s.}$	1.000000963(14)^b	-71773.4(21)	
	Final value:		1.000000955(8)	-71774.3(17)	-71740(50)
^{115}Ru	71	^{133}Cs	0.864742653(23)	-66054.7(2.9)	-66105(25)
^{115}Ru^m	71	^{115}Ru	1.000001181(43)	-65928.2(5.4)	-66110(90)
^{117}Ru	73	^{133}Cs	0.879843739(512)^c	-59526(64)	-59490(430)
^{104}Y	65	^{133}Cs	0.782074118(126)	-53995.3(15.5)	-54080(200)#
^{106}Zr	66	^{133}Cs	0.797085417(35)	-58582.7(4.3)	-58749(200)#
^{104}Nb^{gs}	63	^{133}Cs	0.781930200(14)	-71812.4(18)	-71811.0(18)
^{104}Nb^{gs+m}	63	^{133}Cs	0.390963076(29)	-71802.4(70)	-71801.2(19)
^{109}Nb	68	^{133}Cs	0.819672271(1773)^c	-56809(180)	-56690(430)
^{111}Mo	69	^{133}Cs	0.834695343(70)	-59939.3(86)	-59940(13)
^{112}Mo	70	^{133}Cs	0.842239639(952)^c	-57449(118)	-57480(200)#

^{a} Measured with doubly charged ^{112}Rh^{2+} ions.

^{b} Measured with doubly charged ^{113}Ru^{2+} ions.
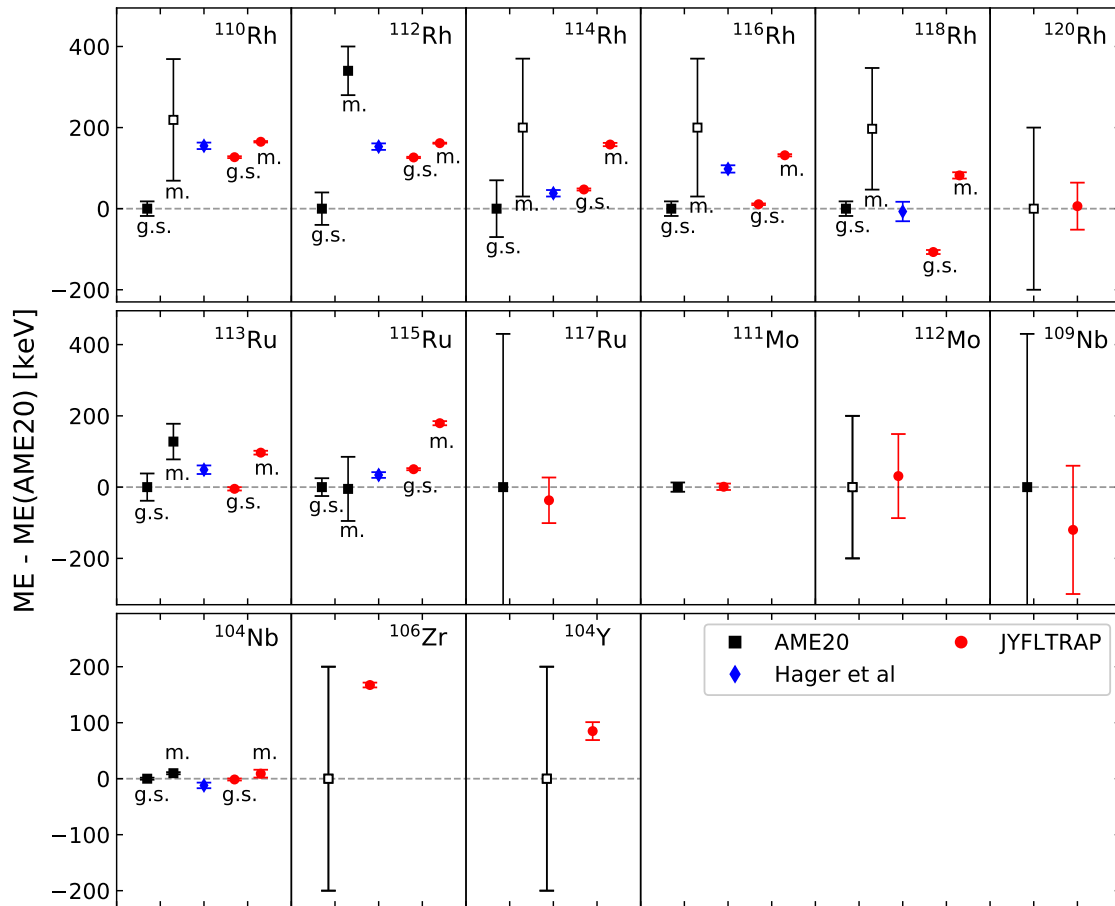
^{c} Measured using TOF-ICR technique.

FIGURE 30   A comparison of the mass-excess values determined in this work (red) to the AME20 [1] (black) values. The previous JYFLTRAP measurements in this region by Hager *et al.* [18, 19] have been marked in blue. The uncertainty of each point is the uncertainty of each individual mass value. The open symbol marks an extrapolated value in AME20.

7.2 Two-neutron separation energies S_{2n}

As introduced in Chapter 2.3 the two-neutron separation energy S_{2n} is an observable sensitive to structural changes. Figure 31 shows the S_{2n} values, calculated from the ground-state masses, for the isotopic chains studied in this work. This work extends the isotopic two-neutron separation energy S_{2n} chains with new mass values in the following elements: yttrium ($Z = 39$), zirconium ($Z = 40$), molybdenum ($Z = 42$) and rhodium ($Z = 45$). The other experimental points marked in red, greatly reduce the uncertainty related to the mass and provide more accurate ground-state masses to calculate the two-neutron separation en-
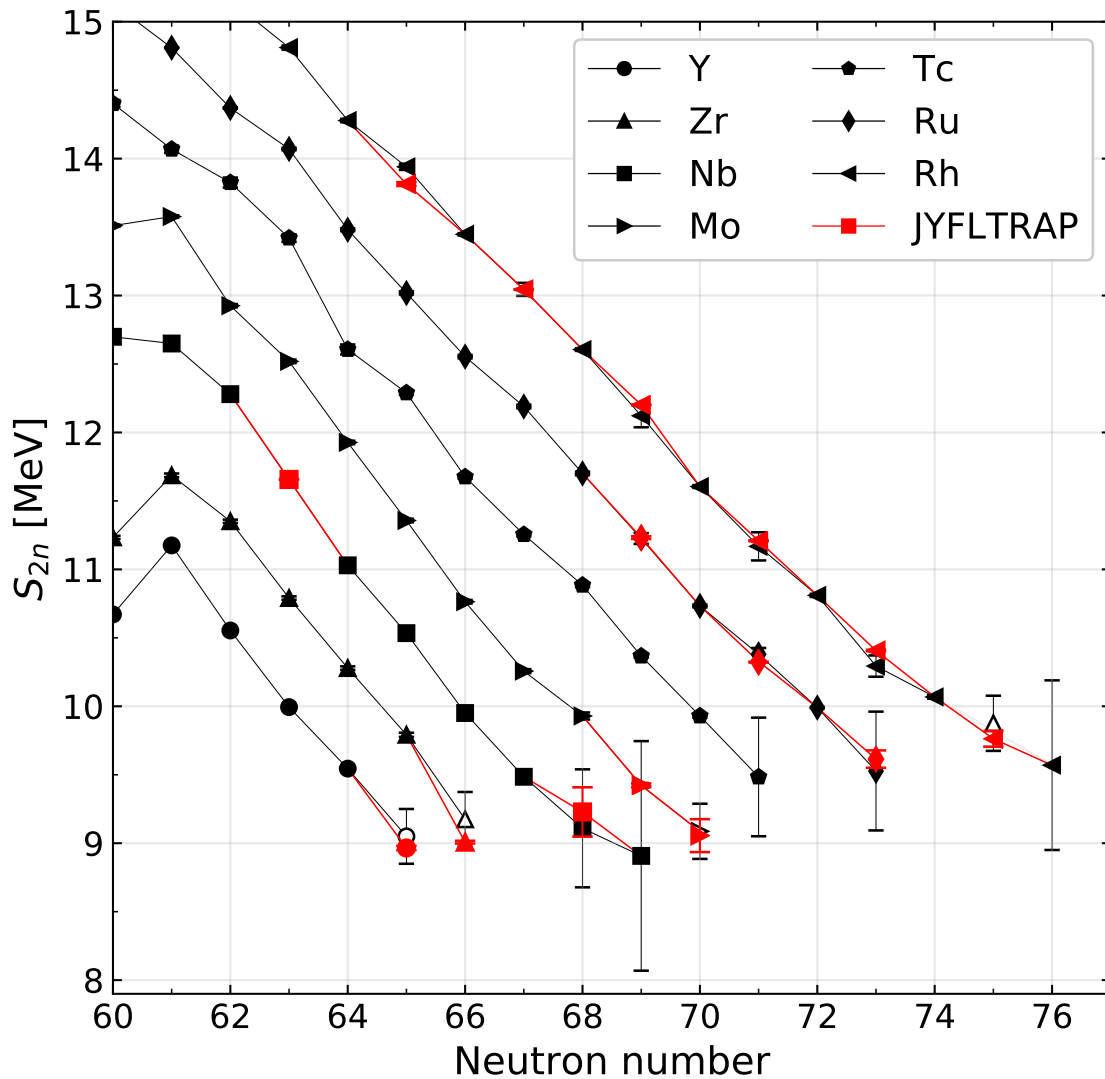
FIGURE 31 Two-neutron separation energy S_{2n} as a function of the neutron number for relevant isotopic chains. In black are the literature values (AME20 [1]) and in red are the values deduced from the masses measured in this work. An empty symbol denotes that at least one mass value used to calculate the two-neutron separation energy was an extrapolated value.

ergies S_{2n}. For example in the case of rhodium isotopes, the isomers were not separated from the ground states previously, hampering also the determination of the two-neutron separation energy S_{2n} (see attached article PI).

It can be noted that no large deviation from the smooth trend in each isotopic chain is seen, except for ^{106}Zr ($Z = 40$, $N = 66$) located at the neutron midshell. ^{106}Zr is less bound than expected from the linear trend of the two-neutron separation energy. More neutron-rich zirconium isotopes need to be measured to fully understand if this change in trend will continue or be an indication of shape change.

In the attached articles PI and PII the two-neutron separation energies S_{2n} calculated from the experimentally measured masses are compared to two-neutron separation energies S_{2n} calculated from the masses of the BSkG1 [31] and/or BSkG2 [50] mass model. Figure 32 shows the difference of the two-neutron separation energies S_{2n} between the experimental values and the BSkG1 model for the isotopic chains studied in this work. From Fig. 32 it can be seen that the BSkG1 model slightly overbinds the nuclei, i.e. according to the model it is slightly harder to separate two neutrons from the nucleus than has been experimentally deduced.

As discussed in Chapter 2.5.2 the BSkG1 model predicts that the Rh and Ru isotopes studied in this work exhibit strong triaxial deformation. For the Rh and Ru isotopic chains, the two-neutron separation energies predicted by the BSkG1 model are in good agreement with the experimental values determined in this work (see Fig. 32). If the BSkG1 mass model is constrained to axial symmetry, the model deviates greatly from the experimental values (shown in article PI), showing the importance of the triaxiality for these nuclei.

For the rhodium isotopes the BSkG1 model predicts a drop of triaxiality going from neutron number $N = 74$ to $N = 75$, which manifests in the two-neutron separation energy S_{2n} as a flattening of the slope (see attached article PI). To see if this trend holds, the mass of ^{121}Rh needs to be measured more precisely and the mass of ^{122}Rh would require to be experimentally determined. In the lighter nuclei, for example yttrium ($Z = 39$) and zirconium ($Z = 40$), the agreement between the model and the experiment is not as good as for rhodium (see Fig. 32).

In the attached articles, the evolution of the two-neutron separation energy S_{2n} has been further studied via the empirical two-neutron shell gap energies $\delta_{2n} = S_{2n}(Z, N) - S_{2n}(Z, N + 2)$. This is not further discussed here, since no large changes to the expected trends were observed.
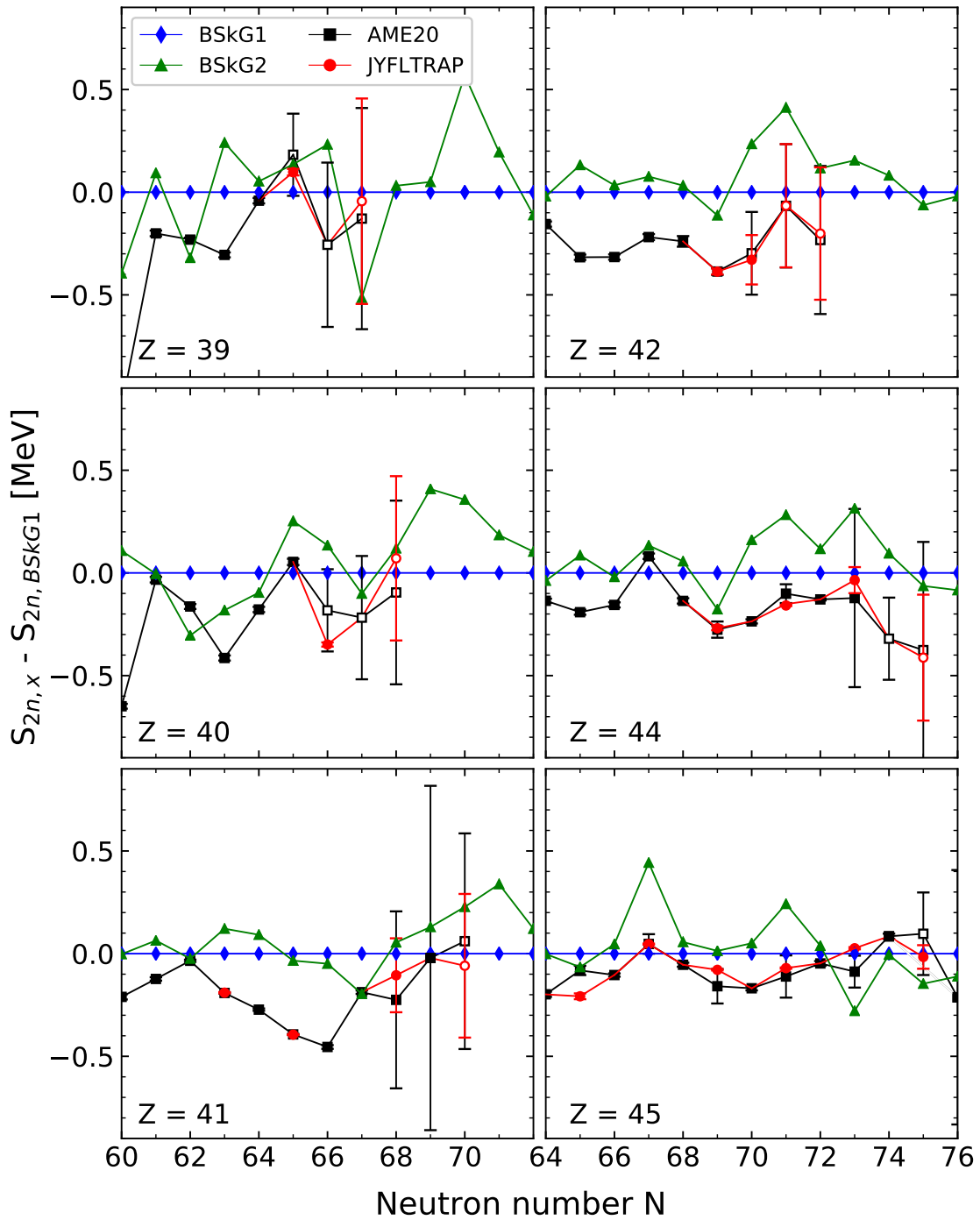
FIGURE 32 Two-neutron separation energies S_{2n} compared to the values calculated from the BSkG1 model [31], as a function of the neutron number N for the nuclei relevant to this work. The BSkG1 model is shown in blue diamonds, the BSkG2 model [32] in green triangles, in black are the literature values (AME20 [1]) and in red are the values deduced from the masses measured in this work. An empty symbol denotes a two-neutron separation energy S_{2n} which is dependent on at least one extrapolated mass value.

7.3   Neutron separation energy S_n

The neutron separation energies exhibit a strong odd-even staggering (OES) as a function of neutron number N which is related to the pairing of nucleons. When the neutrons are paired up, it is harder to separate one of such a neutron due to pairing energy that makes the nucleus more bound (see the discussion in Chapter 2.2.1). This is clearly seen in Fig. 33, which shows the neutron separation energies S_n as a function of the neutron number N for the isotopic chains of interest in this work. It can be seen that the mass measurements reported in this thesis yield more precise neutron separation energies S_n, but otherwise the impact is difficult to see due to the odd-even staggering.

The measurements of this work also extend the neutron separation energy S_n trend of the isotopic chains for yttrium ($Z = 39$), zirconium ($Z = 40$), molybdenum ($Z = 42$) and rhodium ($Z = 45$). The overall trend of the BSkG1 model values agree with the experimental values rather well, but overestimate the odd-even staggering for the odd-Z nuclei (see next Section 7.4). The neutron separation energy S_n is also of importance for the neutron-capture reaction rates calculated for the r process (see Section 7.7).

Since the impact of the new experimental values is difficult to see due to the odd-even staggering effect, a difference between the $S_n(N + 1)$ and $S_n(N)$ can be studied via the odd-even staggering parameter $\Delta_n^{(3)}$, discussed in the next Section.

7.4   Odd-even staggering parameter $\Delta_n^{(3)}$ values

The $\Delta_n^{(3)}$ three-point formula can be calculated as explained in Chapter 2.1 by Eq. (14). The masses determined in this work provide more precise mass values to calculate the odd-even staggering parameter $\Delta_n^{(3)}$ as shown in Fig. 34. It can be noted that for example in the case of the measured neutron-rich rhodium ($Z = 45$) isotopes, the odd-even staggering parameter $\Delta_n^{(3)}$ differs for many isotopes from the literature values. The uncertainties on the experimental points are greatly reduced due to the measurements of this work.

In the studied isotopic chains, the BSkG1 model [31] predicts a change in the staggering at higher neutron numbers, related to the loss of triaxiality, for example in the isotopic chain of rhodium this is seen after $N = 74$. To confirm this predicted trend experimentally, the masses of neutron-rich nuclei in these isotopic chains, like the mass of ^{121}Rh, need to be measured more precisely.

For the even-Z nuclei the absolute magnitude of $\Delta_n^{(3)}$ values are in good agreement between the experiment and the BSkG1 model. During this work while comparing the experimental results of the odd-Z nuclei to the BSkG1 model it was noticed, that the absolute magnitude of $\Delta_n^{(3)}$ values calculated from the
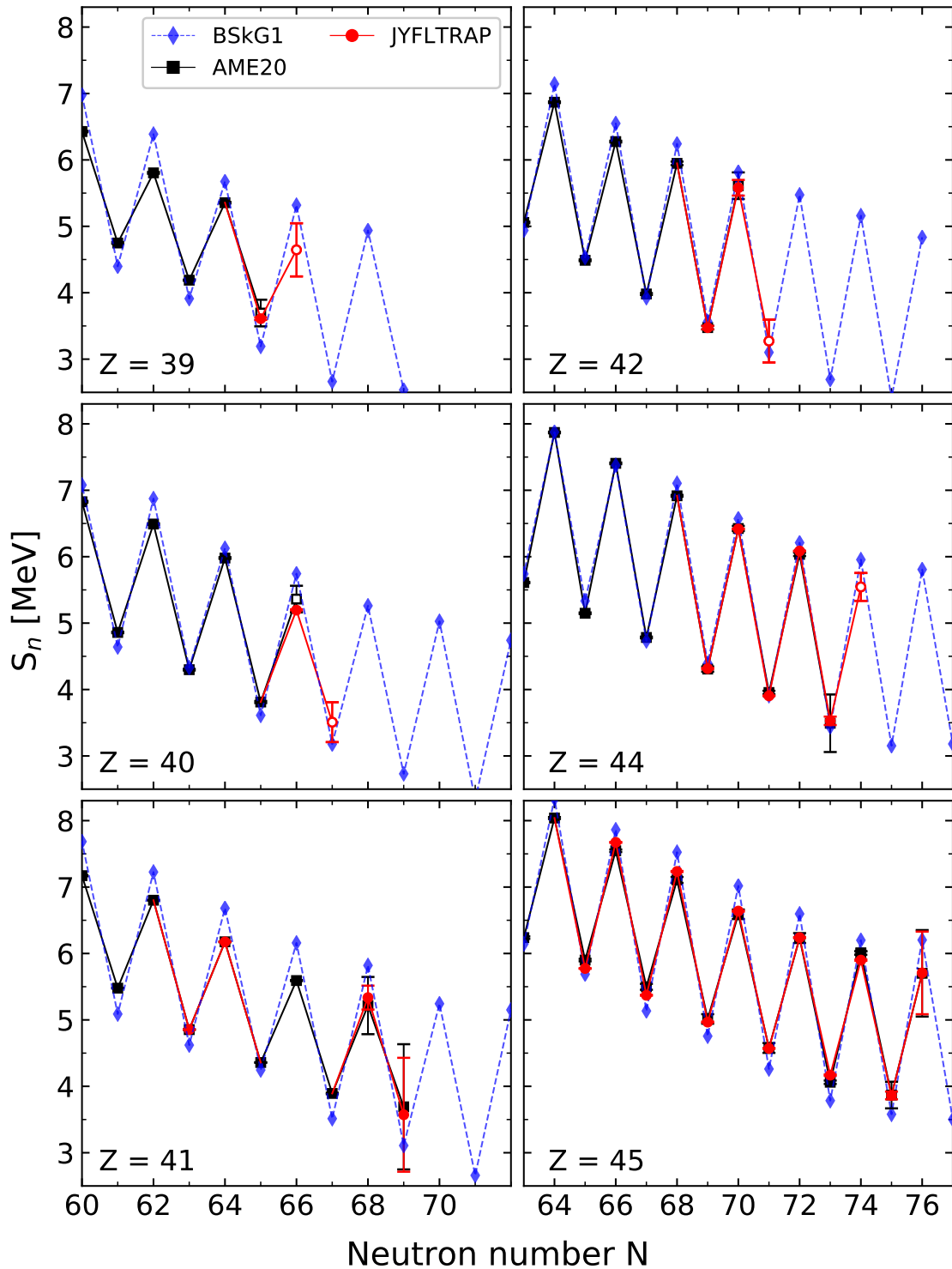
FIGURE 33 Neutron separation energies S_n as a function of neutron number N. The experimental literature values in black are based on AME20 [1], while the experimental results determined in this work are in red. The neutron separation energies S_n calculated from the BSkG1 model [31] values are shown in blue. The open symbol represents a S_n value which is dependent on one or more extrapolated mass value.

BSkG1 model values were differing significantly from the experimentally determined $\Delta_n^{(3)}$ values (see Fig. 34). If the binding energy of the odd-N isotope, for example in neutron-rich rhodium ($Z = 45$) is increased about 250 keV, which is roughly the difference compared to neighboring even-Z isotopic chain trends, the absolute magnitude of the odd-even staggering parameter $\Delta_n^{(3)}$ is then in better agreement with the experiment (see the attached article PI). The need of additional binding energy for the odd-odd nuclei is usually interpreted as a residual interaction between an odd-proton and an odd-neutron, and the effect has been discussed in more detail in Ref. [32]. This overestimation is present for the whole nuclear chart in the BSkG1 model. The size of the staggering of the $\Delta_n^{(3)}$ values is though in rather good agreement between the BSkG1 model values and the experimental results.
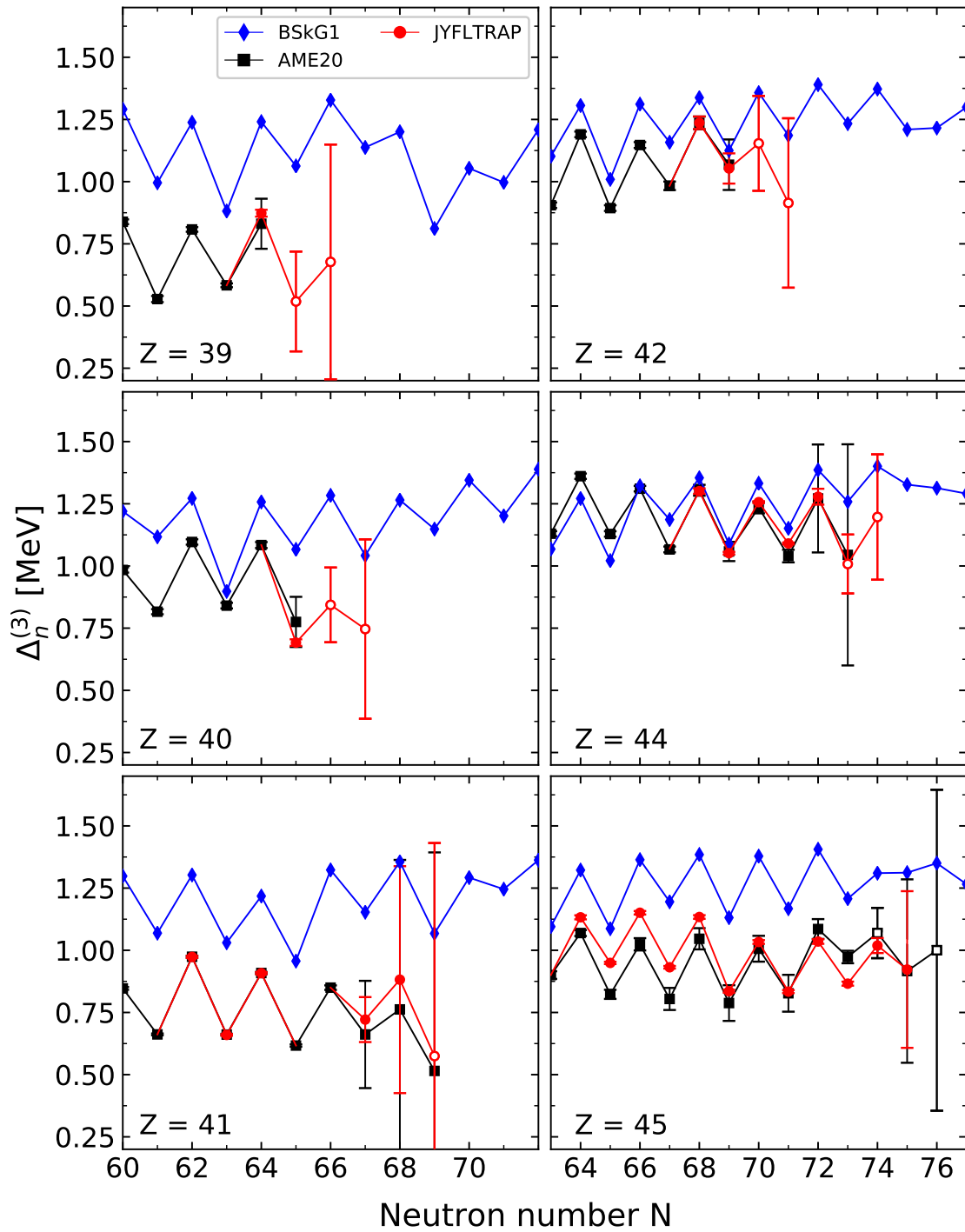
FIGURE 34   The three-point formula $\Delta_n^{(3)}$ shown as a function of the neutron number for the isotopic chains studied in this work. The values affected by the masses measured in this work have been marked in red, while the literature values (AME20 [1]) are marked in black. The values calculated from the masses produced by the BSkG1 model [31] have been marked in blue. The open symbols represent a value that is dependent on at least one extrapolated mass.

7.5 Isomeric states

The region of neutron-rich refractory nuclei is known for low-lying isomeric states. The excitation energies for many of the isomeric states have remained unknown. For example in the neutron-rich rhodium nuclei the isomeric state energies were not known for ^{110,114,116,118}Rh. In this work the PI-ICR technique was utilized to separate and measure the masses of the isomers in this region. Separating the isomers from the ground states with the PI-ICR technique, also provides the ground-state masses without influence of the isomeric state. This is illustrated in Fig. 30, where the ^{110,112,114,116,118}Rh and ^{113,115}Ru masses measured in this work with the PI-ICR technique at JYFLTRAP have been compared to previous TOF-ICR mass measurements that could not resolve the two long-living states. As a result, a mixture of states had been measured in Ref. [18].

The excitation energies measured for the isomeric states in this work have been listed in Table 4 and compared to the literature values (NUBASE20 [2]). For the rhodium isotopes the excitation energy was often estimated from trends of neighbouring nuclei close to 200(150)# keV in the literature [2], when now it can be seen that the measured excitation energies are much lower. For example for ^{110}Rh the excitation energy is only 38.0(15) keV. When the number of neutrons is increased in rhodium, the excitation energy seems to get higher again (see attached article PI). Further interpretation using the Nilsson model, produced by the BSkG1 model [31], of the isomeric states in rhodium can be found in the attached article PI.

In the case of ^{114}Rh, the ground state was more produced, contrary to the other rhodium isotopes. The fission yield at IGISOL is known to favor the higher spin state in the production [111]. The possible explanation of the isomeric yield ratio for ^{114}Rh could be an inversion of the spins of the ground and isomeric states. Another explanation could be that the half-life stated for the high-spin state is much shorter than previously reported $T_{1/2} = 1.85(5)$ s in the literature, resulting in decay losses (this half-life is identical to those of the ground-state [2]). In the future the half-lives and spin/parities of ^{114}Rh should be studied in more detail.

In this work the isomeric state of neutron-rich ^{115}Ru was measured to have an excitation energy of 129(5) keV. Previously an excitation energy of 82(6) keV had been assigned based on a γ-ray spectroscopy study in Ref. [16], where the isomer was discovered. A 61.7 keV γ-ray was observed and it was assumed that a low-energy γ-ray of around 20 keV was not observed. Thus 82(6) keV was assigned as an energy for the isomer and reported in literature [2]. Our measurement is not within the uncertainties of this value. Thus we provide a new experimentally measured excitation energy for the isomeric state of ^{115}Ru. Further discussion of the newly proposed level scheme, based on this measurement, is given in attached article PII. The isomer in ^{115}Ru ($T_{1/2} = 76(6)$ ms) is the shortest isomer measured so far at the JYFLTRAP Penning trap. The ^{113,115}Ru isomeric-state excitation energies have been discussed in more detail in the attached article

TABLE 4   Isomer excitation energies (E_x) measured in this work compared to the excitation energies reported in the literature (NUBASE20 [2]). The spin-parities I^π and half-lives $T_{1/2}$ presented for each nucleus have been taken from NUBASE20 [2], except for ^{112}Rh, for which the half-life was measured in this work. # marks an extrapolated value.

Nuclide	I^π	$T_{1/2}$	Ref.	E_x [keV]	$E_{x,\text{lit.}}$ [keV]
^{110}Rh^m	(6^+)	28.5(13) s	^{133}Cs	38.0(15)	220(150)#
^{112}Rh^m	(6^+)	6.96(8) s^a	^{133}Cs	38.5(26)	
			^{112}Rh	38.3(28)	
		Weighted mean		38.4(19)	340(70)
^{114}Rh^m	(7^-)	1.85(5) s	^{114}Rh	110.9(32)	200(150)#
^{116}Rh^m	(6^-)	570(50) ms	^{116}Rh	120.8(19)	200(150)#
^{118}Rh^m	6^-#	310(30) ms	^{118}Rh	189(6)	200(150)#
^{113}Ru^m	$(7/2^-)$	510(30) ms	^{113}Ru$^{g.s.}$	100.4(9)	131(33)
^{115}Ru^m	$(7/2^-)$	76(6) ms	^{133}Cs	129(5)	82(6)
^{104}Nb^m	$(0^-,1^-)$	4.9(3) s	^{133}Cs	10.4(73)	9.8(26)

[1] Half-life measured in this work, see Section 7.6.

PII.

7.6 Mass and half-life of ^{112}Rh

At the IGISOL facility the ^{112}Rh isotope is often used as a standard for checking the fission yields during experiments, but until now the masses of the ground and isomeric states were only known at best to 40 keV precision. In AME20 [1] the ground-state mass of ^{112}Rh is based on a JYFLTRAP mass measurement ([18] and [112]) and on a privately communicated β-decay study [2, 109]. The isomer was reported to have an energy of $E_x = 340(70)$ keV based on the same privately communicated β-decay study [109]. The spins of 1^+ and (6^+) had been tentatively assigned for the ground- and isomeric state, respectively [2] and the half-lives of both states, the ground-state $T_{1/2} = 3.6(3)$ s and the isomer $T_{1/2} = 6.76(12)$ s [113]. These relevant properties found in literature have been tabulated in Table 5 for clarity.

In this work, the case of ^{112}Rh is specific because its two states were produced in two different ways: first via fission from ^{nat}U target at the IGISOL target chamber (^{112}Rh$^+$) and then via in-trap decay of ^{112}Ru ($T_{1/2} = 1.75(7)$ s, $I^\pi = 0^+$) producing ^{112}Rh^{2+} ions. The fission produced mostly the high-spin isomeric state, whereas the β-decay populated exclusively the low-spin ground state.

Concerning the case where fission was used as production mechanism, since in the literature the excitation energy of the isomer has been reported as $340(70)$ keV, a mass measurement with the PI-ICR technique was prepared using an accumulation time of 240 ms. This should have been enough to separate a 340-keV isomer. At first, during the measurement it was assumed that only one state was observed, see Fig. 35 a). It was unclear which state, ground or isomeric state, was observed, since it is known that fission favors the high-spin state (which in ^{112}Rh is the isomeric state) but the observed mass excess was much
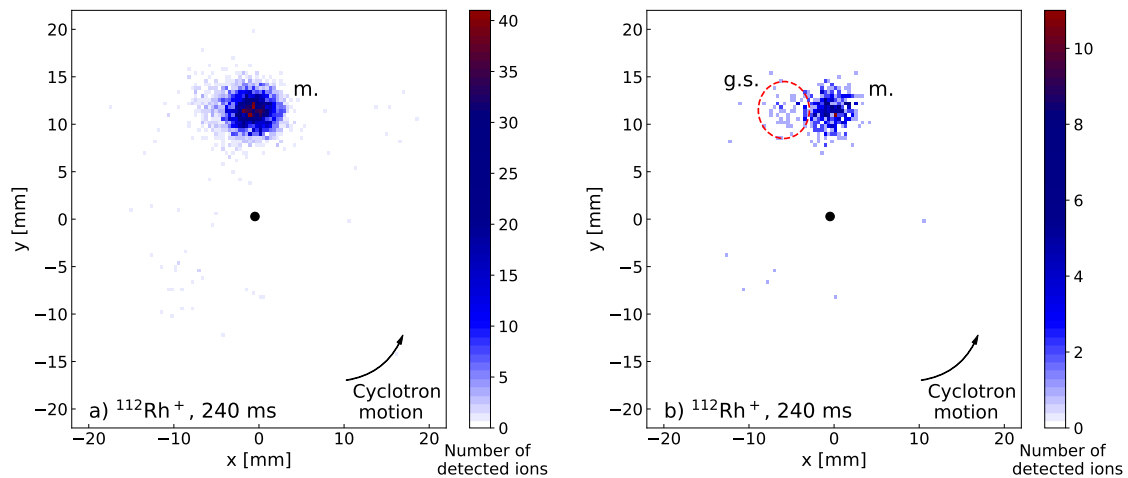

FIGURE 35   The accumulated cyclotron phase ϕ_+ for ^{112}Rh$^+$ with a a) 0-5 ions/bunch gate and b) 1 ion/bunch gate applied. The black point represents the trap center.

TABLE 5   Literature values relevant to measurements performed for ^{112}Rh, the half-lives $T_{1/2}$ and excitation energy E_x determined in this work. Isomer excitation energies ($E_{x,\,\text{lit.}}$), the spin-parities I^π and half-lives $T_{1/2,\text{lit.}}$ presented have been taken from NUBASE20 [2].

Nuclide	I^π	$T_{1/2,\,\text{lit.}}$ [s]	$E_{x,\,\text{lit.}}$ [keV]	E_x [keV]	$T_{1/2}$ [s]
^{112}Rh$^{g.s.}$	1^+	3.4(4)			2.22(12)
^{112}Rh^m	(6^+)	6.73(15)	340(70)	38.4(19)	6.96(8)
^{112}Ru$^{g.s.}$	0^+	1.75(7)			

closer to the literature value of the ground state than expected. It was later discovered during a detailed analysis that both the ground and isomeric states were present, but the ground state was much less populated than the isomer, and the excitation energy of the isomer was much lower than reported in literature, thus with such short accumulation time the phase spots were not fully separated.

To confirm which state was observed, its half-life was measured using a silicon detector located just after the 2D MCP detector. In the article PI (Fig. 5 a) the decay curve obtained is shown, which resulted to a half-life matching with the one given in the literature for the isomeric state.

The ground state was then produced via the in-trap decay of ^{112}Ru$^+$. In the in-trap decay method, the parent nucleus ^{112}Ru$^+$ is taken into the purification trap of JYFLTRAP and held there for a certain decay-time period. The ^{112}Ru$^+$, which is spin $I^\pi = 0^+$, will β-decay to the ground-state of ^{112}Rh, which should have a spin of $I^\pi = 1^+$. No decay to the isomeric state of ^{112}Rh (suggested to be $I^\pi = 6^+$) his expected due to the large spin difference. The ^{112}Rh ground state will be produced in the $q = 2+$ charge state. After enough of decays, the buffer gas cooling (see Chapter 3.4) is applied in the purification trap, using the quadrupolar excitation on the cyclotron frequency of the ^{112}Rh^{2+} ions. This way only the ^{112}Rh^{2+} ions populated via the β decay, were selected for mass measurements in the second trap. The measurement was performed using the PI-ICR technique with an accumulation time of 300 ms.

The resulting ground state mass was only around 30 keV lower from the mass measured for ^{112}Rh^m, produced directly in fission (see Table 3), also differing greatly from the ground state mass reported in the literature (see Fig. 30). Yet again to further confirm the state, a half-life measurement was performed (see decay curve in article PI, Fig. 5 b). A half-life of $T_{1/2} = 2.22(12)$ s was measured, and it is closer to the ground-state half-life (see Table 5). This result though differs by more than 4σ from the half-life reported in the ENSDF evaluation [113]. The ENSDF evaluation is based on two measurements [11, 13] where the contamination of ^{112}Ru decaying to the ^{112}Rh ground-state was not properly taken into account. A previous measurement of the half-life of the ground-state by Jokinen et al. [12] did account for this, resulting in a half-life of $T_{1/2} = 2.1(3)$ s. It agrees very well with the result of this work.

Due to the very low excitation energy of the isomer, it was then suspected that the accumulation time used in the previous measurement, 240 ms, was not

long enough to be able to resolve the two states. Thus the mass measurement of the isomeric state, produced via fission, was repeated with a longer, 1 s accumulation time. With such a long accumulation time and the energy difference of 38.4(19) keV between the ground and isomeric states, it was possible to separate and measure the mass of the isomer. First $^{133}Cs^+$ from the IGISOL offline ion source station [51] was used as a reference against the isomer, after which a measurement using the ground state of ^{112}Rh as a reference against the isomer was performed.

In Fig. 36 the mass values from all four measurements have been compiled. It can be seen that the result obtained using the 240 ms accumulation time is slightly shifted towards the ground-state mass value, which confirms that the ground state was contaminating the isomer phase spot (i.e. the frequency is shifting closer together). All three results of the isomeric-state mass still agree with each other and the contamination based on the observed count-rate would be extremely small. It was decided that the PI-ICR measurements with 1 s accumulation time would be used as final value for the mass of the isomeric state of ^{112}Rh, since the states were fully separated in the measurement.

To summarize, the measured excitation energy of the isomer is $E_x = 38.4(19)$-keV, which is much lower than the literature value. The ground state was found to be much shorter-living than reported in literature (see Table
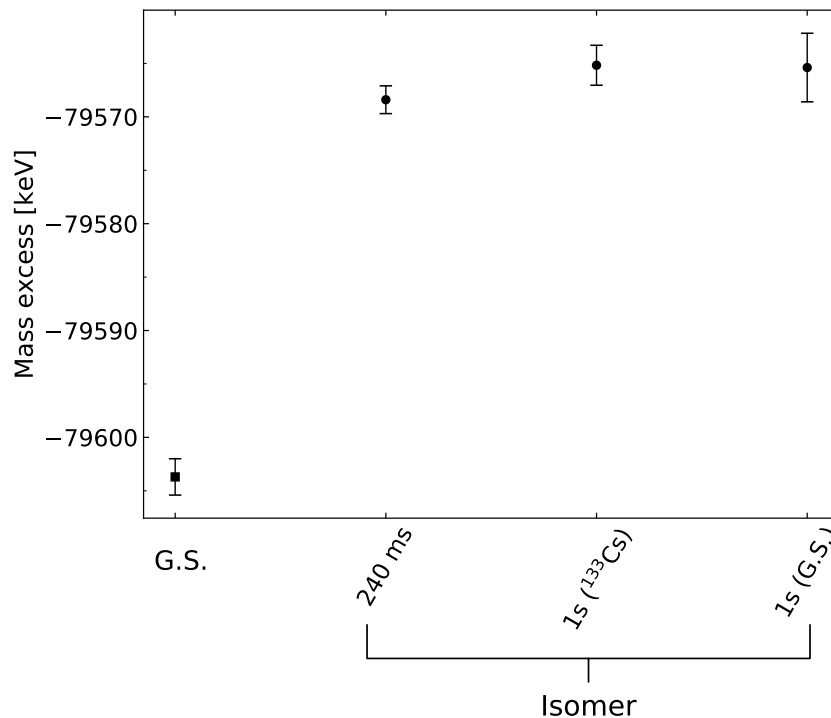

FIGURE 36   The mass-excess values measured for the ground and isomeric states of ^{112}Rh. The isomeric state was measured in three different ways: first with a 240 ms accumulation time and then with an 1 s accumulation time using ^{133}Cs and ^{112}Rh g.s as references (specified in brakets after the accumulation time).

4). The half-life of the isomer, $T_{1/2} = 6.96(8)$ s, agrees well with the literature. This work also confirms the order of the states. The ground state is the lower spin state and the isomer is the high-spin state.

7.7 Neutron-capture reaction rates for r-process calculations

To simulate the r-process path, the neutron-capture reaction rates are needed. During this work the neutron-capture reaction rates have been calculated with the masses from literature (AME20 [1]) and the masses measured in this work. The calculations were performed by Dr. S. Nikas using the statistical Hauser Feshbach TALYS code [114]. As an example, the calculated neutron-capture reaction rates have been plotted as a function of the mass number for the rhodium isotopes in Fig. 37. For comparison, the neutron-capture reaction rates calculated using the AME20 [1] values and three theoretical mass models, FRDM12 [37], Skyrme-HFB [115] and Gogny-HFB [116] are shown. The new masses provide more precise values for the calculation of the neutron separation energy $S_n(Z, N + 1)$ and reduce the uncertainties related to the neutron-capture rates compared to the literature values (AME20) significantly up to $A = 120$. The three theoretical models follow similar pattern as the experimental results, but do not reproduce it exactly. More details about the r-process calculations will be in a future publication.
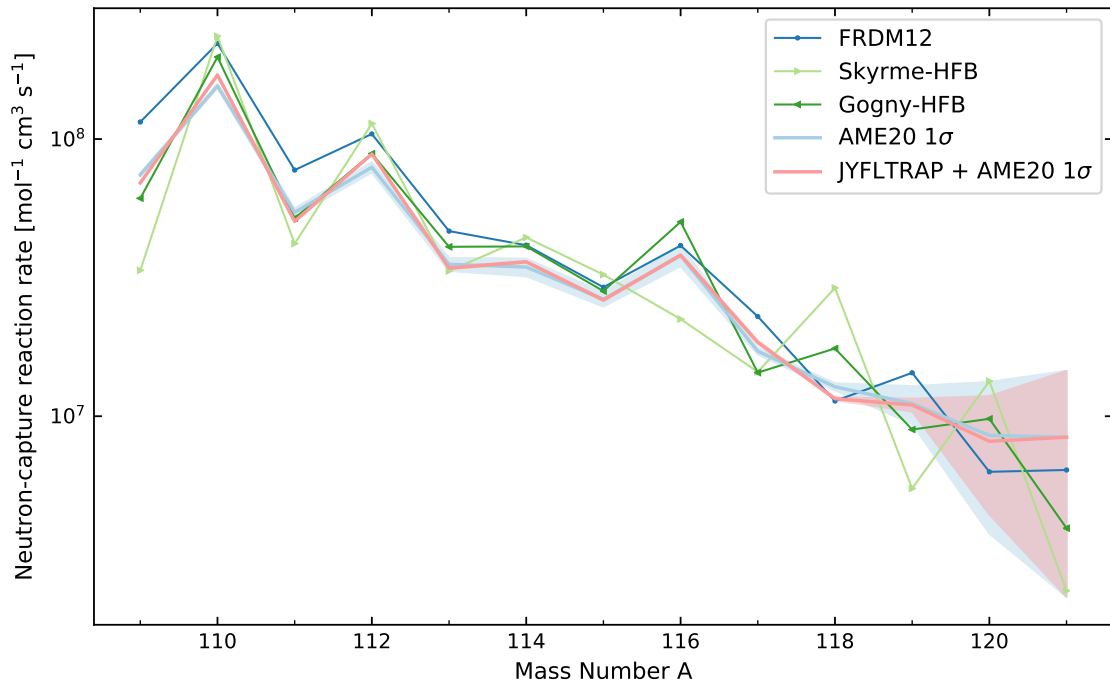

FIGURE 37   The neutron-capture reaction rate shown as a function of the mass number A at the rhodium ($Z = 45$) region of interest. The experimental values found in AME20 [1] are marked in light blue with a $1\,\sigma$ uncertainty band, while the values affected by mass measurements of this work are marked in pink with a $1\,\sigma$ uncertainty band. The neutron-capture reaction rates calculated from the masses produced by the FRDM12 [37], Skyrme-HFB [115] and Gogny-HFB [116] models are also shown.

8 SUMMARY AND OUTLOOK

This thesis reported on two different projects related to Penning trap mass spectrometry. First, this work provides the results of the commissioning of the PIPERADE double Penning trap during years $2020 - 2021$. The commissioning was done and is still ongoing at the LP2I Bordeaux, for the future DESIR facility. At the beginning of this work no ion trapping had been yet performed with PIPERADE. After the ion trapping in the first trap of PIPERADE was successful, the different excitations needed in the buffer gas cooling technique were performed. The buffer-gas cooling technique was successfully commissioned and is now routinely used at the PIPERADE Penning trap. After the buffer gas cooling technique has been used to select the ion of interest, trapping in the second trap of PIPERADE started. During this work the first excitations in the second trap were performed leading up to performing the very first TOF-ICR resonance in late 2021. The commissioning of the TOF-ICR technique for mass measurements at PIPERADE is still ongoing but the first mass measurements were done during late 2022. In the future the position sensitive MCP detector will be used to commission the PI-ICR technique for mass measurements and phase dependent cleaning. The transfer of the PIPERADE Penning trap from LP2I Bordeaux to the radioactive ion beam facility DESIR is planned for 2025.

Secondly, precision mass measurements were performed utilizing the JYFLTRAP double Penning trap at the Accelerator Laboratory of University of Jyväskylä. Altogether masses for 15 ground states and eight isomeric states of neutron-rich refractory nuclei were measured utilizing either the PI-ICR or the TOF-ICR mass measurement technique. The precision mass measurements were performed on the following nuclei : ^{110,112,114,116,118,120}Rh, ^{113,115,117}Ru, ^{104}Y, ^{104}Nb, ^{106}Zr, ^{109}Nb, ^{111}Mo, ^{112}Mo. This region is known for low-lying isomeric states, thus the isomeric states in ^{110,112,114,116,118}Rh and ^{113,115}Ru were separated utilizing the PI-ICR technique and their masses measured independently. This provides the excitation energies for all of the isomeric states. It was found that for example the isomeric state energy in ^{112}Rh is actually $E_x = 38.4(19)$ keV instead of the $E_x = 370(40)$ keV reported on AME20 [1] based on a privately communicated β-decay study. Due to the way the ^{112}Rh isomeric and ground states

were produced, via proton induced fission on a ^{nat}U target and in-trap decay of ^{112}Ru, the identification of the states was done by performing half-life measurements. Thus this work also provides new half-lives for the ground state of ^{112}Rh, $T_{1/2} = 2.22(13)$ s, and for the isomeric state, $T_{1/2} = 6.96(8)$ s. The new ground state half-life differs significantly from the literature value, $T_{1/2} = 3.6(3)$ s, by more than 4σ, while the isomeric state half-life is in good agreement with the literature. This work confirms that indeed the ground-state is the low-spin state and the isomeric-state is the high-spin state. In the future this region would benefit from decay-spectroscopy measurements to determine the spin/parities of the different states more confidently, since at the time of this work most of the spin/parity assignments are tentative.

The masses measured in this work were compared to the global mass model BSkG1 and BSkG2. For the rhodium and ruthenium isotopes, the BSkG1 model agrees well with the experimentally determined values. During the comparison of the mass differences calculated from the experimental and model masses it was noticed that the BSkG1 model produces the trend of the odd-even staggering parameter $\Delta_n^{(3)}$ well, but the absolute magnitude was significantly higher for the odd-Z nuclei than the experimental values. For the even-Z nuclei the agreement was good. The difference seen in odd-Z nuclei was interpreted as the model not correctly accounting for the interaction of the odd-proton and odd-neutron. In the future this will be taken into account in the next evolutions of the model.

The two different projects done in the framework of this thesis were complementary: commissioning a new Penning trap for a future radioactive ion beam facility and utilizing an operational Penning trap for mass measurements of exotic neutron-rich refractory nuclei. The mass measurements have extended and define more precisely the mass surface trends in the region. The new mass measurements of the exotic neutron-rich nuclei were found, yet again, to be important for testing the theoretical mass models. In the future of precision mass spectrometry the reach of Penning traps can be improved using the Multi-Reflection Time-of-Flight (MR-TOF) device for a fast selection of ions of interest, making this step faster. The IGISOL facility has an MR-TOF device and one has been planned to be installed at the upcoming DESIR facility. The region of neutron-rich refractory nuclei of interest in this work proves still to have a lot of experimentally unknown nuclear observables. For example the spins and parities of the states are tentative. In this work the half-life of ^{112}Rh ground state was measured to be over 4σ different than the literature value, highlighting the importance of Penning trap purified ion samples for half-life measurements. In the BSkG1 model the deformation is predicted to decrease when approaching the $N = 82$ shell closure, and for example for rhodium isotopes it was seen as a flattening of the two-neutron separation energy trend. In the future facilities some of these very exotic nuclei will be produced and their masses, as well as other properties, will be measured. This will help to understand the shape evolution from the midshell region up to the $N = 82$ shell closure.

REFERENCES

[1] M. Wang, W. Huang, F. Kondev, G. Audi, and S. Naimi, "The AME 2020 Atomic Mass Evaluation (ii). Tables, graphs and references," *Chin. Phys. C*, vol. 45, no. 3, p. 030003, 2021. [Online]. Available: https://dx.doi.org/10.1088/1674-1137/abddaf

[2] F. Kondev, M. Wang, W. Huang, S. Naimi, and G. Audi, "The NUBASE2020 evaluation of nuclear physics properties," *Chin. Phys. C*, vol. 45, no. 3, p. 030001, 2021. [Online]. Available: https://dx.doi.org/10.1088/1674-1137/abddae

[3] K. Heyde and J. L. Wood, "Shape coexistence in atomic nuclei," *Rev. Mod. Phys.*, vol. 83, pp. 1467–1521, 2011. [Online]. Available: https://link.aps.org/doi/10.1103/RevModPhys.83.1467

[4] E. M. Burbidge, G. R. Burbidge, W. A. Fowler, and F. Hoyle, "Synthesis of the elements in stars," *Rev. Mod. Phys.*, vol. 29, pp. 547–650, 1957. [Online]. Available: https://link.aps.org/doi/10.1103/RevModPhys.29.547

[5] J. Karthein, *https://github.com/jonas-ka/nuclear-chart-plotter/blob/master/nuclear-chart.ipynb*. Under MIT license.

[6] L. S. Brown and G. Gabrielse, "Geonium theory: Physics of a single electron or ion in a Penning trap," *Rev. Mod. Phys.*, vol. 58, pp. 233–311, 1986. [Online]. Available: https://link.aps.org/doi/10.1103/RevModPhys.58.233

[7] H. Dehmelt, "Experiments with an isolated subatomic particle at rest," *Rev. Mod. Phys.*, vol. 62, pp. 525–530, 1990. [Online]. Available: https://link.aps.org/doi/10.1103/RevModPhys.62.525

[8] T. Eronen, V. S. Kolhinen, V. V. Elomaa, D. Gorelov, U. Hager, J. Hakala, A. Jokinen, A. Kankainen, P. Karvonen, I. D. Moore, H. Penttilä, S. Rahaman, S. Rinta-Antila, J. Rissanen, A. Saastamoinen, J. Szerypo, C. Weber, and J. Äystö, "JYFLTRAP: a Penning trap for precision mass spectroscopy and isobaric purification," *The Eur. Phys. J. A*, vol. 48, p. 46, 2012, doi: https://doi.org/10.1140/epja/i2012-12046-1.

[9] J. Ärje, J. Äystö, H. Hyvönen, P. Taskinen, V. Koponen, J. Honkanen, K. Valli, A. Hautojärvi, and K. Vierinen, "The ion guide isotope separator on-line, IGISOL," *Nucl. Instr. Meth. Phys. Rs. Sect. A: Accelerators, Spectrometers, Detectors and Associated Equipment*, vol. 247, no. 3, pp. 431–437, 1986. [Online]. Available: https://www.sciencedirect.com/science/article/pii/0168900286904043

[10] P. Campbell, H. L. Thayer, J. Billowes, P. Dendooven, K. T. Flanagan, D. H. Forest, J. A. R. Griffith, J. Huikari, A. Jokinen, R. Moore,

98

A. Nieminen, G. Tungate, S. Zemlyanoi, and J. Äystö, "Laser spectroscopy of cooled zirconium fission fragments," *Phys. Rev. Lett.*, vol. 89, p. 082501, 2002. [Online]. Available: https://link.aps.org/doi/10.1103/PhysRevLett. 89.082501

[11] J. Äystö, C. Davids, J. Hattula, J. Honkanen, K. Honkanen, P. Jauho, R. Julin, S. Juutinen, J. Kumpulainen, T. Lönnroth, A. Pakkanen, A. Passoja, H. Penttilä, P. Taskinen, E. Verho, A. Virtanen, and M. Yoshii, "Levels in ^{110}Pd, ^{112}Pd, ^{114}Pd and ^{116}Pd from the beta decays of the on-line mass separated Rh isotopes," *Nucl. Phys. A*, vol. 480, no. 1, pp. 104–124, 1988. [Online]. Available: https://www.sciencedirect.com/science/article/pii/ 0375947488903879

[12] A. Jokinen, J. Äystö, P. Dendooven, K. Eskola, Z. Janas, P. P. Jauho, M. E. Leino, J. M. Parmonen, H. Penttilä, K. Rykaczewski, and P. Taskinen, "Spin-flip β^- decay of even-even deformed nuclei ^{110}Ru and ^{112}Ru," *Z. Phys. A*, vol. 340, pp. 21 – 28, 1991. [Online]. Available: https://doi.org/10.1007/BF01284476

[13] G. Lhersonneau, J. C. Wang, S. Hankonen, P. Dendooven, P. Jones, R. Julin, and J. Äystö, "Decays of ^{110}Rh and ^{112}Rh to the near neutron midshell isotopes ^{110}Pd and ^{112}Pd," *Phys. Rev. C*, vol. 60, p. 014315, 1999. [Online]. Available: https://link.aps.org/doi/10.1103/PhysRevC.60.014315

[14] G. Lhersonneau, Y. Wang, R. Capote, J. Suhonen, P. Dendooven, J. Huikari, K. Peräjärvi, and J. C. Wang, "Decay of ^{114}Rh to ^{114}Pd," *Phys. Rev. C*, vol. 67, p. 024303, 2003. [Online]. Available: https: //link.aps.org/doi/10.1103/PhysRevC.67.024303

[15] J. Kurpeta, W. Urban, C. Droste, A. Płochocki, S. G. Rohoziński, T. Rzaca-Urban, T. Morek, L. Próchniak, K. Starosta, J. Äystö, H. Penttilä, J. L. Durell, A. G. Smith, G. Lhersonneau, and I. Ahmad, "Low-spin structure of ^{113}Ru and ^{113}Rh," *The Eur. Phys. J. A*, vol. 33, no. 4, pp. 307–316, 2007. [Online]. Available: https://doi.org/10.1140/epja/i2006-10464-2

[16] J. Kurpeta, J. Rissanen, A. Płochocki, W. Urban, V.-V. Elomaa, T. Eronen, J. Hakala, A. Jokinen, A. Kankainen, P. Karvonen, T. Małkiewicz, I. D. Moore, H. Penttilä, A. Saastamoinen, G. S. Simpson, C. Weber, and J. Äystö, "New isomer and decay half-life of ^{115}Ru," *Phys. Rev. C*, vol. 82, p. 064318, 2010. [Online]. Available: https://link.aps.org/doi/10.1103/PhysRevC.82. 064318

[17] J. Rissanen, "Penning-trap-assisted decay spectroscopy studies of neutron-rich nuclei in the $A = 110$ region," Ph.D. dissertation, University of Jyväskylä, Finland, 2011.

[18] U. Hager, V.-V. Elomaa, T. Eronen, J. Hakala, A. Jokinen, A. Kankainen, S. Rahaman, S. Rinta-Antila, A. Saastamoinen, T. Sonoda, and J. Äystö,

"Precision mass measurements of neutron-rich Tc, Ru, Rh, and Pd isotopes," *Phys. Rev. C*, vol. 75, p. 064302, 2007. [Online]. Available: https://link.aps.org/doi/10.1103/PhysRevC.75.064302

[19] U. Hager, A. Jokinen, V.-V. Elomaa, T. Eronen, J. Hakala, A. Kankainen, S. Rahaman, J. Rissanen, I. Moore, S. Rinta-Antila, A. Saastamoinen, T. Sonoda, and J. Äystö, "Precision mass measurements of neutron-rich yttrium and niobium isotopes," *Nucl. Phys. A*, vol. 793, no. 1, pp. 20–39, 2007. [Online]. Available: https://www.sciencedirect.com/science/article/pii/S0375947407006070

[20] U. Hager, T. Eronen, J. Hakala, A. Jokinen, V. S. Kolhinen, S. Kopecky, I. Moore, A. Nieminen, M. Oinonen, S. Rinta-Antila, J. Szerypo, and J. Äystö, "First Precision Mass Measurements of Refractory Fission Fragments," *Phys. Rev. Lett.*, vol. 96, p. 042504, 2006. [Online]. Available: https://link.aps.org/doi/10.1103/PhysRevLett.96.042504

[21] J. Hakala, R. Rodriguez-Guzmán, V.-V. Elomaa, T. Eronen, A. Jokinen, V. S. Kohlinen, I. D. Moore, H. Penttilä, M. Reponen, J. Rissanen, A. Saastamoinen, and J. Äystö, "Precision mass measurements of neutron-rich Y, Nb, Mo, Tc, Ru, Rh, and Pd isotopes," *The Eur. Phys. J. A*, vol. 47, p. 129, 2011. [Online]. Available: https://doi.org/10.1140/epja/i2011-11129-9

[22] S. Eliseev, K. Blaum, M. Block, A. Dörr, C. Droese, T. Eronen, M. Goncharov, M. Höcker, J. Ketter, E. M. Ramirez, D. Nesterenko, Y. N. Novikov, and L. Schweikhard, "A phase-imaging technique for cyclotron-frequency measurements," *Appl. Phys. B*, vol. 114, no. 1, pp. 107–128, 2014. [Online]. Available: https://doi.org/10.1007/s00340-013-5621-0

[23] M. König, G. Bollen, H.-J. Kluge, T. Otto, and J. Szerypo, "Quadrupole excitation of stored ion motion at the true cyclotron frequency," *Int. J. Mass Spectrom. Ion Proc.*, vol. 142, no. 1, pp. 95–116, 1995. [Online]. Available: https://www.sciencedirect.com/science/article/pii/016811769504146C

[24] K. Krane, *Introductory Nuclear Physics*.   NJ, USA: Wiley, 1988.

[25] D. Lunney, J. M. Pearson, and C. Thibault, "Recent trends in the determination of nuclear masses," *Rev. Mod. Phys.*, vol. 75, pp. 1021–1082, 2003. [Online]. Available: https://link.aps.org/doi/10.1103/RevModPhys.75.1021

[26] P. Moller, J. Nix, W. Myers, and W. Swiatecki, "Nuclear Ground-State Masses and Deformations," *At. Data Nucl. Data Tabl.*, vol. 59, no. 2, pp. 185–381, 1995. [Online]. Available: https://www.sciencedirect.com/science/article/pii/S0092640X85710029

[27] P. Möller, R. Bengtsson, B. G. Carlsson, P. Olivius, and T. Ichikawa, "Global Calculations of Ground-State Axial Shape Asymmetry of

Nuclei," *Phys. Rev. Lett.*, vol. 97, p. 162502, 2006. [Online]. Available: https://link.aps.org/doi/10.1103/PhysRevLett.97.162502

[28] P. Ring and P. Schuck, *The Nuclear Many-Body Problem*. Berlin: Springer, 1980.

[29] S. G. Nilsson, *Shapes and Shells in Nuclear Structure*. New York, USA: Cambridge University Press, 1995.

[30] S. Nilsson, "Binding states of individual nucleons in strongly deformed nuclei," *Mat. Fys. Medd. Dan. Vid. Selsk.*, vol. 29, 1955. [Online]. Available: http://cds.cern.ch/record/212345/files/p1.pdf

[31] G. Scamps, S. Goriely, E. Olsen, M. Bender, and W. Ryssens, "Skyrme-Hartree-Fock-Bogoliubov mass models on a 3D mesh: effect of triaxial shape," *The Eur. Phys. J. A*, vol. 57, no. 12, p. 333, 2021. [Online]. Available: https://doi.org/10.1140/epja/s10050-021-00642-1

[32] W. Ryssens, G. Scamps, G. Grams, I. Kullmann, M. Bender, and S. Goriely, *submitted to INPC 2022 proceedings, arXiv: 2211.03667*.

[33] G. Gamow and E. Rutherford, "Mass defect curve and nuclear constitution," *Proc. R. Soc. Lond. A*, vol. 126, no. 803, pp. 632–644, 1930. [Online]. Available: https://royalsocietypublishing.org/doi/abs/10.1098/rspa.1930.0032

[34] H. A. Bethe and R. F. Bacher, "Nuclear physics a. stationary states of nuclei," *Rev. Mod. Phys.*, vol. 8, pp. 82–229, 1936. [Online]. Available: https://link.aps.org/doi/10.1103/RevModPhys.8.82

[35] W. Pauli, "Über den zusammenhang des abschlusses der elektronengruppen im atom mit der komplexstruktur der spektren," *Z. Phys.*, vol. 31, pp. 765–783, 1925. [Online]. Available: https://doi.org/10.1007/BF02980631

[36] J. Lilley, *Nuclear Physics Principles and Applications*. England: Wiley, 2002.

[37] P. Möller, A. Sierk, T. Ichikawa, and H. Sagawa, "Nuclear ground-state masses and deformations: FRDM(2012)," *At. Data Nucl. Data Tabl.*, vol. 109-110, pp. 1–204, 2016. [Online]. Available: https://www.sciencedirect.com/science/article/pii/S0092640X1600005X

[38] R. F. Casten, *Nuclear Structure from a Simple Perspective*. New York: Oxford University Press, 2005.

[39] J. Suhonen, *From Nucleons to Nucleus*. Berlin, Heidelberg: Springer-Verlag, 2007.

[40] K. L. G. Heyde, *The Nuclear Shell Model*. New York: Springer-Verlag, 1994.

[41] E. Caurier, G. Martínez-Pinedo, F. Nowacki, A. Poves, and A. P. Zuker, "The shell model as a unified view of nuclear structure," *Rev. Mod. Phys.*, vol. 77, pp. 427–488, 2005. [Online]. Available: https://link.aps.org/doi/10.1103/RevModPhys.77.427

[42] R. D. Woods and D. S. Saxon, "Diffuse surface optical model for nucleon-nuclei scattering," *Phys. Rev.*, vol. 95, pp. 577–578, 1954. [Online]. Available: https://link.aps.org/doi/10.1103/PhysRev.95.577

[43] M. G. Mayer, "On closed shells in nuclei. ii," *Phys. Rev.*, vol. 75, pp. 1969–1970, 1949. [Online]. Available: https://link.aps.org/doi/10.1103/PhysRev.75.1969

[44] O. Haxel, J. H. D. Jensen, and H. E. Suess, "On the "magic numbers" in nuclear structure," *Phys. Rev.*, vol. 75, pp. 1766–1766, 1949. [Online]. Available: https://link.aps.org/doi/10.1103/PhysRev.75.1766.2

[45] L. Coraggio, A. Covello, A. Gargano, N. Itaco, and T. Kuo, "Shell-model calculations and realistic effective interactions," *Progr. Part. Nucl. Phys.*, vol. 62, no. 1, pp. 135–182, 2009. [Online]. Available: https://www.sciencedirect.com/science/article/pii/S0146641008000410

[46] S. R. Stroberg, H. Hergert, S. K. Bogner, and J. D. Holt, "Nonempirical interactions for the nuclear shell model: An update," *Ann. Rev. Nucl. Part. Sci.*, vol. 69, no. 1, pp. 307–362, 2019. [Online]. Available: https://doi.org/10.1146/annurev-nucl-101917-021120

[47] B. R. Barrett, P. Navrátil, and J. P. Vary, "Ab initio no core shell model," *Progr. Part. Nucl. Phys.*, vol. 69, pp. 131–181, 2013. [Online]. Available: https://www.sciencedirect.com/science/article/pii/S0146641012001184

[48] W. Ryssens, "Symmetry breaking in nuclear mean-field models," Ph.D. dissertation, Université Libre de Bruxelles, 2016.

[49] M. Hukkanen, W. Ryssens, P. Ascher, M. Bender, T. Eronen, S. Grévy, A. Kankainen, M. Stryjczyk, L. Al Ayoubi, S. Ayet, O. Beliuskina, C. Delafosse, W. Gins, M. Gerbaux, A. Husson, A. Jokinen, D. A. Nesterenko, I. Pohjalainen, M. Reponen, S. Rinta-Antila, A. de Roubin, and A. P. Weaver, "Odd-odd neutron-rich rhodium isotopes studied with the double Penning trap JYFLTRAP," *Phys. Rev. C*, vol. 107, p. 014306, 2023. [Online]. Available: https://link.aps.org/doi/10.1103/PhysRevC.107.014306

[50] W. Ryssens, G. Scamps, S. Goriely, and M. Bender, "Skyrme–Hartree–Fock–Bogoliubov mass models on a 3D mesh: Ii. Time-reversal symmetry breaking," *The Eur. Phys. J. A*, vol. 58, no. 12, p. 246, 2022. [Online]. Available: https://doi.org/10.1140/epja/s10050-022-00894-5

102

[51] M. Vilén, L. Canete, B. Cheal, A. Giatzoglou, R. de Groote, A. de Roubin, T. Eronen, S. Geldhof, A. Jokinen, A. Kankainen, I. Moore, D. Nesterenko, H. Penttilä, I. Pohjalainen, M. Reponen, and S. Rinta-Antila, "A new off-line ion source facility at IGISOL," *Nucl. Instr. Meth. Phys. Res. Sec. B*, vol. 463, pp. 382–383, 2020. [Online]. Available: https://www.sciencedirect.com/science/article/pii/S0168583X19302344

[52] S. A. Giuliani, Z. Matheson, W. Nazarewicz, E. Olsen, P.-G. Reinhard, J. Sadhukhan, B. Schuetrumpf, N. Schunck, and P. Schwerdtfeger, "Colloquium: Superheavy elements: Oganesson and beyond," *Rev. Mod. Phys.*, vol. 91, p. 011001, 2019. [Online]. Available: https://link.aps.org/doi/10.1103/RevModPhys.91.011001

[53] W. Urban, J. Durell, A. Smith, W. Phillips, M. Jones, B. Varley, T. Rzaca-Urban, I. Ahmad, L. Morss, M. Bentaleb, and N. Schulz, "Medium-spin structure of ^{96,97}Sr and ^{98,99}Zr nuclei and the onset of deformation in the A100 region," *Nucl. Phys. A*, vol. 689, no. 3, pp. 605–630, 2001. [Online]. Available: https://www.sciencedirect.com/science/article/pii/S0375947400006126

[54] C. Iliadis, *Nuclear Physics of Stars*. Weinheim: Wiley-WHC, 2015.

[55] J. J. Cowan, C. Sneden, J. E. Lawler, A. Aprahamian, M. Wiescher, K. Langanke, G. Martínez-Pinedo, and F.-K. Thielemann, "Origin of the heaviest elements: The rapid neutron-capture process," *Rev. Mod. Phys.*, vol. 93, p. 015002, 2021. [Online]. Available: https://link.aps.org/doi/10.1103/RevModPhys.93.015002

[56] J. J. Cowan and W. K. Rose, "Production of ^{14}C and neutrons in red giants." *Astrophys. J.*, vol. 212, pp. 149–158, 1977.

[57] P. Denissenkov, G. Perdikakis, F. Herwig, H. Schatz, C. Ritter, M. Pignatari, S. Jones, S. Nikas, and A. Spyrou, "The impact of (n, γ) reaction rate uncertainties of unstable isotopes near N = 50 on the i-process nucleosynthesis in He-shell flash white dwarfs," *J. Phys. G: Nucl. Part. Phys.*, vol. 45, no. 5, p. 055203, 2018. [Online]. Available: https://dx.doi.org/10.1088/1361-6471/aabb6e

[58] B. P. Abbott, R. Abbott, T. D. Abbott, M. R. Abernathy, F. Acernese, K. Ackley, and et al., "Observation of Gravitational Waves from a Binary Black Hole Merger," *Phys. Rev. Lett.*, vol. 116, p. 061102, 2016. [Online]. Available: https://link.aps.org/doi/10.1103/PhysRevLett.116.061102

[59] B. P. Abbott, R. Abbott, T. D. Abbott, F. Acernese, K. Ackley, and el al., "Gravitational waves and gamma-rays from a binary neutron star merger: GW170817 and GRB170817A," *The Astrophys. J. Lett.*, vol. 848, no. 2, p. L13, 2017. [Online]. Available: https://dx.doi.org/10.3847/2041-8213/aa920c

[60] N. R. Tanvir *et al.*, "The emergence of a lanthanide-rich kilonova following the merger of two neutron stars," *The Astrophys. J. Lett.*, vol. 848, no. 2, p. L27, 2017. [Online]. Available: https://dx.doi.org/10.3847/2041-8213/aa90b6

[61] M. R. Mumpower, R. Surman, D.-L. Fang, M. Beard, P. Möller, T. Kawano, and A. Aprahamian, "Impact of individual nuclear masses on *r*-process abundances," *Phys. Rev. C*, vol. 92, p. 035807, 2015. [Online]. Available: https://link.aps.org/doi/10.1103/PhysRevC.92.035807

[62] M. Mumpower, R. Surman, G. McLaughlin, and A. Aprahamian, "The impact of individual nuclear properties on r-process nucleosynthesis," *Progr. Part. Nucl. Phys.*, vol. 86, pp. 86–126, 2016. [Online]. Available: https://www.sciencedirect.com/science/article/pii/S0146641015000897

[63] J. Kurpeta, G. Lhersonneau, J.C. Wang, P. Dendooven, A. Honkanen, M. Huhta, M. Oinonen, H. Penttilä, K. Peräjärvi, J.R. Persson, A. Plochocki, and J. Äystö, "First decay scheme of ^{113}Tc and identification of ^{113}Ru^{m}," *Eur. Phys. J. A*, vol. 2, no. 3, pp. 241–243, 1998. [Online]. Available: https://doi.org/10.1007/s100500050114

[64] A. Navin, M. Rejmund, S. Bhattacharyya, R. Palit, G. Bhat, J. Sheikh, A. Lemasson, S. Bhattacharya, M. Caamaño, E. Clément, O. Delaune, F. Farget, G. de France, and B. Jacquot, "Evolution of triaxial shapes at large isospin: Rh isotopes," *Phys. Lett. B*, vol. 767, pp. 480–484, 2017. [Online]. Available: https://www.sciencedirect.com/science/article/pii/S0370269316306839

[65] J. A. Sheikh and K. Hara, "Triaxial projected shell model approach," *Phys. Rev. Lett.*, vol. 82, pp. 3968–3971, 1999. [Online]. Available: https://link.aps.org/doi/10.1103/PhysRevLett.82.3968

[66] T. Sumikama, K. Yoshinaga, H. Watanabe, S. Nishimura, Y. Miyashita, K. Yamaguchi, K. Sugimoto, J. Chiba, Z. Li, H. Baba, J. S. Berryman, N. Blasi, A. Bracco, F. Camera, P. Doornenbal, S. Go, T. Hashimoto, S. Hayakawa, C. Hinke, E. Ideguchi, T. Isobe, Y. Ito, D. G. Jenkins, Y. Kawada, N. Kobayashi, Y. Kondo, R. Krücken, S. Kubono, G. Lorusso, T. Nakano, M. Kurata-Nishimura, A. Odahara, H. J. Ong, S. Ota, Z. Podolyák, H. Sakurai, H. Scheit, K. Steiger, D. Steppenbeck, S. Takano, A. Takashima, K. Tajiri, T. Teranishi, Y. Wakabayashi, P. M. Walker, O. Wieland, and H. Yamaguchi, "Structural evolution in the neutron-rich nuclei ^{106}Zr and ^{108}Zr," *Phys. Rev. Lett.*, vol. 106, p. 202501, 2011. [Online]. Available: https://link.aps.org/doi/10.1103/PhysRevLett.106.202501

[67] F. Browne, A. Bruce, T. Sumikama, I. Nishizuka, S. Nishimura, P. Doornenbal, G. Lorusso, P.-A. Söderström, H. Watanabe, R. Daido, Z. Patel, S. Rice, L. Sinclair, J. Wu, Z. Xu, A. Yagi, H. Baba, N. Chiga, R. Carroll, F. Didierjean, Y. Fang, N. Fukuda, G. Gey, E. Ideguchi,

104

N. Inabe, T. Isobe, D. Kameda, I. Kojouharov, N. Kurz, T. Kubo, S. Lalkovski, Z. Li, R. Lozeva, H. Nishibata, A. Odahara, Z. Podolyák, P. Regan, O. Roberts, H. Sakurai, H. Schaffner, G. Simpson, H. Suzuki, H. Takeda, M. Tanaka, J. Taprogge, V. Werner, and O. Wieland, "Lifetime measurements of the first 2^+ states in ^{104,106}Zr: Evolution of ground-state deformations," *Phys. Lett. B*, vol. 750, pp. 448–452, 2015. [Online]. Available: https://www.sciencedirect.com/science/article/pii/S0370269315007182

[68] A. Navin, M. Rejmund, C. Schmitt, S. Bhattacharyya, G. Lhersonneau, P. Van Isacker, M. Caamaño, E. Clément, O. Delaune, F. Farget, G. de France, and B. Jacquot, "Towards the high spin–isospin frontier using isotopically-identified fission fragments," *Phys. Lett. B*, vol. 728, pp. 136–140, 2014. [Online]. Available: https://www.sciencedirect.com/science/article/pii/S0370269313009271

[69] C. J. Horowitz, A. Arcones, B. Côté, I. Dillmann, W. Nazarewicz, I. U. Roederer, H. Schatz, A. Aprahamian, D. Atanasov, A. Bauswein, T. C. Beers, J. Bliss, M. Brodeur, J. A. Clark, A. Frebel, F. Foucart, C. J. Hansen, O. Just, A. Kankainen, G. C. McLaughlin, J. M. Kelly, S. N. Liddick, D. M. Lee, J. Lippuner, D. Martin, J. Mendoza-Temis, B. D. Metzger, M. R. Mumpower, G. Perdikakis, J. Pereira, B. W. O'Shea, R. Reifarth, A. M. Rogers, D. M. Siegel, A. Spyrou, R. Surman, X. Tang, T. Uesaka, and M. Wang, "r-process nucleosynthesis: connecting rare-isotope beam facilities with the cosmos," *Journal of Physics G: Nuclear and Particle Physics*, vol. 46, no. 8, p. 083001, 2019. [Online]. Available: https://dx.doi.org/10.1088/1361-6471/ab0849

[70] S. Wanajo and Y. Ishimaru, "The "weak" r-process in core-collapse supernovae," *Proc. Int. Astron. Union*, vol. 1, no. S228, p. 435–438, 2005. [Online]. Available: https://doi.org/10.1017/S1743921305006174

[71] J. Ketter, T. Eronen, M. Höcker, S. Streubel, and K. Blaum, "First-order perturbative calculation of the frequency-shifts caused by static cylindrically-symmetric electric and magnetic imperfections of a Penning trap," *Int. J. Mass Spectrom.*, vol. 358, pp. 1–16, 2014. [Online]. Available: https://www.sciencedirect.com/science/article/pii/S1387380613003722

[72] M. Kretzschmar, "Particle motion in a Penning trap," *The Eur. J. Phys.*, vol. 12, no. 5, p. 240, 1991. [Online]. Available: https://dx.doi.org/10.1088/0143-0807/12/5/010

[73] V. G. F.G. Major and G. Werth, *Charged Particle Traps: Physics and Techniques of Charged Particle Field Confinement*. Springer, 2005.

[74] P. W. Anderson, "Theory of Flux Creep in Hard Superconductors," *Phys. Rev. Lett.*, vol. 9, pp. 309–311, 1962. [Online]. Available: https://link.aps.org/doi/10.1103/PhysRevLett.9.309

[75] D. Nesterenko, T. Eronen, Z. Ge, A. Kankainen, and M. Vilen, "Study of radial motion phase advance during motion excitations in a Penning trap and accuracy of JYFLTRAP mass spectrometer," *Eur. Phys. J. A*, vol. 57, p. 302, 2021. [Online]. Available: https://doi.org/10.1140/epja/s10050-021-00608-3

[76] P. Ascher, L. Daudin, M. Flayol, M. Gerbaux, S. Grévy, M. Hukkanen, A. Husson, A. de Roubin, P. Alfaurt, B. Blank, K. Blaum, B. Lachacinski, D. Lunney, E. M. Ramirez, S. Naimi, S. Perard, and B. Thomas, "PIPERADE: A double Penning trap for mass separation and mass spectrometry at DESIR/SPIRAL2," *Nucl. Instrum. Met. Phys. Res. Sect. A: Accelerators, Spectrometers, Detectors and Associated Equipment*, vol. 1019, p. 165857, 2021. [Online]. Available: https://www.sciencedirect.com/science/article/pii/S0168900221008421

[77] S. Eliseev, C. Roux, K. Blaum, M. Block, C. Droese, F. Herfurth, M. Kretzschmar, M. I. Krivoruchenko, E. Minaya Ramirez, Y. N. Novikov, L. Schweikhard, V. M. Shabaev, F. Šimkovic, I. I. Tupitsyn, K. Zuber, and N. A. Zubova, "Octupolar-excitation Penning-trap mass spectrometry for Q-value measurement of double-electron capture in ^{164}Er," *Phys. Rev. Lett.*, vol. 107, p. 152501, 2011. [Online]. Available: https://link.aps.org/doi/10.1103/PhysRevLett.107.152501

[78] M. Rosenbusch, C. Böhm, C. Borgmann, M. Breitenfeldt, A. Herlert, M. Kowalska, S. Kreim, G. Marx, S. Naimi, D. Neidherr, R. Schneider, and L. Schweikhard, "A study of octupolar excitation for mass-selective centering in Penning traps," *Int. J. Mass Spectrom.*, vol. 314, pp. 6–12, 2012. [Online]. Available: https://www.sciencedirect.com/science/article/pii/S1387380612000188

[79] G. Savard, S. Becker, G. Bollen, H.-J. Kluge, R. Moore, T. Otto, L. Schweikhard, H. Stolzenberg, and U. Wiess, "A new cooling technique for heavy ions in a Penning trap," *Phys. Lett. A*, vol. 158, no. 5, pp. 247–252, 1991. [Online]. Available: https://www.sciencedirect.com/science/article/pii/037596019191082

[80] T. Eronen, V.-V. Elomaa, U. Hager, J. Hakala, A. Jokinen, A. Kankainen, S. Rahaman, J. Rissanen, C. Weber, and J. Äystö, "Preparing isomerically pure beams of short-lived nuclei at JYFLTRAP," *Nucl. Instrum. Meth. Phys. Res. Sect. B: Beam Interactions with Materials and Atoms*, vol. 266, no. 19, pp. 4527–4531, 2008, proceedings of the XVth International Conference on Electromagnetic Isotope Separators and Techniques Related to their Applications. [Online]. Available: https://www.sciencedirect.com/science/article/pii/S0168583X08007696

[81] K. Peräjärvi, T. Eronen, V.-V. Elomaa, J. Hakala, A. Jokinen, H. Kettunen, V. Kolhinen, M. Laitinen, I. Moore, H. Penttilä, J. Rissanen, A. Saastamoinen, H. Toivonen, J. Turunen, and J. Äystö, "Ultra-high resolution

mass separator—application to detection of nuclear weapons tests," *Appl. Rad. Isotop.*, vol. 68, no. 3, pp. 450–453, 2010. [Online]. Available: https://www.sciencedirect.com/science/article/pii/S0969804309007878

[82] N. F. Ramsey, "Experiments with separated oscillatory fields and hydrogen masers," *Rev. Mod. Phys.*, vol. 62, pp. 541–552, 1990. [Online]. Available: https://link.aps.org/doi/10.1103/RevModPhys.62.541

[83] M. Kretzschmar, "The Ramsey method in high-precision mass spectrometry with Penning traps: Theoretical foundations," *Int. J. Mass Spectrom.*, vol. 264, no. 2, pp. 122–145, 2007. [Online]. Available: https://www.sciencedirect.com/science/article/pii/S1387380607001649

[84] G. Bollen, H.-J. Kluge, T. Otto, G. Savard, and H. Stolzenberg, "Ramsey technique applied in a Penning trap mass spectrometer," *Nucl. Instrum. Meth. Phys. Res. Sect. B: Beam Interactions with Materials and Atoms*, vol. 70, no. 1, pp. 490–493, 1992. [Online]. Available: https://www.sciencedirect.com/science/article/pii/0168583X9295971S

[85] S. George, K. Blaum, F. Herfurth, A. Herlert, M. Kretzschmar, S. Nagy, S. Schwarz, L. Schweikhard, and C. Yazidjian, "The Ramsey method in high-precision mass spectrometry with Penning traps: Experimental results," *Int. J. Mass Spectrom.*, vol. 264, no. 2, pp. 110–121, 2007. [Online]. Available: https://www.sciencedirect.com/science/article/pii/S1387380607001662

[86] D. A. Nesterenko, T. Eronen, A. Kankainen, L. Canete, A. Jokinen, I. D. Moore, H. Penttilä, S. Rinta-Antila, A. de Roubin, and M. Vilen, "Phase-Imaging Ion-Cyclotron-Resonance technique at the JYFLTRAP double Penning trap mass spectrometer," *Eur. Phys. J. A.*, vol. 54, p. 154, 2018. [Online]. Available: https://doi.org/10.1140/epja/i2018-12589-y

[87] DESIR, *https://www.ganil-spiral2.eu/scientists/ganil-spiral-2-facilities/experimental-areas/desir/*.

[88] F. Déchery, H. Savajols, M. Authier, A. Drouart, J. Nolen, D. Ackermann, A. Amthor, B. Bastin, A. Berryhill, D. Boutin, L. Caceres, M. Coffey, O. Delferrière, O. Dorvaux, B. Gall, K. Hauschild, A. Hue, B. Jacquot, N. Karkour, B. Laune, F. Le Blanc, N. Lecesne, A. Lopez-Martens, F. Lutton, S. Manikonda, R. Meinke, G. Olivier, J. Payet, J. Piot, O. Pochon, V. Prince, M. Souli, G. Stelzer, C. Stodel, M.-H. Stodel, B. Sulignano, E. Traykov, and D. Uriot, "The Super Separator Spectrometer S3 and the associated detection systems: SIRIUS LEB-REGLIS3," *Nucl. Inst. Meth. Phys. Res. Sect. B: Beam Interactions with Materials and Atoms*, vol. 376, pp. 125–130, 2016, proceedings of the XVIIth International Conference on Electromagnetic Isotope Separators and Related Topics (EMIS2015), Grand Rapids, MI, U.S.A., 11-15 May 2015. [Online]. Available: https://www.sciencedirect.com/science/article/pii/S0168583X1600166X

[89] P. Delahaye, M. Dubois, L. Maunoury, A. Annaluru, J. Angot, O. Bajeat, B. Blank, J. Cam, P. Chauveau, R. Frigot, S. Hormigos, B. Jacquot, P. Jardin, O. Kamalou, V. Kuchi, P. Lecomte, B. Osmond, B. Retailleau, A. Savalle, T. Stora, J. Thomas, V. Toivanen, E. Traykov, P. Ujic, and R. Vondrasek, "New exotic beams from the SPIRAL 1 upgrade," *Nucl. Instr. Meth. Phys. Res. Sect. B: Beam Interactions with Materials and Atoms*, vol. 463, pp. 339–344, 2020. [Online]. Available: https://www.sciencedirect.com/science/article/pii/S0168583X19302472

[90] T. Kurtukian-Nieto, R. Baartman, B. Blank, T. Chiron, C. Davids, F. Delalee, M. Duval, S. El Abbeir, A. Fournier, D. Lunney, F. Méot, L. Serani, M.-H. Stodel, F. Varenne, and H. Weick, "SPIRAL2/DESIR high resolution mass separator," *Nucl. Instr. Meth. Phys. Res. Sect. B: Beam Interactions with Materials and Atoms*, vol. 317, pp. 284–289, 2013, xVIth International Conference on ElectroMagnetic Isotope Separators and Techniques Related to their Applications, December 2–7, 2012 at Matsue, Japan. [Online]. Available: https://www.sciencedirect.com/science/article/pii/S0168583X13008860

[91] M. Gerbaux, P. Ascher, A. Husson, A. de Roubin, P. Alfaurt, M. Aouadi, B. Blank, L. Daudin, S. El Abbeir, M. Flayol, H. Guérin, S. Grévy, M. Hukkanen, B. Lachacinski, D. Lunney, S. Perard, and B. Thomas, "The General Purpose Ion Buncher: A radiofrequency quadrupole cooler-buncher for DESIR at SPIRAL2," *Nucl. Instr. Meth. Phys. Res. Sec. A: Accelerators, Spectrometers, Detectors and Associated Equipment*, vol. 1046, p. 167631, 2023. [Online]. Available: https://www.sciencedirect.com/science/article/pii/S0168900222009238

[92] O. Kaleja, B. Anđelić, O. Bezrodnova, K. Blaum, M. Block, S. Chenmarev, P. Chhetri, C. Droese, C. E. Düllmann, M. Eibach, S. Eliseev, J. Even, P. Filianin, F. Giacoppo, S. Götz, Y. Gusev, M. J. Gutiérrez, F. P. Heßberger, N. Kalantar-Nayestanaki, J. J. W. van de Laar, M. Laatiaoui, S. Lohse, N. Martynova, E. Minaya Ramirez, A. K. Mistry, T. Murböck, Y. Novikov, S. Raeder, D. Rodríguez, F. Schneider, L. Schweikhard, P. G. Thirolf, and A. Yakushev, "Direct high-precision mass spectrometry of superheavy elements with SHIPTRAP," *Phys. Rev. C*, vol. 106, p. 054325, Nov 2022. [Online]. Available: https://link.aps.org/doi/10.1103/PhysRevC.106.054325

[93] P. Schury, T. Niwase, M. Wada, P. Brionnet, S. Chen, T. Hashimoto, H. Haba, Y. Hirayama, D. S. Hou, S. Iimura, H. Ishiyama, S. Ishizawa, Y. Ito, D. Kaji, S. Kimura, H. Koura, J. J. Liu, H. Miyatake, J.-Y. Moon, K. Morimoto, K. Morita, D. Nagae, M. Rosenbusch, A. Takamine, Y. X. Watanabe, H. Wollnik, W. Xian, and S. X. Yan, "First high-precision direct determination of the atomic mass of a superheavy nuclide," *Phys. Rev. C*, vol. 104, p. L021304, Aug 2021. [Online]. Available: https://link.aps.org/doi/10.1103/PhysRevC.104.L021304

[94] L. Daudin, P. Alfaurt, A. Balana, M. Corne, M. Flayol, A. Husson, and B. Lachacinski, "CENBG Control System and Specific Instrumentation Developments for SPIRAL2-DESIR Setups," in *Proc. ICALEPCS'21*, ser. International Conference on Accelerator and Large Experimental Physics Control Systems, no. 18. JACoW Publishing, Geneva, Switzerland, 2022, pp. 98–103. [Online]. Available: https://jacow.org/icalepcs2021/papers/mopv002.pdf

[95] I. D. Moore, P. Dendooven, and J. Ärje, "The IGISOL technique—three decades of developments," *Hyperfine Interact.*, vol. 223, pp. 17–62, 2014, doi: https://doi.org/10.1007/s10751-013-0871-0.

[96] I. D. Moore, T. Eronen, D. Gorelov, J. Hakala, A. Jokinen, A. Kankainen, V. S. Kolhinen, J. Koponen, H. Penttilä, I. Pohjalainen, M. Reponen, J. Rissanen, A. Saastamoinen, S. Rinta-Antila, V. Sonnenschein, and J. Äystö, "Towards commissioning the new IGISOL-4 facility," *Nucl. Instr. Meth. Phys. Res. Sec. B: Beam Interactions with Materials and Atoms*, vol. 317, pp. 208–213, 2013, doi: https://doi.org/10.1016/j.nimb.2013.06.036.

[97] A. Al-Adili, M. Jansson, K.and Lantz, A. Solders, D. Gorelov, C. Gustavsson, A. Mattera, I. D. Moore, A. V. Prokofiev, V. Rakopoulos, H. Penttilä, D. Tarrío, S. Wiberg, M. Österlund, and S. Pomp, "Simulations of the fission-product stopping efficiency in IGISOL," *The Eur. Phys. J. A*, vol. 51, p. 59, 2015. [Online]. Available: https://doi.org/10.1140/epja/i2015-15059-2

[98] J. Äystö, "Development and applications of the IGISOL technique," *Nucl. Phys. A*, vol. 693, no. 1, pp. 477–494, 2001, radioactive Nuclear Beams. [Online]. Available: https://www.sciencedirect.com/science/article/pii/S037594740100923X

[99] I. Pohjalainen, I. D. Moore, T. Eronen, A. Jokinen, H. Penttilä, and S. Rinta-Antila, "Gas purification studies at IGISOL-4," *Hyperfine Interact.*, vol. 227, pp. 169–180, 2014. [Online]. Available: https://doi.org/10.1007/s10751-013-1006-3

[100] P. Karvonen, I. D. Moore, T. Sonoda, T. Kessler, H. Penttilä, K. Peräjärvi, P. Ronkanen, and J. Äystö, "A sextupole ion beam guide to improve the efficiency and beam quality at IGISOL," *Nucl. Instrum. Meth. Phys. Res. Sec. B: Beam Interactions with Materials and Atoms*, vol. 266, pp. 4794–4807, 2008, doi: https://doi.org/10.1016/j.nimb.2008.07.022.

[101] O. S. Kirsebom, M. Hukkanen, A. Kankainen, W. H. Trzaska, D. F. Strömberg, G. Martínez-Pinedo, K. Andersen, E. Bodewits, B. A. Brown, L. Canete, J. Cederkäll, T. Enqvist, T. Eronen, H. O. U. Fynbo, S. Geldhof, R. de Groote, D. G. Jenkins, A. Jokinen, P. Joshi, A. Khanam, J. Kostensalo, P. Kuusiniemi, K. Langanke, I. Moore, M. Munch, D. A. Nesterenko, J. D. Ovejas, H. Penttilä, I. Pohjalainen, M. Reponen,

S. Rinta-Antila, K. Riisager, A. de Roubin, P. Schotanus, P. C. Srivastava, J. Suhonen, J. A. Swartz, O. Tengblad, M. Vilen, S. Vínals, and J. Äystö, "Measurement of the $2^+ \rightarrow 0^+$ ground-state transition in the β decay of ^{20}F," *Phys. Rev. C*, vol. 100, p. 065805, 2019. [Online]. Available: https://link.aps.org/doi/10.1103/PhysRevC.100.065805

[102] A. Nieminen, J. Huikari, A. Jokinen, J. Äystö, P. Campbell, and E. Cochrane, "Beam cooler for low-energy radioactive ions," *Nucl. Instr. Meth. Phys. Res. Sec. A: Accelerators, Spectrometers, Detectors and Associated Equipment*, vol. 469, no. 2, pp. 244–253, 2001. [Online]. Available: https://www.sciencedirect.com/science/article/pii/S0168900200007506

[103] A. Giatzoglou, T. Poomaradee, I. Pohjalainen, S. Rinta-Antila, I. D. Moore, P. M. Walker, L. Marmugi, and F. Renzoni, "A facility for production and laser cooling of cesium isotopes and isomers," *Nucl. Instr. Meth. Phys. Res. Sec. A: Accelerators, Spectrometers, Detectors and Associated Equipment*, vol. 908, pp. 367–375, 2018. [Online]. Available: https://www.sciencedirect.com/science/article/pii/S0168900218310532

[104] T. Eronen, "High Precision Q_{EC} value measurements of superallowed 0^+ to 0^+ beta decays with JYFLTRAP," Ph.D. dissertation, University of Jyväskylä, 2008.

[105] L. Canete, "High Precision Mass Measurements for Nuclear Astrophysics," Ph.D. dissertation, University of Jyväskylä, 2019.

[106] R. T. Birge, "The Calculation of Errors by the Method of Least Squares," *Phys. Rev.*, vol. 40, pp. 207–227, 1932. [Online]. Available: https://link.aps.org/doi/10.1103/PhysRev.40.207

[107] G. Bollen, H.-J. Kluge, M. König, T. Otto, G. Savard, H. Stolzenberg, R. B. Moore, G. Rouleau, G. Audi, and I. Collaboration, "Resolution of nuclear ground and isomeric states by a Penning trap mass spectrometer," *Phys. Rev. C*, vol. 46, pp. R2140–R2143, 1992. [Online]. Available: https://link.aps.org/doi/10.1103/PhysRevC.46.R2140

[108] R. Knöbel, M. Diwisch, H. Geissel, Y. A. Litvinov, Z. Patyk, W. R. Plaß, C. Scheidenberger, B. Sun, H. Weick, F. Bosch, D. Boutin, L. Chen, C. Dimopoulou, A. Dolinskii, B. Franczak, B. Franzke, M. Hausmann, C. Kozhuharov, J. Kurcewicz, S. A. Litvinov, M. Matoš, M. Mazzocco, G. Münzenberg, S. Nakajima, C. Nociforo, F. Nolden, T. Ohtsubo, A. Ozawa, J. Stadlmann, M. Steck, T. Suzuki, P. M. Walker, M. Winkler, and T. Yamaguchi, "New results from isochronous mass measurements of neutron-rich uranium fission fragments with the FRS-ESR-facility at GSI," *The Eur. Phys. J. A*, vol. 52, no. 5, p. 138, 2016. [Online]. Available: https://doi.org/10.1140/epja/i2016-16138-6

[109] K.-L. Kratz and B. Pfeiffer, *Private communication (with AME).*

[110] G. Audi, A. Wapstra, and C. Thibault, "The AME2003 Atomic Mass Evaluation: (ii). tables, graphs and references," *Nucl. Phys. A*, vol. 729, no. 1, pp. 337–676, 2003, the 2003 NUBASE and Atomic Mass Evaluations. [Online]. Available: https://www.sciencedirect.com/science/article/pii/S0375947403018098

[111] V. Rakopoulos, M. Lantz, S. Pomp, A. Solders, A. Al-Adili, L. Canete, T. Eronen, A. Jokinen, A. Kankainen, A. Mattera, I. D. Moore, D. A. Nesterenko, M. Reponen, S. Rinta-Antila, A. de Roubin, M. Vilén, M. Österlund, and H. Penttilä, "Isomeric fission yield ratios for odd-mass Cd and In isotopes using the phase-imaging ion-cyclotron-resonance technique," *Phys. Rev. C*, vol. 99, p. 014617, 2019. [Online]. Available: https://link.aps.org/doi/10.1103/PhysRevC.99.014617

[112] V. Kolhinen, "Penning trap for isobaric purification of radioactive beams at IGISOL," Ph.D. dissertation, University of Jyväskylä, 2003.

[113] S. Lalkovski and F. Kondev, "Nuclear data sheets for A = 112," *Nucl. Data Sheets*, vol. 124, pp. 157–412, 2015. [Online]. Available: https://www.sciencedirect.com/science/article/pii/S0090375214007467

[114] A. Koning and D. Rochman, "Modern nuclear data evaluation with the TALYS code system," *Nucl. Data Sheets*, vol. 113, no. 12, pp. 2841–2934, 2012, special Issue on Nuclear Reaction Data. [Online]. Available: https://www.sciencedirect.com/science/article/pii/S0090375212000889

[115] S. Goriely, N. Chamel, and J. M. Pearson, "Skyrme-Hartree-Fock-Bogoliubov Nuclear Mass Formulas: Crossing the 0.6 MeV Accuracy Threshold with Microscopically Deduced Pairing," *Phys. Rev. Lett.*, vol. 102, p. 152503, 2009. [Online]. Available: https://link.aps.org/doi/10.1103/PhysRevLett.102.152503

[116] S. Goriely, S. Hilaire, M. Girod, and S. Péru, "The Gogny-Hartree-Fock-Bogoliubov nuclear-mass model," *The Eur. Phys. J. A*, vol. 52, p. 202, 2016. [Online]. Available: https://doi.org/10.1140/epja/i2016-16202-3

ORIGINAL PAPERS

PI

ODD-ODD NEUTRON-RICH RHODIUM ISOTOPES STUDIED WITH THE DOUBLE PENNING TRAP JYFLTRAP

by

M. Hukkanen,W. Ryssens, P. Ascher, M. Bender, T. Eronen, S. Grevy,
A. Kankainen, M. Stryjczyk, L. Al Ayoubi, S. Ayet, O. Beliuskina, C. Delafosse,
W. Gins, M. Gerbaux, A. Husson, A. Jokinen, D. A. Nesterenko, I. Pohjalainen,
M. Reponen, S. Rinta-Antila, A. de Roubin and A. P. Weaver 2023

Odd-odd neutron-rich rhodium isotopes studied with the double Penning trap JYFLTRAP

M. Hukkanen [1,2] W. Ryssens [3] P. Ascher [2] M. Bender [4] T. Eronen [1] S. Grévy,[2] A. Kankainen [1] M. Stryjczyk [1]
L. Al Ayoubi [1,5] S. Ayet [6] O. Beliuskina,[1] C. Delafosse [1,*] W. Gins,[1] M. Gerbaux [2] A. Husson [2] A. Jokinen [1]
D. A. Nesterenko [1] I. Pohjalainen [1] M. Reponen [1] S. Rinta-Antila [1] A. de Roubin [1,†] and A. P. Weaver [7,‡]

[1]*University of Jyvaskyla, Department of Physics, Accelerator laboratory, P.O. Box 35(YFL), FI-40014 University of Jyvaskyla, Finland*
[2]*Université de Bordeaux, CNRS/IN2P3, LP2I Bordeaux, UMR 5797, F-33170 Gradignan, France*
[3]*Institut d'Astronomie et d'Astrophysique, Université Libre de Bruxelles, Campus de la Plaine CP 226, 1050 Brussels, Belgium*
[4]*Université de Lyon, Université Claude Bernard Lyon 1, CNRS/IN2P3, IP2I Lyon, UMR 5822, F-69622 Villeurbanne, France*
[5]*Université Paris Saclay, CNRS/IN2P3, IJCLab, 91405 Orsay, France*
[6]*II. Physikalisches Institut, Justus Liebig Universitat Gießen, 35392 Gießen, Germany*
[7]*School of Computing, Engineering and Mathematics, University of Brighton, Brighton BN2 4GJ, United Kingdom*

Precision mass measurements of neutron-rich rhodium isotopes have been performed at the JYFLTRAP Penning trap mass spectrometer at the Ion Guide Isotope Separator On-Line (IGISOL) facility. We report results on ground- and isomeric-state masses in ^{110,112,114,116,118}Rh and the very first mass measurement of ^{120}Rh. The isomeric states were separated and measured for the first time using the phase-imaging ion-cyclotron-resonance (PI-ICR) technique. For ^{112}Rh, we also report new half-lives for both the ground state and the isomer. The results are compared to theoretical predictions using the BSkG1 mass model and discussed in terms of triaxial deformation.

I. INTRODUCTION

Neutron-rich rhodium isotopes (proton number $Z = 45$) are located in a region known for rapid and drastic changes in nuclear structure and coexisting strongly deformed and spherical shapes [1]. At $Z \approx 40$ and neutron number $N \approx 60$, the strongly deformed configuration becomes the ground state. The atomic mass can be used to probe the evolution of nuclear structure along isotopic chains: the sudden onset of prolate ground-state deformation has been observed as a kink in two-neutron separation energies in the isotopic chains from Rb ($Z = 37$) to Mo ($Z = 42$) [2–5]. The same shape change has been observed as a steep increase in the mean-square charge radii [6–11]. This is one of the most dramatic shape changes on the nuclear chart.

Above $Z \approx 42$, the shape transition becomes smoother but the situation remains complex. Coulomb excitation experiments of Ru and Pd isotopes with neutron numbers between $N = 60$ and 66 [12–14] indicate that these nuclei exhibit triaxial deformation. Their nuclear density in the intrinsic frame no longer has any rotational symmetry axis. In addition, the structure of neutron-rich Rh isotopes has been explored via prompt

γ-ray spectroscopy of fission fragments [15,16]. Comparison of the studied band structures with triaxial projected shell model (TPSM) calculations indicate a need for large, nearly constant, triaxial deformation in $^{116-119}$Rh [16]. Several theoretical models [5,17–19] predict an additional contribution to the binding energy of triaxial nuclei compared to axially symmetric configurations. Most theoretical approaches predict the largest energy gains due to triaxial deformation in the vicinity of ^{106}Ru [17,20–22].

The masses of neutron-rich odd-odd Rh isotopes have not been accurately known prior to this work due to the presence of low-lying long-living isomeric states [23]. The previous mass measurements [24,25] on these isotopes at the JYFLTRAP double Penning trap [26] could not resolve the isomeric states, with the exception of ^{108}Rh, because of the techniques used at the time.

The existence of two long-living states in neutron-rich odd-odd Rh isotopes has been well established via β-decay studies. The low-spin (1^+) states are strongly fed in the β decay of even-even ^{110,112,114}Ru nuclei [27,28] and have strong decay branches to the 0^+ states in the Pd isotopes [29–31], whereas the high-spin Rh isomers β decay dominantly to high-spin states in even $^{110-118}$Pd isotopes [29–34]. Because of the large spin difference, the internal transition is not favored and the excitation energies of these isomeric states have remained largely unknown [23]. Only in ^{104}Rh has the excitation energy of the isomeric 5^+ state (129 keV) been precisely established through γ-ray spectroscopy. In ^{106}Rh, a 6^+ state is proposed at 137(13) keV based on β-decay endpoint measurements [23,35] whereas a 5^+ state is proposed at 113.0(75) keV

---

in ^{108}Rh based on a time-of-flight ion-cyclotron-resonance (TOF-ICR) mass measurement performed at JYFLTRAP [25]. For heavier Rh isotopes, the energies of the long-lived isomeric states have not been measured. Finally, it should be noted that the order of the two long-living states is established only in ^{104}Rh and ^{106}Rh, via γ-ray spectroscopy (^{104}Rh) or β-decay endpoint energies (^{106}Rh). For all the other Rh isotopes discussed in this work, the ordering of the two long-lived states is not firmly confirmed.

In this work, we studied odd-odd $^{110-120}$Rh isotopes via high-precision Penning-trap mass spectrometry. With the novel phase-imaging ion-cyclotron-resonance (PI-ICR) technique at JYFLTRAP [36–38], we have resolved the ground and isomeric states in ^{110,112,114,116,118}Rh isotopes for the first time. The reported measurements yield more accurate ground-state mass values as well as first direct determinations of the isomeric-state excitation energies. In ^{120}Rh we report on the first ground-state mass measurement.

The measured masses provide essential data to improve future models of nuclear structure, particularly those that aim to describe nuclear masses. To benchmark existing models, we compare our experimental results to the recent global model BSkG1 [22]. This model is based on self-consistent Hartree-Fock-Bogoliubov (HFB) calculations using a Skyrme energy density functional (EDF) and aims at a global yet microscopic description of nuclear structure. Following the protocol developed for the earlier BSk-models (see Ref. [39] and references therein), the model parameters have been adjusted to essentially all binding energies tabulated in Atomic Mass Evaluation 2016 (AME16) [40], all known charge radii [41] and realistic infinite nuclear matter properties. The resulting model achieves a root-mean-square deviation of 741 keV for the 2457 known masses of nuclei with $Z \geqslant 8$ included in Atomic Mass Evaluation 2020 (AME20) [42].

II. EXPERIMENTAL METHODS

Precision mass measurements of neutron-rich rhodium nuclei were performed at the Ion Guide Isotope Separator On-Line (IGISOL) facility [43] utilizing the JYFLTRAP double Penning trap [26]. The measured isotopes were produced in proton-induced fission, with 25-MeV protons from the K130 cyclotron impinging on a thin (15 mg/cm^2) natural uranium target. The proton beam intensity was varied in the range 1–10 μA depending on the studied case. The fission fragments were stopped in helium gas at about 300 mbar and extracted using a sextupole ion guide (SPIG) [44]. The secondary beam was accelerated to 30q kV and mass separated based on the mass-to-charge m/q ratio with a 55° dipole magnet, which has a mass resolving power of $m/\Delta m \approx 500$. The mass-separated beam was then transported to the buffer-gas filled radio-frequency quadrupole (RFQ) cooler-buncher [45]. To control the number of ions injected into the RFQ cooler-buncher, an electrode after the dipole magnet was connected to a fast switch to serve as a beam gate.

The cooled ion bunches from the RFQ were directed to the JYFLTRAP double Penning trap mass spectrometer [26], which consists of two cylindrical Penning traps housed inside a 7 T superconducting magnet. First, the ion bunch was injected into the purification trap where the ion sample was cooled, centered and cleaned utilizing the mass-selective buffer gas cooling technique [46]. Typically, a mass resolving power of $m/\Delta m \approx 10^5$ is reached, which in most cases allowed removal of the isobaric contamination. The cleaned ion sample was transferred to the precision trap, where the mass determination of an ion was performed through the measurement of its cyclotron frequency ν_c:

$$\nu_c = \frac{1}{2\pi}\frac{q}{m}B, \qquad (1)$$

where q/m is the charge-to-mass ratio of the ion and B is the magnetic field strength. To determine the magnetic field strength with enough precision, the cyclotron frequency of a reference ion with a well-known mass is measured. These references are measured alternatively with the ion of interest, in order to reduce the effect of the drift of the magnetic field. Utilizing the cyclotron frequency ratio $R = \nu_{c,\text{ref}}/\nu_c$, determined with singly charged ions, the atomic mass of the nuclide of interest m is then deduced as

$$m = R(m_{\text{ref}} - m_e) + m_e, \qquad (2)$$

where m_e is the mass of an electron and m_{ref} is the atomic mass of the reference nuclide. In our experiment, $^{133+}$Cs ions from the IGISOL offline ion source station [47] were used for most of the measurements. For $^{1122+}$Rh ions, $^{85+}$Rb ions from the offline ion source station were used as a reference.

When one of the states, ground or isomeric state, was measured against a well-known reference, it was later used as a reference for the other state, i.e., the ground state was measured against the isomeric state or vice versa. The reference for each measurement has been tabulated in Table I. The energy difference between the ground and the low-lying isomeric states, i.e., the excitation energy of the isomer E_x, was calculated utilizing the frequency ratio R determined when these two states were measured against each other:

$$E_x = (R - 1)[m_{\text{ref}} - m_e]c^2. \qquad (3)$$

In the precision trap, the measurement of the ion cyclotron frequency was performed utilizing either the time-of-flight ion-cyclotron-resonance technique (TOF-ICR) [48,49] or the phase-imaging ion-cyclotron-resonance technique (PI-ICR) [36–38]. In the TOF-ICR technique an ion's radial energy is increased by a quadrupolar excitation and converted to axial energy when the ions travel through the magnetic field gradient after extraction from the precision trap. For the resonant ions this results in a shorter time of flight measured with a microchannel plate (MCP) detector. From the time-of-flight resonance the cyclotron frequency of the ion is then determined [49]. To increase the precision, a technique called Ramsey method of time-separated oscillatory fields [50,51] can be applied: a measurement scheme where the quadrupolar excitation is performed by two short pulses separated by a waiting time. The Ramsey technique with a pattern of 10-30-10 ms (on-off-on) was used for the most exotic isotope measured in this work, namely ^{120}Rh (see Fig. 1). The PI-ICR technique was utilized for all the other cases.
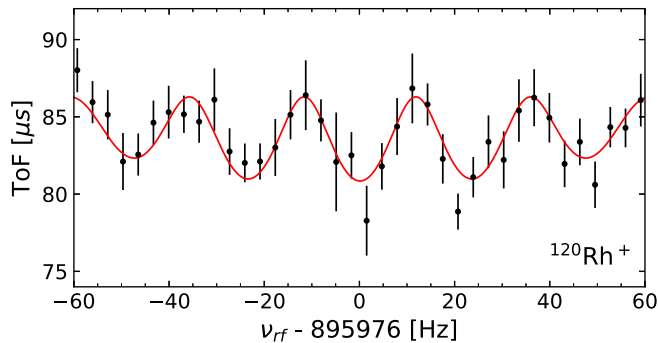
FIG. 1. TOF-ICR resonance using a 10-30-10 ms (on-off-on) Ramsey excitation pattern for ^{120}Rh$^+$. The mean data points are shown in black, the fit of the theoretical curve [50] in red.

In the PI-ICR technique, the determination of the ion's cyclotron frequency is based on a measurement of the propagation of the ion's radial motions, magnetron motion ν_- and modified cyclotron motion ν_+, projected onto a position sensitive MCP detector (2D MCP). For this purpose, first a dipole pulse at the ion's modified cyclotron frequency is applied. The excitation scheme depends on which ion motion propagation is being measured. In the cyclotron phase ϕ_+ measurement, the ion is let to accumulate phase for a time t_{acc} on the modified cyclotron motion which is then converted with a π pulse to magnetron motion. In the magnetron phase ϕ_- measurement, the modified cyclotron motion is first converted with a π pulse to magnetron motion, which is then accumulated for a time t_{acc} before extraction. The measurement pattern utilized at JYLFTRAP is described in more detail in Refs. [37,38] and the PI-ICR measurement technique in general in Ref. [36]. As an example the measurement of the cyclotron phase spot for ^{118}Rh$^+$ is shown in Fig. 2, where the separation of the ground state from the isomeric state is seen with a phase accumulation time of 170 ms.

The measured phase difference of the ion's propagated radial motions $\phi_c = \phi_+ - \phi_-$ is related to the ion cyclotron frequency:

$$\nu_c = \nu_- + \nu_+ = \frac{\phi_c + 2\pi n}{2\pi t_{acc}}, \qquad (4)$$

where n is the number of the full ion revolutions in the precision trap. The accumulation time t_{acc} is selected to be a compromise where the half-life of the ion of interest, phase spot separation of different ion species, vacuum conditions, and the stability of the electric field of the precision trap are considered. The phase accumulation times were 700 ms for the ^{110}Rh$^+$ measurements, 1 s for ^{112}Rh$^+$, 300 ms for ^{112}Rh^{2+}, 450 ms for ^{114}Rh$^+$ and ^{116}Rh$^+$, and 170 ms for ^{118}Rh$^+$. For ^{116}Rh$^+$, ^{100}Y^{16}O$^+$ ions were observed in the precision trap. Therefore an additional cleaning step using the Ramsey cleaning method [52] was applied before the phase accumulation. To unambiguously determine n in Eq. (4), the cyclotron frequency was determined with the TOF-ICR technique and at least two phase accumulation times were applied before the actual mass measurements.
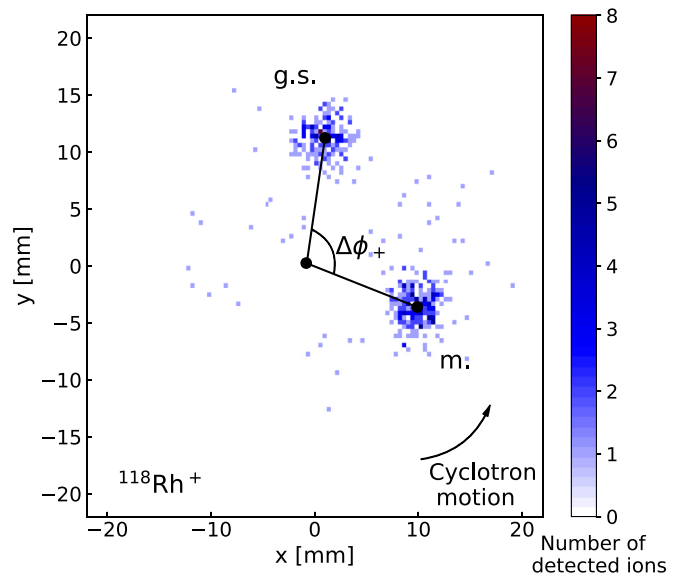

FIG. 2. Ion projection of the cyclotron phase spot of ^{118}Rh$^+$ on the 2D MCP detector. The ^{118}Rh ground state (g.s.) versus the isomeric state (m.) are separated with a 170 ms accumulation time. The phase difference $\Delta\phi_+$ corresponds to an excitation energy of 189(6) keV.

A count-rate class analysis [38,53] to account for the ion-ion interactions was performed when statistically feasible. Temporal magnetic field fluctuations of $\delta B/B = 2.01(25) \times 10^{-12}$ min$^{-1} \times \delta t$ [38], where δt is the time between the measurements, were taken into account in the analysis. For measurements, where ^{133}Cs$^+$ or ^{85}Rb$^+$ ions were used as a reference, a mass-dependent shift of $\delta_m r/r = -2.35(81) \times 10^{-10}$/u $\times (m_{ref} - m)$ [38] and a residual systematic uncertainty of $\delta_{res} r/r = 9 \times 10^{-9}$ [38] were added quadratically to the final frequency ratio uncertainty. For the mass doublets (i.e., ground state vs isomer), the mass-dependent and the residual systematic uncertainties are negligible. Systematic uncertainties of the magnetron phase advancement and systematic angle error [38] were also taken into account.

In addition to mass measurements, the mass-selective buffer gas cooling technique [46] was used to select ^{112}Rh$^+$ and ^{112}Rh^{2+} ions for post-trap spectroscopy in order to identify the states and determine their half-lives. After injection to the purification trap, the ions at $A = 112$ were let to cool for roughly 60 ms, followed by a 10 ms dipolar excitation at the magnetron frequency. During this time, a fraction of the ^{112}Ru$^+$ ions [$J^\pi = 0^+$, $T_{1/2} = 1.75(7)$ s] beta decay to ^{112}Rh^{2+}, feeding only the low-spin (1$^+$) state in ^{112}Rh, whereas fission dominantly produces ^{112}Rh in the high-spin state. The ions of interest were selected using a 120 ms quadrupolar excitation either at the ^{112}Rh$^+$ (from fission) or ^{112}Rh^{2+} (from in-trap decay) cyclotron frequency, extracted out of the trap, and implanted every 194 ms on a thin aluminum foil in front of a silicon detector after the Penning trap. The signals were read and time-stamped with the Nutaq data acquisition system with a 105 MHz clock.

TABLE I. Frequency ratios (R), mass excess values [ME $= (m - Au)c^2$], and isomer excitation energies (E_x) measured in this work. The masses of ^{133}Cs and ^{85}Rb reference ions were taken from the AME20 [54], whereas the masses determined in this work were used for the Rh reference ions (Ref.). The spin-parities I^π and half-lives $T_{1/2}$ were taken from NUBASE20 [23], except for ^{112}Rh, for which the half-lives are from this work. For comparison, the mass-excess values $ME_{lit.}$ from AME20 [54] and excitation energies $E_{x,lit.}$ from NUBASE20 [23] are also provided, where # marks an extrapolated value.

Nuclide	I^π	$T_{1/2}$	Ref.	$R = \nu_{c,ref}/\nu_c$	ME (keV)	$ME_{lit.}$ (keV)	E_x (keV)	$E_{x,lit.}$ (keV)
^{110}Rh	(1^+)	3.35(12) s	^{110}Rh^m	0.999 999 629(15)	$-82\,702.4(23)$	$-82\,829(18)$		
^{110}Rh^m	(6^+)	28.5(13) s	^{133}Cs	0.826 987 604(15)	$-82\,664.3(18)$	$-82\,610(150)$#	38.0(15)	220(150)#
^{112}Rh	(1^+)	2.22(13) s^a	^{85}Rb	0.659 002 526(11)^b	$-79\,603.7(17)$	$-79\,730(40)$		
^{112}Rh^m	(6^+)	6.96(8) s^a	^{133}Cs	0.842 060 991(16)	$-79\,565.2(19)$		38.5(26)	
			^{112}Rh	1.000 000 368(27)	$-79\,565.4(33)$		38.3(28)	
			Weighted mean		$-79\,565.2(17)$	$-79\,390(60)$	38.4(19)	340(70)
^{114}Rh	1^+	1.85(5) s	^{133}Cs	0.857 140 868(21)	$-75\,662.7(26)$	$-75\,710(70)$		
^{114}Rh^m	(7^-)	1.85(5) s	^{114}Rh	1.000 001 045(30)	$-75\,551.8(41)$	$-75\,510(170)$#	110.9(32)	200(150)#
^{116}Rh	1^+	685(39) ms	^{133}Cs	0.872 229 073(17)	$-70\,729(2)$	$-70\,740(70)$		
^{116}Rh^m	(6^-)	570(50) ms	^{116}Rh	1.000 001 119(18)	$-70\,608.3(28)$	$-70\,540(170)$#	120.8(19)	200(150)#
^{118}Rh	1^+#	282(9) ms	^{133}Cs	0.887 323 752(40)	$-64\,994(5)$	$-64\,887(24)$		
^{118}Rh^m	6^-#	310(30) ms	^{118}Rh	1.000 001 720(55)	$-64\,804.9(78)$	$-64\,690(150)$#	189(6)	200(150)#
^{120}Rh	8^-#	129.6(42) ms	^{133}Cs	0.902 423 642(470)	$-58\,614(58)$	$-58\,620(200)$#		

^{a}Half-life determined in this work; see Sec. III B 2.
^{b}Measured with doubly charged ^{112}Rh^{2+} ions.

III. RESULTS

In total, we report six ground-state and five isomeric-state masses, which are summarized in Table I. The mass of ^{120}Rh and the isomeric states in ^{110,114,116,118}Rh were measured for the first time. We have also determined the excitation energies of the isomers for the first time and show that the previously determined excitation energy of ^{112}Rh isomer deviates significantly from our result (see Table I and Fig. 3). Comparison to the previous JYFLTRAP mass measurement by Hager *et al.* [25] and to the AME20 [54] values is given in Fig. 4. Taking into account the ground- and isomeric-state yields, our results show a reasonable agreement with the values reported by Hager *et al.* [25], where the measured masses were unresolved mixtures of the ground and isomeric states. Below, we report the results and compare to the literature for each of the isotopes separately.

A. ^{110}Rh

For ^{110}Rh ($N = 65$), the measured mass excess of the ground state is $-82702.4(23)$ keV and $-82664.3(18)$ keV for the isomer. The excitation energy of the isomer, $E_x = 38.0(15)$ keV, was directly extracted from the measured ground-state-to-isomer frequency ratio. The ground-state mass value determined in this work is 126(18) keV larger than the AME20 value, which is based on β-decay endpoint energies from Jokinen *et al.* [27] and a private communication [55] (see Fig. 4). However, our ground- and isomeric-state results are consistent with the earlier JYFLTRAP measurements done for a mixture of ground and isomeric states using the buffer-gas cooling technique in the first trap, $-82640(70)$ keV [24], and with the TOF-ICR technique in the second trap, $-82674(8)$ keV [25]. Here we provide the first direct mass measurements of the ground and isomeric state of ^{110}Rh.

B. ^{112}Rh

1. Mass measurements

The fission yield of ^{112}Rh ($N = 67$) is largely dominated by the high-spin state, and as explained in Sec. II the low-spin
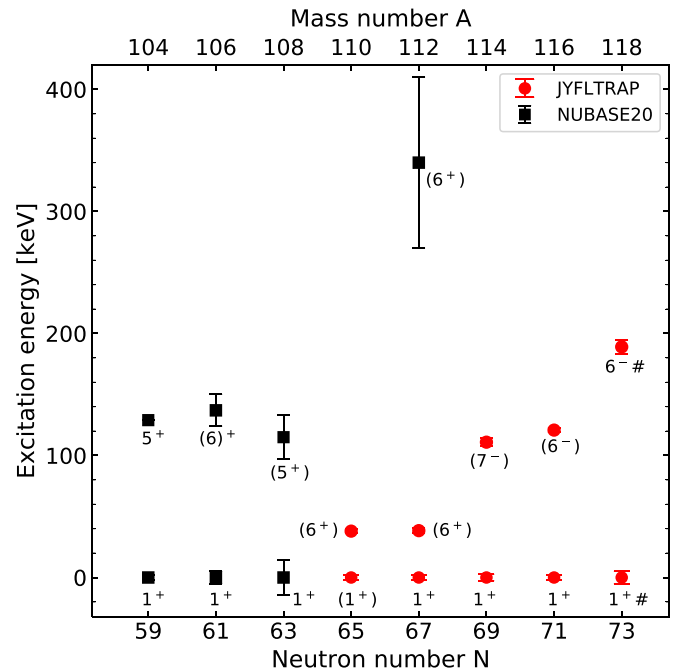

FIG. 3. Systematics of the ground and isomeric states in $^{104-118}$Rh isotopes. The literature values from NUBASE20 [23] are shown in black, while the energies measured in this work at JYFLTRAP are shown in red. The spin-parities are adopted from NUBASE20 [23]. For ^{112}Rh, we confirm the order of the states and show that it was previously significantly overestimated.
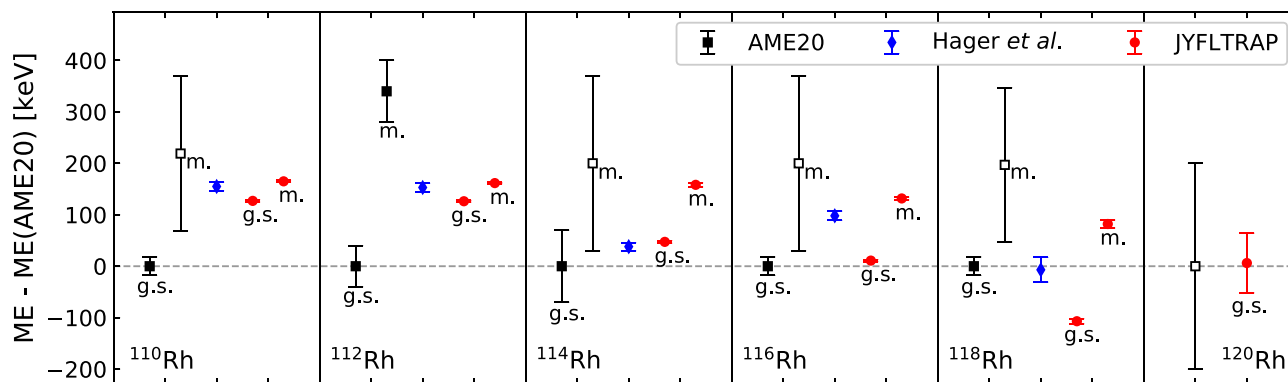
FIG. 4. The mass-excess values (ME) for the Rh isotopes measured in this work at JYFLTRAP (red circles) compared to AME20 [54] and NUBASE20 [23] (black squares) and the earlier JYFLTRAP results obtained with the TOF-ICR technique by Hager *et al.* (blue diamonds) [25]. Prior to this work, only the mass of the ^{112}Rh isomer had been experimentally determined, whereas the rest of the isomeric states were based on extrapolations (shown with open black squares) [23].

state of ^{112}Rh can be exclusively produced by the in-trap decay of the even-even ^{112}Ru. The latter method was therefore used to determine the mass excess of the low-spin state of ^{112}Rh in this work. The resulting mass excess of $-79\,603.7(17)$ keV is 27(9) keV lower than reported for a mixture of the isomeric and ground states in Ref. [25]. We note that our result is 127(44) keV higher than the AME20 value, $-79\,730(40)$ keV [54], in which the previous JYFLTRAP measurements contributed by 16% [24] and 19% [25], whereas a β-decay study based on private communication had a 66% contribution [55].

For the high-spin state produced directly by fission, the final value for the mass excess, $-79\,565.2(17)$ keV, was taken as the weighted mean of the PI-ICR measurements performed with a 1 s accumulation time against (i) the ^{112}Rh ground state [$-79\,565.4(33)$ keV] and (ii) ^{133}Cs [$-79\,565.2(19)$ keV]. In the measurement (i) the reference (ground state) statistics were rather low, thus the measurement was repeated with ^{133}Cs as a reference. Thus, the ^{112}Rh mass measurements now allow us to determine unambiguously that the low-spin state is the ground state of ^{112}Rh whereas the high-spin state is the isomer. The excitation energy of the isomer was determined from the difference between the mass-excess values of the isomer and the ground state, $E_x = 38.5(26)$ keV, as well as directly from the isomer against the ground state measurement, $E_x = 38.3(28)$ keV. The weighted mean, $E_x = 38.4(19)$ keV, was adopted as the final value. The excitation energy is significantly (more than 4σ) lower than the NUBASE20 [23] value, $E_x = 340(70)$ keV, which is based on an unpublished β-decay study [55].

2. Half-life measurements

In order to further confirm the order of the low- and high-spin states, β-decay half-lives of the ground and isomeric states of ^{112}Rh have been determined using a silicon detector located after the JYFLTRAP Penning trap. The first measurement, performed with an isomerically mixed beam of ^{112}Rh$^+$ produced directly in fission [see Fig. 5(a)], was performed with a cycle of 2 s of waiting period, followed by 38.8 s of implantation and 80 s of decay. The second measurement

was performed with the pure beam of the low-spin ^{112}Rh^{2+} ground-state ions produced by in-trap decay of ^{112}Ru$^+$ [see Fig. 5(b)]. In this case, the cycle consisted of 2 s of waiting time, 14.6 s of implantation, and 25 s of decay.

The data were fitted using the Markov chain Monte Carlo (MCMC) method. Depending on the dataset, the fitting models consisted of exponential functions, two for the isomerically mixed ^{112}Rh$^+$ and one for ^{112}Rh^{2+}, as well as a constant background. The choice of this model is justified as the half-life of the daughter isotope ^{112}Pd ($T_{1/2} \approx 21$ h [56]) is much longer than the ^{112}Rh half-lives. Both datasets were fitted simultaneously, with the ^{112}Rh ground-state half-life being a parameter shared by both models.

The extracted half-lives are 2.22(13) s for the ground state and 6.96(8) s for the isomer. The latter is in good agreement with 6.73(15) s from Ref. [30] and 6.8(2) s from Ref. [29]. The ground-state half-life is more than 10σ away from the value reported in the ENSDF evaluation [$T_{1/2} = 3.6(3)$ s [56]]; however, it agrees with the result reported in Ref. [27] [$T_{1/2} = 2.1(3)$ s]. It should be noted that the ENSDF value relies on Refs. [29,30]. In all three publications, the beam had a significant ^{112}Ru contamination which decays to the low-spin ground state of ^{112}Rh. However, only in the work by Jokinen *et al.* [27] was this effect taken into account.

Around 14(2)% of the ^{112}Rh nuclei were in their ground state based on the PI-ICR measurement. This value was measured with 1 s accumulation time, and only statistical uncertainty has been accounted for. The same ratio extracted from the half-life fits, 1 s after the implantation has been stopped, is equal to 16(2)%. The two results are in excellent agreement. The combination of independent mass measurements of the two states, together with the half-life measurements, allow us to unambiguously assign the 1^+ state as the ground state of ^{112}Rh, and the high-spin (6^+) state as the isomer.

C. ^{114}Rh

The measured ground-state mass excess of ^{114}Rh ($N = 69$), $-75\,662.7(26)$ keV, is in agreement with the AME20 [54] value based on Hager *et al.* (59%) [25] and Kolhinen
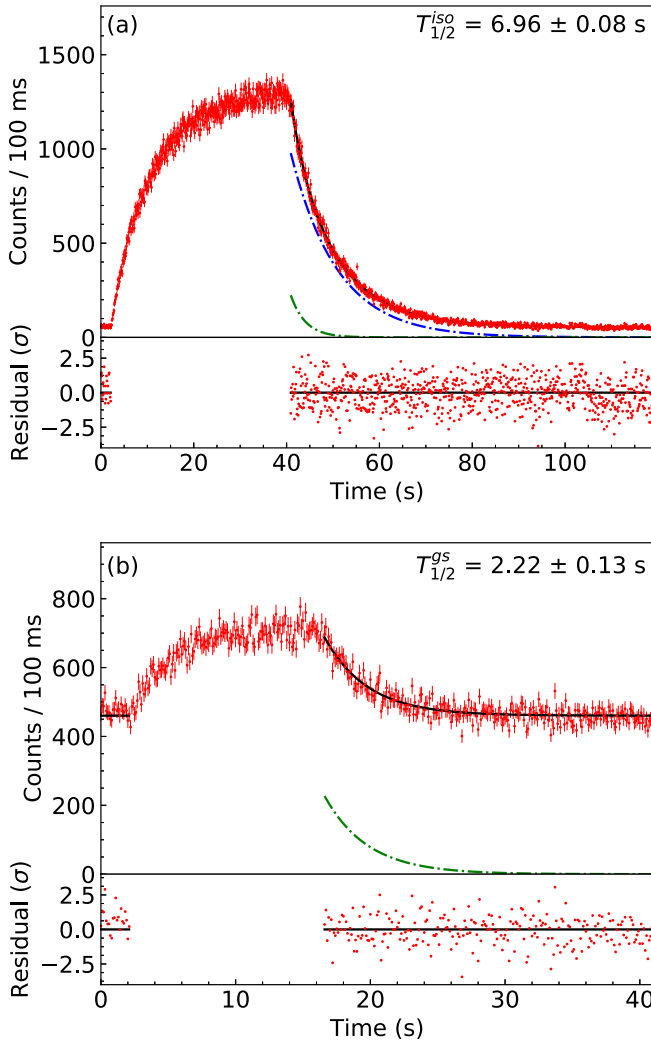
FIG. 5. Decay curves of ^{112}Rh for the Penning-trap purified samples of (a) ^{112}Rh$^+$ directly produced in fission and (b) ^{112}Rh^{2+} produced via in-trap decay of ^{112}Ru$^+$. The green and blue dashdotted lines indicate the contribution of the ground state [$T_{1/2} = 2.22(13)$ s] and the isomer [$T_{1/2} = 6.96(8)$ s] decays, respectively. The lower panels show the residuals of the fit.

et al. (41%) [24]. The mass excess of the isomer ^{114}Rh^m, $-75\,551.8(41)$ keV, was measured for the first time. The excitation energy of ^{114}Rh^m, $E_x = 110.9(31)$ keV, was directly obtained from the measurement against the ground state and determined for the first time. Contrary to the other Rh isotopes studied in this work, the fission yield was dominated by the ground state. The ground state is presumably 1^+ and the isomer (7^-) [23,57]; however, the order of the low- and high-spin states has not yet been confirmed experimentally. Such an inversion in the observed isomeric fission yield ratio could be an indication of an inversion between the low-and high-spin states. Another explanation could be that the half-life for the high-spin state is much shorter than reported in literature, where the states have identical half-lives [23].

D. ^{116}Rh

The measured mass-excess value for the ground state of ^{116}Rh ($N = 71$), $-70\,729(2)$ keV, agrees well with the AME20 [54] value, $-70\,740(70)$ keV, but is 35 times more precise. The AME20 value is based 63% on the JYFLTRAP measurement by Hager *et al.* [25] and 37% on an average between the earlier JYFLTRAP measurement [24] and the storage-ring experiment using isochronous mass spectrometry (IMS) at GSI [58].

The mass of ^{116}Rh^m, $-70\,608.3(28)$ keV, has been determined for the first time in this work. Its excitation energy, $E_x = 120.8(19)$ keV, was directly obtained from the measurement against the ground state. The isomer has been assumed to have spin-parity (6^-) based on the β-decay feeding to a (6^+) state in the daughter nucleus and no feeding to levels with $J \leqslant 4$ [23,59].

E. ^{118}Rh

The measured mass-excess value for the ground state of ^{118}Rh ($N = 73$), $-64\,994(5)$ keV, is 107(25) keV lower than the AME20 value [54] based mainly on the previous study at JYFLTRAP [25], where a mass excess of $-64\,894(24)$ keV was determined for a mixture of the ground and isomeric states. In addition, ^{118}Rh has been measured via IMS at GSI, $-64\,830(270)$ keV [60].

The isomeric state ^{118}Rh^m was resolved from the ground state and measured for the first time (see Fig. 2). Its mass excess is $-64\,804.9(78)$ keV and the excitation energy, directly determined from the measurement against the ground state, is $E_x = 189(6)$ keV. There is no experimental information on the spin-parities of the ground and isomeric states but they are assumed to be 1^+ and 6^- based on systematics [23].

F. ^{120}Rh

The mass of ^{120}Rh ($N = 75$) was measured experimentally for the first time (see Fig. 1). The mass-excess value, $-58\,614(58)$ keV, is very close to the extrapolated value in AME20, $-58\,620(200)\#$ keV [54]. Whereas the ground state has a half-life of around 130 ms [23,61–63], the known isomeric state in ^{120}Rh is too short-lived ($T_{1/2} = 295(16)$ ns [64]) for a Penning-trap measurement. The spin-parities of the ground and isomeric states of ^{120}Rh are unknown.

IV. DISCUSSION

We start by introducing mean-field modeling of nuclear masses and the BSkG1 model in Sec. IV A. The experimental mass values obtained in this work are compared to the predictions from the BSkG1 model in Sec. IV B, whereas two-neutron separation energies, as well as other mass differences, are discussed in Sec. IV C. The quadrupole deformation, its evolution, and their role in the region are further discussed in Sec. IV D and the case of ^{112}Rh in Sec. IV E.

A. Mean-field modeling of nuclear masses

The BSkG1 model is based on self-consistent HFB calculations using a Skyrme EDF [22]. In such approaches one

searches for the nuclear configuration that minimizes the total energy in a large variational space, which generally includes symmetry-broken Bogoliubov states that correspond to nuclei that are not spherically symmetric. In this way, the shape of the nucleus in its ground state arises naturally as a prediction of the model. It is usually characterized in terms of the multipole moments $Q_{\ell m}$ of the nuclear density, which we define in Sec. IV D, and whose relative importance generally quickly decreases with increasing ℓ [22]. Not all possible multipole moments are explored by all nuclei, since many of them take shapes that are symmetric in some way. This fact is often exploited by practical implementations that enforce commonly found symmetries to reduce the computational cost. For example, the triaxial shapes we study here combine nonzero values for both quadrupole moments Q_{20} and Q_{22} but are only encountered in specific regions of the nuclear chart [22]. By assuming axial symmetry, i.e., by considering only shapes with one rotational symmetry axis, a significant amount of computational effort can be saved at the cost of possibly missing some physics.

An EDF-based model is characterized by a sizable number of parameters, which need to be fitted to experimental data using one of many different possible strategies. The standard procedure constructs the objective function for this parameter adjustment from the masses and charge radii of a few, usually spherically symmetric, even-even nuclei, nuclear matter properties, and some spectroscopic information. With only a few exceptions, the parametrizations constructed this way are nevertheless applicable to the modeling of all nuclei, independent of their shape. Some of these parametrizations have been widely used for local studies of nuclear structure in small regions all over the nuclear chart; examples that studied the appearance of triaxial shapes in the mass region of interest here are Refs. [5,17–19]. There also exist more global mass-table calculations with such parametrizations, but in the majority of cases these are limited to even-even nuclei with axial shapes [65,66], with some of them also including nonaxial shapes [67,68]. Large-scale calculations of this kind including odd- and odd-odd nuclei are even more sparse, an exception being Ref. [69]; however, these calculations are restricted to axial shapes only.[1]

Despite their usefulness for the study of differential quantities in small regions of the nuclear chart, such "standard" models usually do not describe *absolute binding energies* well: their objective function includes but a handful of nuclei, resulting in root-mean-square (rms) deviations with respect to the entirety of known masses that can reach 10 MeV [22] and are generally not smaller than 1 MeV. This former strategy has to be contrasted with that adopted by what we refer as *global models*: their adjustment includes, among other things, the binding energies and charge radii of almost *all* nuclei for which data are available, be they even-even, odd, or odd-odd. Including this large amount of data in the fit typically results in rms deviation on all masses that lie between 600–800 keV [39]. The lowest rms deviations, for microscopic

---

[1]The update of the database also considers nonaxial shapes for even-even nuclei.

TABLE II. Mass excesses of the odd-odd Rh isotopes measured in this work (JYFLTRAP) and those obtained with the BSkG1 model [22] and differences (Diff.) between both, all expressed in keV. To illustrate the impact of nonaxial shapes, results from calculations restricted to axial symmetry BSkG1$_{ax}$ and their difference from experiment (Diff.$_{ax}$) are also given. We remind the reader that BSkG1 describes essentially all known masses in AME20 with an rms error of 741 keV.

| Nucleus | N | Mass excess (keV) | | | | |
		JYFLTRAP	BSkG1	Diff.	BSkG1$_{ax}$	Diff.$_{ax}$
^{110}Rh	65	−82 702.4(23)	−83 408	−706	−81 545	+1157
^{112}Rh	67	−79 603.7(17)	−80 263	−660	−78 386	+1218
^{114}Rh	69	−75 662.7(26)	−76 401	−739	−74 538	+1125
^{116}Rh	71	−70 729(2)	−71 538	−809	−70 168	+561
^{118}Rh	73	−64 994(5)	−65 776	−783	−65 090	−96
^{120}Rh	75	−58 613.8(58)	−59 412	−799	−59 373	−763

and microscopic-macroscopic models alike, are generally not lower than 500 keV [21,70].

However, including more than a handful of nuclei requires allowing for nuclear deformation during the parameter adjustment, which is computationally costly. Most global models, EDF-based or not, were adjusted for this reason with the assumption of axial symmetry. The first global model to overcome this limitation is the 2012 version of the semimicroscopic finite-range droplet model [21]. The authors of Ref. [20] achieved a first global EDF fit that allowed for triaxial shapes, although some of the model ingredients for odd- and odd-odd nuclei were interpolated from adjacent even-even nuclei.

Profiting from recent numerical and algorithmic developments, BSkG1 is the first global model based on a Skyrme EDF that allowed for all nuclei to take nonaxial shapes during the parameter adjustment. This was achieved with the MOCCa code [71], a tool that represents the single-particle wave functions on a three-dimensional coordinate-space mesh. It offers both an easily controlled numerical accuracy [72] and also advanced algorithms to achieve a rapid and stable solution of the self-consistent Skyrme-HFB equations [73].

The calculations we report on here were performed using the same tool, in identical numerical conditions as in Ref. [22]. We repeat here only the main features of our treatment of nuclei with an odd neutron number, an odd proton number, or both: for each nucleus we performed multiple self-consistent blocking calculations using the equal-filling approximation [74]. Among such a set of calculations, we selected the ground state as the one with lowest energy after convergence.

B. Comparison of mass values to the BSkG1 model

The measured mass excesses, the BSkG1 values [22] and the differences between both are shown for the Rh isotopes in Table II. The model overbinds all isotopes with a remarkably constant energy difference on the order of 700 keV. This value is close to the overall rms deviation BSkG1 achieves on all nuclear masses, indicating that the Rh isotopes are, on average,

neither better nor worse described than other isotopic chains. The difference between theory and experiment is nevertheless several orders of magnitude larger than the experimental uncertainty, but this reflects the current state of the art of global mass models such as BSkG1.

To illustrate the additional energy gain due to triaxiality, Table II also lists the mass excesses obtained when restricting the calculations to axial shapes (BSkG1$_{ax}$), as well as its difference (Diff.$_{ax}$) from experiment. The full calculation leads to binding energies that are larger than those obtained from an axial calculation, as expected from the variational principle. With the exception of ^{120}Rh, the energy gain due to triaxiality is large, up to 1.9 MeV for ^{112}Rh, and depends on N. Subtracting this energy gain results in calculated mass excesses that increase faster with neutron number than the measured ones, as is reflected also in the mass differences we discuss below.

Calculations spanning the nuclear chart that account for triaxiality are scarce, but all of them predict triaxial deformations in the vicinity of ^{106}Ru [20–22,67,68,75]. The strength of the effect, as evaluated by the theoretical energy gain due to triaxial deformation, is strongly model dependent. The microscopic-macroscopic model of Ref. [75]^2 predicts the largest energy effect for ^{108}Ru at about 500 keV. They obtain triaxial deformations for several isotopes in the Rh chain, but the energy gain is often smaller than 300 keV. These values are much smaller than the ones found for BSkG1, which in this mass region are often significantly larger than 1 MeV, see Table II, and can even reach 2.3 MeV for ^{112}Tc. The larger BSkG1 values are in qualitative agreement with the results of Ref. [20] obtained with the D1M Gogny-type EDF. This model predicts an energy gain of up to 1.6 MeV for ^{110}Pd, but the region of triaxial nuclei is limited to nuclei with $N \leqslant 70$. The authors of Ref. [68] do not report on calculations for odd-mass or odd-odd nuclei, but find a modest effect on the order of a few hundred keV [67] for ^{102,104,106,108}Ru; they find the smallest amount of nuclei with ground state triaxial deformation among the models considered here.

C. Comparison of mass differences to the BSkG1 model

The mass differences are not affected by the global offset of about 700 keV between the experimental and the BSkG1 model values. The two-neutron separation energy is a sensitive probe for structural changes, such as shell closures or the onset of deformation as a function of neutron number [76]. It is defined as

$$S_{2n}(Z, N) = \mathrm{BE}(Z, N) - \mathrm{BE}(Z, N - 2), \qquad (5)$$

where BE is the nuclear binding energy of a nucleus. In terms of mass values, it can be written as $S_{2n} = [m(Z, N - 2) + 2m_n - m(Z, N)]c^2$, where m denotes the masses for the nuclides (Z, N), $(Z, N - 2)$ and the neutron, and c is the speed of light in vacuum.

---

^{2}We note that the latest model in this series includes the effect of triaxiality, but Ref. [21] provides no information on triaxial deformation or its associated energy gain.
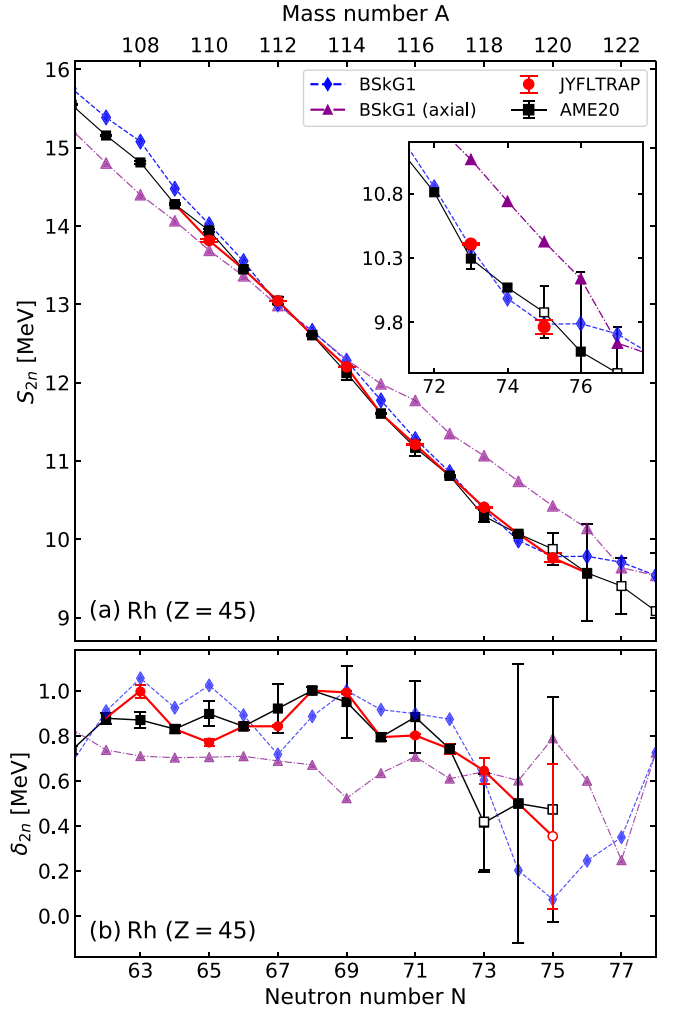

FIG. 6. (a) Comparison of two-neutron-separation energies S_{2n} of the Rh isotopes affected by our new measurements (red circles), AME20 values (full and open black square), and BSkG1 results, as tabulated in Ref. [22] (blue diamonds) or restricted to axially symmetric shapes (purple triangles), see text. Open markers represent values at least partially based on extrapolated mass values from AME20 [54]. (b) Two-neutron shell-gap energies δ_{2n}.

Figure 6(a) shows the experimental and calculated two-neutron separation energies. As before, we compare complete BSkG1 calculations allowing for nonaxial shapes and results from calculations restricted to axial shapes. The BSkG1 model reproduces the experimental data remarkably well when triaxial deformation is allowed for, as could be expected from the near constant offset between the calculated and experimental mass-excess values (seen Table II). The S_{2n} values from axial calculations deviate significantly from the experimental ones. Their slope does not follow that of the experimental data, which is a consequence of the gradual evolution of the energy gain from triaxial shapes with N. For the heaviest Rh isotopes the S_{2n} values from the full and axial calculations become very similar again as the energy gain due to triaxiality is small. We note that older global Skyrme EDF-based models that do not allow for triaxial deformation, such as those of Ref. [39], do not match the smooth trend
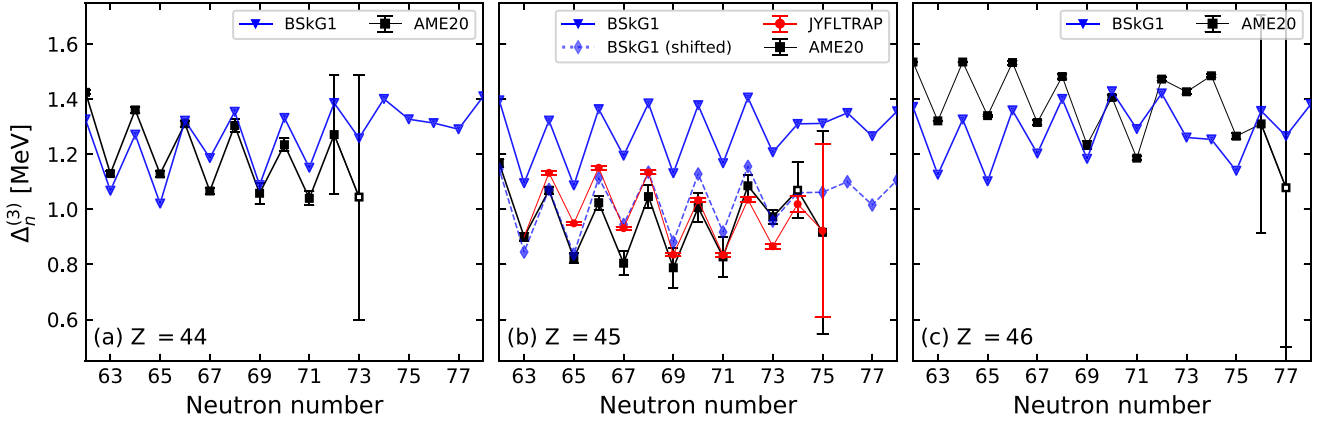
FIG. 7. Three-point neutron gaps $\Delta_n^{(3)}$ for (a) Ru ($Z = 44$), (b) Rh ($Z = 45$), and (c) Pd ($Z = 46$) isotopes. We compare values obtained from BSkG1 (blue triangles with solid line), AME20 (black squares), and from this work at JYFLTRAP (red circles). As illustration, we also show the BSkG1 values with an additional shift of -250 keV for Rh isotopes ($Z = 45$) (blue diamonds with dotted line).

of the experimental S_{2n} as well as BSkG1. They typically predict one or more sudden transitions between prolate and oblate shapes between $N = 70$ and $N = 75$ with associated nonsmooth features of the calculated two-neutron separation energies.

In order to highlight the changes in the evolution of the two-neutron separation energies as a function of N, Fig. 6(b) shows a quantity often called the two-neutron shell gap:

$$\delta_{2n}(Z, N) = S_{2n}(Z, N) - S_{2n}(Z, N + 2), \qquad (6)$$

which quantifies the changes in slope of the S_{2n} and filters out discontinuities. It is also often used to analyze the evolution of magicity in spherical nuclei [77], but can also indicate a change of shape. The experimental δ_{2n} values stay rather constant until $N = 71$, implying a near-constant slope of the S_{2n} caused by near-parabolic behavior of the masses of odd and odd-odd Rh isotopes, respectively. From $N = 71$ with added neutron numbers the δ_{2n} values have a decreasing trend signaling a change in the slope of the S_{2n} values, or, equivalently, a discontinuity in the N dependence of the masses. At $N = 73$, the slope decreases less with newly measured ^{120}Rh ($N = 75$) mass compared to the AME20 based on an extrapolated mass value of ^{120}Rh. The δ_{2n} from the full BSkG1 model follow the experimental values up to $N = 73$, as expected from the good reproduction of the experimental S_{2n} values. Beyond, the BSkG1 values fall to even lower values of δ_{2n}, reflecting the nearly flat trend of the S_{2n} and signaling a structural change in the isotopic chain associated with the disappearance of triaxial deformation; see Sec. IV D. The experimental data for $N = 74$ and $N = 75$ indicate a less dramatic change, but their precision is degraded by the large uncertainty on the masses of ^{121,122}Rh. Of these, ^{121}Rh is based on a storage-ring measurement [78], and only an extrapolated value for ^{122}Rh is given in AME20 [54]. To better constrain the trend with neutron number, masses of more exotic rhodium nuclides have to be measured to high precision.

The masses of odd-even and odd-odd Rh isotopes fall on two distinct curves that smoothly evolve with N in a similar way, but that are separated by an energy gap. The distance, or the gap, between the two curves can be estimated by a

three-point formula,

$$\Delta_n^{(3)}(Z, N) = \frac{(-1)^{N+1}}{2} [\mathrm{BE}(Z, N + 1) \\ - 2\,\mathrm{BE}(Z, N) + \mathrm{BE}(Z, N - 1)]. \qquad (7)$$

The gap is usually associated with the size of the neutron pairing gap, but is also affected by discontinuities such as shell closures and shape transitions [79,80]. We compare the $\Delta_n^{(3)}$ values for the Rh chain obtained from our measurements to those derived from AME20 and to calculated values in Fig. 7(b).[3] We have drastically reduced the uncertainties of the experimental $\Delta_n^{(3)}$ values of neutron-rich Rh isotopes in this work. Interestingly, the new $\Delta_n^{(3)}$ values do not agree with AME20 for many of the studied Rh isotopes. This is a consequence of the differences between the mass-excess values determined in this work and AME20 (see Table I and Fig. 4). For instance $N = 65$ and 67, the $\Delta_n^{(3)}$ value increases by slightly more than 100 keV, whereas for $N = 73$ it decreases by a similar amount.

The amplitude of the odd-even staggering of the $\Delta_n^{(3)}$ is well reproduced by the BSkG1 model, while the absolute size of the $\Delta_n^{(3)}$ is not. It turns out that the model's systematic overestimation of the neutron pairing gaps in the Rh chain that is visible in Fig. 7(b) is a deficiency particular to isotopic chains of elements with odd proton number Z. For isotopic chains with even Z, the $\Delta_n^{(3)}$ values are in general reasonably well described in this region of the nuclear chart; we illustrate this for the adjacent Ru ($Z = 44$) isotopes in the Fig. 7(a) but have also checked this for other isotopic chains. The experimental

---

[3]Note that the $\Delta_n^{(3)}$ values in Fig. 7 exhibit an odd-even staggering, but this does not indicate a difference in neutron pairing correlations between isotopes with odd and even neutron number. Compared to finite difference formulas of higher order, a three-point formula does not perfectly eliminate mean-field, i.e., non-pairing, contributions to the evolution of the nuclear binding energy with N [79,80]. We stick to Eq. (7), however, as it allows us to extend the experimental curves Rh ($Z = 45$) in Fig. 7 to $N = 75$.

$\Delta_n^{(3)}$ values of the Rh isotopes are systematically smaller than the values in the adjacent Pd and Ru isotopes with the same N, while the calculated ones are of the same size.

The differences in the size of calculated and experimental gaps appear systematically all across the chart of nuclei, which points to missing physics in the BSkG1 model. The effect in question is usually interpreted as an interaction between the unpaired proton and neutron in odd-odd nuclei that produces additional binding energy [21,81]. Roughly speaking, the offset between experimental $\Delta_n^{(3)}$ values of the Rh isotopes and those in the adjacent Pd and Ru chains is about 250 keV. If we subtract this estimate from the BSkG1 masses of the odd-odd Rh isotopes, the $\Delta_n^{(3)}$ values shift down along the entire chain. As an illustration we show the BSkG1 values for the Rh isotopes shifted this way for the Rh isotopes on Fig. 7(b): the shifted BSkG1 three-point gaps agree quite well with the experimental values.

To further clarify the systematic difference between odd-Z and even-Z chains, we also show values for the three-point gaps for Ru isotopes in Fig. 7(a) and for Pd isotopes in Fig. 7(c). In any event, this discussion implies that, for nuclides with odd Z, the $\Delta_n^{(3)}$ values systematically contain a sizable contribution that has nothing to do with neutron pairing correlations. The same applies of course also to three-point formula for protons, $\Delta_p^{(3)}(Z)$, for nuclides with odd N. The pattern of the calculated $\Delta_n^{(3)}(N)$ becomes irregular for Rh and Pd beyond $N = 73$ while for the Ru beyond $N = 74$. This can be attributed to the same structural change that is at the origin of the decrease of the δ_{2n} in panel (b) of Fig. 6. We discuss the change in the shape of the nuclides with N in the next section.

D. Evolution of quadrupole deformation

To better understand the experimental results and the role of deformation and triaxiality for the structure of neutron-rich Rh isotopes, in what follows we will analyze the evolution of the ground-state shape as predicted by BSkG1 for this region. To this end, we will discuss the quadrupole deformation of a nucleus of mass A in terms of the dimensionless deformation β_2 and the triaxiality angle γ as

$$\beta_2 = \frac{4\pi}{3R^2A}\sqrt{Q_{20}^2 + 2Q_{22}^2}, \tag{8}$$

$$\gamma = \mathrm{atan}(\sqrt{2}Q_{22}/Q_{20}), \tag{9}$$

where $R = 1.2A^{1/3}$ fm. The quadrupole moments Q_{20} and Q_{22} are defined in terms of integrals of the nuclear density distribution and spherical harmonics Y_{2m} as $Q_{2m} \equiv \int d^3r\, r^2\, \rho(\mathbf{r})\,\mathrm{Re}\{Y_{2m}(\mathbf{r})\}$, where $\rho(\mathbf{r})$ is the nuclear matter density and $\mathrm{Re}\{Y_{2m}(\mathbf{r})\}$ is the real part of the relevant spherical harmonic, for $m = 0$ and 2 [22]. The quantity β_2 characterizes the total size of the quadrupole deformation and is always positive such that its sign cannot be used to distinguish between prolate and oblate shapes. The triaxiality angle γ can make the distinction: values of $0°$ and $60°$ correspond to an axially symmetric prolate or oblate shape, respectively. Values in between these extremes indicate triaxial shapes that no longer posses a rotational symmetry axis.
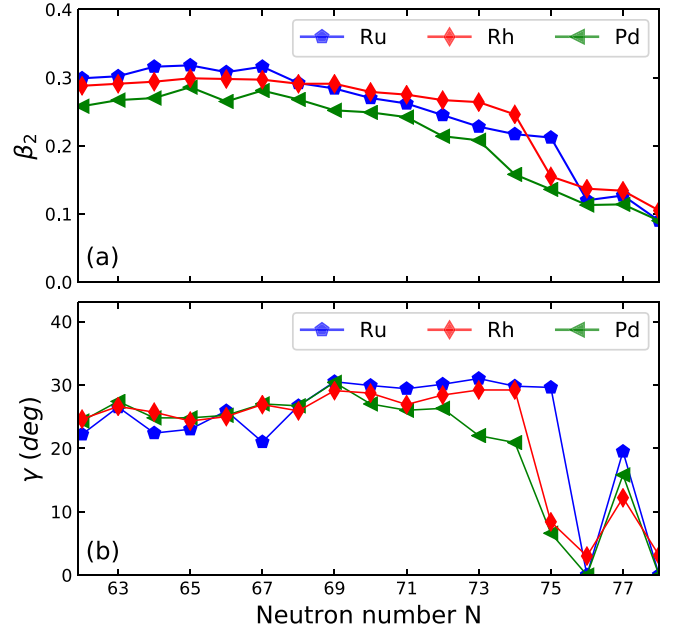

FIG. 8. (a) Deformation parameter β_2 and (b) the triaxiality angle γ for neutron-rich ruthenium ($Z = 44$), rhodium ($Z = 45$) and palladium ($Z = 46$) isotopes as calculated from the BSkG1 model.

Figure 8(a) shows the calculated β_2 and Fig. 8(b) γ values for the neutron-rich odd-Z Rh isotopes, as well as for the neighboring Ru ($Z = 44$) and Pd ($Z = 46$) isotopic chains. From $N = 63$ up to $N = 74$, Rh nuclei exhibit a fairly large deformation ($\beta_2 \simeq 0.25$–0.3) which evolves smoothly. For these neutron numbers, BSkG1 predicts γ values close to $30°$, i.e., the nuclear shapes are close to being maximally triaxial. For the heaviest Rh isotopes, the model predicts a return to axial shapes: beyond $N = 74$, the calculated values for γ drop significantly as does the total quadrupole deformation β. This change in deformation coincides with the reduction of the additional binding from triaxial shapes in Table II that is responsible for different changes in Figs. 6 and 7 around $N = 75$. More precisely, it leads to (i) the flattening of the S_{2n} in panel (a) of Fig. 6, (ii) the drop in δ_{2n} in panel (b) of Fig. 6, and (iii) the irregularities in the odd-even staggering of the $\Delta_n^{(3)}$ in Fig. 7.

The trends in even-Z Ru and Pd chains follow the same general lines: strong deformation that evolves smoothly for the lighter isotopes, and smaller deformation and values of γ for neutron-rich isotopes. The details differ between chains: the transition between both regimes happens one neutron later ($N = 75$) in the Ru chain, while the calculated β values in the Pd chain vary more smoothly than those in the other two chains.

Direct experimental information on triaxial deformation in nuclear ground states is scarce, especially for odd-mass and odd-odd nuclei. For even-even nuclei, information on quadrupole deformation can be extracted from experimental data in a model-independent way through the use of rotational invariants [82,83]. The authors of Ref. [12], the only such study in this region of the nuclear chart that we are aware of, report γ values for the stable ^{106,108,110}Pd isotopes

($Z = 46$, $N = 60, 62, 64$) as 20^{+2}_{-2}, 19^{+4}_{-5}, and 16^{+1}_{-1} degrees, respectively. These values are somewhat smaller than the calculated triaxiality angles for these nuclei [22], but we consider this a satisfactory level of description for a global model. Coulomb excitation data for ^{104}Ru ($Z = 44$, $N = 60$) [13] and ^{110}Ru ($N = 66$) [14] also point towards triaxiality of these two nuclides.

Also, as already mentioned in the Introduction, the interpretation of the available information about rotational bands of neutron-rich Rh isotopes and nuclides in adjacent isotopic chains [15–17,84–88] consistently requires the assumption of triaxial shapes within the various approaches used to model them.

E. More detailed look at ^{112}Rh

As illustrated in Table II and Fig. 6, the effect of triaxiality on the BSkG1 mass values for the Rh isotopes is large, and the largest effect is seen for ^{112}Rh. The trend in the isomeric-state excitation energies (see Fig. 3) has a minimum around the midshell at $N = 66$, i.e., at ^{110}Rh ($N = 65$) and ^{112}Rh ($N = 67$). Thus, ^{112}Rh is a special case among the studied Rh isotopes. In the following, we will discuss its structure in detail.

To obtain a correct description of an odd-odd nucleus in a mean-field calculations, one has to construct a quasiparticle excitation for each nucleon species on top of a reference state that describes an even-even nucleus [89]. Among a multitude of possible choices for such *blocked* states, the combination leading to the lowest total energy varies with deformation in a discontinuous way rendering it impossible to draw consistent potential energy surfaces (PES) for such nuclei. Instead, one can forego the construction of quasiparticle excitations and perform a false-vacuum calculation, which fixes the average number of protons and neutrons to be odd but otherwise treats the nucleus as even-even [80,90]. We show the PES for such a calculation for ^{112}Rh in Fig. 9. While we obtain for this nucleus the largest difference between the triaxial minimum and the axially symmetric saddle among all Rh isotopes, the topography of the surface is representative for $^{108-119}$Rh. A peculiar aspect of the PES in this region is that the triaxial minimum is at a slightly larger total deformation β_2 than either of the prolate and oblate saddle points.

The appearance of triaxial deformation in this region can be understood qualitatively by inspecting the single-particle spectra as a function of deformation. Figure 10 shows the eigenvalues of the single-particle Hamiltonian of neutrons (top row) and protons (bottom row) for ^{112}Rh ($Z = 45$, $N = 67$) along the path indicated by black arrows in Fig. 9. The left column explores the variation of the single-particle spectrum as a function of quadrupole deformation β at $\gamma = 0°$, i.e., for axially symmetric prolate shapes. The rightmost column shows the same for oblate shapes with $\gamma = 60°$, while the center column is drawn for fixed quadrupole deformation $\beta_2 = 0.3$ while varying γ. For axially symmetric shapes it is possible to assign the single-particle states the quantum number K according to the projection of their angular momentum on the symmetry axis. This quantum number is indicated by colors in the left and right columns of Fig. 10, but cannot be
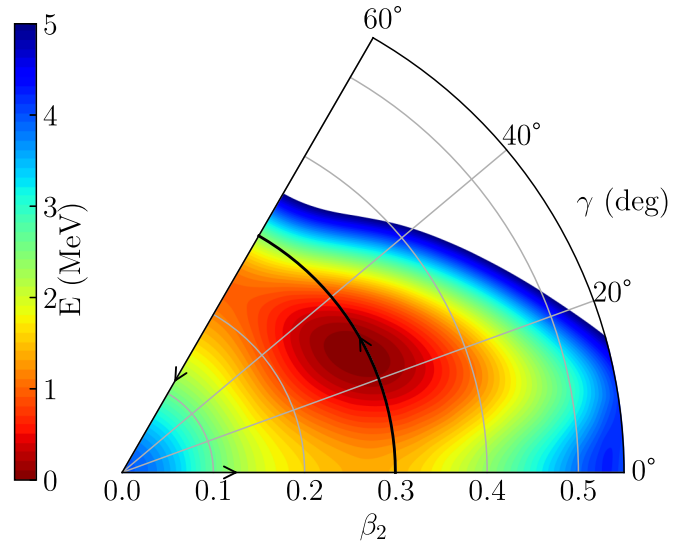

FIG. 9. Potential energy surface in the (β, γ) plane for false-vacuum calculations (see text) of ^{112}Rh. The shape-trajectory followed by the Nilsson diagram in Fig. 10 is indicated by black arrows.

used in the center column where configurations are not axially symmetric.

The origin of the drive towards triaxial shapes can be found in the proton single-particle spectrum. According to Strutinsky's theorem [91,92], local minima (maxima) in deformation energy surfaces correspond to regions where the bunching of single-particle levels around the Fermi energy is very low (high). At spherical shape, the proton Fermi energy is in the middle of the highly degenerate $1g_{9/2^+}$ shell, leading to large level density. Through prolate deformation, the substates of the spherical proton $1g_{9/2^+}$ spread out strongly and produce a very sparse spectrum with large gaps among the positive-parity states. The upsloping negative-parity states spoil these gaps though, particularly the $K^\pi = 1/2^-$ level coming from the spherical $2p_{1/2^-}$ shell. However, this state curves up strongly for increasing values of γ, such that triaxial deformation allows the nucleus to decrease the level density near the Fermi energy significantly, opening up a gap at $Z = 44$. Similarly large gaps open up as well for $Z = 42$ and $Z = 46$, explaining the preference for non-axial deformation in this region. Whether a given nucleus takes a triaxial shape, however, depends also on the neutron spectrum at these deformations.

For the midshell nucleus ^{112}Rh, the overall density of neutron levels around the Fermi energy is much larger than the one of protons. The former is also not visibly decreased when going from spherical to prolate or oblate shapes with $\beta_2 \simeq 0.3$. Still, for $N = 68$ and some other adjacent neutron numbers, modest single-particle gaps open up for finite values of γ. When increasing the neutron number however, the neutron Fermi energy rises and encounters larger shell gaps at smaller prolate deformations. Sufficiently close to $N = 82$, this effect trumps the preference of the protons for triaxial deformation.
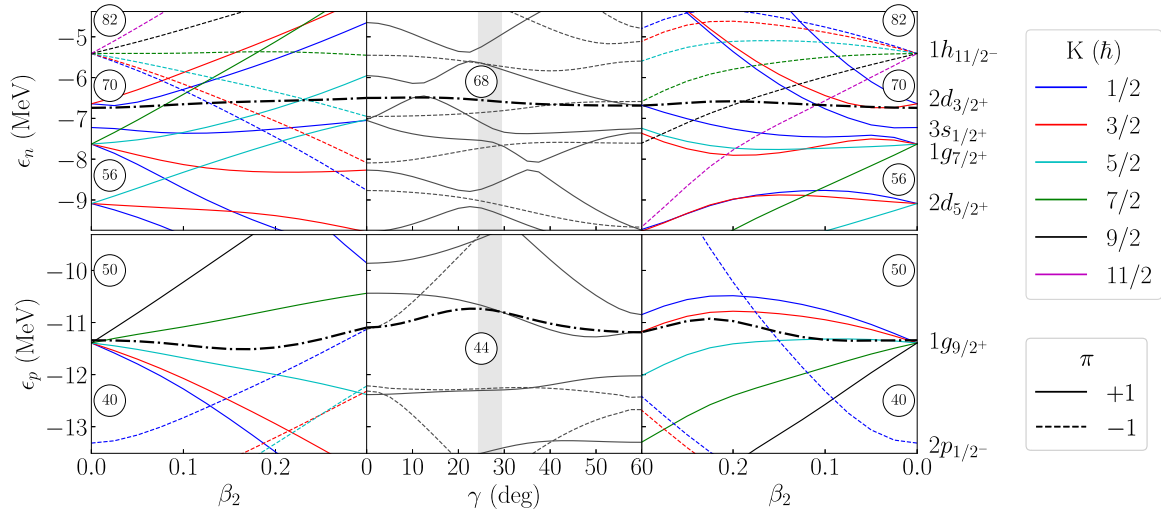
FIG. 10. Nilsson diagram of the eigenvalues of the single-particle Hamiltonian for neutrons (top row) and protons (bottom row) along the path in the β-γ plane indicated by arrows in Fig. 9 for ^{112}Rh (see text for details). The Fermi energy is drawn as a dash-dotted line, while full (dashed) lines indicate single-particle levels of positive (negative) parity. The three indicated regions correspond to axially symmetric prolate shape with $\gamma = 0°$ (left column), fixed quadrupole deformation $\beta_2 = 0.3$ with varying γ (center column), and axially oblate shape with $\gamma = 60°$ (right column). The vertical gray band in the center panels is centered at $\gamma = 27°$, the value obtained in a complete calculation of ^{112}Rh. The quantum numbers of the shells at sphericity are indicated on the right-hand side.

The staggering of the triaxiality angle at $N = 77$ in Fig. 8 can be understood in a similar way. The mean-field minimum for $N \geqslant 76$ is axially symmetric for all three isotopic chains, as neutrons close to the shell closure strongly prefer axially symmetric shapes. Nevertheless, the potential energy surface of a false-vacuum calculation at $N = 77$ remains sufficiently soft with respect to γ such that the creation of a neutron quasiparticle excitation is sufficient to break the symmetry for ^{121}Ru and ^{123}Pd. As the level density of neutrons is much larger than that of protons, the polarizing effect of a blocked neutron is larger than that of a blocked protons; the latter cannot generate triaxial deformation in ^{121}Rh.

Without symmetry restoration techniques, the symmetry-broken mean-field calculations we report on here cannot produce definite spin assignments for ground or excited states. For even-N Rh isotopes however, we can make tentative assignments due to the sparsity of the single-particle proton spectrum. The picture that emerges is consistent with experimental spectroscopic information: a positive parity proton state, linked to the $K^\pi = 7/2^+$ state on the prolate side, is located close to the Fermi energy in the center of Fig. 10. This matches well the $J^\pi = 7/2^+$ ground states of the ^{105,107,109}Rh isotopes.[4] Without triaxial deformation, theory would not reproduce the spin-parities: on the prolate side the $K^\pi = 1/2^-$ state suggests a negative-parity ground state, whereas an oblate shape would result in a state with a lower spin. These considerations seem to be independent of the type of EDF that is employed: calculations with the Gogny D1S parametrization lead to a similar single-particle spectrum for the protons [19].

_____

[4] The ground states of the neutron-rich even-N Rh isotopes with $111 \leqslant A \leqslant 125$ have also been tentatively assigned $J^\pi = 7/2^+$ [23].

For odd-N Rh isotopes, however, extracting spin-parity assignments for the ground and isomeric states is particularly difficult due to the large number of states near the Fermi energy that are all K mixed. Based on the (often tentative) experimental information on spin-parities in this mass region, we can, however, offer some observations. For both ^{110}Rh and ^{112}Rh, the ground and isomeric states have been assigned $(1)^+$ and $(6)^+$, i.e., states of identical parity that differ by a large amount of angular momentum. In the strong-coupling limit, these assignments can be naturally explained by combining the angular momentum of a $K^\pi = 7/2^+$ proton and a $K^\pi = 5/2^+$ neutron in two different ways: a parallel (antiparallel) coupling results in a high (low) spin. Such spin assignment for the odd nucleons would make the ground and isomeric state a so-called Gallagher-Moszkowski pair [93]. The appearance of triaxial deformation stops us from relying on the K-quantum number, but we observe that the central panel of the top row of Fig. 10 shows two neutron single-particle states near the Fermi energy that link to $K^\pi = 7/2^+$ states on the prolate side. Although the negative parity neutron state linked to the $K^\pi = 7/2^-$ state on the prolate side could lead to a negative parity ground state in a symmetry-restored calculation, the BSkG1 Nilsson scheme in Fig. 10 is thus not incompatible with this scenario for the ground and isomeric states in ^{110,112}Rh.

Assuming that the isomeric states in ^{110,112}Rh are the Gallagher-Moszkowski partners of their respective ground states also offers a possible, albeit tentative, interpretation for the extremely low excitation energy of their isomers of ^{110,112}Rh. For other nuclei in this mass region, the excitation energy of spin isomers is often of the order of 100 keV; see for example Fig. 3. This splitting is generally interpreted as being the result of the relative orientation of the intrinsic spins of the odd neutron (s_n) and odd proton (s_p): depending on the relative

orientation of spin, the proton-neutron spin-spin interaction is either attractive or repulsive, leading to a small difference in total binding energy. The state with lowest energy has spins that are parallel ($s_n \cdot s_p > 0$) while the excited partner has antiparallel spins ($s_n \cdot s_p < 0$). The situation of ^{110}Rh and ^{112}Rh is somewhat peculiar due to the presence of *two* positive parity neutron levels with similar angular momenta near the Fermi energy that are candidates for the observed states. These two single-particle states differ, at least for axial prolate shapes, in their relative orientation between their orbital (ℓ_n) and spin (s_n) angular momentum, although they have roughly similar total angular momentum ($j_n = \ell_n + s_n$). The neutron level originating from the spherical $1g_{7/2^+}$ has both mostly antiparallel ($\ell_n \cdot s_n \leqslant 0$), while the one connected to the $2d_{5/2^+}$ shell has both mostly parallel ($\ell_n \cdot s_n \geqslant 0$). For triaxial shapes these two single-particle states mix, and in the many-body wave functions of the two partner states the quasiparticle configurations in which either is blocked might also be mixed. This could lead to a situation where the spins of the odd nucleons are almost perpendicular ($s_n \cdot s_p \approx 0$), resulting in a very small Gallagher-Moszkowski splitting and hence a very low excitation energy of the isomers in ^{110}Rh and ^{112}Rh. This interpretation also naturally explains why such low-lying isomers are only observed only for a small number (two) of the Rh isotopes; as N increases (decreases), the neutron Fermi energy moves up (down) in Fig. 10, further away from the $K^\pi = 7/2^+$ neutron state with highest (lowest) energy and removing the possibility of this mixing. Although we cannot provide definite predictions, it is natural to expect a larger, i.e., normal, Gallagher-Moszkowski splitting for neutron numbers sufficiently far from $N = 65, 67$.

We emphasize this discussion is no substitute for more advanced many-body calculations capable of constructing spectra with the associated quantum numbers for these nuclei. Performing such calculations with predictive power based on nuclear EDFs might however not be possible in the near future. On top of the technical challenges inherent in employing symmetry-restoration techniques for odd-odd nuclei, it has been argued that virtually all existing EDF-based models are not suited to describe the attraction between the odd nucleons in such nuclei [94].

V. CONCLUSIONS

We have determined the ground- and isomeric-state masses of ^{110,112,114,116,118}Rh and determined the isomeric state excitation energies accurately for the first time. Also the mass of ^{120}Rh was measured for the first time. The new ground-state mass values revealed deviations up to around 100 keV from the adopted mass values of ^{110,112,118}Rh in AME20 [54]. We

have unambiguously determined the masses and half-lives of the ground and isomeric states in ^{112}Rh and confirm that the low-spin 1^+ state is the ground state. The new ground-state half-life was found to be more than 10σ shorter than the value reported in the ENSDF evaluation [56], but to agree with the result reported in Ref. [27] which had taken into account ^{112}Ru contamination. The experimental results have been compared to the results of the global BSkG1 mass model [22] that was adjusted allowing nuclei to take triaxial shapes. The trends of mass excesses and two-neutron separation energies of the Rh isotopes are very well reproduced with the full BSkG1 model, whereas limiting the variational space to axial shapes leads to substantial deviations from the experimental values. This result underlines the important role of triaxiality in the region of studied Rh isotopes. The predictions of BSkG1 for the potential energy surface as well as the deformation dependence of the single-particle energies have been studied in detail for ^{112}Rh, the nucleus for which the effect of triaxiality is largest in the BSkG1 model. The results indicate that the proton shell effects drive the Rh nuclides to triaxial shapes, and that neutron shell effects moderate for which isotopes this happens. A drastic change in the deformation is predicted to take place at $N = 75$ (^{120}Rh), which is imprinted on several mass differences. In the future, mass measurements of the more exotic Rh isotopes are needed to explore if this effect can be seen as a change in the slope of the two-neutron separation energies beyond $N = 75$.

[1] K. Heyde and J. L. Wood, Rev. Mod. Phys. **83**, 1467 (2011).

[2] S. Rahaman, U. Hager, V.-V. Elomaa, T. Eronen, J. Hakala, A. Jokinen, A. Kankainen, P. Karvonen, I. D. Moore, H. Penttilä *et al.*, Eur. Phys. J. A **32**, 87 (2007).

[3] U. Hager, T. Eronen, J. Hakala, A. Jokinen, V. S. Kolhinen, S. Kopecky, I. Moore, A. Nieminen, M. Oinonen, S. Rinta-Antila, J. Szerypo, and J. Äystö, Phys. Rev. Lett. **96**, 042504 (2006).

[4] U. Hager, A. Jokinen, V.-V. Elomaa, T. Eronen, J. Hakala, A. Kankainen, S. Rahaman, J. Rissanen, I. Moore, S. Rinta-Antila *et al.*, Nucl. Phys. A **793**, 20 (2007).

[5] J. Hakala, R. Rodriguez-Guzman, V. V. Elomaa, T. Eronen, A. Jokinen, V. S. Kolhinen, I. D. Moore, H. Penttilä, M. Reponen, J. Rissanen *et al.*, Eur. Phys. J. A **47**, 129 (2011).

[6] C. Thibault, F. Touchard, S. Büttgenbach, R. Klapisch, M. de Saint Simon, H. T. Duong, P. Jacquinot, P. Juncar, S. Liberman, P. Pillet *et al.*, Phys. Rev. C **23**, 2720 (1981).

[7] P. Lievens, E. Arnold, W. Borchers, U. Georg, M. Keim, A. Klein, R. Neugart, L. Vermeeren, and R. E. Silverans, Europhys. Lett. **33**, 11 (1996).

[8] B. Cheal, M. Gardner, M. Avgoulea, J. Billowes, M. Bissell, P. Campbell, T. Eronen, K. Flanagan, D. Forest, J. Huikari *et al.*, Phys. Lett. B **645**, 133 (2007).

[9] P. Campbell, H. L. Thayer, J. Billowes, P. Dendooven, K. T. Flanagan, D. H. Forest, J. A. R. Griffith, J. Huikari, A. Jokinen, R. Moore *et al.*, Phys. Rev. Lett. **89**, 082501 (2002).

[10] B. Cheal, K. Baczynska, J. Billowes, P. Campbell, F. C. Charlwood, T. Eronen, D. H. Forest, A. Jokinen, T. Kessler, I. D. Moore *et al.*, Phys. Rev. Lett. **102**, 222501 (2009).

[11] F. Charlwood, K. Baczynska, J. Billowes, P. Campbell, B. Cheal, T. Eronen, D. Forest, A. Jokinen, T. Kessler, I. Moore *et al.*, Phys. Lett. B **674**, 23 (2009).

[12] L. E. Svensson, C. Fahlander, L. Hasselgren, A. Bäcklin, L. Westerberg, D. Cline, T. Czosnyka, C. Y. Wu, R. M. Diamond, and H. Kluge, Nucl. Phys. A **584**, 547 (1995).

[13] J. Srebrny, T. Czosnyka, C. Droste, S. Rohoziński, L. Próchniak, K. Zajac, K. Pomorski, D. Cline, C. Y. Wu, A. Bäcklin *et al.*, Nucl. Phys. A **766**, 25 (2006).

[14] D. Doherty, J. Allmond, R. Janssens, W. Korten, S. Zhu, M. Zielińska, D. Radford, A. Ayangeakaa, B. Bucher, J. Batchelder *et al.*, Phys. Lett. B **766**, 334 (2017).

[15] S. H. Liu, J. H. Hamilton, A. V. Ramayya, Y. S. Chen, Z. C. Gao, S. J. Zhu, L. Gu, E. Y. Yeoh, N. T. Brewer, J. K. Hwang *et al.*, Phys. Rev. C **83**, 064310 (2011).

[16] A. Navin, M. Rejmund, S. Bhattacharyya, R. Palit, G. Bhat, J. A. Sheikh, A. Lemasson, M. Caamaño, E. Clément, O. Delaune *et al.*, Phys. Lett. B **767**, 480 (2017).

[17] C. L. Zhang, G. H. Bhat, W. Nazarewicz, J. A. Sheikh, and Y. Shi, Phys. Rev. C **92**, 034307 (2015).

[18] H. Abusara, S. Ahmad, and S. Othman, Phys. Rev. C **95**, 054302 (2017).

[19] B. Bucher, H. Mach, A. Aprahamian, L. M. Robledo, G. S. Simpson, J. Rissanen, D. G. Ghiţă, B. Olaizola, W. Kurcewicz, J. Äystö, T. Eronen, L. M. Fraile, A. Jokinen, P. Karvonen, I. D. Moore, H. Penttilä, M. Reponen, E. Ruchowska, A. Saastamoinen, M. K. Smith, and C. Weber, Phys. Rev. C **98**, 064320 (2018).

[20] S. Goriely, S. Hilaire, M. Girod, and S. Péru, Phys. Rev. Lett. **102**, 242501 (2009).

[21] P. Möller, A. Sierk, T. Ichikawa, and H. Sagawa, At. Data Nucl. Data Tables **109-110**, 1 (2016).

[22] G. Scamps, S. Goriely, E. Olsen, M. Bender, and W. Ryssens, Eur. Phys. J. A **57**, 333 (2021).

[23] F. Kondev, M. Wang, W. Huang, S. Naimi, and G. Audi, Chin. Phys. C **45**, 030001 (2021).

[24] V. Kolhinen, Ph.D. thesis, University of Jyväskylä, 2003.

[25] U. Hager, V.-V. Elomaa, T. Eronen, J. Hakala, A. Jokinen, A. Kankainen, S. Rahaman, S. Rinta-Antila, A. Saastamoinen, T. Sonoda *et al.*, Phys. Rev. C **75**, 064302 (2007).

[26] T. Eronen, V. Kolhinen, V.-V. Elomaa, D. Gorelov, U. Hager, J. Hakala, A. Jokinen, A. Kankainen, P. Karvonen, S. Kopecky *et al.*, Eur. Phys. J. A **48**, 46 (2012).

[27] A. Jokinen, J. Äystö, P. Dendooven, K. Eskola, Z. Janas, P. P. Jauho, M. E. Leino, J. M. Parmonen, H. Penttilä, K. Rykaczewski *et al.*, Z. Phys. A **340**, 21 (1991).

[28] A. Jokinen, J. Äystö, P. Jauho, M. Leino, J. Parmonen, H. Penttilä, K. Eskola, and Z. Janas, Nucl. Phys. A **549**, 420 (1992).

[29] J. Äystö, C. Davids, J. Hattula, J. Honkanen, K. Honkanen, P. Jauho, R. Julin, S. Juutinen, J. Kumpulainen, T. Lönnroth *et al.*, Nucl. Phys. A **480**, 104 (1988).

[30] G. Lhersonneau, J. C. Wang, S. Hankonen, P. Dendooven, P. Jones, R. Julin, and J. Äystö, Phys. Rev. C **60**, 014315 (1999).

[31] G. Lhersonneau, Y. Wang, R. Capote, J. Suhonen, P. Dendooven, J. Huikari, K. Peräjärvi, and J. C. Wang, Phys. Rev. C **67**, 024303 (2003).

[32] Y. Wang, P. Dendooven, J. Huikari, A. Jokinen, V. S. Kolhinen, G. Lhersonneau, A. Nieminen, S. Nummela, H. Penttilä, K. Peräjärvi *et al.*, Phys. Rev. C **63**, 024309 (2001).

[33] A. Jokinen, J. Wang, J. Äystö, P. Dendooven, S. Nummela, J. Huikari, V. Kolhinen, A. Nieminen, K. Peräjärvi, and S. Rinta-Antila, Eur. Phys. J. A **9**, 9 (2000).

[34] J. C. W. Wang You-Bao, P. Dendooven, J. Huikari, A. Jokinen, V. S. Kolhinen, G. Lhersonneau, A. Nieminen, S. Nummela, H. Penttilä, K. Peräjärvi, S. Rinta-Antila, J. Szerypo, and J. Äystö, Chin. Phys. Lett. **23**, 808 (2006).

[35] G. Gürdal and F. Kondev, Nucl. Data Sheets **113**, 1315 (2012).

[36] S. Eliseev, K. Blaum, M. Block, A. Dörr, C. Droese, T. Eronen, M. Goncharov, M. Höcker, J. Ketter, E. Minaya Ramirez *et al.*, Appl. Phys. B **114**, 107 (2014).

[37] D. A. Nesterenko, T. Eronen, A. Kankainen, L. Canete, A. Jokinen, I. D. Moore, H. Penttilä, S. Rinta-Antila, A. de Roubin, and M. Vilen, Eur. Phys. J. A **54**, 154 (2018).

[38] D. Nesterenko, T. Eronen, Z. Ge, A. Kankainen, and M. Vilén, Eur. Phys. J. A **57**, 302 (2021).

[39] S. Goriely, N. Chamel, and J. M. Pearson, Phys. Rev. C **93**, 034337 (2016).

[40] M. Wang, G. Audi, F. G. Kondev, W. J. Huang, S. Naimi, and X. Xu, Chin. Phys. C **41**, 030003 (2017).

[41] I. Angeli and K. P. Marinova, At. Data Nucl. Data Tables **99**, 69 (2013).

[42] W. Huang, M. Wang, F. Kondev, G. Audi, and S. Naimi, Chin. Phys. C **45**, 030002 (2021).

[43] I. D. Moore, T. Eronen, D. Gorelov, J. Hakala, A. Jokinen, A. Kankainen, V. Kolhinen, J. Koponen, H. Penttilä, I. Pohjalainen *et al.*, Nucl. Instrum. Methods Phys. Res., Sect. B **317**, 208 (2013).

[44] P. Karvonen, I. D. Moore, T. Sonoda, T. Kessler, H. Penttilä, K. Peräjärvi, P. Ronkanen, and J. Äystö, Nucl. Instrum. Methods Phys. Res., Sect. B **266**, 4794 (2008).

[45] A. Nieminen, J. Huikari, A. Jokinen, J. Äystö, P. Campbell, and E. C. A. Cochrane, Nucl. Instrum. Methods Phys. Res., Sect. A **469**, 244 (2001).

[46] G. Savard, S. Becker, G. Bollen, H.-J. Kluge, R. B. Moore, T. Otto, L. Schweikhard, H. Stolzenberg, and U. Wiess, Phys. Lett. A **158**, 247 (1991).

[47] M. Vilén, L. Canete, B. Cheal, A. Giatzoglou, R. de Groote, A. de Roubin, T. Eronen, S. Geldhof, A. Jokinen, A. Kankainen *et al.*, Nucl. Instrum. Methods Phys. Res., Sect. B **463**, 382 (2020).

[48] G. Gräff, H. Kalinowsky, and J. Traut, Z. Phys. A **297**, 35 (1980).

[49] M. König, G. Bollen, H.-J. Kluge, T. Otto, and J. Szerypo, Int. J. Mass Spectrom. Ion Process. **142**, 95 (1995)

[50] M. Kretzschmar, Int. J. Mass Spectrom. **264**, 122 (2007).

[51] S. George, K. Blaum, F. Herfurth, A. Herlert, M. Kretzschmar, S. Nagy, S. Schwarz, L. Schweikhard, and C. Yazidjian, Int. J. Mass Spectrom. **264**, 110 (2007).

[52] T. Eronen, V.-V. Elomaa, U. Hager, J. Hakala, A. Jokinen, A. Kankainen, S. Rahaman, J. Rissanen, C. Weber, and J. Äystö, Nucl. Instrum. Methods Phys. Res., Sect. B **266**, 4527 (2008).

[53] A. Kellerbauer, K. Blaum, G. Bollen, F. Herfurth, H.-J. Kluge, M. Kuckein, E. Sauvan, C. Scheidenberger, and L. Schweikhard, Eur. Phys. J. D **22**, 53 (2003).

[54] M. Wang, W. Huang, F. Kondev, G. Audi, and S. Naimi, Chin. Phys. C **45**, 030003 (2021).

[55] K.-L. Kratz and B. Pfeiffer (private communication).

[56] S. Lalkovski and F. Kondev, Nucl. Data Sheets **124**, 157 (2015).

[57] J. Blachot, Nucl. Data Sheets **113**, 515 (2012).

[58] R. Knöbel, Ph.D. thesis, Justus-Liebig-Universität Giessen, 2008.

[59] J. Blachot, Nucl. Data Sheets **111**, 717 (2010).

[60] M. Matos, Ph.D. thesis, Justus-Liebig-Universität Giessen, 2004.

[61] F. Montes, A. Estrade, P. T. Hosmer, S. N. Liddick, P. F. Mantica, A. C. Morton, W. F. Mueller, M. Ouellette, E. Pellegrini, P. Santi *et al.*, Phys. Rev. C **73**, 035801 (2006).

[62] G. Lorusso, S. Nishimura, Z. Y. Xu, A. Jungclaus, Y. Shimizu, G. S. Simpson, P.-A. Söderström, H. Watanabe, F. Browne, P. Doornenbal *et al.*, Phys. Rev. Lett. **114**, 192501 (2015).

[63] O. Hall, T. Davinson, A. Estrade, J. Liu, G. Lorusso, F. Montes, S. Nishimura, V. Phong, P. Woods, J. Agramunt *et al.*, Phys. Lett. B **816**, 136266 (2021).

[64] D. Kameda, T. Kubo, T. Ohnishi, K. Kusaka, A. Yoshida, K. Yoshida, M. Ohtake, N. Fukuda, H. Takeda, K. Tanaka *et al.*, Phys. Rev. C **86**, 054319 (2012).

[65] J. Erler, N. Birge, M. Kortelainen, W. Nazarewicz, E. Olsen, A. M. Perhac, and M. Stoitsov, Nature (London) **486**, 509 (2012).

[66] S. E. Agbemava, A. V. Afanasjev, D. Ray, and P. Ring, Phys. Rev. C **89**, 054320 (2014).

[67] K. Q. Lu, Z. X. Li, Z. P. Li, J. M. Yao, and J. Meng, Phys. Rev. C **91**, 027304 (2015).

[68] Y. L. Yang, Y. K. Wang, P. W. Zhao, and Z. P. Li, Phys. Rev. C **104**, 054312 (2021).

[69] S. Hilaire and M. Girod, Eur. Phys. J. A **33**, 237 (2007).

[70] S. Goriely, N. Chamel, and J. M. Pearson, Phys. Rev. C **88**, 061302(R) (2013).

[71] W. Ryssens, Ph.D. thesis, Université Libre de Bruxelles, 2016.

[72] W. Ryssens, P.-H. Heenen, and M. Bender, Phys. Rev. C **92**, 064318 (2015).

[73] W. Ryssens, M. Bender, and P. H. Heenen, Eur. Phys. J. A **55**, 93 (2019).

[74] S. Perez-Martin and L. M. Robledo, Phys. Rev. C **78**, 014304 (2008).

[75] P. Möller, R. Bengtsson, B. G. Carlsson, P. Olivius, and T. Ichikawa, Phys. Rev. Lett. **97**, 162502 (2006).

[76] D. Lunney, J. M. Pearson, and C. Thibault, Rev. Mod. Phys. **75**, 1021 (2003).

[77] M. Bender, G. F. Bertsch, and P.-H. Heenen, Phys. Rev. C **78**, 054312 (2008).

[78] R. Knöbel, M. Diwisch, H. Geissel, Yu. A. Litvinov, Z. Patyk, W. R. Plaß, C. Scheidenberger, B. Sun, H. Weick, F. Bosch *et al.* Eur. Phys. J. A **52**, 138 (2016).

[79] M. Bender, K. Rutz, P.-G. Reinhard, and J. A. Maruhn, Eur. Phys. J. A **8**, 59 (2000).

[80] T. Duguet, P. Bonche, P.-H. Heenen, and J. Meyer, Phys. Rev. C **65**, 014311 (2001).

[81] Z. Wu, S. A. Changizi, and C. Qi, Phys. Rev. C **93**, 034334 (2016).

[82] K. Kumar, Phys. Rev. Lett. **28**, 249 (1972).

[83] D. Cline, Annu. Rev. Nucl. Part. Sci. **36**, 683 (1986).

[84] S. H. Liu, J. H. Hamilton, A. V. Ramayya, S. J. Zhu, Y. Shi, F. R. Xu, J. C. Batchelder, N. T. Brewer, J. K. Hwang, Y. X. Luo *et al.*, Phys. Rev. C **87**, 057302 (2013).

[85] N. Fotiades, J. A. Cizewski, R. Krücken, D. P. McNabb, J. A. Becker, L. A. Bernstein, W. Younes, R. M. Clark, P. Fallon, I. Y. Lee *et al.*, Phys. Rev. C **67**, 064304 (2003).

[86] P.-A. Söderström, G. Lorusso, H. Watanabe, S. Nishimura, P. Doornenbal, G. Thiamova, F. Browne, G. Gey, H. S. Jung, T. Sumikama *et al.*, Phys. Rev. C **88**, 024301 (2013).

[87] Y. X. Luo, S. C. Wu, J. Gilat, J. O. Rasmussen, J. H. Hamilton, A. V. Ramayya, J. K. Hwang, C. J. Beyer, S. J. Zhu, J. Kormicki *et al.*, Phys. Rev. C **69**, 024315 (2004).

[88] T. W. Hagen, A. Görgen, W. Korten, L. Grente, M. D. Salsac, F. Farget, T. Braunroth, B. Bruyneel, I. Celikovic, E. Clément *et al.*, Eur. Phys. J. A **54**, 50 (2018).

[89] P. Ring and P. Schuck, *The Nuclear Many-Body Problem* (Springer-Verlag, Berlin, 1980).

[90] T. Duguet, P. Bonche, P.-H. Heenen, and J. Meyer, Phys. Rev. C **65**, 014310 (2001).

[91] V. M. Strutinsky, Nucl. Phys. A **95**, 420 (1967).

[92] M. Brack, J. Damgaard, A. S. Jensen, H. C. Pauli, V. M. Strutinsky, and C. Y. Wong, Rev. Mod. Phys. **44**, 320 (1972).

[93] C. Gallagher and S. A. Moszkowski, Phys. Rev. **111**, 1282 (1958).

[94] L. M. Robledo, R. N. Bernard, and G. F. Bertsch, Phys. Rev. C **89**, 021303(R) (2014).

PII

BINDING ENERGIES OF GROUND AND ISOMERIC STATES IN NEUTRON-RICH RU ISOTOPES: MEASUREMENTS AT JYFLTRAP AND COMPARISON TO THEORY

by

M. Hukkanen,W. Ryssens, P. Ascher, M. Bender, T. Eronen, S. Grevy,
A. Kankainen, M. Stryjczyk, L. Al Ayoubi, S. Ayet, O. Beliuskina, C. Delafosse,
Z. Ge, M. Gerbaux, W. Gins, A. Husson, A. Jaries, S. Kujanpaa, M. Mougeot,
D. A. Nesterenko, S.Nikas, H. Penttila, I. Pohjalainen, A. Raggio, M. Reponen,
S. Rinta-Antila, A. de Roubin, J. Ruotsalainen, V. Virtanen and A. P. Weaver

Binding energies of ground and isomeric states in neutron-rich Ru isotopes: measurements at JYFLTRAP and comparison to theory

M. Hukkanen,[1,2] W. Ryssens,[3] P. Ascher,[2] M. Bender,[4] T. Eronen,[1] S. Grévy,[2] A. Kankainen,[1] M. Stryjczyk,[1] L. Al Ayoubi,[1,5] S. Ayet,[6] O. Beliuskina,[1] C. Delafosse,[1,*] Z. Ge,[7] M. Gerbaux,[2] W. Gins,[1] A. Husson,[2] A. Jaries,[1] S. Kujanpää,[1] M. Mougeot,[1] D.A. Nesterenko,[1] S. Nikas,[1] H. Penttilä,[1] I. Pohjalainen,[1] A. Raggio,[1] M. Reponen,[1] S. Rinta-Antila,[1] A. de Roubin,[1,†] J. Ruotsalainen,[1] V. Virtanen,[1] and A.P. Weaver[8,‡]

[1] University of Jyvaskyla, Department of Physics, Accelerator Laboratory,
P.O. Box 35(YFL) FI-40014 University of Jyvaskyla, Finland
[2] Université de Bordeaux, CNRS/IN2P3, LP2I Bordeaux, UMR 5797, F-33170 Gradignan, France
[3] Institut d'Astronomie et d'Astrophysique, Université Libre de Bruxelles,
Campus de la Plaine CP 226, 1050 Brussels, Belgium
[4] Université de Lyon, Université Claude Bernard Lyon 1,
CNRS/IN2P3, IP2I Lyon, UMR 5822, F-69622 Villeurbanne, France
[5] Université Paris Saclay, CNRS/IN2P3, IJCLab, 91405 Orsay, France
[6] II. Physikalisches Institut, Justus Liebig Universität Gießen, 35392 Gießen, Germany
[7] GSI Helmholtzzentrum für Schwerionenforschung, 64291 Darmstadt, Germany
[8] School of Computing, Engineering and Mathematics,
University of Brighton, Brighton BN2 4GJ, United Kingdom
(Dated: June 7, 2023)

We report on precision mass measurements of ^{113,115,117}Ru performed with the JYFLTRAP double Penning trap mass spectrometer at the Accelerator Laboratory of University of Jyväskylä. The phase-imaging ion-cyclotron-resonance technique was used to resolve the ground and isomeric states in ^{113,115}Ru and enabled for the first time a measurement of the isomer excitation energies, $E_x(^{113}\text{Ru}^m) = 100.4(9)$ keV and $E_x(^{115}\text{Ru}^m) = 129(5)$ keV. The ground state of ^{117}Ru was measured using the time-of-flight ion-cyclotron-resonance technique. The new mass-excess value for ^{117}Ru is around 37 keV lower and 7 times more precise than the previous literature value. With the more precise ground-state mass values, the evolution of the two-neutron shell-gap energies is further constrained and a similar trend as predicted by the BSkG1 model is obtained up to the neutron number $N = 71$.

I. INTRODUCTION

Neutron-rich nuclei between zirconium ($Z = 40$) and tin ($Z = 50$) exhibit a variety of shapes; several of them even exhibit shape coexistence, where excited states are linked to shapes which differ from that of the nuclear ground state. The diversity of collectivity in general and of the nuclear shape in particular in this region of the nuclear chart has been studied widely, both theoretically and experimentally, see e.g. Ref. [1] and references therein. The relevant nuclear configurations are not limited to shapes with a comparatively high degree of symmetry such as spheres or axially symmetric ellipsoids with prolate or oblate deformation, but also includes shapes with no remaining rotational symmetry axis: triaxial shapes. There is evidence that the ground states of neutron-rich ruthenium isotopes ($Z = 44$) fall in the latter category [1, 2], an interpretation that is further supported by different models [3, 4]. These models

typically agree that the effect of triaxial deformation is largest at the mid-shell and that the effect tapers off when even more neutrons are added to the nucleus, i.e. that sufficiently neutron-rich nuclei revert to an axially symmetric or even spherical shape towards the shell closure at $N = 82$.

Structural changes can be studied via a wide range of experimental methods, including laser- and decay-spectroscopy as well as Coulomb excitation. At the same time, Penning-trap mass spectrometry can be used to explore differences in binding energy which can reveal possible shape transitions [5–7]. With the development of the phase-imaging ion-cyclotron-resonance (PI-ICR) technique [8, 9], not only the ground-state binding energies but also the isomer excitation energies down to a few tens of keV [10, 11] can be extracted, allowing to obtain new insight into the nuclear structure.

Masses of neutron-rich ruthenium isotopes up to $A = 116$ [12, 13] have been measured before with the JYFLTRAP double Penning trap mass spectrometer [14]. However, for the cases where long-lived isomers are present, namely ^{113,115}Ru, the time-of-flight ion-cyclotron-resonance (TOF-ICR) [15] technique used at that time did not provide enough resolving power to separate the ground- and isomeric-states in ^{113}Ru or to detect the isomer in ^{115}Ru unknown at that time. Therefore these results might have suffered from a system-

* Present address: Université Paris Saclay, CNRS/IN2P3, IJCLab, 91405 Orsay, France
† Present address: KU Leuven, Instituut voor Kern- en Stralings-fysica, B-3001 Leuven, Belgium
‡ Present address: TRIUMF, 4004 Wesbrook Mall, Vancouver, British Columbia V6T 2A3, Canada

atic shift for the reported ground-state mass-excess values [11]. More exotic ruthenium isotopes were studied using the Experimental Storage Ring at GSI [16]. However, ^{117}Ru had the uncertainty 2.4-times increased by the Atomic Mass Evaluation 2020 (AME20) evaluators while the mass-excess value of ^{118}Ru was rejected due to a significant 700-keV deviation from the mass trends [17].

In this work, we report on the direct mass measurement of the ground states of ^{113,115,117}Ru and the isomeric states in ^{113}Ru and ^{115}Ru, the latter being the shortest-lived state ($T_{1/2} = 76(6)$ ms) ever measured at JYFLTRAP so far. The role of deformation for the systematics of masses in this region and the nature of the isomeric state in ^{115}Ru are analysed within the context of the recent global microscopic models BSkG1 [4] and BSkG2 [18, 19] that are based on self-consistent Hartree-Fock-Bogoliubov (HFB) calculations using a Skyrme energy density functional (EDF).

II. EXPERIMENTAL METHOD

The masses of neutron-rich ruthenium isotopes were studied at the Ion Guide Isotope Separator On-Line (IGISOL) facility [20] using the JYFLTRAP double Penning trap mass spectrometer [14] during two experiments. The isotopes of interest were produced in proton-induced fission by impinging a 25-MeV proton beam onto a thin target, ^{232}Th for ^{113}Ru and ^{nat}U for ^{115,117}Ru. First, the fission fragments were stopped in a helium gas cell operating close to 300 mbar from which they were extracted and guided using a sextupole ion guide [21]. Then, the produced ions were accelerated to $30q$ keV and mass-separated based on their mass-to-charge ratio using a 55 degree dipole magnet. The continuous mass-separated beam was cooled and bunched using the helium buffer gas-filled radio-frequency quadrupole cooler-buncher [22]. Finally, the ion bunches were injected into the JYFLTRAP double Penning trap.

In the first trap of JYFLTRAP, known as the purification trap, the ion bunch was cooled, centered and the ions of interest were selected utilizing the mass-selective buffer gas cooling technique [23]. After that, the purified ion sample was sent into the second trap, called the precision trap, where the mass measurements took place.

In addition, ^{113}Ru^{2+} ions were produced via the in-trap decay of ^{113}Tc ($T_{1/2} = 152(8)$ ms [24]). The ^{113}Tc$^+$ ions, produced via fission, were captured in the first trap after which, the ion motion was let to cool for 102 ms. Then a dipolar excitation on the magnetron frequency was applied for 10 ms. During the trapping time a fraction of the ^{113}Tc$^+$ ion sample β-decay to ^{113}Ru^{2+}. Quadrupolar excitation of 100 ms was used to select the ions of interest by matching the excitation frequency of ^{113}Ru^{2+} ions. After, the ^{113}Ru^{2+} ions were sent to the second trap for the precision mass measurement.

In the presence of a magnetic field of strength B, the mass m of an ion is related to its cyclotron frequency ν_c:

$$\nu_c = \frac{1}{2\pi}\frac{q}{m}B, \tag{1}$$

where q/m is the charge-to-mass ratio of the measured ion. To determine the magnetic field strength precisely, ^{133}Cs$^+$ ions from the IGISOL offline surface ion source station [25] were used as a reference for the mass measurement of ^{113,115}Ru$^+$ ground states and ^{117}Ru$^+$. For the mass measurement of isomeric states in ^{113,115}Ru, the ground-state masses were used as a reference. To account for the temporal magnetic field fluctuations, ruthenium ions and their references were measured alternately. The atomic mass m is determined from the frequency ratio $r = \nu_{c,ref.}/\nu_c$ between the singly-charged reference ions and the ions of interest:

$$m = r(m_{ref} - m_e) + m_e, \tag{2}$$

where m_e and m_{ref} are the mass of an electron and the atomic mass of the reference, respectively. The isomer excitation energies were extracted as follows:

$$E_x = (r - 1)[m_{gs} - m_e]c^2, \tag{3}$$

where m_{gs} is the ground-state atomic mass and c is the speed of light in vacuum. Contribution from electron binding energies are on the order of eV and have thus been neglected.

To measure the masses of the ground- and isomeric states in ^{113,115}Ru, the PI-ICR technique [9, 26] was utilized in the precision trap. The determination of the ion's cyclotron frequency with PI-ICR is based on a measurement of the phase difference ϕ_c between the accumulated magnetron and cyclotron motion phases projected onto a position-sensitive microchannel plate (2D MCP) detector after a phase accumulation time t_{acc}:

$$\nu_c = (\phi_c + 2\pi n)/2\pi t_{acc}, \tag{4}$$

with n being the number of the ions' full revolutions in the precision trap. We used the following accumulation times for the PI-ICR mass measurements: 557 ms for the ^{113}Ru$^+$ ground and isomeric state, 220 ms for the $q = 2+$ ions of ^{113}Ru isomeric state, 200 ms for the ^{115}Ru$^+$ ground state and 100 ms for the ^{115}Ru$^+$ isomer (see Fig. 1). The measurement pattern utilized at JYLF-TRAP is described in more detail in Refs. [26, 27] and the PI-ICR measurement technique in Ref. [9].

For ^{117}Ru$^+$, the TOF-ICR technique [15, 28] was applied. The ion's cyclotron frequency ν_c in TOF-ICR technique is determined from a time-of-flight resonance measured with the 2D MCP detector, located outside the strong magnetic field of the trap. To enhance the resolving power, the Ramsey method of time-separated oscillatory fields [29, 30] was utilised. A short 10-30-10 ms (on-off-on) pattern was used in order to minimize the decay losses (see Fig. 2).

In the mass measurement of ^{113}Ru and ^{115}Ru, the ground state and the isomer were in the precision trap
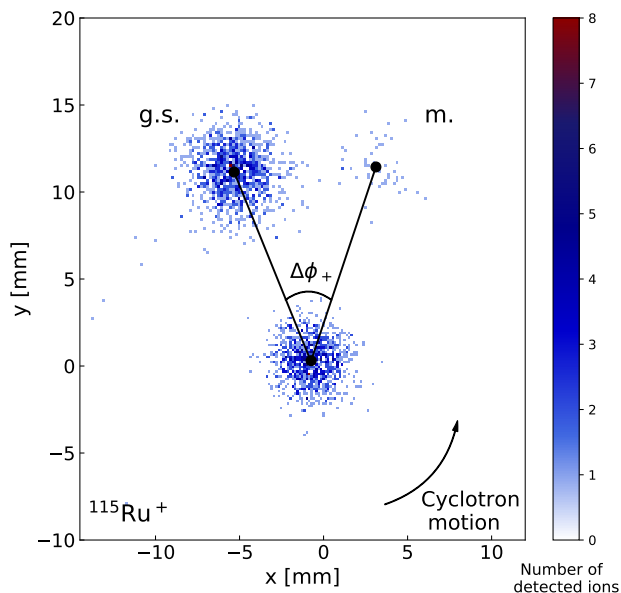
Figure 1: A PI-ICR measurement of ^{115}Ru ground state versus the isomeric state with a 100 ms accumulation time. Only the projection of cyclotron motion on the 2D MCP is shown. The angle difference $\Delta\phi_+$ leads to an excitation energy of 129(5) keV. The center spot, i.e. without any excitation, is also shown.
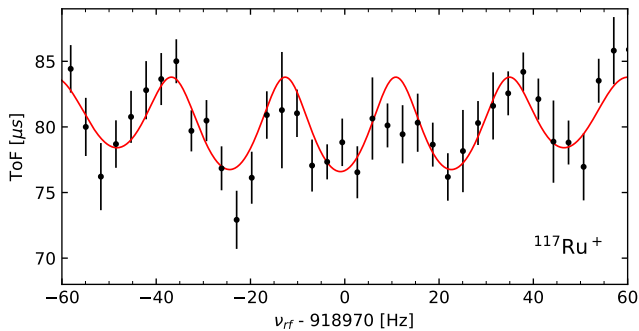

Figure 2: A TOF-ICR measurement of ^{117}Ru$^+$ using a 10-30-10 ms (on-off-on) Ramsey excitation pattern. The mean data points are shown in black, the fit of the theoretical curve [29] in red.

at the same time. It is known that when two or more ions of different masses are present in the trap simultaneously, the ion-ion interaction can cause a frequency shift [27]. To account for the ion-ion interaction, a count-rate class analysis [27, 31] was performed for the ground state ion of ^{115}Ru, while for other cases it was not statistically feasible. At JYFLTRAP the systematic uncertainty related to temporal magnetic field fluctuation has been determined to be $\delta B/B = 2.01(25) \times 10^{-12}$ min^{-1} $\times \delta t$ [27], where δt is the time between the measurements. In all of the measurements the maximum systematic uncertainty related to the temporal magnetic

field fluctuations was calculated but was found to be negligible compared to the statistical uncertainty. We added a further mass-dependent uncertainty of $\delta_m r/r = -2.35(81) \times 10^{-10}$/u $\times (m_{\text{ref}} - m)$ and a residual systematic uncertainty of $\delta_{\text{res}} r/r = 9 \times 10^{-9}$ for measurements where the A/q for the reference and ion-of-interest were not the same, i.e. when using the ^{133}Cs ions as reference [27]. A systematic uncertainty related to the magnetron phase advancement and systematic angle error were also accounted for in the PI-ICR measurements. A more detailed description on the systematic uncertainties and their determination at JYFLTRAP can be found in Ref. [27].

III. RESULTS

The ground- and isomeric-state mass of ^{113,115}Ru and the ground-state mass of ^{117}Ru are reported in detail below. The measured frequency ratios (r), mass-excess values (ME) and excitation energies (E_x) are summarized in Table I.

A. ^{113}Ru

The ground-state mass excess of ^{113}Ru, $-71874.7(15)$ keV, was determined using ^{133}Cs$^+$ ions as a reference. The isomer excitation energy, $E_x = 100.4(9)$ keV, was determined against the ground state, both as singly-charged ions produced directly in fission as well as doubly-charged ions produced via in-trap decay of ^{113}Tc$^+$ (for details see Sect. II). This yields a mass excess of $-71774.3(17)$ keV for the isomer.

The mass of ^{113}Ru has been previously measured at JYFLTRAP by Hager et al. [12], using the TOF-ICR technique with a 400-ms quadrupolar excitation time and ^{105}Ru$^+$ ions as a reference. With the AME20 [32] mass value for ^{105}Ru, this results in a mass-excess value of $-71826(12)$ keV. The revised value is in between the ground- and isomeric-state mass-excess values reported in this work (see Fig. 3.(a)) suggesting that a mixture of states was measured in Ref. [12]. A similar effect was observed in Rh isotopes, as reported in Ref. [11].

The reported mass-excess values are in agreement with the NUBASE20 evaluation [24] where it was correctly assumed that the value measured in Ref. [12] was a mixture of the ground state and an isomer at 131(33) keV. To date, the isomeric-state excitation energy was not based on direct experimental observations but on the suggestion that it has to lie in between the states at 98 and 164 keV in ^{113}Ru [37, 38]. In this work, we have confirmed this hypothesis by determining the excitation energy for the first time and by placing the isomer just above the 98-keV state (see Fig. 4). The production of both long-lived states in ^{113}Ru in the β-decay of ^{113}Tc is also in agreement with the work by Kurpeta et al. [37].

Table I: The measured frequency ratios ($r = \nu_{c,\text{ref.}}/\nu_c$) and corresponding mass-excess values determined in this work (ME) using the listed reference ions (Ref.). The mass-excess values from the AME20 [32] and NUBASE20 [24] (ME$_{\text{lit.}}$) and the differences Diff. = ME $-$ ME$_{\text{lit.}}$ are given for comparison. All the half-lives $T_{1/2}$ and spin-parity assignments J^π of ^{113,113m,117}Ru are taken from the NUBASE2020 evaluation [24] while spin-parity assignments for ^{115}Ru$^{\text{gs,m}}$ are taken from Ref. [33] and this work. # denotes that the spin is based on systematics while parentheses indicate a tentative assignment.

Ion	$T_{1/2}$ (ms)	J^π	Ref.	r	ME (keV)	ME$_{lit.}$ (keV)	E_x (keV)	$E_{x,lit.}$ (keV)	Diff. (keV)
^{113}Ru	800(50)	$(1/2^+)$	^{133}Cs	0.849647289(12)	-71874.7(15)	-71870(40)			-5(40)
^{113}Ru^m	510(30)	$(7/2^-)$	^{113}Ru	1.000000951(10)[a]	-71774.6(18)		100.0(10)		
				1.000000963(14)[b]	-71773.4(21)		101.3(15)		
			Final value: [c]	1.000000955(8)	-71774.3(17)	-71740(50)	100.4(9)	131(33)	-34(50)
^{115}Ru	318(19)	$(3/2)^+$	^{133}Cs	0.864742653(23)	-66054.7(29)	-66105(25)			50(26)
^{115}Ru^m	76(6)	$(9/2)^-$	^{115}Ru	1.000001206(47)	-65925.6(58)	-66110(90)	129(5)	82(6)	184(91)
^{117}Ru	151(3)	$3/2^+$#	^{133}Cs	0.87984374(52)	-59527(64)	-59490(430)			-37(435)

[a] Measured with 1^+ ions produced directly in fission.
[b] Measured with 2^+ ions produced in in-trap-decay of ^{113}Tc.
[c] Weighted average of frequency ratio r, from which the final ME and E_x is calculated.
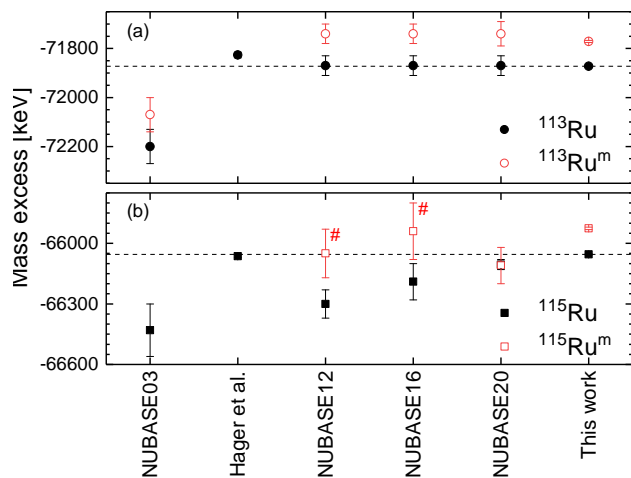

Figure 3: The mass-excess values determined in this work for the ground states (solid black symbols) and isomers (open red symbols) in (a) ^{113}Ru and (b) ^{115}Ru, in comparison with the revised JYFLTRAP value reported by Hager *et al.* [12, 32] and different NUBASE compilations [24, 34–36]. The dashed black lines show the ground-state mass-excess values determined in this work. # denotes mass-excess values based on systematics.

B. ^{115}Ru

The ground state mass excess, $-66054.7(29)$ keV, was measured against a ^{133}Cs$^+$ reference. The isomer excitation energy, $E_x = 129(5)$ keV, was determined against the ground state resulting in a mass excess of $-65925.6(58)$ keV for the isomer.

Our ground-state mass excess value is in agreement with the previous TOF-ICR-based JYFLTRAP measurement (ME $= -66064.0(69)$ [12, 32]) after adjusting for
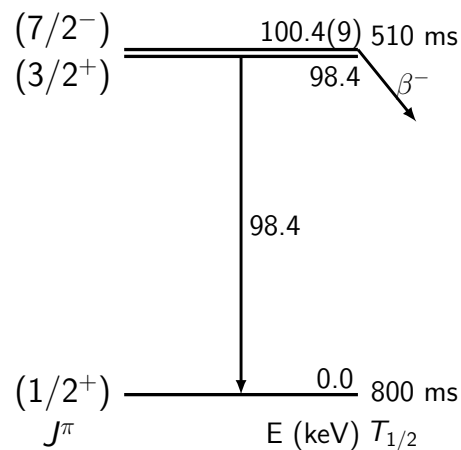

Figure 4: Proposed partial level scheme of ^{113}Ru based on this work and Ref. [39].

the updated mass of the reference ^{120}Sn ion. In our previous work we have observed that for nuclei with low-lying isomeric states the masses obtained with the TOF-ICR method are a weighted average of the ground state and the isomer masses [11]. In the case of ^{115}Ru, an apparent absence of the isomer influence on the measured mass can be explained by a relatively short half-life of the isomeric state ($T_{1/2} = 76$ ms [24]) compared to the 300 ms excitation time used in Ref. [12].

Figure 3.(b) shows a comparison of our measurement with the values reported in NUBASE evaluations on nuclear and decay properties from 2003 [34], 2012 [35], 2016 [36] and 2020 [24] as well as the revised JYFLTRAP value of Ref. [12]. Changes between different editions of NUBASE can be explained as due to varying input data. In NUBASE03 [34], the only entry for ^{115}Ru was from a β-decay end-point energy study [40]. After the JYFLTRAP measurement by Hager et al. [12], a long-

lived isomeric state in ^{115}Ru was discovered [41], and the evaluators of NUBASE12 [35] applied a special procedure for mixtures of isomeric states assuming the excitation energy to be 250(100) keV. In NUBASE16 [36], the β-decay end-point energy study was excluded from the global fit and the only remaining information was from Ref. [12]. Finally, in NUBASE20 [24], the energy of the isomeric state was adjusted to 82(6) keV based on the value originally proposed in Ref. [41]. However, the isomeric-state excitation energy seems not to be taken into account for the mass-excess value of the isomer but only for its uncertainty.

C. ^{117}Ru

The value determined in this work, $-59527(64)$ keV, is in agreement with AME20 [32] and it is almost seven times more precise. The mass-excess value adopted in AME20, $-59490(430)$ keV [32], is based on storage-ring measurements [16, 42] but with the uncertainty artificially increased by evaluators [17]. The only known isomeric state has a half-life of 2.49(6) μs [24] which is much shorter than the measurement cycle used in this work.

IV. DISCUSSION

In this section, we discuss the experimental results and compare them to the BSkG-family of models of nuclear structure [4, 18, 19]. This section is organised as follows: we first establish the theoretical framework in Sec. IV A and then proceed to study first the trends of the ground state (g.s.) binding energies of neutron-rich Ru isotopes in Sec. IV B. Sec. IV C discusses the isomeric state in ^{115}Ru as well as the implication of our measurement of its excitation energy.

A. Theoretical framework

The BSkG-family of models responds to the need for reliable data on the structural properties of exotic nuclei in different fields of research and in astrophysics in particular. These models are based on an empirical Energy Density Functional (EDF) of Skyrme type that models the effective in-medium nucleon-nucleon interaction. The concept of an EDF allows for a global yet microscopic description of all relevant quantities at a reasonable computational cost. The coupling constants of the EDF are the main element of phenomenology in this type of model and have to be adjusted to experimental data. Since binding energies are crucial ingredients for the modeling of nuclear reactions, the ensemble of known nuclear masses is a key ingredient of the parameter adjustment of the BSkG models. Because of this, these models reach root-mean-square (rms) deviations better than 800 keV on the

thousands of masses included in AME20 [32]. This performance is not at all competitive with the uncertainties of the measurements we report on here, but it nevertheless reflects the state-of-the-art in global mass modeling: it is only matched by some of the older BSk models that were adjusted in the same spirit [43], microscopic-macroscopic approaches [44] and empirical models [45]. The latter two types of model become particularly accurate when refined with machine learning techniques [46], but either do not extend their predictions to other observables or struggle to describe them with the same parameter values deduced from the masses.

The BSkG-family so far counts two entries: BSkG1 [4] and BSkG2 [18, 19]. Both models combine a description of many hundreds of measured charge radii and realistic predictions for the properties of infinite nuclear matter with a description of the AME20 masses with similar accuracy (rms deviations of 741 and 678 keV, respectively). Although some of the BSk models reach an rms deviation below 600 keV [43], BSkG1 and BSkG2 are better adapted to study the neutron-rich Ru isotopes as they rely on a three-dimensional representation of the nucleus, thereby accomodating naturally the triaxial deformation that is known to be particularly relevant for this region of the nuclear chart. BSkG2 incorporates a full treatment of the so-called 'time-odd' terms in an EDF [18] and improves systematically on the description of fission properties compared to its predecessor [19]. Since (i) the inclusion of the time-odd terms did not result in a meaningful improvement of our global description of binding energies and (ii) fission properties are not directly related to the masses, *a priori* we expect BSkG1 and BSkG2 to be of roughly equal quality for the task at hand and therefore we will compare experiment to both models in what follows.

Large-scale EDF-based models of nuclear structure such as the BSk- and BSkG-models describe the nucleus in terms of one single product wavefunction, typically of the Bogoliubov type. The simplicity of such an *ansatz*, as compared to the complexity of the many-body problem, is compensated for by allowing for spontaneous symmetry breaking in the mean fields. By considering such deformed configurations EDF-based models can account for a large part of the effects of nuclear collectivity on bulk properties such as masses while remaining at the mean-field level and thus keeping calculations tractable. Nevertheless, symmetry breaking comes at considerable computational cost. For all calculations that we report on, we employed the MOCCa code [47] to represent the single-nucleon wavefunctions on a three-dimensional coordinate mesh. All numerical parameters such as the mesh point spacing are identical to those employed in the adjustment of both BSkG models [4, 18].

In a three-dimensional calculation, the quadrupole deformation of a nucleus of mass A can be described by way of the (dimensionless) deformation β_2 and the triaxiality

angle γ, defined as

$$\beta_2 = \frac{4\pi}{3R^2A}\sqrt{Q_{20}^2 + 2Q_{22}^2}\,, \qquad (5)$$

$$\gamma = \mathrm{atan}\left(\sqrt{2}Q_{22}/Q_{20}\right)\,, \qquad (6)$$

where $R = 1.2A^{1/3}$ fm. The quadrupole moments Q_{20} and Q_{22} are defined in terms of integrals of the total nuclear density and spherical harmonics, see for instance Ref. [4]. Axially symmetric prolate and oblate shapes correspond to $\gamma = 0°$ and $60°$, respectively, while intermediate values of the triaxiality angle in between those two extremes indicate triaxial shapes.

We show in Fig. 5 the potential energy surface (PES) of ^{115}Ru in the $\beta - \gamma$ plane as obtained with BSkG2, calculations with BSkG1 leading to a similar PES. Since ^{115}Ru has an odd number of nucleons, Fig. 5 shows the result of so-called 'false-vacuum' calculations, where we constrained the expected number of neutrons to $\langle N \rangle = 71$, but otherwise treated the nucleus as if it were even-even. We emphasize that all the calculations for which we report masses do not rely on this approximation: for both BSkG1 and BSkG2 our treatment of the odd-mass Ru isotopes includes self-consistent blocking of a neutron quasiparticle. For BSkG2, we also include the energy contribution of the finite spin and current densities induced by the presence of the odd neutrons. For more details on our treatment of odd-mass and odd-odd nuclei, see the discussion in Ref. [18]. A complete calculation for ^{115}Ru that includes blocking leads to the deformation shown as a black star on Fig. 5; its offset with respect to the minimum of the false-vacuum calculations is due to the polarisation induced by the odd neutron.

Qualitatively, the false-vacuum PES of ^{115}Ru looks similar to the PES of ^{112}Rh that we discussed in Ref. [11]: we observe a somewhat broad triaxial minimum near $\gamma = 30°$ of significant quadrupole deformation. Close inspection reveals some quantitative differences: $\beta_2 \sim 0.27$ is here somewhat smaller than the value 0.3 obtained for ^{112}Rh for instance. Another difference is the energy gain due to triaxiality: the difference between the oblate saddle point and the minimum on Fig. 5 is about 800 keV, while it exceeds 1 MeV for ^{112}Rh. This can be linked to the four additional neutrons in ^{115}Ru compared to ^{112}Rh: as we approach the $N = 82$ shell closure, the neutrons have less freedom to exploit quadrupole correlations and the importance of (static) quadrupole deformation in general and triaxial deformation in particular diminishes.

B. The g.s. masses of Ru isotopes and their trends

For the chain of Ru isotopes between $N = 65$ and $N = 73$, BSkG1 reproduces the absolute g.s. binding energies best: the deviation with respect to experiment for the absolute mass excesses averages to 360 keV and never exceeds 640 keV. The performance of BSkG2 is not
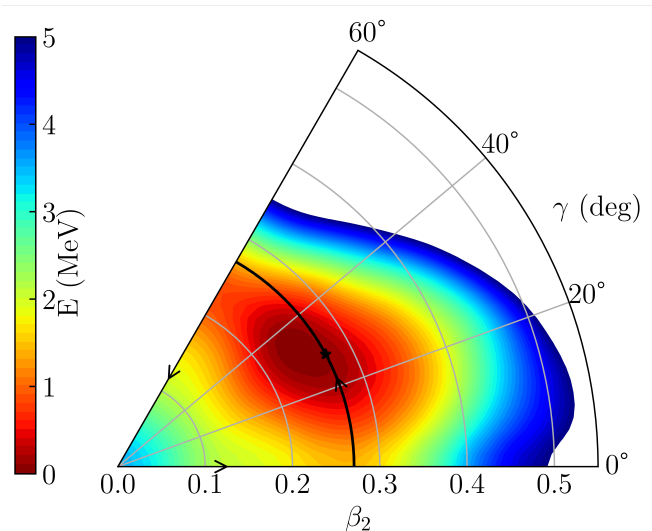

Figure 5: Potential energy surface in the (β, γ) - plane for false-vacuum calculations (see text) of ^{115}Ru with BSkG2. The trajectory followed by the Nilsson diagram in Fig. 9 is indicated by black arrows. The location of the minimum obtained in a complete calculation of ^{115}Ru is indicated by a black star.

as good: an average deviation of 650 keV with a deviation of up to 1.175 MeV for ^{115}Ru. Interestingly, the sign of the deviation is consistent: both models overbind these Ru isotopes and hence produce mass excesses that are too large in absolute size. As discussed before, the experimental uncertainties are several orders of magnitude beyond the accuracy of global models like BSkG1 and BSkG2: instead of comparing absolute masses in more detail, we will focus in what follows primarily on the trends of mass differences.

We start with the two-neutron separation energy S_{2n}, defined as:

$$S_{2n}(Z,N) = ME(Z, N-2) - ME(Z,N) + 2ME(0,1), \qquad (7)$$

where $ME(Z,N)$ is the mass excess of a nucleus with Z protons and N neutrons. The top panel of Fig. 6 compares the S_{2n} values derived from the newly measured masses to the values reported in the AME20 [32] evaluation and the two mass models. We also show the results of the less general calculations with BSkG1 reported on in Ref. [4, 11], which restrict the nucleus to axially symmetric configurations.

For the less exotic ^{109,111,113}Ru, all three calculations with BSkG-models reproduce the general trend of the experimental S_{2n} rather well, although deviations on the order of several hundred keV are clearly visible. For the BSkG1 model, the description of the more neutron-rich isotopes follows the trend of the more stable ones, systematically overestimating the S_{2n} values by a small value. BSkG2 also overestimates the separation energies and describes their overall trend, but with deviations that are
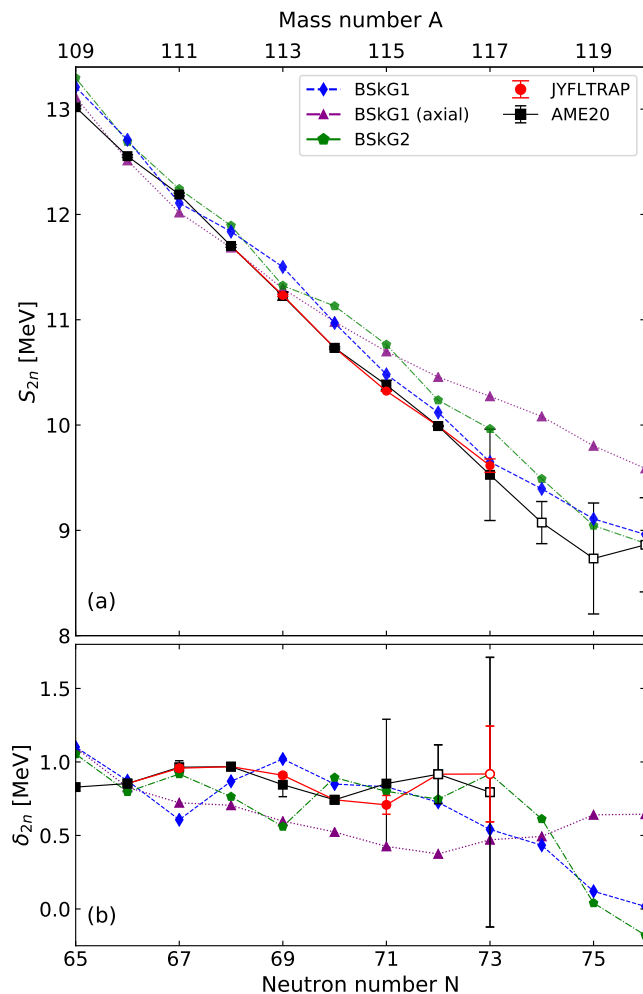
Figure 6: Comparison of mass differences along the Ru isotopic chain: experimental values either as tabulated in AME20 (black squares) or updated with the results of our new measurements (red circles) versus calculated values obtained with BSkG1 (blue diamonds), BSkG1 axial (purple triangles, see text) and BSkG2 (green pentagons). Open markers for the experimental results represent values at least partially based on extrapolated mass values from AME20 [32]. Top panel: two-neutron separation energies S_{2n}. Bottom panel: two-neutron shell gaps δ_{2n}.

somewhat larger than those of its predecessor. Calculations with BSkG1 that are restricted to axial shapes, however, entirely miss the experimental trend.

We can furthermore discuss the slope of the S_{2n} curve by introducing the empirical two-neutron shell gaps δ_{2n}:

$$\delta_{2n}(Z, N) = S_{2n}(Z, N) - S_{2n}(Z, N + 2), \qquad (8)$$

which we show in the bottom panel of Fig. 6. The new JYFLTRAP measurement for ^{115}Ru clearly establishes that the slope of the S_{2n} in this isotopic chain evolves smoothly at least until $N = 71$. Although the corresponding curves are less regular, the BSkG1 and BSkG2

results produce δ_{2n} values that remain close to experiment up to $N = 71$. For the heavier $N = 72$, 73 and 74 isotopes, whose experimental δ_{2n} values are at least partially based on extrapolated AME20 values, the two models predict no major change in slope either. It is only for $N = 75 - 76$ that BSkG1 and BSkG2 predict a change in slope that is correlated with the disappearance of triaxial deformation for $N \geq 76$. For ^{120}Ru and even more neutron-rich isotopes, the models predict axially symmetric prolate shapes with deformation that gradually diminishes towards $N = 82$.

Finally, we discuss the three-point neutron gaps $\Delta_n^{(3)}(Z, N)$:

$$\Delta_n^{(3)}(Z, N) = \frac{(-1)^N}{2} \big[ME(Z, N + 1) \\ + ME(Z, N - 1) - 2ME(Z, N) \big]. \qquad (9)$$

This quantity estimates the average distance between the curves that interpolate the masses of the even-N and odd-N isotopes, respectively, as a function of neutron number. It is particularly sensitive to the neutron pairing, but it can also be affected by variations in the structure of these isotopes with N. The new experimental results confirm the continuation of the trend of less exotic isotopes: the three-point gaps for the even-N isotopes at $N = 66$, 68, 70, and 72 are all equal within error-bars. For $N = 70$, our new result actually brings the $\Delta_n^{(3)}$ value more in line with this trend. The updated value of $\Delta_n^{(3)}$ for $N = 71$ falls significantly out of the uncertainty range of AME20, which reflects the lack of accuracy of the AME20 estimate for the excitation energy of the isomeric state of ^{115}Ru. Nevertheless, it is not dramatically larger than the gap values for $N = 69$ and $N = 71$.

The BSkG2 model generally overestimates $\Delta_n^{(3)}$ and its curve exhibits features at $N = 68$, 69, and 70 that are not seen in the experimental data. BSkG1 on the other hand, provides a fair description of the experimental results, whether including or not triaxial deformation. Yet even this model is clearly not without flaws: the deviation of the full calculation w.r.t. experiment grows with N from $N = 69$ onwards. In this respect, the deviation between the calculated BSkG1 value and the updated point at $N = 73$ (which incorporates the recommended AME20 binding energy for ^{118}Ru) seems ominous. We note in passing that both BSkG models systematically overestimate $\Delta_n^{(3)}$ along odd-Z isotopic chains, which we discovered for the first time during the study of neighbouring Rh isotopes in Ref. [11]. Similarly, both models overestimate the calculated three-point proton gaps in odd-N isotopic chains. The common origin of these issues is the failure of both models to account for a small amount of binding energy in odd-odd nuclei that is usually ascribed to the residual interaction between the two odd nucleons, see Ref. [18]. This issue does not affect our discussion here, but it explains why both models describe much better the three-point neutron gaps in even-Z Ru isotopes than in odd-Z Rh isotopes.
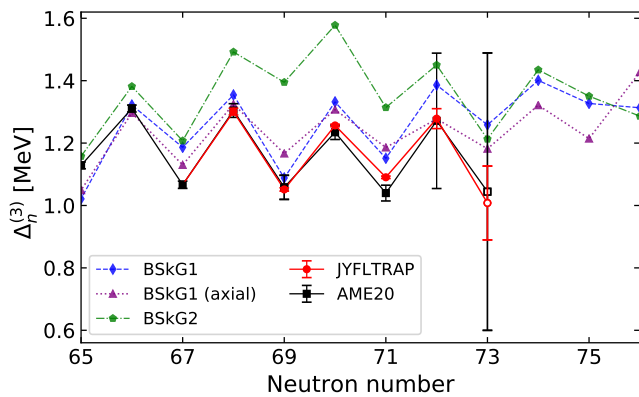
Figure 7: Same as for Fig. 6, but for the three-point neutron gap $\Delta_n^{(3)}$.

We have established that performance of BSkG2 for the $N = 65 - 71$ Ru isotopes is worse than that of BSkG1 for absolute masses as well as all mass differences discussed. Since these models are the result of a complicated parameter adjustment which is global in scope, it is hard to pinpoint a particular source of this (local) deficiency. As we remarked in the previous section, we did not a priori expect that BSkG2 would offer an improved description of the measured masses. Although the difference we observe between models indicates BSkG1 as the tool of choice for future studies of this region, this does not imply that BSkG2 is a step backwards compared to its predecessor. The newer model presents a different compromise on the very large number of observables included in the parameter adjustment, leading to a worse description of the nuclei we study here but also to an improved description of other observables [18].

To close this section, we note again that our new measurement indicates a rather uneventful continuation to $N = 71$ of the trends of binding energies and mass differences as established for less exotic isotopes. This can be interpreted as experimental confirmation that the structural evolution of nuclei in this isotopic chain is smooth rather than dramatic. From the point of view of the BSkG models this was expected: from $N = 55$ onwards, the Ru isotopes exhibit triaxial deformation that smoothly evolves with neutron number until $N = 76$. The authors of Ref. [33] relied on the Woods-Saxon single-particle spectrum of Ref. [48] to interpret the change in (tentative) ground state spin assignment in $^{113-115}$Ru ($(1/2)^+$ and $(3/2)^+$, respectively) as a sign of a shape transition from prolate to oblate deformation. The trend of masses and mass differences does not seem to support such scenario.

C. The isomer in ^{115}Ru

The isomeric state in ^{115}Ru was reported for the first time in Ref. [41], discussing the analysis of a β decay

experiment. The authors observed that the 61.7-keV γ ray is not in coincidence with a β particle or any other γ ray. In addition, the half-life extracted from this transition, $T_{1/2} = 76(6)$ ms, differed from the half-life obtained for the ^{115}Ru ground-state ($T_{1/2} = 318(19)$ ms). Consequently, it was assumed that the isomeric state de-excites via an unobserved γ ray having energy below Ru K x-rays ($E \approx 20$ keV), which we label γ_1, followed by an emission of the 61.7-keV γ ray, labeled as γ_2.

With the assumption of the energy of γ_1 being below 20 keV, the observed ruthenium K x-rays were associated solely with the emission of K internal conversion electrons from the γ_2 transition. This observation enabled a determination of the γ_2 K-internal conversion coefficient ($\alpha_K = 2.7(6)$ [41]) by calculating the ratio of the ruthenium K x-rays and the γ_2 transitions.
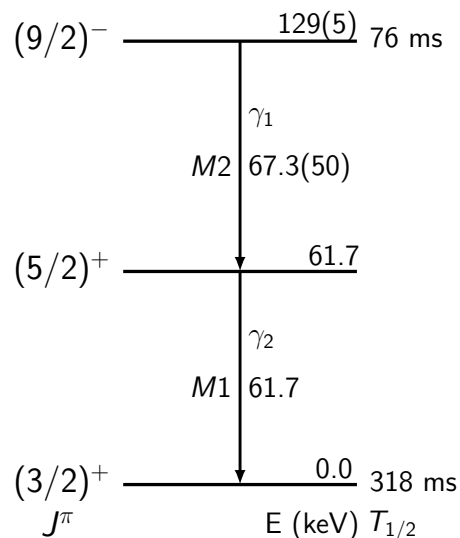

Figure 8: Proposed level scheme of ^{115}Ru based on this work and Refs. [33, 41].

The new isomer excitation energy reported in this work renders previous calculations incorrect. However, if one assumes that (i) the total intensity (γ rays and internal conversion electrons emission) of γ_1 and γ_2 is identical, (ii) γ_1 has a pure $M2$ character and (iii) γ_2 has a pure $M1$ character, the observed ratio of the ruthenium K x-rays to γ_2 would be equal to 2.8(8). Any other assumptions regarding the multipolarity of both transitions would lead to a ratio that differs significantly from the experimental value of 2.7(6) [41]. Therefore, we propose $M2$ and $M1$ multipolarities for γ_1 and γ_2, respectively. By assigning $(3/2)^+$ as the ground-state spin-parity as proposed in [33] from a detailed β-decay spectrsocopy experiment of ^{115}Ru, a tentative $(9/2)^-$ isomer assignment can be adopted, see Fig. 8.

A precise description of the level scheme of ^{115}Ru is beyond the capabilities of current large-scale models such as BSkG1 and BSkG2, but we can use them to gain a qualitative understanding of the existence of the isomeric
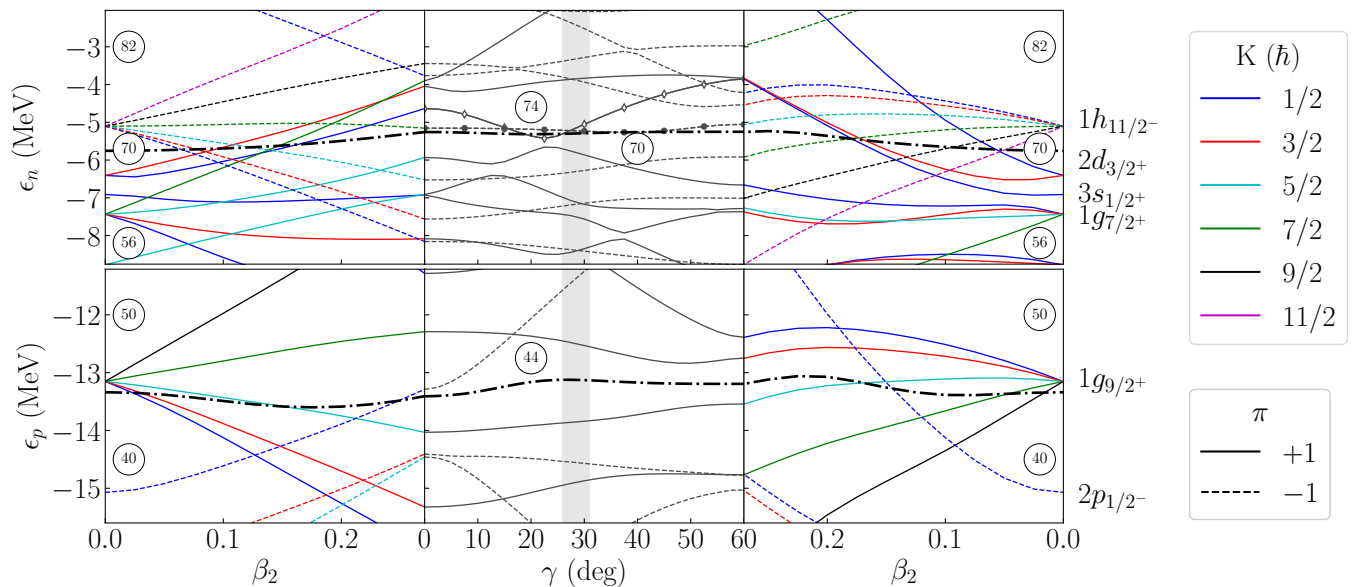
Figure 9: (Color online) Eigenvalues of the single-particle Hamiltonian for neutrons (top row) and protons (bottom row) along the path in the $\beta - \gamma$ plane indicated by arrows in Fig. 5 for ^{115}Ru (see text for details). The Fermi energy is drawn as a dash-dotted line, while full (dashed) lines indicate single-particle levels of positive (negative) parity. The three indicated regions correspond to axially symmetric prolate shape with (left column), fixed total quadrupole deformation $\beta_2 = 0.27$ with varying γ (center column) and axially oblate shape with $\gamma = 60°$ (right column). The vertical gray band in the center panels is centered at $\gamma = 28.4°$, the value obtained in a complete, i.e. blocked, calculation of ^{115}Ru. The quantum numbers of the shells at sphericity are indicated on the right-hand-side. Two-neutron levels near the Fermi energy are highlighted by markers in the middle column: these are the negative and positive parity levels referred to in the text, respectively, as $|\diamond\rangle$ and $|\bullet\rangle$.

state. To this end, we show in Fig. 9, the Fermi energy and the single-particle energies for both neutrons and protons obtained in false-vacuum calculations for ^{115}Ru with BSkG2 along the trajectory in the $\beta - \gamma$ plane indicated by the arrows in Fig. 5. Although symmetry-breaking allows models such as BSkG1 and BSkG2 to grasp a significant part of the effect of collectivity on nuclear structure, here is where we pay the price: we can no longer use the quantum numbers of an operator associated with a broken symmetry to label single-particle states. At the spherical point, on the utmost left and right of Fig. 9, no symmetry is broken and all single-particle levels are simultaneously eigenstates of three operators with three associated quantum numbers: the angular momentum squared $\hat{J}^2$ with quantum number J, parity $\hat{P}$ with quantum number π and the z-component of the angular momentum $\hat{J}_z$ with quantum number K. The quantum numbers of the orbitals at the spherical point are indicated in the traditional spectroscopic notation on the right of Fig. 9. Along the first segment of the path on Fig. 5, we break rotational symmetry but conserve axial symmetry: the levels in the left-most column are no longer eigenstates of $\hat{J}^2$ but retain the K quantum number[1], which is indicated by colors on Fig. 5. When

exploring finite values of γ along the second segment of the path on Fig. 5 axial symmetry is broken and K can no longer be used to label the single-particle states, hence the absence of colors in the middle column of Fig. 9. The final segment of the path explores oblate shapes which are axially symmetric, such that levels in the right column of Fig. 9 can again be color-coded. For all our calculations we conserve parity, such that π is a good single-particle quantum number along the entire path that we can use to distinguish between levels of positive (full lines) and negative parity (dashed lines) in all columns of Fig. 9.

This loss of single-particle quantum numbers also translates to the many-body state: the BSkG-models cannot currently offer definite angular momentum assignments for calculated ground states for odd-mass and odd-odd nuclei. Doing so would require symmetry-restoration techniques [50] whose application is presently still out of the scope of global models for reasons of their numerical cost and because of formal issues with the type of EDF assumed for the BSkG models. We are however not entirely without options: we can calculate expectation values $\langle i|\hat{J}_z|i\rangle$, which will not be half-integer multiples of $\hbar$ but which nevertheless tell us something about the

_____

[1] For axially symmetric configurations, we always align the symmetry axis with the z-axis in the simulation volume.

angular momentum of the single-particle state $|i\rangle$. In the limit of a non-interacting particle-core model of the ground states of odd-mass Ru isotopes, the angular momentum expectation value of the odd neutron will also be the expectation value of angular momentum of the many-body state.

We discussed a qualitatively similar Nilsson diagram obtained for ^{112}Rh in Ref. [11] and repeat here a few observations that are common to both nuclei before discussing the isomer. Local minima in the PES correspond to deformations for which the single-particle level density near the Fermi energy is low: for nuclei with $Z = 43$, 44, and 45, the protons drive the appearance of triaxial deformation since their single-particle spectrum at $\beta_2 \sim 0.28 - 0.3, \gamma \sim 30°$ is very sparse. In this region of the PES only positive parity state orbitals are near the Fermi energy, matching the parity assignments of all even-N Tc and Rh isotopes. The single-particle level density of the neutrons on the other hand is much higher, resulting in a closely-spaced set of levels with different parities near the Fermi energy.

We interpret the close interleaving of positive and negative parity neutron states with different angular momentum content as the origin of the isomeric state in ^{115}Ru. Two neutron states are nearly degenerate near the Fermi energy at the location of the minimum of the PES: these are highlighted in the middle column of Fig. 9 and we will refer to them by their markers: $|\diamond\rangle$ and $|\bullet\rangle$. These levels differ in their parity, but also in their angular momentum content: near $\gamma = 30°$ the positive parity state has an average $\langle \diamond | \hat{J}_z | \diamond \rangle \approx 0.73\hbar$, while that of the negative parity state is significantly larger, $\langle \bullet | \hat{J}_z | \bullet \rangle \approx 4.13\hbar$. Since the odd-neutron can be assigned to each of these levels, we expect the appearance of two low-lying levels with opposite parity in the spectrum of ^{115}Ru that are close in energy yet differ substantially in their angular momentum, hence one of them being an isomer. Finally, the $(5/2)^+$ state in between the g.s. and the isomer on Fig. 8 could be rotational in character: taking the calculated moments of inertia of ^{115}Ru and under the assumption of a rigid triaxial rotor, a $1\hbar$ change in total angular momentum corresponds to about 88 keV of excitation energy.

Moving beyond simple arguments based on a non-interacting particle-core picture and the Nilsson diagram, we explicitly calculated the lowest-lying configuration of each parity in ^{115}Ru with both BSkG1 and BSkG2. One of these is the calculated g.s. , whose binding energy figured in the previous section: for BSkG1 this is the state with positive parity and for BSkG2 this is the one with negative parity. In both cases, we find an excited state of opposite parity at low excitation energy; 33 keV and 90 keV for BSkG1 and BSkG2 respectively. For BSkG2, we have direct access to the average many-body angular momentum along the z-axis: a small value $\langle J_z \rangle \approx 0.7\hbar$ for the positive parity state and a large one, $\langle J_z \rangle \approx 3.1\hbar$, for the negative parity state. These calculations support our conclusions drawn from the Nilsson diagram and the cal-

culated excitation energy are very roughly comparable to the experimental isomer excitation energy. These results should not be overinterpreted: all relevant energy differences are very small and the neutron spectrum in Fig. 9 is very complicated. Small changes to any aspect of the model will affect the precise location of level crossings and therefore the ordering of levels. Our calculated excitation energies should thus not be taken as a precise prediction, but rather as a confirmation that two states of opposite parity that differ little in energy can be constructed with different angular momentum content. Predicting their ordering and energy difference with accuracy is beyond BSkG1 and BSkG2, or for that matter, any large-scale model that we are aware of.

The same mechanism can be used to interpret the isomerism in nearby $N = 71$ isotones: isomeric states with half-lives on the order of seconds or longer have been observed in ^{116}Rh, ^{118}Ag and ^{119}Cd whereas shorter-lived isomeric states are known in ^{114}Tc and ^{117}Pd [24]. For $Z = 42 - 46$, one can expect from Fig. 9 triaxial deformation with a sparse proton single-particle spectrum and two low-lying states arising from neutron orbitals of different parities. The experimental systematics extend much further: in the entire range of $Z = 43 - 57$, low-lying isomers have been observed [24]. A more in-depth study of isomerism in the $N = 71$ isotones would certainly require more diagrams like Fig. 9 for larger proton numbers and is outside of the scope of this study. Nevertheless, we remark that both BSkG1 and BSkG2 predict triaxial deformation for almost all $N = 71$ isotones in the range $Z = 40 - 60^2$.

V. SUMMARY

The masses of ^{113,115,117}Ru have been measured using the Penning-trap mass spectrometry at the JYFLTRAP double Penning trap. The ground- and isomeric states in ^{113,115}Ru have been separated and masses measured using the PI-ICR technique. The isomer excitation energies were determined directly for the first time. The high-precision measurement reported in this work place the $(7/2)^-$ isomeric state in ^{113}Ru at 100.4(9) keV, just above the $(3/2^+)$ level at 98.4(3) keV [39], but still in agreement with the previous prediction of 133(33) keV [24]. For ^{115m}Ru, the excitation energy was found to be 129(5) keV, which is significantly larger than proposed in Ref. [41] or the value listed in the most recent NUBASE evaluation, 82(6) keV [24].

The determined ground-state masses of ^{113,117}Ru are in excellent agreement with the atomic mass evaluation [32]. For ^{115}Ru, we report a mass-excess value which is 50(26) keV larger than reported in AME20 [32]. However, it is in agreement with the previous JYFLTRAP

---

^{2} The only exceptions occur for BSkG1 near the $Z = 50$ shell closure: ^{118}Ag, ^{119}Cd, ^{120}In and ^{121}Sn remain axially symmetric.

mass measurement by Hager et al. [12]. With the mass values determined in this work, the trend in the two-neutron separation energies continues smoothly.

The experimental results have been compared with the global BSkG1 [4] and BSkG2 [18, 19] models, which allow for triaxially deformed shapes. Detailed calculations were performed for the structure of ^{115}Ru. In the predicted triaxial deformation, the proton single-particle spectrum was found to be sparse and the predicted low-lying states arise from neutron orbitals with different parities. More systematic studies on the isomeric states in this triaxially deformed region would be needed to shed more light on the reasons for the isomerism in these nuclei.

[1] P. E. Garrett, M. Zielińska, and E. Clément, Progress in Particle and Nuclear Physics **124**, 103931 (2022), ISSN 0146-6410, URL https://www.sciencedirect.com/science/article/pii/S0146641021000922.

[2] J. Srebrny, T. Czosnyka, C. Droste, S. Rohoziński, L. Próchniak, K. Zając, K. Pomorski, D. Cline, C. Wu, A. Bäcklin, et al., Nuclear Physics A **766**, 25 (2006), ISSN 03759474, URL https://linkinghub.elsevier.com/retrieve/pii/S0375947405012029.

[3] P. Möller, R. Bengtsson, B. Gillis Carlsson, P. Olivius, and T. Ichikawa, Phys. Rev. Lett. **97**, 162502 (2006), URL https://doi.org/10.1103/PhysRevLett.97.162502.

[4] G. Scamps, S. Goriely, E. Olsen, M. Bender, and W. Ryssens, The European Physical Journal A **57**, 333 (2021), ISSN 1434-601X, URL https://doi.org/10.1140/epja/s10050-021-00642-1.

[5] U. Hager, T. Eronen, J. Hakala, A. Jokinen, V. Kolhinen, S. Kopecky, I. Moore, A. Nieminen, M. Oinonen, S. Rinta-Antila, et al., Phys. Rev. Lett. **96**, 042504 (2006), URL https://doi.org/10.1103/PhysRevLett.96.042504.

[6] S. Naimi, G. Audi, D. Beck, K. Blaum, C. Böhm, C. Borgmann, M. Breitenfeldt, S. George, F. Herfurth, A. Herlert, et al., Phys. Rev. Lett. **105**, 032502 (2010), URL https://link.aps.org/doi/10.1103/PhysRevLett.105.032502.

[7] A. Chaudhuri, C. Andreoiu, T. Brunner, U. Chowdhury, S. Ettenauer, A. T. Gallant, G. Gwinner, A. A. Kwiatkowski, A. Lennarz, D. Lunney, et al., Phys. Rev. C **88**, 054317 (2013), URL https://link.aps.org/doi/10.1103/PhysRevC.88.054317.

[8] S. Eliseev, K. Blaum, M. Block, C. Droese, M. Goncharov, E. Minaya Ramirez, D. A. Nesterenko, Y. N. Novikov, and L. Schweikhard, Phys. Rev. Lett. **110**, 082501 (2013), URL https://link.aps.org/doi/10.1103/PhysRevLett.110.082501.

[9] S. Eliseev, K. Blaum, M. Block, A. Dörr, C. Droese, T. Eronen, M. Goncharov, M. Höcker, J. Ketter, E. Minaya Ramirez, et al., Appl. Phys. B **114**, 107 (2014), URL https://doi.org/10.1007/s00340-013-5621-0.

[10] D. Nesterenko, A. Kankainen, J. Kostensalo, C. Nobs, A. Bruce, O. Beliuskina, L. Canete, T. Eronen, E. Gamba, S. Geldhof, et al., Physics Letters B **808**, 135642 (2020), ISSN 0370-2693, URL https://www.sciencedirect.com/science/article/pii/S0370269320304457.

[11] M. Hukkanen, W. Ryssens, P. Ascher, M. Bender, T. Eronen, S. Grévy, A. Kankainen, M. Stryjczyk, L. Al Ayoubi, S. Ayet, et al., Phys. Rev. C **107**, 014306 (2023), URL https://link.aps.org/doi/10.1103/PhysRevC.107.014306.

[12] U. Hager, V.-V. Elomaa, T. Eronen, J. Hakala, A. Jokinen, A. Kankainen, S. Rahaman, S. Rinta-Antila, A. Saastamoinen, T. Sonoda, et al., Phys. Rev. C **75**, 064302 (2007), URL https://link.aps.org/doi/10.1103/PhysRevC.75.064302.

[13] J. Hakala, R. Rodríguez-Guzmán, V. V. Elomaa, T. Eronen, A. Jokinen, V. S. Kolhinen, I. D. Moore, H. Penttilä, M. Reponen, J. Rissanen, et al., The European Physical Journal A **47**, 129 (2011), ISSN 1434-601X, URL https://doi.org/10.1140/epja/i2011-11129-9.

[14] T. Eronen, V. Kolhinen, V.-V. Elomaa, D. Gorelov, U. Hager, J. Hakala, A. Jokinen, A. Kankainen, P. Karvonen, S. Kopecky, et al., Eur. Phys. J. A **48**, 46 (2012), URL https://doi.org/10.1140/epja/i2012-12046-1.

[15] M. König, G. Bollen, H.-J. Kluge, T. Otto, and J. Szerypo, Int. J. Mass Spectrom. Ion Process **142**, 95 (1995), URL https://doi.org/10.1016/0168-1176(95)04146-C.

[16] R. Knöbel, M. Diwisch, H. Geissel, Y. A. Litvinov, Z. Patyk, W. R. Plaß, C. Scheidenberger, B. Sun, H. Weick, F. Bosch, et al., The European Physical Journal A **52**, 138 (2016), ISSN 1434-601X, URL https://doi.org/10.1140/epja/i2016-16138-6.

[17] W. Huang, M. Wang, F. Kondev, G. Audi, and S. Naimi, Chinese Physics C **45**, 030002 (2021), URL https://dx.doi.org/10.1088/1674-1137/abddb0.

[18] W. Ryssens, G. Scamps, S. Goriely, and M. Bender, The European Physical Journal A **58**, 246 (2022), ISSN 1434-601X, URL https://doi.org/10.1140/epja/s10050-022-00894-5.

[19] W. Ryssens, G. Scamps, S. Goriely, and M. Bender, Eur. Phys. J. A **59**, 96 (2023), ISSN 1434-601X, URL https://doi.org/10.1140/epja/s10050-023-01002-x.

[20] I. D. Moore, T. Eronen, D. Gorelov, J. Hakala, A. Jokinen, A. Kankainen, V. Kolhinen, J. Koponen, H. Penttilä, I. Pohjalainen, et al., Nuc. Inst. and Meth. in Physics Research Section B: Beam Interactions with Materials and Atoms **317**, 208 (2013), URL https://doi.org/10.1016/j.nimb.2013.06.036.

[21] P. Karvonen, I. D. Moore, T. Sonoda, T. Kessler, H. Penttilä, K. Peräjärvi, P. Ronkanen, and J. Äystö, Nucl. Instrum. Meth. Phys. Res. B **266**, 4794 (2008), URL https://doi.org/10.1016/j.nimb.2008.07.022.

[22] A. Nieminen, J. Huikari, A. Jokinen, J. Äystö, P. Campbell, and E. C. A. Cochrane, Nucl. Instrum. Meth. Phys. Res. A **469**, 244 (2001), URL https://doi.org/10.1016/S0168-9002(00)00750-6.

[23] G. Savard, S. Becker, G. Bollen, H.-J. Kluge, R. B. Moore, T. Otto, L. Schweikhard, H. Stolzenberg, and U. Wiess, Phys. Lett. A **158**, 247 (1991), URL https://doi.org/10.1016/0375-9601(91)91008-2.

[24] F. Kondev, M. Wang, W. Huang, S. Naimi, and G. Audi, Chinese Physics C **45**, 030001 (2021), URL https://doi.org/10.1088/1674-1137/abddae.

[25] M. Vilén, L. Canete, B. Cheal, A. Giatzoglou, R. de Groote, A. de Roubin, T. Eronen, S. Geldhof, A. Jokinen, A. Kankainen, et al., Nuclear Instruments and Methods in Physics Research Section B: Beam Interactions with Materials and Atoms **463**, 382 (2020), ISSN 0168-583X, URL https://www.sciencedirect.com/science/article/pii/S0168583X19302344.

[26] D. A. Nesterenko, T. Eronen, A. Kankainen, L. Canete, A. Jokinen, I. D. Moore, H. Penttilä, S. Rinta-Antila, A. de Roubin, and M. Vilen, Eur. Phys. J. A **54**, 154 (2018), URL https://doi.org/10.1140/epja/i2018-12589-y.

[27] D. Nesterenko, T. Eronen, Z. Ge, A. Kankainen, and M. Vilen, Eur. Phys. Jour. A **57**, 302 (2021), URL https://doi.org/10.1140/epja/s10050-021-00608-3.

[28] G. Gräff, H. Kalinowsky, and J. Traut, Z Physik A **297**, 35 (1980), URL https://doi.org/10.1007/BF01414243.

[29] M. Kretzschmar, Int. J. Mass Spectrom. **264**, 122 (2007), URL https://doi.org/10.1016/j.ijms.2007.04.002.

[30] S. George, K. Blaum, F. Herfurth, A. Herlert, M. Kretzschmar, S. Nagy, S. Schwarz, L. Schweikhard, and C. Yazidjian, Int. J. Mass Spectrom. **264**, 110 (2007), URL https://doi.org/10.1016/j.ijms.2007.04.003.

[31] A. Kellerbauer, K. Blaum, G. Bollen, F. Herfurth, H.-J. Kluge, M. Kuckein, E. Sauvan, C. Scheidenberger, and L. Schweikhard, Eur. Phys. J. D **22**, 53 (2003), URL https://doi.org/10.1140/epjd/e2002-00222-0.

[32] M. Wang, W. Huang, F. Kondev, G. Audi, and S. Naimi, Chinese Physics C **45**, 030003 (2021), URL https://doi.org/10.1088/1674-1137/abddaf.

[33] J. Rissanen, J. Kurpeta, A. Plochocki, V. V. Elomaa, T. Eronen, J. Hakala, A. Jokinen, A. Kankainen, P. Karvonen, I. D. Moore, et al., Eur. Phys. J. A **47**, 97 (2011), URL https://doi.org/10.1140/epja/i2011-11097-0.

[34] G. Audi, O. Bersillon, J. Blachot, and A. Wapstra, Nucl. Phys. A **729**, 3 (2003), ISSN 0375-9474, the 2003 NUBASE and Atomic Mass Evaluations, URL https://www.sciencedirect.com/science/article/pii/S0375947403018074.

[35] G. Audi, F. G. Kondev, M. Wang, B. Pfeiffer, X. Sun, J. Blachot, and M. MacCormick, Chin. Phys. C **36**, 1157 (2012), URL https://dx.doi.org/10.1088/1674-1137/36/12/001.

[36] G. Audi, F. G. Kondev, M. Wang, W. J. Huang, and S. Naimi, Chin. Phys. C **41**, 030001 (2017), URL https://dx.doi.org/10.1088/1674-1137/41/3/030001.

[37] J. Kurpeta, G. Lhersonneau, J.C. Wang, P. Dendooven, A. Honkanen, M. Huhta, M. Oinonen, H. Penttilä, K. Peräjärvi, J.R. Persson, et al., Eur. Phys. J. A **2**, 241 (1998), URL https://doi.org/10.1007/s100500050114.

[38] J. Kurpeta, W. Urban, C. Droste, A. Płochocki, S. G. Rohoziński, T. Rzaca-Urban, T. Morek, L. Próchniak, K. Starosta, J. Äystö, et al., The European Physical Journal A **33**, 307 (2007), ISSN 1434-601X, URL https://doi.org/10.1140/epja/i2006-10464-2.

[39] J. Blachot, Nucl. Data Sheets **111**, 1471 (2010), ISSN 0090-3752, URL https://www.sciencedirect.com/science/article/pii/S0090375210000529.

[40] K.-L. Kratz and B. Pfeiffer, private communication to G. Audi, June 2000.

[41] J. Kurpeta, J. Rissanen, A. Płochocki, W. Urban, V.-V. Elomaa, T. Eronen, J. Hakala, A. Jokinen, A. Kankainen, P. Karvonen, et al., Phys. Rev. C **82**, 064318 (2010), URL https://link.aps.org/doi/10.1103/PhysRevC.82.064318.

[42] M. Matos, Ph.D. thesis, Justus-Liebig-Universität Giessen (2004), URL http://dx.doi.org/10.22029/jlupub-9512.

[43] S. Goriely, N. Chamel, and J. M. Pearson, Physical Review C **93**, 034337 (2016), ISSN 2469-9985, 2469-9993, URL https://link.aps.org/doi/10.1103/PhysRevC.93.034337.

[44] P. Möller, A. Sierk, T. Ichikawa, and H. Sagawa, Atomic Data and Nuclear Data Tables **109-110**, 1 (2016), ISSN 0092-640X, URL https://www.sciencedirect.com/science/article/pii/S0092640X1600005X.

[45] J. Duflo and A. Zuker, Physical Review C **52**, R23 (1995), ISSN 0556-2813, 1089-490X, URL https://link.aps.org/doi/10.1103/PhysRevC.52.R23.

[46] Z. M. Niu and H. Z. Liang, Physical Review C **106**, L021303 (2022), URL https://link.aps.org/doi/10.1103/PhysRevC.106.L021303.

[47] W. Ryssens, Ph.D. thesis, Université Libre de Bruxelles, Brussels (2016), URL https://inspirehep.net/files/3011a13e26b3c2dbf7429a4020f855bd.

[48] F. R. Xu, P. M. Walker, and R. Wyss, Phys. Rev. C **65**, 021303 (2002), URL https://link.aps.org/doi/10.1103/PhysRevC.65.021303.

[49] Note1, for axially symmetric configurations, we always align the symmetry axis with the z-axis in the simulation volume.

[50] B. Bally and M. Bender, Phys. Rev. C **103**, 024315 (2021), URL https://link.aps.org/doi/10.1103/PhysRevC.103.024315.

[51] Note2, the only exceptions occur for BSkG1 near the $Z = 50$ shell closure: ^{118}Ag, ^{119}Cd, ^{120}In and ^{121}Sn remain axially symmetric.

PIII

PIPERADE: A DOUBLE PENNING TRAP FOR MASS SEPARATION AND MASS SPECTROMETRY AT DESIR/SPIRAL2

by

P. Ascher, L. Daudin, M. Flayol, M. Gerbaux, S. Grevy, M. Hukkanen, A. Husson, A. de Roubin, P. Alfaurt, B. Blank, K. Blaum, B. Lachacinski, D. Lunney, E. Minaya Ramirez, S. Naimi, S. Perard and B. Thomas 2021

Contents lists available at ScienceDirect

Nuclear Inst. and Methods in Physics Research, A

journal homepage: www.elsevier.com/locate/nima

PIPERADE: A double Penning trap for mass separation and mass spectrometry at DESIR/SPIRAL2

P. Ascher [a],[*], L. Daudin [a], M. Flayol [a], M. Gerbaux [a], S. Grévy [a], M. Hukkanen [a],[b],
A. Husson [a], A. de Roubin [a], P. Alfaurt [a], B. Blank [a], K. Blaum [c], B. Lachacinski [a],
D. Lunney [d], E. Minaya Ramirez [d], S. Naimi [e], S. Perard [a], B. Thomas [a]

[a] *Université de Bordeaux, CNRS/IN2P3, CENBG, UMR5797, 33175 Gradignan, France*
[b] *University of Jyväskylä, P.O. Box 35, FI 40014, Jyväskylä, Finland*
[c] *Max–Planck-Institut für Kernphysik, Saupfercheckweg 1, 69117 Heidelberg, Germany*
[d] *Université Paris-Saclay, CNRS/IN2P3, IJCLab, 91405 Orsay, France*
[e] *RIKEN Nishina Center, Wako, Saitama 351-0198, Japan*

ARTICLE INFO

ABSTRACT

A double Penning trap is being commissioned at CENBG Bordeaux for the future DESIR/SPIRAL2 facility of GANIL. The setup is designed to perform both high-resolution mass separation of the ion beam for trap-assisted spectroscopy, and high-accuracy mass spectrometry of short-lived nuclides. In this paper, the technical details of the new device are described. First offline tests with the purification trap are also presented, showing a mass resolving power of about 10^5.

1. Introduction

The use of ion traps in radioactive ion beam (RIB) facilities has become essential these last decades [1,2], both for beam quality/purity improvement and for high-accuracy mass spectrometry. After the pioneering ISOLTRAP experiment at ISOLDE/CERN [3], Penning traps have been implemented in various facilities, such as JYFLTRAP/IGISOL [4], LEBIT/MSU [5], TITAN/TRIUMF [6], SHIPTRAP/GSI [7], CPT/CARIBU [8] and TRIGA-TRAP/TRIGA [9], all of them showing that this technique, widely used in other fields (atomic physics, quantum computing, …), is also extremely powerful in terms of nuclear mass precision, accuracy, sensitivity, efficiency as well as ion manipulation for high-resolution beam purification.

In this context, a double Penning trap named PIPERADE (PIèges de PEnning pour les RAdionucléides à DEsir, i.e. Penning traps for radionuclides at DESIR) [10,11] is being developed at Centre d'Etudes Nucléaires de Bordeaux-Gradignan (CENBG) for the future DESIR/ SPIRAL2 facility [12,13] of GANIL. DESIR will be dedicated to low-energy studies through precision measurements of nuclear ground and excited state properties. Decay spectroscopy, laser spectroscopy and trap-based devices will benefit from new 10–60 keV exotic ion beams from: (i) the upgraded SPIRAL1 facility [14], producing light nuclei by ISOL-fragmentation and (ii) the super separator spectrometer S3 [15] under commissioning, producing a wide range of neutron-deficient nuclei (including the refractory elements) by in-flight fusion–evaporation

with unprecedented intensities. A second phase may well emerge in the SPIRAL2 project, providing the accessibility to very neutron-rich nuclei by fission reactions.

DESIR will thus be unique in terms of beam intensities. While the production rate is crucial to study exotic nuclei, beam purity is also critically important. Isobaric contamination from non-selective ion production and/or ionization, as well as chemical reactions producing molecular contaminants, are often present with much higher intensities than the ions of interest, preventing certain types of measurements.

Beam purification can be performed using a magnetic dipole separator, such as the DESIR-HRS [16] developed at CENBG for DESIR. It has the advantage to be extremely fast (in-flight separation, i.e. a few tens of μs), to be able to handle high-intensity beams and it aims to push the current mass resolution limits of such a system, up to 2×10^4.

Nevertheless, even a higher resolution is required to separate a few ions of interest from a large number of contaminants, and more generally to separate very close isobars or even long-lived isomers. Indeed, high-precision measurements can be achieved only if the beam is isobarically-pure but also isomerically-pure. Penning traps are known to reach the highest resolving power, from 10^5 to 10^7 depending on the separation techniques, such as the standard sideband buffer gas cooling [17], Ramsey cleaning [18,19] or phase splitting [20–22]. All these techniques will be presented in this paper. However, the high-resolution performances of the Penning trap technique come at the

---

price of long separation times (>100 ms) and limited numbers of ions, up to 10^2–10^3 ions per bunch for the buffer gas cooling technique and only a few ions per bunch for the other methods. This is a consequence of space-charge effects which decrease the resolution and the efficiency for larger number of ions [23]. In order to push the limitations of existing devices further, the first trap of the double Penning trap PIPERADE will be a new type of high-capacity large trap that aims to separate up to 10^4–10^5 ions per bunch using the buffer gas cooling technique. In addition, other cleaning techniques allowing to reach the highest resolution, and requiring a gas-free trap, will be implemented in the second trap.

The pure beams extracted from the device will be re-injected in the main DESIR beam line, so that various experimental setups, such as total absorption spectrometry, collinear laser spectroscopy and decay measurements, will benefit from the trap performances.

Besides purification purposes, PIPERADE will be used as a mass-measurement setup on its own. The mass of an atomic nucleus is one of its most fundamental properties and is therefore a key observable to guide and constrain the current theoretical descriptions of the nucleus and the nucleon–nucleon interaction. Binding energy measurements along isotopic chains reveal structure effects [24], such as shell closures [25,26] or onsets of deformation [27]. In addition to fundamental nuclear physics questions, experimental masses are crucial to constrain nucleosynthesis models [28,29] (rp-process and r-process) and precise Q-value measurements of specific beta transitions have different applications, as tests of the weak interaction in the Standard Model [30] or the search of candidates for the neutrino mass measurement [31].

In this paper, details on the Penning trap technique will be given, followed by a full technical description of the PIPERADE system. The setup being now fully in operation, the tests with offline beam are ongoing ; first results using the first trap will briefly be presented whereas a detailed description of the offline studies will be given in another publication, in preparation.

2. Basics of Penning traps and operational modes of PIPERADE

2.1. Principle of a Penning trap and excitation techniques

A Penning trap allows the storage of charged particles thanks to the combination of a strong homogeneous magnetic field for the radial confinement and a static quadrupole electric field for the axial confinement. The electric potential is obtained by applying a voltage difference U_0 between a central ring electrode and two so-called endcap electrodes and can be expressed as

$$V(z, \rho) = \frac{U_0}{d^2}(2z^2 - \rho^2) \tag{1}$$

where z is the distance along the trap axis from the trap center, ρ the radial coordinate, and $d = \sqrt{z_0^2 + r_0^2/2}$ the characteristic trap geometry parameter, with z_0 the distance between the ring center and the endcaps, and r_0 the inner trap radius. The repulsive character of this electric field in the radial direction is compensated by the strong magnetic field obtained by installing the Penning trap in a superconducting magnet. For creating this quadrupole electric field, electrodes can be shaped as hyperboloids of revolution. An alternate way is to use a cylindrical trap and by choosing the potentials and lengths of the electrodes appropriately [32], the electric field can be made very close to a pure quadrupolar one near the trap center. It is the case of the PIPERADE traps, which are shown in Fig. 1.(a).

The resulting ion motion in a Penning trap is a superposition of three eigenmotions: (i) an harmonic axial motion along the trap axis at the frequency ν_z, (ii) a modified cyclotron motion at the frequency ν_+, and (iii) a magnetron motion at the frequency ν_-. The two latter motions are in the radial plane, the slow magnetron motion is centered at the trap axis and its orbit defines the center of the modified cyclotron motion. The true cyclotron frequency $\nu_c = qB/2\pi m$, with q the ion

charge, m the ion mass and B the strength of the magnetic field, corresponds, for an ideal trap, to the sum of the two radial frequencies.

The main interest of a Penning trap lies in the manipulation of these ion motions. Each motion has its own fixed frequency, defined by the electric and magnetic fields and the charge-to-mass ratio q/m of the trapped ions. However, the amplitude of these motions can be modified by bringing/removing energy to/from the motions. There are different ways of doing so, one being to fill the trap with a buffer gas. The ion collisions with the gas atoms will lead to a fast decrease of the amplitude of both the axial and the modified cyclotron motions, whereas the magnetron motion radius will slowly increase.

The second powerful way to manipulate the ions is to apply radio-frequency (RF) fields on the trap electrodes. Excitations of the axial motion can be performed by applying RF fields on the endcaps, but in the following only radial motion excitations will be described. For this, the central ring electrode is used and has to be segmented. In the case of PIPERADE, as can be seen in Fig. 1.(b), the ring electrode of the first trap, called the purification trap (PT), is 8-fold segmented whereas the ring electrode of the second trap, called the measurement trap (MT), is 4-fold segmented. There are two main modes for performing excitations: the dipolar and the quadrupolar modes.

The dipolar mode consists of applying an RF field in one radial direction. If the RF signal is applied at one of the eigenfrequencies, the radius of the corresponding motion will be modified without changing the others. When the excitation and the ion motion are in phase, the ions will be pushed from the electrode where the RF signal is applied every time it passes in front of it, and therefore the radius will increase. Fig. 1.(b) shows how the two different dipolar excitations at ν_- or ν_+ are applied on the ring segments. One should note that each trap segment is connected to a given function generator providing a specific frequency and phase. For the purification trap, opposite phases 0 and π are applied on opposite segments whereas for the measurement trap, only one phase is applied on a single segment, also creating a dipolar field component but with lower amplitude.

The quadrupolar mode consists of applying an RF signal with the same phase on two opposite segments (see ν_c excitation in Fig. 1.(b). For the purification trap, the same RF signal with the opposite phase is additionally applied to the two other orthogonal segments for a higher quadrupolar field component. This type of field is applied only on sums of eigenfrequencies and allows to couple motions. A quadrupolar RF excitation at $\nu_c = \nu_+ + \nu_-$ will couple the modified cyclotron motion to the magnetron motion, i.e. as long as the excitation is applied there will be a periodic conversion between the amplitudes of both motions. Therefore, what is called a π-pulse excitation corresponds to a single conversion from a pure motion to another pure one. The period of the interconversion process depends on the amplitude of the excitation field. An alternate way to couple the radial motions is to use an octupolar mode, which increases the resolving power [33]. This is technically achieved by using an 8-segmented ring like the purification trap and by applying the same phase on the four opposite segments at the frequency $2\nu_c$.

These dipolar and quadrupolar fields are usually applied by one RF pulse at a given amplitude and for a given duration, which will be inversely proportional to the frequency width of the excitation. Therefore the longer the excitation, the higher the resolution. An alternate way is to use time-separated oscillatory fields, called Ramsey fields [18,34], by applying two identical pulses separated by a certain time duration, which increases the resolution and the precision of the technique, as it will be explained in the next Section.

2.2. Mass separation and mass spectrometry techniques

All the various mass separation and mass measurement techniques that will be used at PIPERADE will be based on the above-described manipulation methods. The double-Penning trap PIPERADE device consists of two cylindrical traps, separated by a diaphragm for selection
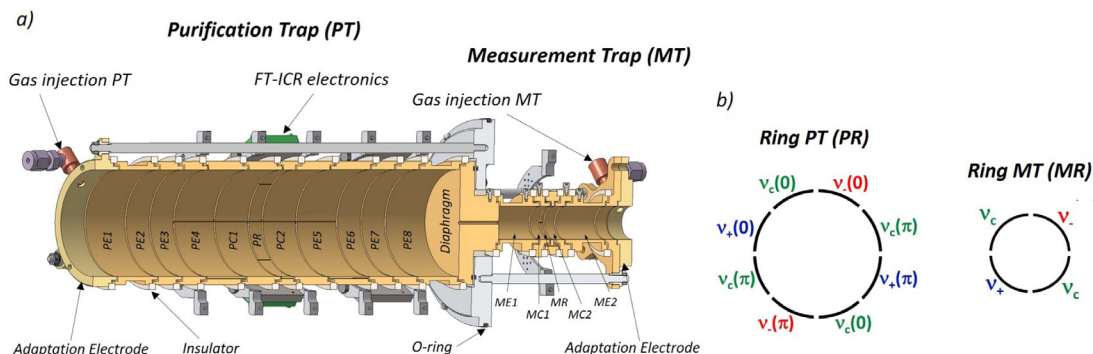
Fig. 1. (a) The two Penning traps of PIPERADE separated by a diaphragm. The purification trap (PT) consists of eleven electrodes, i.e. two endcap electrodes, which are four-fold axially-segmented (PE1-PE4, PE5-PE8), two correction electrodes (PC1, PC2) and one central ring electrode (PR). The measurement trap (MT) consists of five electrodes, i.e. two endcap electrodes (ME1, ME2), two correction electrodes (MC1, MC2) and one central ring electrode (MR). The electronics for broad-band FT-ICR detection can be seen on top of the purification trap. Gas inlets for helium feedings are fixed on the adaptation electrodes on the far sides of the purification and measurement traps. (b) Schematic view of the central ring electrodes of PT and MT. Dipolar excitation at ν_- is shown in red, dipolar excitation at ν_+ is shown in blue, whereas quadrupolar excitation at ν_c is shown in green. (For interpretation of the references to color in this figure legend, the reader is referred to the web version of this article.)

purposes but also to act as a pumping barrier. Indeed, depending on the operational mode the pressure in both traps will have to be different. These different techniques and the main operational modes of PIPERADE are described in the following.

2.2.1. PIPERADE as a mass separator

PIPERADE will be used for mass separation and will deliver pure beams to the DESIR users for post-trap spectroscopy. The standard separation technique, which will be used in the purification trap of PIPERADE is the so-called sideband buffer gas cooling technique [17]. It consists of two main steps: first a dipolar excitation is applied at the magnetron frequency ν_-. This frequency being in first-order mass-independent, it results in an increased magnetron radius for all ion species in the trap. The second step uses the combination of a quadrupolar field at ν_c, which converts the magnetron motion into a modified cyclotron motion, and the effect of the buffer gas, which cools the modified cyclotron motion. As the quadrupolar excitation is highly selective, only the ions of interest are re-centered in the trap. By ejecting the ions through the diaphragm, only the re-centered ones are transferred to the measurement trap. This powerful technique has the advantage of removing multiple contaminants, even unidentified ones, to handle large ion bunches (up to 10^2–10^3 ions) and to reach resolutions up to 10^5. The limitation in terms of number of ions is due to space-charge effects, leading to frequency shifts, peak broadening and screening effects, which makes the re-centering inefficient [23,35]. As it is shown for example from simulations in [10], reducing the cloud density, i.e. expanding the cloud for a given number of ions, is a way to limit these space-charge effects. By increasing the trap size, the field anharmonicities are further from the center thus the cloud size can be larger. This is why the purification trap of PIPERADE has a large diameter (64 mm) and aims at separating larger ion bunches (more than 10^4 ions). More recently, promising variants of this sideband buffer gas cooling technique have emerged, such as the octupolar excitation for the re-centering [36] or the so-called buffer-gas-free SIMCO excitation [37]. They will be studied using PIPERADE.

The purification trap will mostly be used for sideband buffer gas cooling, whereas the measurement trap could be used for accumulation purposes. One can repeat the purification cycle by sending each time a newly cleaned sample to the measurement trap, where He gas is injected for an efficient trapping. Once the accumulated sample is large enough for a measurement, a final cleaning is needed to get rid of the daughter nuclei produced during the accumulation time and the highly-purified sample of ions of interest can be sent to the downstream experiments.

The measurement trap could also be used for further high-resolution mass separation. With very few ions and in a gas-free trap, other

techniques can be used to reach a very high resolving power and separate close isobars or isomers. The so-called dipole cleaning can be used by applying a dipolar field at the modified cyclotron frequency ν_+ of a well-known contaminant, whose radius is increased enough to not be extracted from the trap. By applying time-separated pulses, as described in the previous section, the so-called Ramsey cleaning is very powerful for a highly-selective cleaning of a given contaminant. More details can be found in [19]. Such cleaning methods can reach resolutions up to about 10^6, which makes this technique also suitable for isomeric cleaning.

Finally, a very recent method, which has been implemented at JYFLTRAP for post-trap spectroscopy, is the phase-splitting method, inspired by the Phase-Imaging Ion-Cyclotron-Resonance (PI-ICR) measurement technique [20]. Details can be found in [21,22]. The first step of this method is to excite the modified cyclotron motion of the trapped ions by applying a short broad-band dipolar excitation. The excitation being short, it is not highly selective and the radial amplitudes of all the isobars and any isomers are thus increased. Then the basic principle of this separation is to let the ions oscillate at the fast modified cyclotron frequency ν_+ for a given time, so that the species are separated in phase. This technique requires the use of a position-sensitive micro-channel plate (MCP) detector, in order to project the radial position of the ion cloud on the detector. One should note here that extracting the ions moving at the higher ν_+ frequency will lead to a smearing of the ion spot on the MCP. Therefore, before the ion extraction, a π-pulse excitation has to be applied to convert the pure modified cyclotron motion into a pure magnetron motion, which then is slow enough to observe a well-defined spot on the detector. After the separation, the isobar or the state of interest can be transported to the post-trap spectroscopy device through a diaphragm with a hole at the appropriate angle and radius from the center. The selection method used at JYFLTRAP is to adapt the accumulation time so that the two species are separated by 180 degrees. A magnetron excitation in opposite phase with the motion of the ions of interest will center them in the trap while moving contaminants off-axis [22]. The selection method proposed in [21] is to apply a static excitation, to shift the center of the trap and then re-center the ions of interest. This has never been tested. The phase splitting method is very powerful in terms of resolution, which can even reach 10^7 for long accumulation times.

In the case of isomeric cleaning, before sending the isomeric beam to post-trap spectroscopy, the excitation energy of the isomeric state could also be measured with the techniques presented in the next section.

2.2.2. PIPERADE as a mass spectrometer

When using PIPERADE as a mass spectrometer, a highly-purified sample is required. Therefore both traps will still be used for various mass separations explained in the previous section before the
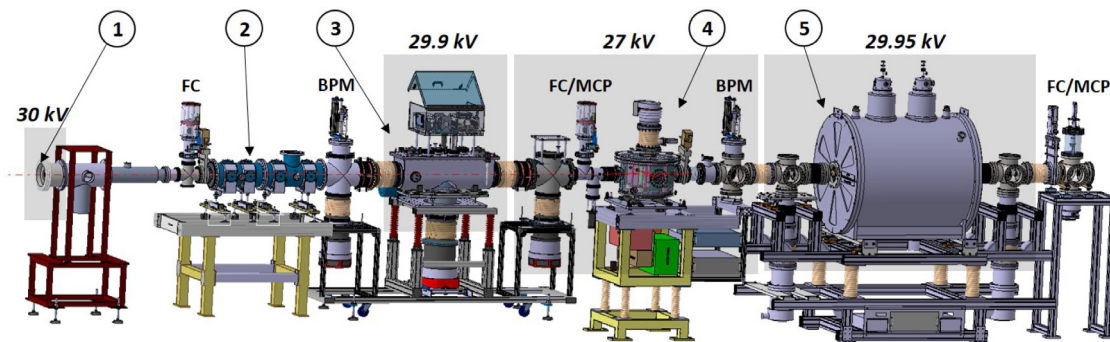
Fig. 2. Experimental setup at CENBG, consisting of (1) a stable ion source floated at 30 kV, (2) a DESIR - quadrupole triplet, (3) the GPIB (General Purpose Ion Buncher) floated at about 29.9 kV, (4) an electrostatic deflector floated at 27 kV and (5) the 7-Tesla Penning-trap system floated at about 29.95 kV. Faraday cups (FC), beam profile monitors (BPM) and micro-channel plates (MCP) detectors are installed in the beam line for ion beam diagnostics.

precision mass measurement in the second trap is realized. The mass measurement of an ion is performed through the determination of its true cyclotron frequency $v_c = qB/2\pi m$. Once the cyclotron frequency is measured, only the magnetic field has to be measured to extract the mass of the ion. This is performed by alternatively measuring the cyclotron frequency of the ion of interest and that of a very well-known reference isotope. Even if the magnetic field is not monitored during the measurement of the ion of interest, if the field drift and fluctuations are small enough, a linear interpolation is sufficient, not to add systematic uncertainties to the measured mass.

The standard technique for cyclotron frequency determination used since decades is the ToF-ICR technique and is described in detail in [38]. The precision achieved with this method is of the order of 10^{-8} for short-lived nuclides. As for the dipole cleaning method, the Ramsey method has boosted this technique, with an increase of a factor of 3 in the precision on the mass determination [18].

A few years ago, the PI-ICR method has been introduced in the field and implemented in many Penning-trap mass spectrometers, such as SHIPTRAP [39] where it was first developed, CPT [40], ISOLTRAP [41] and JYFLTRAP [22]. It has been shown to reach a fivefold gain for the precision on the cyclotron frequency determination compared to the Ramsey ToF-ICR technique. This non-scanning method opens the way to mass measurements of very exotic nuclei but also long-lived isomers, due to the excellent resolution it can reach (see the previous subsection).

3. Overview of the experimental setup at CENBG

The PIPERADE setup is currently being developed and commissioned at CENBG before its currently scheduled installation at DESIR/GANIL in 2024. A FEBIAD ion source is used to produce stable ions, either by ionizing a gas injected in the source, or by surface-ionizing the alkali naturally present on the filament surface. The injection into the Penning trap requires a bunched and cooled beam, mostly to optimize the transmission efficiency but also to reduce the phase-space volume when trapping the ions. For this purpose, a gas-filled Radio Frequency Quadrupole (called GPIB for General Purpose Ion Buncher) is also developed at CENBG. The GPIB will be installed on the entrance beam line of the DESIR hall, acting as the main cooler-buncher of DESIR. Details on this device will be found in [42]. As displayed in Fig. 2, the PIPERADE setup is placed directly downstream of the GPIB. At its final position at DESIR/GANIL, PIPERADE will be displaced in parallel to the GPIB and the main beam line. Ion bunches will thus be sent to PIPERADE via a transfer line equipped with two 90° electrostatic deflectors. One of these electrostatic deflectors has been constructed and installed at CENBG (see Fig. 2) between the GPIB and PIPERADE devices for test purposes (e.g. transverse and longitudinal emittance measurements).

As can be seen in Fig. 2, the different devices are held on separate platforms electrically floated with respect to the ion source potential of 30 kV. The difference of the GPIB and PIPERADE platforms to the main source platform is tunable via 0–400V power supplies (DELTA Electronika SM1500) with negative polarity, one dedicated to each platform. This allows to adjust the ion energy for an optimized injection in the devices (about 29.9 kV for the GPIB and about 29.95 kV for PIPERADE). The transfer line from the GPIB to the PIPERADE setup through the deflector is floated at 27 kV, to be in the same electrostatic configuration as in DESIR where the 3-keV ions will be deflected. The ions extracted from the Penning-trap system are then accelerated to almost 30 keV and sent to a detection system dedicated to tests or mass measurements. In the future, the ion bunches will be sent back to the main DESIR beam line via a 45° bending.

Different beam optics systems are used to control the shape and the position of the beam all along the beam line: a DESIR quadrupole triplet is located between the source and the GPIB to optimize the injection into the GPIB and an einzel lens is located downstream the GPIB for an optimum injection of the beam into the magnetic field of PIPERADE. In addition, sets of horizontal and vertical steerers are located upstream of both GPIB and Penning-trap devices, in order to correct the angle and position of the ion beam. As can be seen in Fig. 2, retractable beam profile monitors are used to monitor the radial distribution and position of the ion beam injected in the GPIB and PIPERADE setups. Three Faraday cups along the beam line are used to optimize the ion beam transmission efficiency in continuous mode. When bunched with the GPIB, the ions are detected by micro-channel plates (MCP) detectors behind the GPIB at 27 kV and behind the traps at ground potential. The different beam diagnostics and their electronics are described in detail in Section 4.3. The whole PIPERADE beam line, starting after the deflector, composed of DN160 crosses, bellows and a DN125 vacuum tube inserted into the magnet, use the CF standard and a very low magnetic susceptibility stainless steel (316L-1.4435). Two magnetically-levitated turbomolecular pumps (Edwards STP-1003) are located at both ends of the setup, far from the magnet axis, as are the vacuum gauges. A third pump (Edwards STP-A803C) is located below the MCP chamber after the trap system. The pressures at the injection and extraction sides, are 8×10^{-8} mbar and 1×10^{-8} mbar, respectively. The injection side pressure is higher because of the GPIB helium gas. It will be lower at DESIR because the GPIB will be further upstream and additional pumping systems will be installed on the deflector chambers. As it will be mentioned later, this pressure is higher when injecting He gas in the first trap. The pressure at the MCP chamber is of the order of 10^{-8} mbar.

4. Technical description of the Penning-trap system

4.1. Double Penning trap

The double Penning trap of PIPERADE is shown in Fig. 1. As mentioned before, with a radius of 32 mm, the purification trap is one

of the largest Penning trap installed at any RIB facility (see [43] for details on the 90 mm-radius Penning trap of the TAMUTRAP facility), whereas the measurement trap has a radius of 10 mm. For both traps, deviations from the ideal quadrupole field are compensated by correction electrodes added between the rings and the endcaps electrodes. In addition, the dimensions of all electrodes and the voltages applied on them have been calculated to limit the anharmonicities of the electric trapping potentials (see Tables 1 and 2).

As can be seen in Fig. 1.(a), the endcaps of the purification trap are 4 times axially segmented, to offer the possibility to apply DC gradients at the injection and the extraction of the ions. In trapping configuration, they are all at the same potential. In the radial direction, as can be seen in Fig. 1.(b), the purification trap and the measurement trap have an 8-fold and 4-fold segmented central ring electrode, respectively, allowing to apply RF excitations. The correction electrodes are also radially segmented (two parts) for implementing a broad-band Fourier-Transform Ion-Cyclotron-Resonance (FT-ICR) detection [44], allowing a quick broad identification of the highly-abundant trapped contaminants. Filters and pre-amplifiers boards are directly mounted on the trap structure inside the vacuum, in order to reduce the noise of the very small induced current signal picked up on the electrodes. The full electronics system has been designed and built by Stahl-Electronics [45]. This detection technique has not been commissioned yet. Different diameters for the diaphragm have been machined in order to test different excitation patterns. The presently installed one has a 4 mm diameter. In addition, adaptation electrodes (see Fig. 1.a) are added on both sides of the double Penning trap, in order to fix the optics electrodes towers, which have a different diameter than the traps. As mentioned earlier, the double Penning trap will be used in different configurations, which require He buffer gas, in one and/or the other trap. For that reason, the gas feedings to both traps are independent and consist of PEEK tubes connected to the adaptation electrodes via gas inlets, made of brass. Outside the vacuum, stainless steel gas tubes allow to transfer the gas from the two mass flow controllers (BROOKS SLA5850S) to the gas feedthroughs. With the present diaphragm diameter of 4 mm, when injecting He gas in the first trap, the pressure upstream the magnet measured by the gauge can be increased up to about 5×10^{-6} mbar without degrading the vacuum downstream the Penning-trap setup. Monte Carlo simulations using the Molflow+ software [46] have been performed to estimate the pressure inside the first trap cavity when He gas is injected, under the assumption of being in a molecular regime. A factor of 12 between the pressure measured by the gauge and the pressure inside the trap has been determined.

4.2. Tower structure

The trap tower structure located in the superconducting magnet is divided into 3 independent parts: the double Penning-trap structure and two sets of 10 and 11 cylindrical electrodes for the injection and the extraction of the ions, respectively, in the critical areas of the magnetic field gradients (see Fig. 3). On both sides of the double Penning trap, the last injection electrode and the first extraction electrode are specific adaptation electrodes (see Fig. 1.a), with the same radius as the traps, to fix the optics electrodes, which all have a radius of 20 mm and 51 mm length. The full tower has been designed and machined at the Max Planck Institut für Kernphysik (MPIK) in Heidelberg, Germany.

The measurement trap electrodes and the diaphragm are made of oxygen-free copper, chosen for its high conductivity and low magnetic susceptibility. All the injection, extraction and purification trap electrodes are made of aluminum alloy (AW-5083), a compromise to have a reasonable weight, critical for a precise alignment and for an easier assembly of the full structure. The aluminum electrodes have first been plated with a 5-μm copper layer, and all the electrodes have then been silver (15 μm) and gold (5 μm) plated. The gold layer is to prevent oxidation whereas the silver one prevents gold from diffusing into the

Table 1
Dimensions (in mm) of the trap electrodes. The electrodes are separated from each other by a gap of 1 mm.

Electrode	Length (mm)
Purification trap (r = 32 mm)	
Endcap 1 (PE1)	30.0
Endcap 2 (PE2)	17.5
Endcap 3 (PE3)	17.5
Endcap 4 (PE4)	30.0
Correction 1 (PC1)	25.1
Ring (PR)	9.310
Correction 2 (PC2)	25.1
Endcap 5 (PE5)	30.0
Endcap 6 (PE6)	17.5
Endcap 7 (PE7)	17.5
Endcap 8 (PE8)	30.0
Diaphragm (r = 2 mm)	30
Measurement trap (r = 10 mm)	
Endcap 1 (ME1)	29.7
Correction 1 (MC1)	7.185
Ring (MR)	2.224
Correction 2 (MC2)	7.185
Endcap 2 (ME2)	29.7

Table 2
Voltages (V) applied to the entrance electrodes (ENT01-ENT10), the injection electrodes (INJ01-INJ10), the extraction electrodes (EXT01-EXT11) and the exit electrodes (OUT01-OUT10). For the purification trap, voltages (V) applied in "opening mode", i.e. when the ions are either injected in the trap (voltages from PE1 to PR) or extracted from the trap (voltages from PR to PE8), and in "closed" mode, i.e. when ions are trapped. The setup and the power supplies are installed on a high-voltage platform. All these voltages are thus relative to the platform reference.

Electrode	Voltage (V)
ENT01 - ENT10	from −2950 to −1000
INJ01 - INJ10	from −800 to −85
Purification trap	Open/Closed
Endcap 1 - Endcap 4 (PE1 - PE4)	−84/ 0
Correction 1 (PC1)	−82/−70
Ring (PR)	−80/−80
Correction 2 (PC2)	−82/−70
Endcap 5 - Endcap 8 (PE5-PE8)	−84/0
Diaphragm/Measurement trap	from −85 to −90
EXT01 - EXT11	from −100 to −120
OUT01 - OUT10	from −130 to −3000

copper material. In general, a tolerance of ±30 μm has been achieved for the dimensions of all the electrodes. All electrodes are insulated from each other by MACOR® rings. The tower electrodes are designed in such a way that the insulator rings cannot be seen by the ions (see Fig. 1.a). Concerning the radially-segmented electrodes, the segments are insulated from each other by saphire balls of 1.5 mm diameter. The kapton-insulated wires are connected to each electrode with M2.5 titanium screws. This tower is inserted in a DN125 vacuum tube and held via three rods screwed on metal landmarks soldered on the flanges at each extremity of the tube. Since the tower is thus radially and axially self-aligned in the tube, the latter can then be aligned in the magnet thanks to screws from a special system fixed to the magnet in vertical and horizontal directions. The radial alignment will be described in Section 4.6.3. In addition to the main trap tower, two other 10-electrode towers are installed on each side of the superconducting magnet, in the regions of deceleration/acceleration of the ions, and were also designed and manufactured at MPIK. They are made of aluminum alloy and have a radius of 20 mm and 60 mm length.

4.3. Beam diagnostics and detectors

Monitoring the ion beam is crucial to optimize the beam line and the in-trap techniques. As the trap device is on a high-voltage platform, there is no pulsed drift tube, the transmission efficiency can thus be
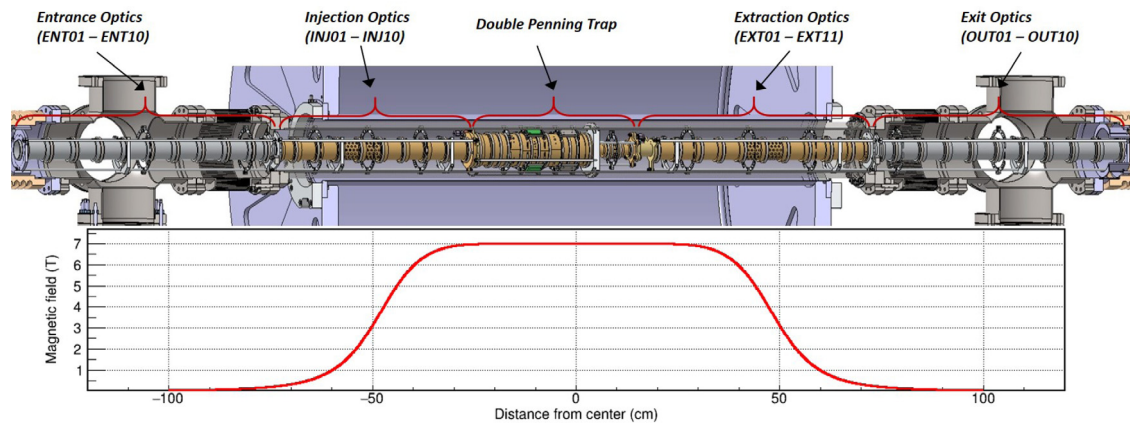
Fig. 3. Top: Trap tower in the superconducting magnet consisting of injection/extraction optics and the double Penning trap separated by a diaphragm and entrance/exit beam optics on both sides of the magnet. Bottom: Magnetic field in Tesla along the trap tower.

optimized with a continuous beam along the whole beam line. To do so, three movable Faraday cups (FC) are installed in the beam line, as can be seen in Fig. 2. These are DESIR-standard FC developed by GANIL, covering a very wide range of current intensities, from only 50 fA to 100 μA. To achieve such a high sensitivity, each FC is coupled to a low-bandwidth transimpedance linear amplifier called PicoLIN [47], also developed by GANIL within the SPIRAL2 project. The beam position, size and shape is monitored with SPIRAL2 beam profile monitors (BPM), based on secondary electron emission of 47 tungsten wire harps (0.5 mm step) for both horizontal and vertical planes [48]. Equipped with high-sensitivity charge preamplifiers, these semi-interceptive BPM are used to monitor down to a few tens of pA ion beams with a transparency higher than 90%.

Ion bunches generated by the GPIB can be detected by the FC, coupled to a fast commercial I/V converter (FEMTO DHPCA-100). This detection system can be used only for high-intensity bunches ($>10^4$ particles in a 1 μs bunch), the lower ion number limit strongly depending on the time distribution of the bunch. The voltage image of the bunch intensity is digitized with a Red Pitaya board, which is also controlling the amplifier using digital I/O (switchable gain from 10^2 to 10^8 V/A). The Red Pitaya board is a cost-efficient data acquisition platform based on a Xilinx FPGA and a dual-core ARM processor running a Linux operating system. Amplifier output signal sampling and quantization are achieved with a 14-bit ADC at 125 MSample/s in parallel with the digital I/O processing without any dead time. The Australian Synchrotron EPICS driver support is used to run the Faraday Cup EPICS server (see Section 4.5) in the Red Pitaya itself [49].

In case of low-intensity bunches, there are two MCP's (Topag MCP-MA33/2) installed in the beam line, one after the GPIB and one after the Penning-trap setup. They allow measuring the absolute number of ions in a bunch as well as performing time-of-flight measurements. The MCP anode signal is discriminated and a specific counting system has been developed. This FPGA development called RedPiTOF has been implemented into a dedicated Red Pitaya. Thanks to the use of two digital inputs (MCP counts and bunch gate signals), it allows to benefit from 50 MHz counters, time measurements with 10 ns time resolution and TOF spectrum construction in 16k channels without any dead time. The modified embedded EPICS server (see Section 4.5) allows from any EPICS Client to monitor online the MCP counting rate, the number of counts per bunch and the TOF spectrum. More details about this new development will be presented in a dedicated paper, under preparation.

A position-sensitive MCP (delay-line detector) is planned to replace the MCP after the trap, in order to implement the phase-splitting [21, 22] and PI-ICR [20] methods described in Section 2.2.

4.4. Trap electronics

In order to meet the DESIR High Voltage-Power Supplies (HV-PS) requirements, ISEG multichannel crates are used for providing the DC voltages to the DESIR instruments. The reasons of such a choice are (i) the large variety of low-noise, precise and stable HV-PS proposed, (ii) its ability to concentrate a large number of HV channels in a single crate, and (iii) the CC-24 ISEG crate controller with its built-in EPICS server (see Section 4.5). A SPIRAL2-like EPICS records database is developed and used on all DESIR ISEG crates. The PIPERADE electronics stands in a dedicated 19" rack placed on a 29.95 kV platform and require 75 HV-PS, all with negative polarity. The DC signals for the trap electrodes and the diaphragm are provided by 0–500V high-precision supplies (ISEG EHS-F205N). The injection and extraction electrodes are supplied by 0–1 kV modules (ISEG EHS F010n) whereas the entrance and exit electrodes on both sides of the magnet are supplied by 0–6 kV modules (ISEG EHS F060n). The switching of the trapping potentials is required to be fast, in order to capture efficiently the ions and to extract them from the traps without degrading their energy distribution. This is performed by homemade fast switches (see [42] for more details), capable of switching up to 100 V in about 30 ns. The RF fields for the different motion excitations are supplied by Agilent 33510B function generators with a 1 μHz frequency resolution. The ring electrode of both traps being supplied by both RF and DC signals, AC/DC couplings are performed before the connection to the trap electrodes. Another main instrument used as the conductor of the traps has been developed on a National Instruments CompactRIO device: the Pulse Pattern Generator (PPG). This real-time and FPGA-based device triggers the function generators and the fast switches with respect to a given time pattern defined by the users with a 12 ns time resolution. Ion bunch injection, trapping, cooling and excitation times, ion bunch transfer and extraction are controlled by this PPG.

4.5. Control system

Control System (CS) developments performed at CENBG for DESIR are based on the Experimental Physics and Industrial Control System (EPICS) architecture [50], being the basic framework for the SPIRAL2 control system [51]. PIPERADE is therefore also fully remotely controlled under EPICS. This system is based on Clients (Operator Interfaces) and Servers (Input Output Controllers IOC) communicating together via shared Process Variables (PVs) on an Ethernet Network using a dedicated communication protocol named Channel Access (CA). Most of the PIPERADE electronics is embedded on a high-voltage platform. Therefore, fiber optics coupled to Ethernet switches ensure galvanic insulation and TCP communication of the equipment with the EPICS IOCs running on a CentOS Linux PC. Some IOCs are embedded

into the equipment: this is the case for the ISEG HV multichannel crate (ISEG CC24 Controller) and the Red Pitaya used for beam intensity, ion counting and time-of-flight (RedPiTOF) measurements. SPIRAL2 vacuum systems and interlocks are controlled using dedicated PLCs (Siemens S7-1500). The Profibus Fieldbus is used by the vacuum PLC to communicate with turbo-molecular pumps and Profinet (Profibus on Ethernet Network) is deployed to manage Input-Ouput terminal modules (ET 200S) distributed along the beam line and on the high-voltage platforms. Each PLC has its own HMI (Human Machine Interface) on a dedicated Touch Panel.

Shared software development tools are used such as the SPIRAL2 version of CSS/BOY (CSS-Dev) used to build most of the Graphical User Interfaces (GUIs) and will handle central services like the data archiver or the alarm handler system in the near future. EPICS with its CA protocol makes possible to monitor and control any beam line equipment through its PVs in many programming languages. Using this EPICS feature, a Python program is under development to operate the traps, i.e. scan the different trapping and excitation parameters, control the PPG and read on-line output data from the RedPiTOF instrument. Bunch counts and TOF spectra are processed and plotted as a function of the scanned parameters. It is inspired by the PyMassScanner program [52] developed at JYFLTRAP.

4.6. Superconducting magnet

The superconducting magnet is a 7-Tesla magnet manufactured by CRYOGENIC [53], consisting of a set of NbTi windings immersed in liquid helium at 4.2 K. The main magnet has a 160 mm room-temperature bore in which the vacuum tube is installed and a cryostat with an overall diameter of 1112 mm and a length of 1250 mm. It has a 500 liter helium reservoir suspended within the cryostat vacuum space by stainless steel necks attached inside the turrets, surrounded by a 125 liter annular nitrogen reservoir. The main coil has been loaded to 118 A, leading to a magnetic field of 7 T. There is also an independent active shield coil wound onto the main winding magnet where no current is applied. However, a low current created by inductive coupling to the main coil is increasing with time, and might slightly modify the magnetic field. Therefore, every few months or before a precision measurement, the current on this coil has to be released. Two other superconducting compensation coils connected to the main coil, i.e. with the same current, are positioned on both ends of the magnet, allowing a first rough compensation of the inhomogeneity along the magnet axis. In addition, there are two sets of superconducting shim coils, allowing to adjust independently the homogeneity over two specific regions separated by 20 cm, corresponding to the two trap regions. Each set of coils has three 1st-order shim coils in the three directions X, Y and Z and an additional 2nd-order shim coil in Z direction (magnet axis) to compensate non-linear inhomogeneities.

4.6.1. Field homogeneity

The field homogeneity in the trapping region is crucial because the radial motion frequencies as well as the true cyclotron frequency depend on the magnetic field. As ion motions have non-zero amplitude, any inhomogeneity of the field in the space where the motions take place leads to frequency shifts, resulting in a loss of resolving power in mass separation or precision in mass measurements. The shimming has been done by adjusting currents of the order of a few ampere on X and Y shim coils for radial shimming, and on the Z shim coil for axial shimming. The 2nd-order coils were finally not needed for the adjustment. Since the latter have a strong inductive coupling to the main magnet, having in principle no current on these shim coils allows us to release from time to time, as for the shield coil, the accumulated induced current. An NMR probe coupled to a precision teslameter (Metrolab PT2025) has been used to precisely measure the magnetic field along the axis and around the two trap center regions. Fig. 4 shows the magnetic field homogeneity, i.e. the relative deviation
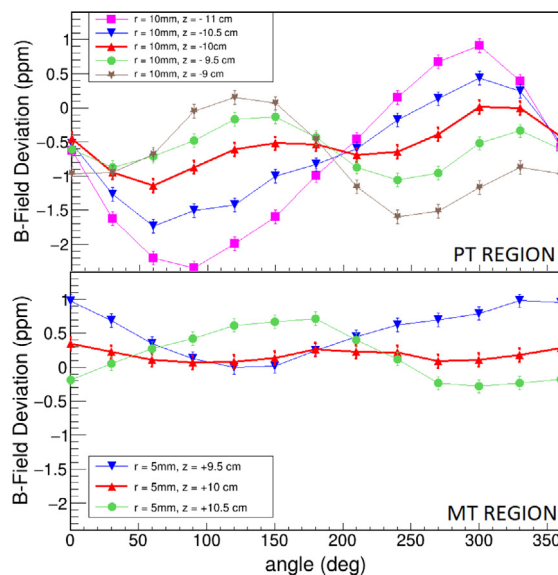

Fig. 4. Relative azimuthal magnetic field deviation from the centers of the PT (purification trap) and MT (measurement trap) trapping regions. The centers of these regions are at r = 0, z = −10 cm and z = +10 cm, for the PT and MT regions, respectively. Deviations are shown for different azimuth angles at a radius of 10 mm and over 20 mm length for the PT region and at a radius of 5 mm and over 10 mm length for the MT region. For both regions, the red bold lines correspond to the axial centers of the trapping regions.

from the centers of the trapping regions, separated by 20 cm. A wider region is shown for PT (purification trap), which has larger dimensions, and where ions will move further from the trap center. Even over a very large region of 10 mm radius and 20 mm length the homogeneity is still of the order of 3 ppm. On the MT (measurement trap) side, an homogeneity below 1.3 ppm has been obtained over a region of 5 mm radius and 10 mm length.

One should note that with the NMR-probe installed in the vacuum tube, the homogeneity determination was performed without the trap electrodes inserted in the tube. However, as it is described in Section 4.1, all materials were carefully chosen to be of very low magnetic susceptibility, so as not to induce any additional field inhomogeneity.

4.6.2. Field drift

Due to the so-called flux creep phenomenon [54], the magnetic field decreases over time. The active shield coil allows to reduce this drift from 0.13 ppm/h to 0.04 ppm/h. However, for precision mass measurements, this drift is still too high. Therefore, an additional warm coil has been added afterwards in the magnet bore, allowing to compensate very precisely the linear drift by applying a ramp of the order of +100 µA/h. This has been tested with the NMR-probe located at the center of the measurement trap's region and showed that the field drift can be reduced by about two orders of magnitude, as can be seen in Fig. 5. Due to the limited precision of the NMR-probe and the sensitivity of the teslameter to temperature fluctuations, this will have to be determined more precisely with the cyclotron frequency of trapped ions.

4.6.3. Tube alignment with respect to the magnetic field

Another cause of ion frequency shifts is a misalignment between the electric trapping field and the magnetic field axes. The way the main coil is suspended in the cryostat does not guarantee a perfect alignment of the coil in the main magnet structure. The coil also slightly moves when cooling the magnet, therefore the alignment procedure has to be performed when the magnet is warmed up and cooled again, i.e. after the move of the setup to GANIL.
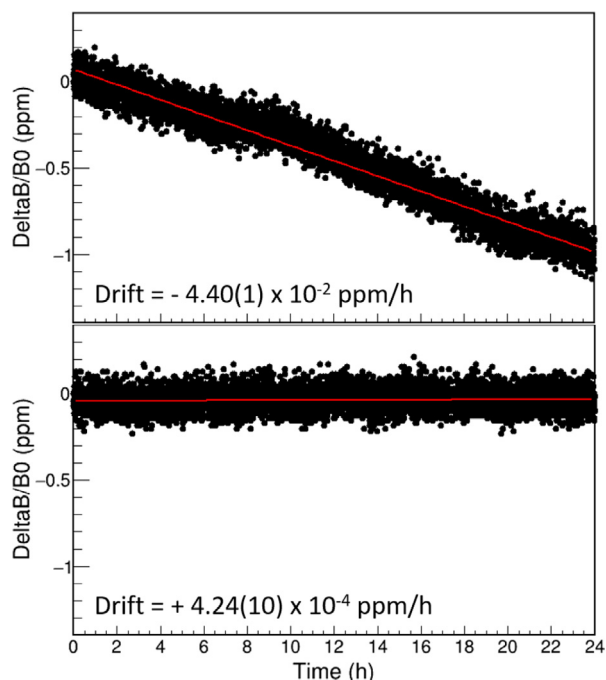
Fig. 5. Magnetic field B relative to the initial magnetic field B0 as a function of time. The red lines correspond to a fit of the data to a linear function ; the resulting slope is shown on the Figure. Top: No current is applied on the additional warm coil. Bottom: A positive ramp current is applied on the warm coil.
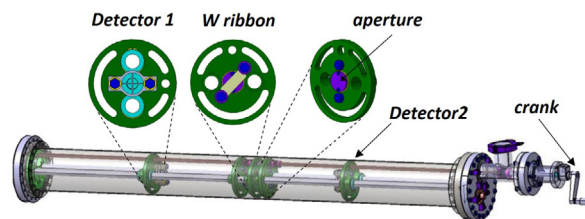

Fig. 6. Electron gun device installed in the vacuum tube, consisting of a tungsten ribbon in the center, apertures on both sides, as well as 8-fold segmented detectors with a hole and a plate behind. A crank connected to a worm gear is used to change the axial position of the detectors with respect to the filament.

The trap electrodes are mechanically aligned in the vacuum tube but this assembly must be aligned with the magnetic field axis. The option to move the vacuum tube with respect to the magnetic field axis has been chosen. It prevents moving the magnet while it is cold, which can be risky.

A standard procedure using an electron-gun device inserted in the vacuum tube has been used (see Fig. 6). By heating a tungsten ribbon positioned at the center of the magnet with a current of 10–15 A and by floating it to a potential of about −50 V, low-energy electrons are created and thus spiral closely around the magnetic field lines on both sides of the magnet. Two plates with apertures of 0.5 mm diameter each fixed on both sides of the filament and at a distance of 15 mm, define the initial shape and size of the electron beam. Detectors are placed at both ends of the magnet, each of them consisting of a metallic plate acting as a Faraday cup on which another 8-fold segmented plate (4 inner quadrants surrounded by 4 outer ones) with a 0.5 mm pinhole in the center is fixed. The aim of the procedure is to move the vacuum tube in such a way that the electron beam travels through the pinhole in the first layer of the detector and thus the electron current on the main detection plate is maximized. The segments of the first plate allow to estimate the position of the beam. The further the detectors are from the filament, the more precise is the alignment. However, starting the procedure with very far detectors is not convenient if the beam is not observed at all. Therefore, the two sets of detectors were mounted on elements sliding on rods, such that the axial position of the detectors could be controlled by a crank from outside the vacuum (see Fig. 6), so that the setup does not have to be opened every time the position has to be changed.

The vacuum tube inclination was finally corrected by 2.7(13) mrad. It is thus not perfectly aligned with the rest of the beamline anymore, but now well aligned with the magnetic field axis. The resulting cyclotron frequency shift from the possible remaining angle can be calculated from the formula given in [55,56]:

$$\Delta \nu_c = \frac{9}{8\pi} \nu_- \theta^2 \tag{2}$$

with θ the angle between the electric and magnetic field axes and ν_- the magnetron frequency of the trapped ions, being expressed, in first-order approximation, as $\nu_- = U_0/(4\pi d^2 B)$. One can notice from Eq. (2) that the absolute frequency shift is, in first-order, mass-independent. As explained in the following section, the trap parameter d^2 can be determined from the simulated electric field and is equal, for the measurement trap, to 134.49 mm^2. With $\theta = 1.3$ mrad, corresponding to the uncertainty on the angle, the resulting cyclotron frequency shift in the second trap will be from 0.5 mHz for a trapping potential of 10 V, to 5 mHz for a trapping potential of 100 V. The relative uncertainty on the true cyclotron frequency ν_c depends then on ν_c itself, the heavier the mass the larger the uncertainty. However, as it is explained in Section 2.2, the cyclotron frequency of an ion of interest ν_c is always measured relatively to a well-known reference ion with a cyclotron frequency ν_c^{ref}. Therefore, the resulting relative uncertainty we are interested in is the one on the ratio $r = \nu_c/\nu_c^{ref}$. In [56], it is given by the formula:

$$\frac{\delta r}{r} = \frac{9}{4} \theta^2 \frac{\nu_-}{\nu_+^{ref}} \left(\frac{\nu_+^{ref} - \nu_+}{\nu_+} \right) \tag{3}$$

By assuming that $\nu_+ \approx \nu_c$ for both the ions of interest and the reference ions, one can simplify Eq. (3) and define a shift factor R depending only on the trap parameters, the magnetic field strength and the misalignment of the magnetic field to the trap axis. For a mass measurement, the relative uncertainty will then be given by the trapping potential U_0 and the mass difference between the ions of interest and the reference ions ΔA:

$$\frac{\delta r}{r} = R \cdot U_0 \Delta A = \frac{9}{4} \theta^2 \frac{1}{2d^2 B^2} \frac{u}{q_e} \cdot U_0 \Delta A \tag{4}$$

with u the atomic mass unit and q_e the elementary charge (assuming all trapped ions are of 1^+ charge state). The final relative uncertainty resulting from an angle of 1.3 mrad between the magnetic and electric field axes is:

$$\frac{\delta r}{r} = 3.0 \times 10^{-12} V^{-1} \cdot U_0 \Delta A \tag{5}$$

Even with a trapping potential U_0 of 100 V and a ΔA of 10, the relative uncertainty of 3.0×10^{-9} is still negligible on the level of the expected precision of the Penning trap, i.e. of the order of 10^{-8} for short-lived ions.

5. First offline tests with the purification trap

We report here the first offline tests of the PIPERADE mass spectrometer. As no gas was injected in the stable ion source, the ion beam consisted only of surface-ionized elements. The ion beam was first cooled and bunched by the GPIB, with RF parameters set to transmit light ions, such as ^{39}K$^+$ or ^{40}Ca$^+$, and then sent to the PIPERADE traps. A so-called beam gate was implemented using one of the steerers at the exit of the ion source. Switching this electrode for a short moment allows to inject in the GPIB a well-defined number of ions, and also to

avoid the GPIB to be fed constantly with "hot" ions that mix with the cold ones when extracting an ion bunch.

The ion bunches are extracted from the GPIB floated at 29.9 kV towards the deflector at 27 kV with an energy of about 2.9 keV, and are then sent to the Penning-trap platform, which is at 29.95 kV. In order to attenuate the strong defocusing effect of the platform voltage change from 27 kV to 29.95 kV and a abrupt drop of the ion energy, the first entrance electrodes are set at about −2950 V, and then a smooth gradient is applied, in order to decelerate the ions for the injection in the purification trap, where the ion energy has to be lower than the trapping potential, in this case 80 V. Table 2 shows the voltages applied on the different electrodes. For the purification trap electrodes, "Open" and "Closed" correspond to the settings for injection/extraction and trapping modes, respectively. For the first tests, the four axial segments of each endcap were all connected together.

Before performing any trapping in the purification trap, the bunches were shot through the Penning trap tower and detected on the MCP detector behind the setup. The absolute transmission efficiency through the trap device is difficult to determine, because the MCP's before and after the traps have not been precisely calibrated and despite the fact they are identical, they might have slightly different detection efficiencies. This is mostly due to different time and spatial distributions of the bunches hitting the detector leading to different saturation effects, but also due to the difference in ion energy (3 keV after the GPIB and 30 keV after PIPERADE) and the fact that there are grids in front of the GPIB MCP (to measure the bunch energy dispersion) which might impact the detection efficiency. A test bench with another offline ion source is being mounted in the hall of CENBG, in order to precisely calibrate the detectors, depending on the ion beam conditions. Despite the difficulty of precisely determining the efficiency, the number of counts/bunch detected on the MCP after the GPIB and on the one after PIPERADE were similar for a given beam gate duration, which shows that the overall transmission efficiency is excellent, most probably above 30%–50%. One should note that in continuous mode, by detecting the beam on the Faraday cups, the transmission efficiency through the traps has been estimated to about 60%–70%. All these efficiencies will more precisely be measured during the on-going commissioning.

The trapping mode has then been tested. In order to capture the ions coming from the GPIB, the injection endcaps (PE1-PE4) are open while the extraction endcaps (PE5-PE8) are kept closed. Then, when the ions reach the trap center, the injection endcaps have to be closed, i.e. switched up to 0 V. The capture efficiency can be determined by the ratio of the number of counts of the MCP detector after a trapping cycle to the number of the counts in "shooting-through" mode, i.e. without any trapping. This has been determined to be >80% and is reliable because the MCP detector is the same one for both measurements.

The first sideband buffer gas cooling technique was performed with the following time pattern:

(1) Extraction from the GPIB (triggers the PPG of the trap)
(2) Waiting time while the ions fly from the GPIB to the PT (62 μs)
(3) Closing of the injection endcaps and first correction electrode
(4) Axial cooling time (200 ms)
(5) Dipolar magnetron excitation (15 ms)
(6) Quadrupolar cyclotron excitation (200 ms)
(7) Waiting time for cooling (200 ms)
(8) Opening of the extraction endcaps and second correction electrode
(9) Trigger for the MCP detection gate

As can be seen from the above time pattern, after the capture of the ions, a waiting time is needed to axially cool the ions before applying the magnetron excitation. This time is strongly dependent on the amount of buffer gas injected in the trap, the higher the pressure the shorter the time.

The magnetron excitation was first tested, meaning that step 6 was omitted. The dipolar field was applied during 10 magnetron periods with an amplitude of 2.2 Vpp. Fig. 7 shows the number of counts/bunch
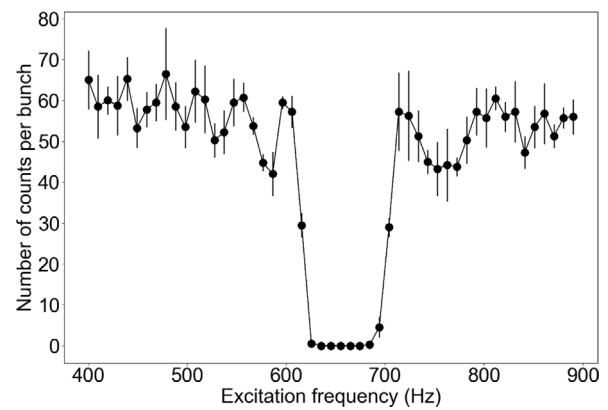

Fig. 7. Number of counts/bunch detected on the MCP detector behind the trap as a function of the frequency of the dipolar magnetron excitation.

detected on the MCP detector behind the trap as a function of the frequency of the RF excitation. We can see that at the resonance frequency ν_-, the counts/bunch drops to zero because the ion's magnetron radius has been increased to an orbit higher than the diaphragm radius, and thus no ions can be extracted from the trap. The amplitude of the magnetron excitation was tuned, so that it is high enough to radially push the ions beyond the diaphragm, but low enough so that the ions are not too far from the center. The further they are, the harder it is to re-center them because of frequency shifts induced by anharmonicities of the electric field and inhomogeneities of the magnetic field. The magnetron frequency has been determined to be about 660 Hz. This is in perfect agreement with the magnetron frequency calculation from the formula $\nu_- = U_0/(4\pi d^2 B)$, with $d^2 = 1360.90$ mm^2 determined from a linear fit of the trap electric field simulated by SIMION [57] (see Eq. (1)). The geometric formula for the characteristic trap parameter $d = \sqrt{z_0^2 + r_0^2/2}$ is actually not correct anymore for a real cylindrical Penning trap. All these offline tests were performed with He gas injected in the trap, giving a pressure of 2.6×10^{-7} mbar on the injection side of the magnet. From the Molflow simulations described in Section 4.1, the pressure inside the trap cavity was then of the order of 3×10^{-6} mbar.

A quadrupolar excitation of 200 ms duration was then applied (step 6 in the above time pattern) with 2 Vpp amplitude, in order to re-center the ions. Fig. 8 shows the number of counts/bunch detected on the MCP detector behind the trap as a function of the quadrupolar excitation RF frequency. This first resonance allows to confirm that ^{39}K$^+$ ions are indeed produced from the ion source. The resonance curve was fitted with a Gaussian function, resulting in a sigma of 11.0 Hz. With a FWHM of about 26 Hz, the resolution ν_c/FHWM is then 106 000. The targeted resolution of this technique has thus been achieved. Studies are ongoing to investigate the evolution of the resolution and the re-centering efficiency with respect to the different excitation parameters. The magnetron and cyclotron excitation amplitudes, as well as the amount of gas and the different pattern step times are strongly correlated and they all affect the sideband buffer-gas cooling performances. The next step is then to study separation performance as a function of the total number of trapped ions and for different ratios between the ions of interest and the contaminants.

6. Conclusions and outlook

A double Penning trap has been developed for mass separation and mass spectrometry at the future DESIR/SPIRAL2 facility. The installation of this device at CENBG has been finalized and is now under commissioning. First offline tests using the purification trap have shown that a resolution of 10^5 can be achieved. The next main step is to implement the mass spectrometry and high-resolution separation techniques for the measurement trap of PIPERADE. The first on-line experiments at DESIR with PIPERADE are foreseen in 2026.
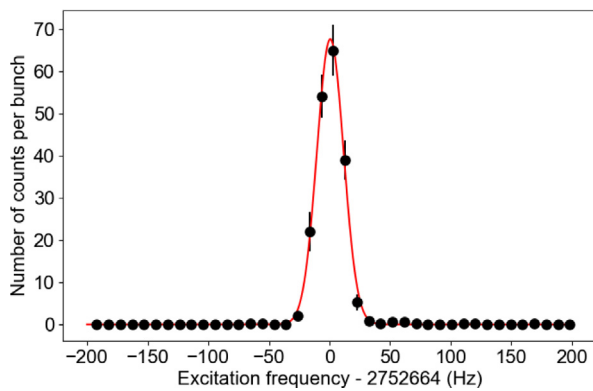
Fig. 8. Number of counts/bunch detected on the MCP detector behind the trap as a function of the frequency of the quadrupolar RF excitation. At the resonance frequency ν_c, $^{39}K^+$ ions are centered in the trap. The gaussian fit to the data, shown in red, has a sigma of 11.0 Hz. (For interpretation of the references to color in this figure legend, the reader is referred to the web version of this article.)

Declaration of competing interest

The authors declare that they have no known competing financial interests or personal relationships that could have appeared to influence the work reported in this paper.

Acknowledgments

References

[1] H.J. Kluge, Penning trap mass spectrometry of radionuclides, Int. J. Mass Spectrom. 349 (2013) 26, https://doi.org/10.1016/j.ijms.2013.04.017.

[2] T. Eronen, et al., Ion traps in nuclear physics - Recent results and achievements, Prog. in Part. and Nucl. Phys. 91 (2016) 259, http://dx.doi.org/10.1016/j.ppnp.2016.08.001.

[3] M. Mukherjee, et al., ISOLTRAP: An on-line penning trap for mass spectrometry on short-lived nuclides, Eur. Phys. J. A 35 (2008) 1, https://doi.org/10.1140/epja/i2007-10528-9.

[4] T. Eronen, et al., JYFLTRAP: A penning trap for precision mass spectrometry and isobaric purification, Eur. Phys. J. A 48 (2012) 46, http://dx.doi.org/10.1140/epja/i2012-12046-1.

[5] R. Ringle, et al., Penning trap mass spectrometry of rare isotopes produced via projectile fragmentation at the LEBIT facility, Int. J. Mass Spectrom. 349–350 (2013) 87–93, https://doi.org/10.1016/j.ijms.2013.04.001.

[6] A. Kwiatkowski, et al., Precision mass measurements at TITAN with radioactive ions, Nucl. Instrum. Methods Phys. Res. B 317 (2013) 517, https://doi.org/10.1016/j.nimb.2013.05.087.

[7] M. Block, et al., Towards direct mass measurements of nobelium at SHIPTRAP, Eur. Phys. J. D 45 (2007) 39, https://doi.org/10.1140/epjd/e2007-00189-2.

[8] G. Savard, et al., Studies of neutron-rich isotopes with the CPT mass spectrometer and the CARIBU project, Int. J. Mass Spectrom. 251 (2006) 252, https://doi.org/10.1016/j.ijms.2006.01.047.

[9] J. Grund, et al., First online operation of TRIGA-TRAP, Nucl. Instrum. Methods Phys. Res. A 972 (2020) 164013, https://doi.org/10.1016/j.nima.2020.164013.

[10] P. Ascher, et al., PIPERADE: A penning-trap isobar separator for the DESIR low-energy facility of SPIRAL2, EPJ Web of Conf. 66 (2014) 11002, https://doi.org/10.1051/epjconf/20146611002.

[11] E. Minaya Ramirez, et al., Conception of PIPERADE: A high-capacity penning-trap mass separator for high isobaric contamination at DESIR, Nucl. Instrum. Methods Phys. Res. B 376 (2016) 298, https://doi.org/10.1016/j.nimb.2016.01.044.

[12] B. Blank, S. Grévy, P.G. Thirolf, C. Weber, Perspectives for mass spectrometry at the DESIR facility of SPIRAL2, Int. J. Mass Spectrom. 349 (2013) 264, https://doi.org/10.1016/j.ijms.2013.03.006.

[13] https://heberge.cenbg.in2p3.fr/desir.

[14] P. Delahaye, et al., New exotic beams from the SPIRAL1 upgrade, Nucl. Instrum. Methods Phys. Res. B 463 (2020) 339, https://doi.org/10.1016/j.nimb.2019.04.063.

[15] F. Déchery, et al., The super separator spectrometer S3 and the associated detection systems: SIRIUS and LEB-REGLIS3, Nucl. Instrum. Methods Phys. Res. B 376 (2016) 125, https://doi.org/10.1016/j.nimb.2016.02.036.

[16] T. Kurtukian-Nieto, et al., SPIRAL2/DESIR high resolution mass separator, Nucl. Instrum. Methods Phys. Res. B 317 (2013) 284–289, https://doi.org/10.1016/j.nimb.2013.07.066.

[17] G. Savard, et al., A new cooling technique for heavy ions in a penning trap, Phys. Lett. A 158 (1991) 247, https://doi.org/10.1016/0375-9601(91)91008-2.

[18] S. George, et al., The ramsey method in high-precision mass spectrometry with penning traps: Experimental results, Int. J. Mass Spectrom. 264 (2007) 110, https://doi.org/10.1016/j.ijms.2007.04.003.

[19] T. Eronen, et al., Preparing isomerically pure beams of short-lived nuclei at JYFLTRAP, Nucl. Instrum. Methods Phys. Res. B 266 (2008) 4527, https://doi.org/10.1016/j.nimb.2008.05.076.

[20] S. Eliseev, et al., A phase-imaging technique for cyclotron-frequency measurements, Appl. Phys. B 114 (2014) 107, http://dx.doi.org/10.1007/s00340-013-5621-0.

[21] P. Dupré, et al., High-resolution mass separation by phase splitting and fast centering of ion motion in a penning trap, Int. J. Mass Spectrom. 379 (2015) 33, https://doi.org/10.1016/j.ijms.2014.12.007.

[22] D. Nesterenko, et al., Phase-imaging ion-cyclotron-resonance technique at the JYFLTRAP double penning trap mass spectrometer, Eur. Phys. J. A 54 (2018) 154, https://doi.org/10.1140/epja/i2018-12589-y.

[23] S. Van Gorp, Ph.D. thesis, KU Leuven, 2012.

[24] T. Yamaguchi, et al., Masses of exotic nuclei, Prog. in Part. and Nucl. Phys. (2021) https://doi.org/10.1016/j.ppnp.2021.103882.

[25] V. Manea, et al., First glimpse of the N = 82 shell closure below Z = 50 from masses of neutron-rich cadmium isotopes and isomers, Phys. Rev. Lett. 124 (2020) 092502, https://doi.org/10.1103/PhysRevLett.124.092502.

[26] E. Leistenschneider, et al., Precision mass measurements of neutron-rich scandium isotopes refine the evolution of N = 32 and N = 34 shell closures, Phys. Rev. Lett. 126 (2021) 042501, https://doi.org/10.1103/PhysRevLett.126.042501.

[27] A. de Roubin, et al., Nuclear deformation in the A = 100 region: Comparison between new masses and mean-field predictions, Phys. Rev. C 96 (2017) 014310, https://doi.org/10.1103/PhysRevC.96.014310.

[28] H. Schatz, et al., Nuclear masses in astrophysics, Int. J. Mass Spectrom. 349 (2014) 181, https://doi.org/10.1016/j.ijms.2013.03.016.

[29] M.R. Mumpower, et al., The impact of individual nuclear properties on r-process nucleosynthesis, Prog. in Part. and Nucl. Phys. 86 (2016) 86, https://doi.org/10.1016/j.ppnp.2015.09.001.

[30] T. Eronen, et al., High-precision QEC-value measurements for superallowed decays, Eur. Phys. J. A 48 (2012) 48, https://doi.org/10.1140/epja/i2012-12048-y.

[31] S. Eliseev, et al., Penning-trap mass spectrometry for neutrino physics, Int. J. Mass Spectrom. 349 (2013) 102, https://doi.org/10.1016/j.ijms.2013.03.010.

[32] G. Gabrielse, et al., Open-endcap penning traps for high precision experiments, Int. J. Mass Spectrom. 88 (1989) 319, https://doi.org/10.1016/0168-1176(89)85027-X.

[33] S. Eliseev, et al., Octupolar-excitation penning-trap mass spectrometry for Q-value measurement of double-electron capture in ^{164}er, Phys. Rev. Lett. 107 (2009) 152501, https://doi.org/10.1103/PhysRevLett.107.152501.

[34] N.F. Ramsey, Experiment with separated oscillatory fields and hydrogen masers, Rev. Modern Phys. 62 (1990) 541, https://doi.org/10.1103/RevModPhys.62.541.

[35] M. Heck, Ph.D. thesis, University of Heidelberg, 2013.

[36] M. Rosenbusch, et al., A study of octupolar excitation for mass-selective centering in penning traps, Int. J. Mass Spectrom. 314 (2012) 6–12, https://doi.org/10.1016/j.ijms.2012.01.002.

[37] M. Rosenbusch, et al., Buffer-gas-free mass-selective ion centering in penning traps by simultaneous dipolar excitation of magnetron motion and quadrupolar excitation for interconversion between magnetron and cyclotron motion, Int. J. Mass Spectrom. 325–327 (2012) 51–57, https://doi.org/10.1016/j.ijms.2012.06.008.

[38] M. Koenig, et al., Quadrupole excitation of stored ion motion at the true cyclotron frequency, Int. J. Mass Spectrom. 31 (1995) 95, https://doi.org/10.1016/0168-1176(95)04146-C.

[39] S. Eliseev, et al., Phase-imaging ion-cyclotron-resonance measurements for short-lived nuclides, Phys. Rev. Lett. 110 (2013) 082501, https://doi.org/10.1103/PhysRevLett.110.082501.

[40] R. Orfordand the others, Precision mass measurements of neutron-rich Neodymium and Samarium isotopes and their role in understanding rare-earth peak formation, Phys. Rev. Lett., 120 262702, https://link.aps.org/doi/10.1103/PhysRevLett.120.262702.

[41] J. Karthein, et al., Direct decay-energy measurement as a route to the neutrino mass, in: 7th International Conference on Trapped Charged Particles and Fundamental Physics, vol. 240, p. 61, Traverse City, United States, http://dx.doi.org/10.1007/s10751-019-1601-z.

[42] M. Gerbaux, et al., The general purpose ion buncher: A radiofrequency quadrupole cooler-buncher for DESIR at SPIRAL2, 2021, in preparation.

[43] P.D. Shidling, et al., The TAMUTRAP facility: A penning trap facility at texas a&m university for weak interaction studies, Int. J. Mass Spectrom. 468 (2021) 116636, https://doi.org/10.1016/j.ijms.2021.116636.

[44] M. Ubieto Diaz, et al., A broad-band FT-ICR penning trap system for KATRIN, Int. J. Mass Spectrom. 288 (2009) 1, https://doi.org/10.1016/j.ijms.2009.07.003.

[45] http://www.stahl-electronics.com.

[46] R. Kersevan, M. Ady, Recent developments of Monte-Carlo codes Molflow + and Synrad +, in: 10th Int. Particle Accelerator Conf., IPAC2019, Melbourne, Australia, pp. 1327–1330, http://dx.doi.org/10.18429/JACoW-IPAC2019-TUPMP037.

[47] C. Jamet, et al., Beam diagnostic overview of the SPIRAL2 RNB section, in: Proc. 10th European Workshop on Beam Diagnostics and Instrumentation for Particle Accelerators (DIPAC'11), 2011, pp. 314–316.

[48] J.L. Vignet, et al., The beam profile monitors for SPIRAL2, in: Proceedings of DIPAC2009, http://dx.doi.org/10.13140/2.1.4214.6569.

[49] Australian Synchrotron redpitatya-epics driver, https://github.com/AustralianSynchrotron/redpitaya-epics.

[50] L. Dalesio, et al., The experimental physics and industrial control system architecture: past, present and future, Nucl. Instrum. Methods Phys. Res. A 352 (1994) 179, https://doi.org/10.1016/0168-9002(94)91493-1.

[51] E. Lécorché, et al., Overview of the GANIL Control Systems for the Different Projects Around the Facility, in: Proc. of International Conference on Accelerator and Large Experimental Control Systems (ICALEPCS'17), Barcelona, Spain, 8-13 October 2017, 2018, pp. 406–410, https://doi.org/10.18429/JACoW-ICALEPCS2017-TUPHA016.

[52] T. Eronen, Private communication.

[53] http://www.cryogenic.co.uk.

[54] P. Anderson, Theory of flux creep in hard superconductors, Phys. Rev. Lett. 9 (1962) 309, https://doi.org/10.1103/PhysRevLett.9.309.

[55] L.S. Brown, G. Gabrielse, Geonium theory: Physics of a single electron or ion in a penning trap, Rev. Modern Phys. 58 (1986) 233, https://doi.org/10.1103/RevModPhys.58.233.

[56] G. Gabrielse, Why is sideband mass spectrometry possible with ions in a penning trap ? Phys. Rev. Lett. 102 (2009) 172501, https://doi.org/10.1103/PhysRevLett.102.172501.

[57] http://www.simion.com.